UNIVERSITY OF CALIFORNIA SAN DIEGO

Bayesian Time-Domain Finite Element Model Updating of Civil Infrastructure Systems

A dissertation submitted in partial satisfaction of the requirements for the degree
Doctor of Philosophy

in

Structural Engineering

by

Mukesh Kumar Ramancha

Committee in charge:

Professor Joel P. Conte, Chair
Professor Jose I. Restrepo
Professor Michael D. Todd
Professor Behrouz Touri

2022

The dissertation of Mukesh Kumar Ramancha is approved, and it is acceptable in quality and form for publication on microfilm and electronically.

University of California San Diego

2022

DEDICATION

To my parents, Rama Devi Ramancha and Ramesh Babu Ramancha, thank you for encouraging me in all my pursuits and supporting me to pursue my dreams.

To my friends, thank you for being there through all my hardships.

EPIGRAPH

“Genius is 1% talent and 99% percent hard work...”

— Albert Einstein

TABLE OF CONTENTS

LIST OF FIGURES

LIST OF TABLES

ACKNOWLEDGEMENTS

The work shown in this dissertation would not have been possible without the constant help, guidance, and support of many individuals. First, I would like to sincerely thank my advisor, Prof. Joel P. Conte, for the guidance over the past few years and for teaching me many valuable personal and professional life skills such as critical thinking, persistence, owning a project versus simply doing it, and the art of teaching and presenting. I'll always cherish these skills throughout my entire life.

I want to thank my committee members, Prof. José I. Restrepo and Prof. Michael D. Todd, for their contributions to my research, sitting through my prolonged presentations, and providing critical feedback and expert guidance over the past few years. Their comments and engineering insights have certainly helped me improve the quality of my work. Next, I would like to thank my committee member, Prof. Behrouz Touri from the ECE Department, for accepting my request to be part of my thesis committee and providing critical feedback during my candidacy and Ph.D. defense exams.

I would like to thank my co-authors and collaborators, Dr. Rodrigo Astroza, Dr. Matthew D. Parno, Dr. Manuel A. Vega, Dr. Zhen Hu, Dr. Ramin Madarshahian, and Dr. Rodrigo Carreño. Without these people, my research life would have been much more difficult.

I would like to thank my colleagues at UC San Diego, Angshuman Deb, Athul Parayancode, Mayank Chadha, and Amanpreet Singh, for countless insightful discussions over the past few years, which helped me clean out my strangled thoughts.

I would like to thank engineers from USACE, specifically Travis Fillmore, Mark Shultz, and Matthew D. Smith, for their valuable engineering insights about the miter gate and dam. I would also like to thank the USACE engineers for organizing the site visits to locks and dams

(located along the Ohio river) and providing us with a high-fidelity FE model of the Greenup gate.

I would like to thank Dr. Tim Cockerill from the Texas Advanced Computing Center located at UT Austin for providing me with access to Stampede2 and Frontera supercomputing resources, which accelerated my research progress. I would also like to thank Dr. Aakash Bangalore Satish and Dr. Frank McKenna from NHERI SimCenter located at UC Berkeley for their assistance with high-performance computing and OpenSees.

I would like to thank Dr. Zhijian Qiu and Dr. Quan Gu from Xiamen university for their help on dam modeling as well as Dr. Matthias Neuner and Dr. Guenter Hofstetter from the University of Innsbruck, Austria for their assistance on concrete material modeling. I would like to thank Daryl Rysberg for the IT support at UC San Diego.

I can arguably say that I spent most of my time in my lab (SME 416) over the past few years. I had great fun working with my lab mates, Angshuman Deb, Alex Zha, Kiida Lai, Lin Sun, Maitreya Kurumbhati, Michael Kohler, and Zachary Austin. I would like to thank them for the wonderful memories.

I would like to thank all the professors and teaching assistants of all 25 courses taken at UC San Diego. These courses helped me gain a tremendous background, thereby enabling me to do the research presented in this dissertation.

I would like to thank the UC San Diego structural engineering staff, Yvonne Wollman, Julie Storing, Lindsay Walton, and Kyung Brown, for taking care of all the logistical issues and making my research life much easier.

I would like to sincerely thank my parents (Rama Devi Ramancha and Ramesh Babu Ramancha) and my siblings (Mounika Ramancha and Sai Rithik Komuravelly) for always

believing in me, for being a backbone to me, and for always supporting me in pursuit of my dreams.

I'm incredibly fortunate to have a great group of friends in San Diego and back home in India. I firmly believe that you are an average of all the people you spend the most time with. I'm thankful to all my friends for filling my life with beautiful memories. I'm looking forward to many more memories with them. I would like to give a special mention to two of my friends or brothers, Rahul Hazra and Angshuman Deb, for always being there for me.

Last but not least, and if I may quote Snoop Dogg, "I would like to thank me!". I would like to thank myself for putting in all the hard work.

Portions of this dissertation have been published or are currently being considered for publication. Chapter 2, in part, is a reprint of the material as it appears in the following papers (the dissertation author is the first author of these papers):

Ramancha, M. K., Astroza, R., Madarshahian, R., and Conte, J. P. (2022). "Bayesian updating and identifiability assessment of nonlinear finite element models." *Mechanical Systems and Signal Processing*, 167, 108517. https://doi.org/10.1016/j.ymssp.2021.108517

Ramancha, M. K., Madarshahian, R., Astroza, R., and Conte, J. P. (2020). "Non-unique Estimates in Material Parameter Identification of Nonlinear FE Models Governed by Multiaxial Material Models Using Unscented Kalman Filtering." *Conference Proceedings of the Society for Experimental Mechanics Series*, 257–265. https://doi.org/10.1007/978-3-030-12075-7_29

Chapter 3, in full, is a reprint of the material as it appears in the following paper (the dissertation author is the first author of this paper):

Ramancha, M. K., Conte, J. P., and Parno, M. D. (2022). "Accounting for model form uncertainty in Bayesian calibration of linear dynamic systems." *Mechanical Systems and Signal Processing*, 171, 108871. https://doi.org/10.1016/j.ymssp.2022.108871

Chapter 4, in full, has been submitted for publication of the material as it may appear in the following paper (the dissertation author is the first author of this paper):

Ramancha, M. K., Vega, M. A., Conte, J. P., Todd, M. D., and Hu, Z. (2022). "Bayesian model updating with finite element vs. surrogate models: application to a miter gate structural system." Submitted to *Engineering Structures*.

Chapter 5, in part, is a reprint of the material as it appears in the following paper (the dissertation author is the first author of this paper):

Ramancha, M. K., Astroza, R., Conte, J. P., Restrepo, J. I., and Todd, M. D. (2020). "Bayesian nonlinear finite element model updating of a full-scale bridge-column using sequential monte carlo." *Model Validation and Uncertainty Quantification*, 389–397. https://doi.org/10.1007/978-3-030-47638-0_43

VITA

2015	Bachelor of Technology, Indian Institute of Technology, Guwahati, India
2016-2017	Teaching Assistant, University of California San Diego
2017	Master of Science, University of California San Diego
2017-2022	Research Assistant, University of California San Diego
2022	Doctor of Philosophy, University of California San Diego

PUBLICATIONS

Journal Papers:

Ramancha, M. K., Astroza, R., Madarshahian, R., and Conte, J. P. (2022). "Bayesian updating and identifiability assessment of nonlinear finite element models." *Mechanical Systems and Signal Processing*, 167, 108517. https://doi.org/10.1016/j.ymssp.2021.108517

Ramancha, M. K., Conte, J. P., and Parno, M. D. (2022). "Accounting for model form uncertainty in Bayesian calibration of linear dynamic systems." *Mechanical Systems and Signal Processing*, 171, 108871. https://doi.org/10.1016/j.ymssp.2022.108871

Ramancha, M. K., Vega, M. A., Conte, J. P., Todd, M. D., and Hu, Z. (2022). "Bayesian model updating with finite element vs. surrogate models: application to a miter gate structural system." Submitted to *Engineering Structures*.

Kurumbhati, M. M., **Ramancha, M. K.**, Aakash, B. S., Conte, J. P., Lotfizadeh, K. H., and Restrepo, J. I. (2022). "Hierarchical Bayesian modeling for calibration and validation of constitutive material models." Under preparation for submission to *Mechanical Systems and Signal Processing*.

Chadha, M., **Ramancha, M. K.**, Vega, M. A., Conte, J. P., and Todd, M. D. (2022). "The modeling of risk perception in the use of structural health monitoring information for optimal maintenance decisions." Submitted to *Reliability Engineering & System Safety*.

Hu, Z., Jiang, C., Vega, M. A., **Ramancha, M. K.**, Todd, M. D., Conte, J. P., and Parno, M. D. (2022). "Bayesian calibration of multi-level model with unobservable distributed response and application to miter gates." *Mechanical Systems and Signal Processing*, 170, 108852, https://doi.org/10.1016/j.ymssp.2022.108852

Conference Papers

Ramancha, M. K., Madarshahian, R., Astroza, R., and Conte, J. P. (2020). "Non-unique Estimates in Material Parameter Identification of Nonlinear FE Models Governed by

Multiaxial Material Models Using Unscented Kalman Filtering." *Conference Proceedings of the Society for Experimental Mechanics Series*, 257–265. https://doi.org/10.1007/978-3-030-12075-7_29

Ramancha, M. K., Astroza, R., Conte, J. P., Restrepo, J. I., and Todd, M. D. (2020). "Bayesian nonlinear finite element model updating of a full-scale bridge-column using sequential monte carlo." *Model Validation and Uncertainty Quantification*, 389–397. https://doi.org/10.1007/978-3-030-47638-0_43

Vega, M. A., **Ramancha, M. K.**, Conte, J. P., and Todd, M. D. (2020). "Efficient Bayesian Inference of Miter Gates Using High-Fidelity Models." *Model Validation and Uncertainty Quantification*, 375–382. https://doi.org/10.1007/978-3-030-47638-0_41

ABSTRACT OF THE DISSERTATION

Bayesian Time-Domain Finite Element Model Updating of Civil Infrastructure Systems

by

Mukesh Kumar Ramancha

Doctor of Philosophy in Structural Engineering

University of California San Diego, 2022

Professor Joel P. Conte, Chair

The American Society of Civil Engineers (ASCE) 2021 report card rated the U.S. infrastructure at a C- grade. Therefore, there is an operational need for structural health monitoring (SHM) and damage prognosis (DP) for large-scale civil infrastructure systems. An effective way of performing SHM/DP of structural systems is by using a hybrid physics-based

and data-driven digital twin or cyber model. A potential approach for constructing digital twins of civil structural systems consists of using the Bayesian finite element (FE) model updating framework. The process of calibrating probabilistically, using the Bayesian inference framework, a FE model of a structural system using sensor measurement data collected from the system is termed as Bayesian FE model updating.

Most methods of FE model updating for SHM consist of updating linear FE models based on changes in modal parameters identified before and after a potentially damaging event (e.g., an earthquake) using low amplitude vibration data. However, these modal methods only identify damage as loss of effective stiffness and can only be used to detect the existence of damage and localize it. This dissertation focuses on the Bayesian FE model updating framework applied in the time domain. This framework can be used to update linear and nonlinear FE models. In contrast to updated linear FE models, a mechanics-based nonlinear FE model of the system (able to capture the damage states and failure modes of interest) updated using measurement data can provide information about other crucial characteristics of damage such as loss of strength, ductility capacity, and low cycle fatigue life, etc., which are very important to identify for comprehensive damage diagnosis and prognosis. The updated mechanics-based nonlinear FE model can be directly used to detect, localize, classify, and assess the severity of the damage and perform damage prognosis.

The Bayesian time-domain FE model updating framework is illustrated using three civil infrastructure testbed structures – a concrete gravity dam, a miter gate, and a bridge column. The framework is further extended to account for model form uncertainty, arguably the most significant source of uncertainty in model calibration, in linear dynamic systems. The extended framework is illustrated and validated on simple structural benchmark problems.

Surrogate models can be used as fast emulators of FE models to accelerate the extremely computationally expensive model updating process. Part of this dissertation focuses on evaluating the loss of accuracy and the gain in computational time while performing Bayesian model updating by using surrogate model evaluations compared to using direct FE model evaluations.

1 Introduction

1.1 Background

Infrastructure conditions have a cascading impact on the nation's economy and the U.S. infrastructure is aging. The average age of dams in the U.S. is 57 years, 7.5% of the bridges in the U.S. are structurally deficient, and most of the locks (integral part of the inland waterways network) have exceeded their 50-year economic design life. The American Society of Civil Engineers (ASCE) 2021 report card rated the U.S. infrastructure (17 categories) at a C- grade, where C stands for mediocre, and D poor. Given these statistics, there is an operational need for optimal asset management: active monitoring, condition-based inspection and maintenance, optimal operation, predictive planning. There is a need for a rational guide (or a framework) to prioritize the allocation of resources for retrofit and replacement of the degrading infrastructure systems. This requires a framework for comprehensive damage diagnosis and prognosis of infrastructure systems.

Structural health monitoring (SHM) is the process of implementing a damage identification strategy (for damage diagnosis) for any aerospace, civil, or mechanical engineering system. Damage is defined as changes to the material and/or geometric properties of the system which adversely affect the system's performance. SHM is also currently being extended to biological systems such as humans under the name of human health monitoring. Damage prognosis (DP) is the process of forecasting system performance by combining SHM assessments with probabilistic description of future loading. A comprehensive SHM/DP framework should inform us about the: (1) existence of damage, (2) location of damage (localization), (3) type of damage (classification), (4) extent of damage, and (5) future metrics

such as remaining useful life of the system. The level of data/information needed and the level of sophistication in mathematical models increases from (1) to (5). The goal is to rely on physics/mechanics-based linear/non-linear finite element (FE) models for comprehensive damage assessment in structural systems.

Mathematical models are used in many fields of science and engineering to understand and predict the behavior of the system of interest. The fundamental governing equations of mathematical models describing physical phenomena in many fields consist of coupled partial differential equations – a form of mathematical model. The finite element (FE) method, first developed in the 1960s, is a numerical analysis technique to approximately solve the governing partial differential equations of a system. In the field of civil engineering, FE methods have been used by engineers in the analysis and design of structural, geo-structural, and soil-foundation-structural systems. Tremendous progress in FE modeling and analyses methods over the last few decades enables us to appropriately capture the complex behavior of large-scale civil structural systems subjected to static, quasi-static, and dynamic loading, particularly in the case of natural hazards, such as earthquakes. Physics/mechanics-based nonlinear FE models of civil structural systems (e.g., buildings, bridges, dams, miter gates) can reasonably capture the damage and failure mechanisms developing in such systems under critical loading environment or progressive deterioration over time.

1.2 Structural Digital Twin

Digital twins are at the heart of cybermodeling for intelligent infrastructure asset management. A structural digital twin is an up-to-date representation in terms of structural behavior of an individual/unique physical asset in operation. It is usually a hybrid physics-based

and data-driven model which is dynamically updated with data collected from its physical twin throughout its lifecycle and informs decisions that realize value. Combining physics-based models and data can really bring value to decision making. Digital twins have the potential to revolutionize decision-making across science and engineering. Figure 1.1 shows the schematic representation of a digital twin development for SHM/DP.

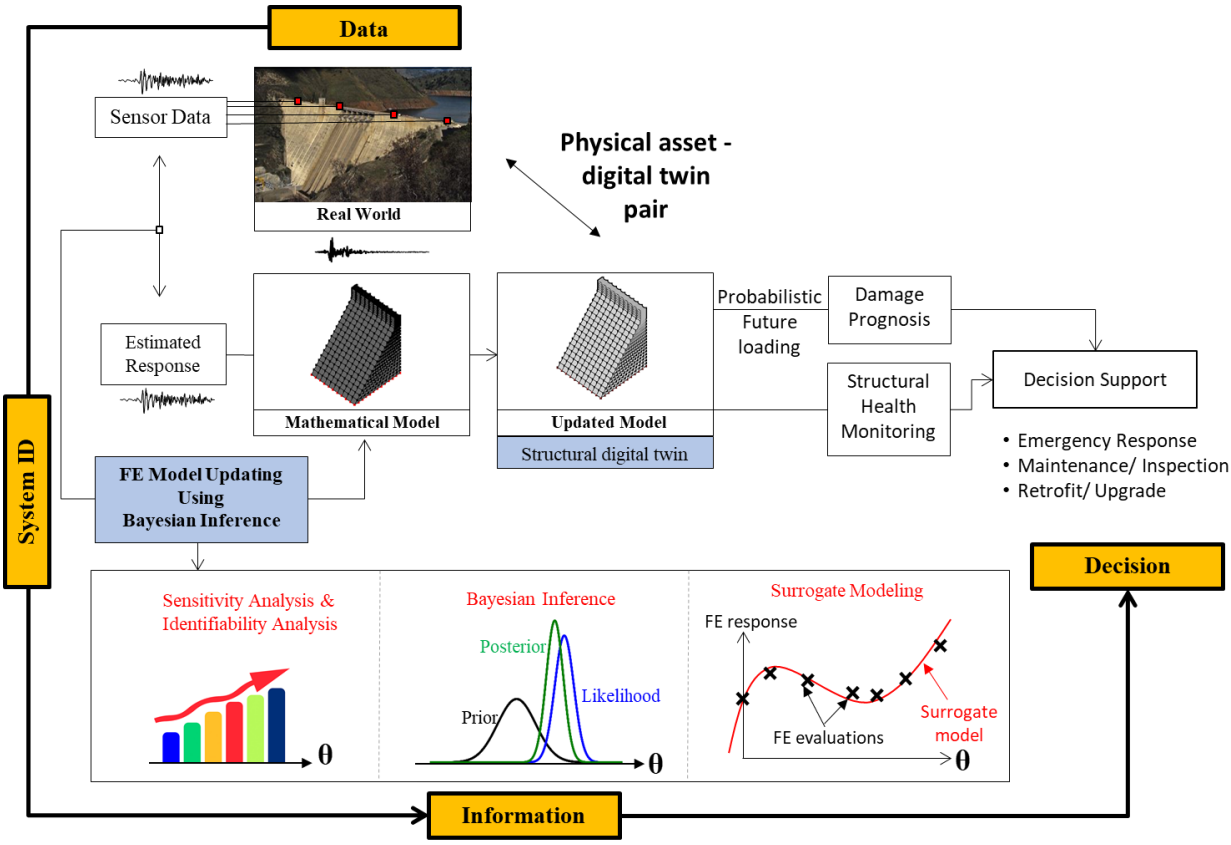

Figure 1.1: Schematic representation of a digital twin development for SHM/DP

1.3 FE Model Updating using Bayesian Inference

Consider a real structure equipped with sensors to measure the input-output or output-only response of the system. The input loading can be due to ambient vibrations or forced vibrations from a planned event or seismic vibrations from an unexpected earthquake event. The heterogenous sensor array to measure global and local output response of the systems may

consist of accelerometers, GPS-based displacement sensors, fiber-optic sensors, LVDTs, string potentiometers, strain gauges, etc. Assume a physics/mechanics-based linear or non-linear FE model of the structure is developed from design or as-built drawings of the system and using explicitly formulated assumptions and hypotheses. Often the system response predicted by the FE model differs from the measured output response of the system. The discrepancy between these responses can be attributed to numerous sources of uncertainties. These include:

(1) Uncertainty in the measured input and output due to measurement noise.

(2) Unmeasured/partially measured/erroneous input.

(3) Uncertainty about the parameters of the FE model due to lack of knowledge, assuming that the structure/form of the model is known.

(4) Uncertainty about the structure/form of the model, i.e., the selected model class cannot represent the real system appropriately. This model form error, if not accounted for, can introduce bias in parameter estimation and handicap the predictive utility of the model.

(5) Uncertainty due to environmental variability and operational variability

(6) …

Let the vector of time-invariant unknown model parameters be denoted by $\boldsymbol{\theta}$. For the methodology described in this thesis, the parameter vector $\boldsymbol{\theta}$ can include any unknown time-invariant parameters such as geometric, inertial, damping, hysteretic material law, boundary conditions, and loading parameters characterizing the FE model. The measurement data is denoted by $\mathcal{D}$. The process of estimating/calibrating the unknown parameter vector $\boldsymbol{\theta}$ of a FE model of a structural system using the probabilistic Bayesian inference framework and the measurement data $\mathcal{D}$ is termed Bayesian FE model updating in the engineering literature.

The Bayesian methodology provides a rigorous probabilistic framework that allows to explicitly and accurately account for the various sources of real-world uncertainties in the model updating process. The framework also allows incorporation of prior knowledge about the unknown parameter vector $\boldsymbol{\theta}$ of the FE model using a prior probability distribution $p(\boldsymbol{\theta})$. The framework quantifies uncertainty in parameter estimates after calibration through the posterior probability distribution $p(\boldsymbol{\theta}|\mathcal{D})$. All the uncertainties can be carried forward into the future predictions using posterior predictive distribution thus enabling robust predictions. The Bayesian updating of the unknown parameter vector $\boldsymbol{\theta}$ is obtained using Bayes theorem as

$$p(\boldsymbol{\theta}|\mathcal{D}) = \frac{p(\mathcal{D}|\boldsymbol{\theta}) \times p(\boldsymbol{\theta})}{p(\mathcal{D})} \tag{1.1}$$

The prior distribution $p(\boldsymbol{\theta})$ is a probability distribution over $\boldsymbol{\theta}$ and is formulated using domain knowledge and expert opinion. The likelihood function is a function over $\boldsymbol{\theta}$ and conveys the likelihood of observing the measured data $\mathcal{D}$ through the lens of a measurement model at each value of $\boldsymbol{\theta}$. This measurement model incorporates the FE model and is discussed in Chapters 2, 3, 4, and 5. The posterior distribution $p(\boldsymbol{\theta}|\mathcal{D})$ is an updated probability distribution over $\boldsymbol{\theta}$ which fuses both prior knowledge and measured data. In Bayesian parameter estimation, $p(\mathcal{D})$ is just a normalizing constant that ensures the posterior distribution $p(\boldsymbol{\theta}|\mathcal{D})$ integrates to 1. Figure 1.2 shows a schematic representation of Bayesian FE model updating. The FE model characterized by the posterior distribution $p(\boldsymbol{\theta}|\mathcal{D})$ of the parameter vector $\boldsymbol{\theta}$ is termed the updated FE model.

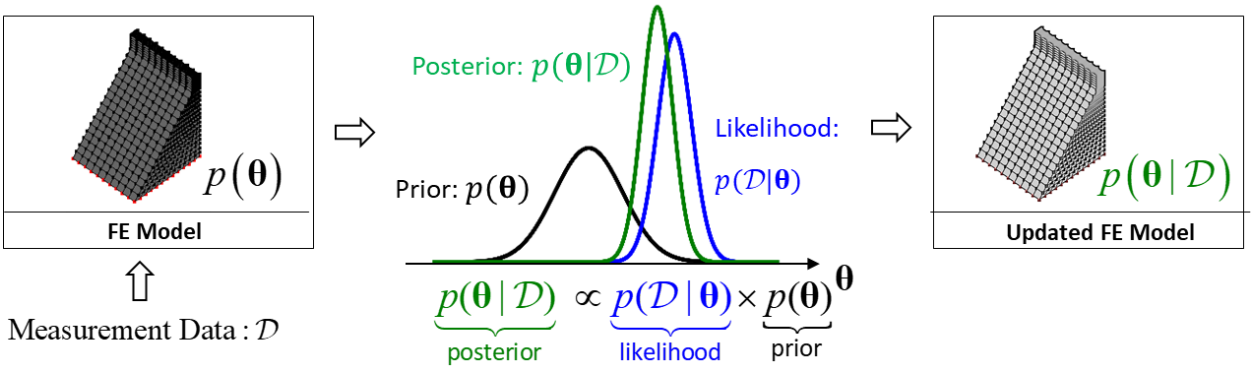

Figure 1.2: Schematic representation of Bayesian FE model updating

1.4 Linear vs Non-linear FE Models for Model Updating of Civil Structures

Most methods of FE model updating for SHM consist of updating linear FE models based on changes in modal parameters identified before and after a potentially damaging event (e.g., an earthquake) using low amplitude vibration data (Doebling et al. 1998; Farrar et al. 2001), see Figure 1.3. Such vibration-based SHM techniques have been successfully applied to large scale civil structures (Astroza et al. 2016; Moaveni et al. 2010, 2011). With linear FE model updating methods, however, damage is only identified as loss of effective stiffness in various elements or groups of elements of the FE model of the structure. Moreover, these methods can only detect the existence of damage and localize it. These methods fail to accurately classify and assess the severity of damage. In addition, the updated linear FE model cannot be used for DP purposes since the system response during damage-inducing loading events (and sometimes even during normal operational events) deviates significantly from the linear elastic behavior. This dissertation focuses on the Bayesian FE model updating framework applied in the time domain. This framework can be used to update linear and nonlinear FE models. In contrast to linear FE model updating methods operating in the modal domain, when a mechanics-based nonlinear FE

model of the system (able to capture the damage states and failure modes of interest) is updated in the time domain using measurement data, it can provide information about, for example, the loss of strength and ductility capacity and loss of low cycle fatigue life, which are even more important metrics of structural damage in civil structural systems as compared to the mere loss of effective stiffness. For civil structural systems, the sources of nonlinear behavior can be attributed to multiple sources (i.e., material and geometric nonlinearities, force and displacement boundary condition nonlinearities, friction, fracture, …). The updated mechanics-based nonlinear FE model can be directly interrogated to detect, localize, classify, and assess the severity of damage. It can also be used to perform DP (for example, estimate the remaining useful life of a system) by defining future service, operational, and extreme loads in probabilistic terms, see Figure 1.3.

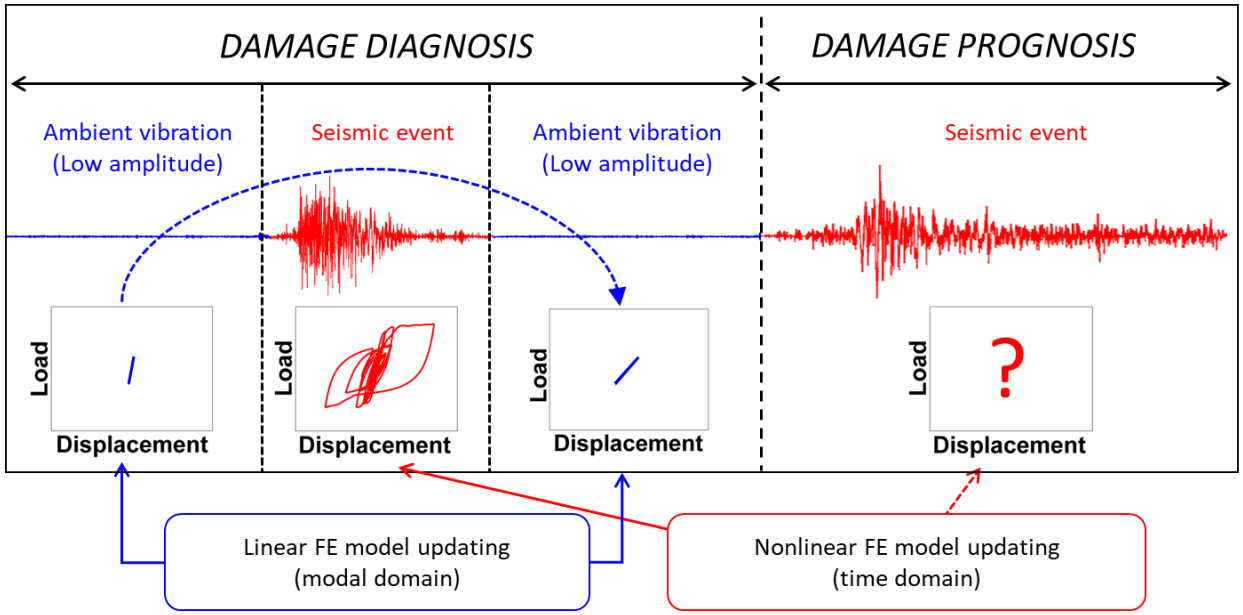

Figure 1.3: Nonlinear vs Linear FE Model Updating

1.5 Three-Phased Research Strategy

The final objective of this research is to use measurement data collected from a physical structure in the lab or the field to perform FE model updating. This is a complex and challenging task. Therefore, we devised a systematic and progressive three-phased research strategy to develop the Bayesian FE model updating methodology. The three-phased approach allows us to investigate and overcome the stumbling blocks in methodology development and enables us to move systematically and progressively towards the final objective. Figure 1.4 shows a schematic representation of the proposed 3-phased research strategy.

In phase 1, simulated data is used as measurement data for model updating. The same FE model is used to simulate the measurement data and perform model updating (parameter estimation). In this phase, only the uncertainty due to input and output measurement noise are accounted for in the model updating framework.

In phase 2, simulated data is again used as measurement data for model updating. However, the FE model used to simulate the measurement data is different from the one used to perform model updating. For example, an FE model with refined mesh can be used to simulate the measurement data and an FE model with a coarser mesh can be used to conduct model updating; or different material constitutive models can be used to simulate the data and to perform model updating. This enables us to study the effect of modeling errors in FE model updating in addition to input and output measurement noise – a step closer to reality.

Phase 3 is the real-world scenario where data recorded from a physical structure tested in the lab or existing in the field is used as measurement data for model updating. All the sources of real-world uncertainties (measurement noise, modeling errors, environmental and operational variability, …) are accounted for in this phase.

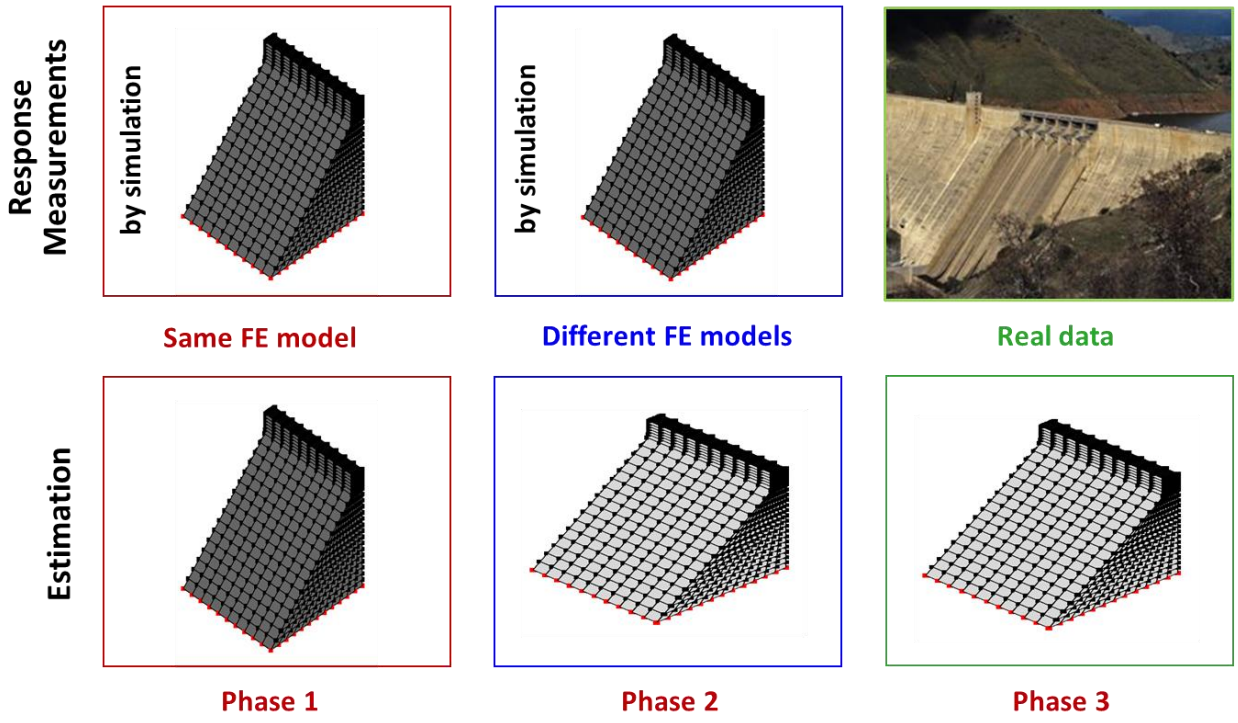

Figure 1.4: Proposed three-phased research strategy

1.6 Organization of Dissertation

This dissertation consists of six chapters, a brief description of the content in each chapter is provided below:

Chapter 1 introduces and motivates the topic of structural health monitoring and damage prognosis of civil infrastructure systems. This chapter also introduces Bayesian linear and non-linear FE model updating of civil structures.

Chapter 2 focuses on the Bayesian time-domain FE model updating framework and illustrates the methodology to update an idealized nonlinear FE model of a concrete gravity dam using data simulated according to phase 1 of the research strategy. This chapter also introduces the concept of identifiability and shows its importance in model updating. Two meta-algorithms are proposed to identify the identifiable parameters.

Chapter 3 extends the proposed FE model updating framework to account for model form uncertainty for linear dynamic systems. The extended framework is validated on simple structural benchmark problems using data simulated according to phase 2 of the research strategy. Note that model form uncertainty is the major source of uncertainty in model calibration.

Chapter 4 considers surrogate modeling and parallel computing to reduce the computational burden of model updating. Loss in accuracy of model updating results and gain in computational time is studied when model updating is performed using direct FE model evaluations versus surrogate model evaluations. In this chapter, a high-fidelity FE model of a real-world miter gate structure is considered for model updating using data simulated according to phase 1 of the research strategy.

Chapter 5 considers FE model updating of a full-scale bridge column tested on the shake table at UC San Diego. The heterogenous experimental data is used to update a nonlinear FE model of the bridge column (phase 3 of the research strategy). The prospects and limitations of a living digital twin are highlighted in this chapter.

Chapter 6, the last chapter, provides conclusions of the dissertation, some avenues for future research, and final thoughts about the future of the structural digital twin technology for SHM/DP purposes.

2 Bayesian Updating and Identifiability Assessment of Nonlinear Finite Element Models

2.1 Abstract

A promising and attractive way of performing structural health monitoring (SHM) and damage prognosis (DP) of engineering systems is through utilizing a nonlinear finite element (FE) model. Often, FE models contain parameters that are unknown or known with significant level of uncertainty. Such parameters need to be estimated/updated/calibrated using data measured from the physical system. The Bayesian paradigm to model updating/calibration is attractive as it accounts, using a rigorous probabilistic framework, for numerous sources of uncertainties existing in the real-world. However, applying Bayesian methods to nonlinear FE models of large-scale civil structural systems is computationally very prohibitive. Additionally, non-identifiability of FE model parameters poses challenges in the model updating process. This paper presents Bayesian model updating and identifiability analysis of nonlinear FE models with a specific testbed civil structure, Pine Flat concrete gravity dam, as illustration example. Model updating is performed in the recursive mode using the unscented Kalman filter (UKF) and in the batch mode using the transitional Markov chain Monte Carlo (TMCMC) method. Limitations in terms of applicability and computational challenges of each method for model updating of large-scale nonlinear FE models are addressed and discussed. Identifiability and sensitivity analyses of the model are then performed using local and global methods. Local practical identifiability analysis using local sensitivity in conjunction with the Fisher information matrix is used to assess the parameter identifiability in a certain local region in the parameter space. Due to the

nonexistence of a method to assess global practical identifiability, variance-based global sensitivity analysis (Sobol's method) is used herein. Identifiability and sensitivity analysis results are used to choose the parameters to be included in the model updating phase.

Keywords: Structural health monitoring, Model updating, Model calibration, Finite element model, Nonlinear system identification, Bayesian parameter estimation, Identifiability analysis, Sensitivity analysis, Sobol' Indices

2.2 Introduction

Structural health monitoring (SHM) is the process of implementing a damage identification strategy (damage diagnosis) for aerospace, civil, and mechanical engineering infrastructure (Farrar and Worden 2007). Damage prognosis (DP) extends this process by combining SHM assessment with probabilistic modeling of the future loading environments to forecast metrics such as remaining useful life of the system (Farrar and Lieven 2007). An effective way of doing SHM/DP of civil structural systems is by utilizing a calibrated nonlinear finite element (FE) model of the system able to capture the pertinent damage and failure modes (Hemez and Farrar 2014). This involves collecting measurement data (input-output or output-only data) using heterogeneous sensor arrays deployed on the system. Then, a FE model is developed from design or as-built drawings of the system and using explicitly formulated assumptions and hypotheses. Due to the inherently complex nature of civil structural systems and the presence of wide-ranging uncertainties, it is extremely difficult to model these systems accurately. Often, FE models contain parameters that are unknown or known with significant uncertainty, combinedly referred to as unknown parameters in this paper. These parameters need to be calibrated (or estimated or updated) using the measured data accounting for numerous

sources of uncertainties. The process of calibrating/estimating/updating the unknown parameters of the developed FE model using Bayesian inference is known as Bayesian FE model updating/calibration.

Most methods of FE model updating for SHM consist of updating linear FE models based on changes in modal parameters identified before and after a potentially damaging event (e.g., an earthquake) using low amplitude vibration data (Doebling et al. 1998; Farrar et al. 2001). Such vibration-based SHM techniques have been successfully applied to large scale civil structures (Astroza et al. 2016; Moaveni et al. 2010, 2011). With linear FE model updating methods, however, damage is only identified as loss of effective stiffness in various elements or groups of elements of the FE model of the structure. Moreover, these methods can only detect the existence of damage without being able to localize it, barring a few cases. Another important drawback is that these methods fail to accurately classify and assess the severity of damage. In addition, the updated linear FE model cannot be used for DP purposes since the system response during damage-inducing loading events (and sometimes even during normal operational events) deviates significantly from linear elastic behavior. In contrast to linear FE model updating methods, when a mechanics-based nonlinear FE model of the system (able to capture the damage states and failure modes of interest) is updated using measurement data, it can provide information about, for example, the loss of strength and ductility capacity and loss of low cycle fatigue life, which are more meaningful and important metrics of structural damage in civil structural systems as compared to the mere loss of stiffness. For civil structural systems, the sources of nonlinear behavior can be attributed to multiple sources (i.e., material and geometric nonlinearities, force and displacement boundary condition nonlinearities, friction, fracture, …) with material nonlinearity being the most important. The updated mechanics-based nonlinear FE

model can be directly used to detect, localize, classify and assess the severity of damage. It can also be used to perform DP (for example, estimate the remaining useful life of a system) by defining future service, operational and extreme loads in probabilistic terms. Most work in nonlinear FE model updating consists of using simplified models with concentrated/lumped nonlinearities described by empirical nonlinear models (e.g., Bouc-Wen) to represent the hysteretic behavior (Chatzi and Smyth 2009; Yang et al. 2014). However, such empirical models are not mechanics-based and thus inadequate to capture the real nonlinear behavior of large-scale civil systems. Only recently, researchers have started updating mechanics-based nonlinear FE models of civil structural systems using simulated measurement data (Astroza et al. 2015, 2019b; Ebrahimian et al. 2015, 2018; Ramancha et al. 2020b; Vega et al. 2020) and experimental data (Ramancha et al. 2020a). Updating mechanics-based nonlinear FE model of large-scale civil structural systems is highly computationally intensive. However, it is rewarding in terms of accuracy in damage detection, localization, classification, severity assessment and prognosis.

The model updating process should be complemented or preceded by some sort of identifiability analysis to assess the identifiability of the model parameters. In the Bayesian paradigm, the concept of identifiability has not been free from controversies, polemics, and confusion (San Martın and González 2010). Aldrich (Aldrich 2002) describes the transfer of the term “identification” to the Bayesian theory and how its transfer has led to a protracted debate. In this paper, the term “identifiability” of a model parameter refers to the possibility of uniquely determining its value from the measurement data. A model is identifiable if all its parameters are identifiable. It is important to perform some sort of identifiability analysis before solving the actual inverse problem to answer questions such as “which model parameters or parameter combinations can be uniquely estimated from the measurement data?”. In theory, model

identifiability poses no real difficulty in the Bayesian approach to model updating (Wechsler et al. 2013). However, numerical approximations such as Markov chain Monte Carlo methods do not perform well when non-identifiable parameters are included in the inference stage (Hines et al. 2014; Raue et al. 2013). In the case of approximate inference methods that operate on point estimates (e.g., maximum likelihood, maximum-a-posteriori, Kalman filters and its variants), non-identifiability brings undesirable non-uniqueness (Ramancha et al. 2020b; Wechsler et al. 2013). Additionally, the computationally intensive nature of Bayesian methods often requires a parameter screening and selection process to select the most significant/influent parameters to be used in the updating process. Identifiability and sensitivity analysis are used to detect/identify the influent/identifiable parameters.

Identifiability is commonly distinguished between structural versus practical and local versus global (see Section 2.4 for more details). This paper is mainly concerned with practical, both local and global, identifiability. Many analytical and numerical methods are available in the literature for identifiability analysis of mathematical models. Most analytical methods (e.g., Laplace transform approach, Taylor series approach, similarity transform approach, differential algebra approach) answer questions about structural (local and global) identifiability of the model. Analytical methods require implementing the model symbolically and using symbolic differentiation, which is impractical for FE models as they are generally implemented in software external to the software for performing the Bayesian estimation and identifiability analysis. Analytical methods also have limitations with large models due to computational reasons (RAM limitations). On the other hand, most numerical methods (e.g., Fisher information matrix (Rothenberg 1971), profile likelihood (Raue et al. 2009), Bayesian approaches (Hines et al. 2014), sloppy models (Chis et al. 2016), active subspaces (Constantine 2015)) can achieve

structural and practical identifiability analysis. Numerical methods are often computationally fast and doesn't require symbolic implementation of the model. However, existing numerical methods are typically local, i.e., these methods can only answer questions about local (structural and practical) identifiability of the model. To the best of the authors' knowledge, no analytical or numerical methods exist that can evaluate the practical global identifiability of a model. The best possible tool currently available to investigate global identifiability is global sensitivity analysis. Also, most numerical approaches also only provide a binary yes-no answer to model identifiability (refer to introduction of (Ebrahimian et al. 2019)). However, even when a model is not identifiable, a few parameters of the model might still be identifiable. Therefore, it is important to detect such parameters using some sort of identifiability analysis and estimate only these parameters in the model updating stage.

Identifiability of structural models is a topic of emerging interest in structural engineering research. While some researchers have used the determinant and trace of the Fisher information matrix to evaluate the binary yes-no answer to model identifiability (Heredia-Zavoni and Esteva 1998; Kirkegaard and Brincker 1994; Udwadia 1994), others have used the concept of information theory to study model identifiability (Papadimitriou et al. 2000; Yuen and Kuok 2015). The application examples of these studies, however, are linear elastic structural models. Chatzis et al. (Chatzis et al. 2015) looked at the identifiability of nonlinear models using Observability Rank Condition. This analytical method requires symbolic differentiation of the FE model which is impractical (highly challenging) for large scale nonlinear mechanics-based FE models. Ebrahimian et al. (Ebrahimian et al. 2019) proposed an information-theoretic approach (which does not require the symbolic state-space implementation of the FE model) for identifiability assessment and investigated the identifiability of mechanics-based nonlinear FE

models of civil structures. Most of the mentioned studies also focused on local identifiability only. The problem with local methods is that the identifiability of parameters is only valid in the local region around the evaluation point. Therefore, these methods are not appropriate for models with a nonlinear relation between the parameter vector and the model output of interest. Due to the lack of a practical global identifiability analysis method, most researchers have focused on global sensitivity analysis (GSA), namely Sobol's method (a variance-based GSA method). GSA is a tool primarily used in systems modeling to discriminate between influent and non-influent parameters (Saltelli et al. 2007). The link between global sensitivity and identifiability is discussed in (Dobre et al. 2010). GSA of structural models is a relatively less studied topic in the literature. Researchers have proposed algorithms and metrics based on Sobol's method and have applied them to idealized linear elastic structural models (Hu and Mahadevan 2019; Zhou et al. 2017). These studies also do not focus on detecting the most significant/influent parameters to be used in the updating process.

This paper discusses the general process of updating unknown parameters of a FE model from measurement data using batch and recursive Bayesian estimation methods. Popular algorithms for recursive estimation, i.e., unscented Kalman filter (UKF), and batch estimation, i.e., transitional Markov chain Monte Carlo (TMCMC), are briefly summarized from the FE model updating perspective (in Section 0 and 2.3.2, respectively), highlighting their advantages and disadvantages in the context of updating large-scale nonlinear FE models. It is very likely that a nonlinear FE model of a large-scale civil structural system will contain nonidentifiable parameters. Therefore, an algorithm is proposed for ranking and detecting the parameters that are practically locally identifiable based on Fisher information and the generalized notion of Cramer-Rao lower bound (Section 2.4.2). A novel method to find the globally influent parameters based

on variance-based GSA of individual and groups of parameters is also proposed (Section 2.4.3). These proposed methods do not require symbolic implementation of the mathematical model, thus ideal for FE models. Also, the updating and identifiability methodologies described in the paper are general and applicable to any mathematical model. Model updating and identifiability methodologies are applied to a testbed civil structure (Section 2.5). This paper aptly illustrates the challenges in updating mechanics-based FE models of large-scale real-world systems as well as the importance of identifiability – the primary objective of this paper.

2.3 Bayesian Finite Element Model Updating

At time step k (or discrete time t_k), let $\mathbf{u}_k \in \mathbb{R}^{n_\mathbf{u}}$ and $\mathbf{y}_k \in \mathbb{R}^{n_\mathbf{y}}$ be the measured input and output response, respectively, where $n_\mathbf{u}$ and $n_\mathbf{y}$ denote the number of input and output measurement channels, respectively. Assuming that the measurements are obtained for N time steps, the measurement input and output vectors are $\mathbf{u}_{1:N} = \left[\mathbf{u}_1^T, \mathbf{u}_2^T, ..., \mathbf{u}_N^T\right]^T \in \mathbb{R}^{(n_\mathbf{u} \times N)\times 1}$ and $\mathbf{y}_{1:N} = \left[\mathbf{y}_1^T, \mathbf{y}_2^T, ..., \mathbf{y}_N^T\right]^T \in \mathbb{R}^{(n_\mathbf{y} \times N)\times 1}$, respectively. Thus, the input-output measurement dataset is defined as $\mathcal{D} = \left\{(\mathbf{u}_1, \mathbf{y}_1), ..., (\mathbf{u}_N, \mathbf{y}_N)\right\} \equiv \left(\mathbf{u}_{1:N}, \mathbf{y}_{1:N}\right)$. For civil structural systems, the input and output measurements are typically obtained from heterogenous sensor arrays which may consist of accelerometers, GPS-based displacement sensors, fiber-optic sensors, LVDTs, string potentiometers, strain gauges, etc., deployed on the system (Ramancha et al. 2020a).

Let $\mathbf{y}_k^{FE} = \mathbf{h}_k\left(\mathbf{u}_{1:k}; \boldsymbol{\theta}\right) \in \mathbb{R}^{n_\mathbf{y}}$ be the output response of the FE model $\mathbf{h}$ at time step k when subjected to the measured input time history $\mathbf{u}_{1:k} = \left[\mathbf{u}_1^T, \mathbf{u}_2^T, ..., \mathbf{u}_k^T\right]^T \in \mathbb{R}^{(n_\mathbf{u} \times k)\times 1}$. The FE

model $\mathbf{h}$ is parameterized by the unknown parameter vector $\boldsymbol{\theta} = \left[\theta_1, \theta_2, ..., \theta_{n_{\boldsymbol{\theta}}}\right]^T \in \mathbb{R}^{n_{\boldsymbol{\theta}}}$, where $n_{\boldsymbol{\theta}}$ denotes the number of unknown parameters. For the methodology described in this paper, the parameter vector $\boldsymbol{\theta}$ can include any unknown time-invariant parameters such as geometric, inertial, damping, hysteretic material law, boundary conditions, and loading parameters characterizing the FE model.

The measured output response $\mathbf{y}$ and predicted response $\mathbf{y}^{FE}$ do not match due to the numerous sources of uncertainties observed in the real-world (Chatfield 1995; Kennedy and O'Hagan 2001). These include:

(1) Uncertainty in the measured input and output due to measurement noise.

(2) Unmeasured/partially measured/erroneous input.

(3) Uncertainty about the parameters of the FE model, assuming that the structure/form of the model is known.

(4) Uncertainty about the structure/form of the model, i.e., the selected model class cannot exactly represent the real system. This model form error, if not accounted for, can introduce bias in parameter estimation and handicap the predictive utility of the model.

The goal of model updating is to estimate the unknown parameters of the model using measurement data (see Remark 1 below). However, the measurement data of civil structural systems are typically noisy, sparse (limited in number), and susceptible to unknown environmental artifacts, thus unable to completely constrain the unknown parameters of the FE model. Mathematically, the model updating problem is ill-posed. Deterministic/classical approaches such as least squares or generalized/weighted least squares can be used for model updating. However, these methods need regularization while solving an ill-posed problem. In

addition, deterministic methods are not strictly appropriate for dealing with real-world uncertainties. Alternatively, the Bayesian approach to model updating is attractive because it provides the framework to (1) account explicitly for the various sources of real-world uncertainties during the estimation process of unknown parameters and (2) characterize probabilistically the remaining estimation uncertainty (Kennedy and O'Hagan 2001). The remaining estimation uncertainty provided by the Bayesian approach is extremely useful in SHM/DP as it supports reliable and robust decision making. Unlike classical approaches, the Bayesian approach models the unknown parameter vector $\boldsymbol{\theta}$ as a random vector thereby providing a means to incorporate prior knowledge of the unknown parameters through a prior probability density function (PDF) $p(\boldsymbol{\theta})$. Some prior knowledge is usually available for most parameters in the FE model of a civil structural system. For example, if the parameter of interest is "the tensile strength of concrete" then its nominal value can be used to construct the prior PDF.

Three main ingredients are required to perform Bayesian model updating: (1) measurement data $\mathcal{D}$, (2) the prior PDF of the unknown parameters $p(\boldsymbol{\theta})$, and (3) a measurement equation (i.e., a model of the measurement process). The measurement equation is essentially a joint physical-statistical model that relates model parameters to measurements. The following measurement equation is used in this paper:

$$\text{At time step } k: \quad \underset{\textit{measured output}}{\mathbf{y}_k} = \underbrace{\mathbf{h}_k\left(\mathbf{u}_{1:k};\boldsymbol{\theta}\right)}_{\textit{FE predicted response}} + \underset{\textit{error/noise}}{\mathbf{w}_k} \quad ; \quad k \in [1,2,...,N] \tag{2.1}$$

where $\mathbf{w}_k = \left[w_{1,k}, w_{2,k}, ..., w_{n_{\mathbf{y}},k} \right]^T \in \mathbb{R}^{n_{\mathbf{y}}}$ is the error/noise vector at time step k, $w_{i,k}$ denotes the discrepancy between measured output and the FE predicted response corresponding

to the i^{th} output measurement channel at time step k. Note that in this paper, the noise term is assumed additive to the FE predicted response in the measurement equation (Eq. (2.1)). With such measurement equation, all the sources of real-world uncertainties are lumped and accounted for in the noise term. Therefore, accurate statistical description of the noise process $\mathbf{w} = \left[\mathbf{w}_1^T, \mathbf{w}_2^T, ..., \mathbf{w}_N^T \right]^T \in \mathbb{R}^{\left(n_\mathbf{y} \times N\right) \times 1}$ is crucial for accurate model updating. In this paper, the error/noise vectors $\mathbf{w}_1, \mathbf{w}_2, ..., \mathbf{w}_N$ are assumed statistically independent and identically distributed with the random vector $\mathbf{w}_k$ modeled as zero-mean Gaussian with independent components (i.e., noise/error terms across all measurement channels, $w_{1,k}, w_{2,k}, ..., w_{n_\mathbf{y},k}$, are assumed statistically independent). Thus,

$$\mathbf{w}_k \sim \mathcal{N}\left(\underset{n_\mathbf{y} \times 1}{\mathbf{0}}, \mathbf{R} = \begin{pmatrix} \sigma_1^2 & 0 & \cdots & 0 \\ 0 & \sigma_2^2 & \cdots & 0 \\ \vdots & \vdots & \ddots & \vdots \\ 0 & 0 & \cdots & \sigma_{n_\mathbf{y}}^2 \end{pmatrix}_{n_\mathbf{y} \times n_\mathbf{y}} \right), \mathbf{w} \sim \mathcal{N}\left(\underset{\left(n_\mathbf{y} \times N\right) \times 1}{\mathbf{0}}, \mathbf{C} = \begin{pmatrix} \mathbf{R} & \mathbf{0} & \cdots & \mathbf{0} \\ \mathbf{0} & \mathbf{R} & \cdots & \mathbf{0} \\ \vdots & \vdots & \ddots & \vdots \\ \mathbf{0} & \mathbf{0} & \cdots & \mathbf{R} \end{pmatrix}_{\substack{\left(n_\mathbf{y} \times N\right) \\ \times \left(n_\mathbf{y} \times N\right)}} \right) \quad (2.2)$$

where $\mathcal{N}\left(\boldsymbol{\mu}, \boldsymbol{\Sigma}\right)$ denotes a Gaussian joint PDF with mean vector $\boldsymbol{\mu}$ and covariance matrix $\boldsymbol{\Sigma}$, σ_i^2 denotes the variance of the discrepancy between measured and FE predicted output responses for the i^{th} output measurement channel. Note that the covariance matrix of the error/noise $\mathbf{w}_k$ is assumed to be a diagonal time-invariant matrix $\mathbf{R}$. Assuming the noise process to have zero-mean and time-invariant diagonal covariance matrix (as in Eq. (2.2)) may not be sufficiently accurate especially in the presence of model-form error. However, this is outside the scope of this paper. Refer to (Astroza et al. 2019a; Kennedy and O'Hagan 2001) for representation of the model-form error in Bayesian model updating.

In the measurement equation (Eq. (2.1)), the mapping between the unknown parameter vector $\boldsymbol{\theta}$ and measured output $\mathbf{y}_k$ is not linear. Hence, the model updating problem is nonlinear. Note that even for a linear (between input and output response) FE model $\mathbf{h}$, the model updating problem can still be nonlinear depending on the mapping between $\boldsymbol{\theta}$ and $\mathbf{y}_k$. Thus, most FE model updating problems require the use of nonlinear model updating tools.

The objective of Bayesian model updating is to obtain $p(\boldsymbol{\theta}|\mathcal{D}) \equiv p(\boldsymbol{\theta}|\mathbf{u}_{1:N}, \mathbf{y}_{1:N})$, referred to as posterior/updated PDF of $\boldsymbol{\theta}$. This posterior PDF of $\boldsymbol{\theta}$ accounts for both the prior knowledge $p(\boldsymbol{\theta})$ and the measurement data $\mathcal{D}$. This generic Bayesian parameter estimation problem can be solved in a batch mode or a recursive mode. In the recursive mode, updating is performed at each time step k accounting for the "new" measurement data at time step k $(\mathbf{u}_k, \mathbf{y}_k)$ yielding an updated PDF $p(\boldsymbol{\theta}|\mathbf{u}_{1:k}, \mathbf{y}_{1:k})$. Whereas in the batch mode, the prior $p(\boldsymbol{\theta})$ is updated to $p(\boldsymbol{\theta}|\mathbf{u}_{1:N}, \mathbf{y}_{1:N})$ in one go accounting for the entire measurement data $\mathcal{D}$ at once. Batch Bayesian estimation is a special case of recursive Bayesian estimation (Sarkka 2013). The batch estimation framework does not allow estimation of parameters that vary with time (i.e., time-varying parameters). However, recursive estimation can be used for time-varying parameters as the parameters can be modeled to change between measurement steps using a state equation. More details about recursive and batch mode estimations are provided in Section 2.3.1 and Section 2.3.2, respectively.

Remark 1: Parameter-only estimation

This paper does not deal with the joint state and parameter estimation problem but rather considers the parameter-only estimation problem. In mechanics-based nonlinear FE models, the state vector consists of displacement and velocity at each node and all the history-dependent

variables at each integration point (material history variables of the constitutive material model used). This results in an extremely high-dimensional state vector for large-scale models and thus a joint state-parameter estimation problem becomes intractable. Extensive research in the field of nonlinear modeling and analysis of civil structures has shown that adequate mechanics-based FE models can predict with reasonable accuracy the actual structural response provided that realistic and well-calibrated material constitutive models are used. Therefore, relying on the mechanics-based FE model developed for a given structure, the estimation of the state variables can be omitted because they can be obtained as the output of the FE model with well identified unknown parameters. As a result, a parameter-only estimation problem can be formulated instead of a joint (state-parameter) estimation problem. Refer to the Proposed Framework section of (Astroza et al. 2015) for more details.

Remark 2: Time-invariant parameters

It is important to note that although parameters of nonlinear inelastic material constitutive models are time-invariant, the resulting nonlinear inelastic FE models of civil structures capture material and therefore structural degradation such as stiffness degradation and strength deterioration through the material history variables of the constitutive models. These material history variables are updated through evolution equations integrated over the deformation history of the materials.

2.3.1 Recursive Bayesian Parameter Estimation

Recursive Bayesian parameter estimation (also known as Bayes Filter) consists of obtaining the PDF $p(\boldsymbol{\theta} \mid \mathbf{u}_{1:k}, \mathbf{y}_{1:k})$ recursively over time (i.e., at time step $k = 1, 2, ..., N$) (Sarkka 2013). At any time step k, the PDF $p(\boldsymbol{\theta} \mid \mathbf{u}_{1:k-1}, \mathbf{y}_{1:k-1})$ is updated to $p(\boldsymbol{\theta} \mid \mathbf{u}_{1:k}, \mathbf{y}_{1:k})$ accounting

for the "new" measurement $(\mathbf{u}_k, \mathbf{y}_k)$. Therefore, the updated PDF $p(\boldsymbol{\theta} | \mathbf{u}_{1:k}, \mathbf{y}_{1:k})$ accounts for both the prior PDF $p(\boldsymbol{\theta})$ and measurements until time step k $(\mathbf{u}_{1:k}, \mathbf{y}_{1:k})$. This process is repeated until $k = N$. Particle filters and nonlinear variants of Kalman filters such as the extended Kalman filter (EKF) and the unscented Kalman filter (UKF) can be used to achieve this task. A state-space representation (state and measurement equation) of the problem is needed to utilize these algorithms (van der Merwe and Wan 2004). The following discrete-time state-space representation is used in this paper:

$$\begin{aligned} &\text{State Equation:} && \boldsymbol{\theta}_k = \boldsymbol{\theta}_{k-1} + \mathbf{v}_{k-1} \\ &\text{Measurement Equation:} && \mathbf{y}_k = \mathbf{h}_k\left(\mathbf{u}_{1:k}; \boldsymbol{\theta}_k\right) + \mathbf{w}_k \end{aligned} \tag{2.3}$$

In this representation, the unknown parameter vector $\boldsymbol{\theta}$ at each time step k is denoted as $\boldsymbol{\theta}_k$. The state equation governing the parameter vector $\boldsymbol{\theta}_k \in \mathbb{R}^{n_{\boldsymbol{\theta}}}$ is a simple random walk model driven by the "artificial" process noise $\mathbf{v}_k \in \mathbb{R}^{n_{\boldsymbol{\theta}}}$. The artificial process noise $\mathbf{v}_k$ is only used to model the evolution in time of the estimates of the time-invariant unknown parameters (during their recursive estimation) by a random walk and its variance controls the convergence and tracking performance of the filter (see Section 2.6.2 of (van der Merwe and Wan 2004)). The measurement equation is similar to Eq. (2.1), except that the FE model is now characterized by the unknown parameter vector $\boldsymbol{\theta}_k$.

In recursive Bayesian estimation, $\boldsymbol{\theta}_k$ at each time step k is modeled as a random vector. In addition, the PDF $p(\boldsymbol{\theta}_{k-1} | \mathbf{u}_{1:k-1}, \mathbf{y}_{1:k-1})$ is updated to $p(\boldsymbol{\theta}_k | \mathbf{u}_{1:k}, \mathbf{y}_{1:k})$ at each time step k. This involves computing $p(\boldsymbol{\theta}_k | \mathbf{u}_{1:k-1}, \mathbf{y}_{1:k-1})$, referred to as the predicted parameter distribution at time step k, using $p(\boldsymbol{\theta}_{k-1} | \mathbf{u}_{1:k-1}, \mathbf{y}_{1:k-1})$ and then updating the predicted distribution to

$p(\boldsymbol{\theta}_k \mid \mathbf{u}_{1:k}, \mathbf{y}_{1:k})$. For the state-space model shown in Eq. (2.3), the prediction and updating steps are performed as follows.

$$\underline{\text{At time step } k: \;\; p(\boldsymbol{\theta}_{k-1} \mid \mathbf{u}_{1:k-1}, \mathbf{y}_{1:k-1}) \;\; \rightarrow \;\; p(\boldsymbol{\theta}_k \mid \mathbf{u}_{1:k}, \mathbf{y}_{1:k})}$$

$$\text{Prediction step:} \;\; p(\boldsymbol{\theta}_k \mid \mathbf{u}_{1:k-1}, \mathbf{y}_{1:k-1}) = \int \overbrace{p(\boldsymbol{\theta}_k \mid \boldsymbol{\theta}_{k-1})}^{\text{From state equation}} \times p(\boldsymbol{\theta}_{k-1} \mid \mathbf{u}_{1:k-1}, \mathbf{y}_{1:k-1}) \, d\boldsymbol{\theta}_{k-1} \tag{2.4}$$

$$\text{Updating step:} \;\; p(\boldsymbol{\theta}_k \mid \mathbf{u}_{1:k}, \mathbf{y}_{1:k}) = \frac{\overbrace{p(\mathbf{y}_k \mid \boldsymbol{\theta}_k, \mathbf{u}_{1:k})}^{\text{From measurement equation}} \times \; p(\boldsymbol{\theta}_k \mid \mathbf{u}_{1:k-1}, \mathbf{y}_{1:k-1})}{p(\mathbf{y}_k \mid \mathbf{u}_{1:k}, \mathbf{y}_{1:k-1})}$$

Note that the prediction step is a Chapman-Kolmogorov equation and the update step is Bayes rule (Sarkka 2013). The conditional PDFs $p(\boldsymbol{\theta}_k \mid \boldsymbol{\theta}_{k-1})$ and $p(\mathbf{y}_k \mid \boldsymbol{\theta}_k, \mathbf{u}_{1:k})$ are obtained from the state and measurement equation, respectively.

Numerical approximation methods such as Particle filters and nonlinear variants of the Kalman filter can be used to solve the prediction and updating step of Eq. (2.4). Particle filters use a Monte Carlo representation (particles or weighted samples) for the distribution of the unknown parameter vector and the computational requirements are much higher than for Kalman filters (Sarkka 2013). Kalman filter is the classical optimal filter (best linear unbiased estimator, minimum mean square error estimator) for linear Gaussian models and is widely used for tracking, navigation, telecommunication, audio processing, control systems, etc. For nonlinear (between the state $\boldsymbol{\theta}$ and response measurement $\mathbf{y}$) state-space models, variants of Kalman filter such as the extended Kalman filter (EKF) and unscented Kalman filter (UKF) can be used. EKF is a linearization-based extension of Kalman filter to nonlinear state-space models. Hence, it requires the derivative of the response with respect to the parameter vector $\boldsymbol{\theta}$. UKF is a sigma-point transformation-based extension of Kalman filter. In this paper, UKF is applied to the testbed structure for recursive estimation of the unknown parameter vector $\boldsymbol{\theta}$.

2.3.1.1 Unscented Kalman Filter

A nonlinear Kalman filter is a Bayes filter for which:

(1) The prior PDF $p(\boldsymbol{\theta})$ is a Gaussian distribution. Therefore, $\boldsymbol{\theta}_0$ is modeled as Gaussian with mean vector $\hat{\boldsymbol{\theta}}_{0|0}$ and covariance matrix $\hat{\mathbf{P}}_{0|0}^{\boldsymbol{\theta}\boldsymbol{\theta}}$, i.e., $p(\boldsymbol{\theta}) = \mathcal{N}\left(\hat{\boldsymbol{\theta}}_{0|0}, \hat{\mathbf{P}}_{0|0}^{\boldsymbol{\theta}\boldsymbol{\theta}}\right)$.

(2) The process noise $\mathbf{v}_k$ and measurement noise $\mathbf{w}_k$ are assumed to be Gaussian: $\mathbf{v}_k \sim \mathcal{N}(\mathbf{0}, \mathbf{Q}_k)$ and $\mathbf{w}_k \sim \mathcal{N}(\mathbf{0}, \mathbf{R}_k)$ for all k, where $\mathbf{Q}_k$ and $\mathbf{R}_k$ are the process and measurement noise covariances, respectively, at time step k. Therefore, $p(\boldsymbol{\theta}_k \mid \boldsymbol{\theta}_{k-1}) = \mathcal{N}\left(\boldsymbol{\theta}_{k-1}, \mathbf{Q}_{k-1}\right)$ and $p(\mathbf{y}_k \mid \boldsymbol{\theta}_k, \mathbf{u}_{1:k}) = \mathcal{N}\left(\mathbf{h}_k\left(\mathbf{u}_{1:k}; \boldsymbol{\theta}_k\right), \mathbf{R}_k\right)$ in Eq. (2.4). In this paper, $\mathbf{Q}_k$ and $\mathbf{R}_k$ are assumed time-invariant diagonal matrices. The measurement noise covariance matrix $\mathbf{R}_k = \mathbf{R}$ is described in Eq. (2.2).

(3) The process noise, $\mathbf{w}_k$, and measurement noise, $\mathbf{v}_k$, across all time steps k ($k = 1, 2, ..., N$), along with the initial parameter vector, $\boldsymbol{\theta}_0$, are assumed to be mutually statistically independent.

(4) The posterior/updated PDF $p(\boldsymbol{\theta}_k \mid \mathbf{u}_{1:k}, \mathbf{y}_{1:k})$ at each time step k is forced (assumed) to be Gaussian via approximation. Thus $p(\boldsymbol{\theta}_k \mid \mathbf{u}_{1:k}, \mathbf{y}_{1:k}) = \mathcal{N}\left(\hat{\boldsymbol{\theta}}_{k|k}, \hat{\mathbf{P}}_{k|k}^{\boldsymbol{\theta}\boldsymbol{\theta}}\right)$, where $\hat{\boldsymbol{\theta}}_{k|k}$ and $\hat{\mathbf{P}}_{k|k}^{\boldsymbol{\theta}\boldsymbol{\theta}}$ are the updated mean vector and covariance matrix, respectively, at time step k. All variants of Kalman filters only update the mean vector and covariance matrix instead of computing the entire joint PDF, thus reducing the computational cost. In the context of Bayesian

parameter estimation, Kalman filters are approximate inference techniques that operates using point estimates (mean).

In nonlinear variants of Kalman filter, statistics of a random vector, say $\mathbf{x}$, undergoing some nonlinear transformation $\mathbf{g}(\mathbf{x})$, for an arbitrary nonlinear function $\mathbf{g}$, must be evaluated. To this end, the UKF relies on unscented transformations (UTs). The UT is a method for calculating the statistics of a transformed random vector $\mathbf{g}(\mathbf{x})$ (e.g., mean vector $E_{\mathbf{x}}[\mathbf{g}(\mathbf{x})]$ and covariance matrix $Var_{\mathbf{x}}[\mathbf{g}(\mathbf{x})]$) by using a minimal set of deterministically chosen sample points $\mathcal{V}^{(i)}$, also known as sigma-points (SPs), to represent the random vector $\mathbf{x}$. The SPs are selected such that they exactly capture the mean vector and covariance matrix of random vector $\mathbf{x}$. These SPs when propagated through the nonlinear function $\mathbf{g}$, capture the mean vector and covariance matrix of the transformed random vector $\mathbf{g}(\mathbf{x})$ up to 2nd order accuracy (3rd order accuracy if $\mathbf{x}$ follows a Gaussian distribution) (van der Merwe and Wan 2004; Simon 2006). Note that the linearization used in the EKF can only capture the mean vector and covariance matrix of $\mathbf{g}(\mathbf{x})$ up to 1st order accuracy (van der Merwe and Wan 2004; Simon 2006). A specific type of UT known as scaled unscented transformation is used in this paper. Refer to (van der Merwe and Wan 2004) for more details about the UT and scaled UT. Table 2.1 shows the UKF algorithm used in this paper. For more details about this algorithm, refer to (Astroza et al. 2015; van der Merwe and Wan 2004).

Table 2.1: Unscented Kalman filtering algorithm for parameter estimation using the scaled unscented transformation

Definitions:

From state-space model : $p(\boldsymbol{\theta}_k \mid \boldsymbol{\theta}_{k-1}) = \mathcal{N}\left(\boldsymbol{\theta}_{k-1}, \mathbf{Q}_{k-1}\right)$, $p(\mathbf{y}_k \mid \boldsymbol{\theta}_k, \mathbf{u}_{1:k}) = \mathcal{N}\left(\mathbf{h}_k\left(\mathbf{u}_{1:k}; \boldsymbol{\theta}_k\right), \mathbf{R}_k\right)$

Prediction PDF at time step k: $p\left(\boldsymbol{\theta}_k \mid \mathbf{u}_{1:k-1}, \mathbf{y}_{1:k-1}\right) = \mathcal{N}\left(\hat{\boldsymbol{\theta}}_{k|k-1}, \hat{\mathbf{P}}^{\boldsymbol{\theta}\boldsymbol{\theta}}_{k|k-1}\right)$

Denominator of updated PDF at time step k: $p\left(\mathbf{y}_k \mid \mathbf{u}_{1:k}, \mathbf{y}_{1:k-1}\right) = \mathcal{N}\left(\hat{\mathbf{y}}_{k|k-1}, \hat{\mathbf{P}}^{\mathbf{yy}}_{k|k-1}\right)$

Joint PDF: $p\left(\boldsymbol{\theta}_k, \mathbf{y}_k \mid \mathbf{u}_{1:k}, \mathbf{y}_{1:k-1}\right) = \mathcal{N}\left(\begin{pmatrix} \hat{\boldsymbol{\theta}}_{k|k-1} \\ \hat{\mathbf{y}}_{k|k-1} \end{pmatrix}, \begin{pmatrix} \hat{\mathbf{P}}^{\boldsymbol{\theta}\boldsymbol{\theta}}_{k|k-1} & \hat{\mathbf{P}}^{\boldsymbol{\theta}\mathbf{y}}_{k|k-1} \\ \hat{\mathbf{P}}^{\mathbf{y}\boldsymbol{\theta}}_{k|k-1} & \hat{\mathbf{P}}^{\mathbf{yy}}_{k|k-1} \end{pmatrix}\right)$

Updated PDF at time step k: $p\left(\boldsymbol{\theta}_k \mid \mathbf{u}_{1:k}, \mathbf{y}_{1:k}\right) = \mathcal{N}\left(\hat{\boldsymbol{\theta}}_{k|k}, \hat{\mathbf{P}}^{\boldsymbol{\theta}\boldsymbol{\theta}}_{k|k}\right)$

$W_m^{(i)}$ and $W_c^{(i)}$ are weight coefficients of the SPs to estimate the mean vector and covariance matrix, respectively (van der Merwe and Wan 2004)

Initialize: $p\left(\boldsymbol{\theta}\right) = \mathcal{N}\left(\hat{\boldsymbol{\theta}}_{0|0}, \hat{\mathbf{P}}^{\boldsymbol{\theta}\boldsymbol{\theta}}_{0|0}\right)$

for $k = 1, 2, 3, ..., N$

Prediction step:

Generate SPs based on $\hat{\boldsymbol{\theta}}_{k-1|k-1}$ and $\hat{\mathbf{P}}^{\boldsymbol{\theta}\boldsymbol{\theta}}_{k-1|k-1}$: $\mathcal{V}^{(i)}_{k-1|k-1}, i = 1, 2, ..., 2n_{\boldsymbol{\theta}} + 1$

Propagate each $\mathcal{V}^{(i)}_{k-1|k-1}$ through the state equation: $\mathcal{V}^{(i)}_{k|k-1} = \mathcal{V}^{(i)}_{k-1|k-1}, i = 1, 2, ..., 2n_{\boldsymbol{\theta}} + 1$

Prediction: $\hat{\boldsymbol{\theta}}_{k|k-1} = \sum_{i=1}^{2n_{\boldsymbol{\theta}}+1} W_m^{(i)} \mathcal{V}^{(i)}_{k|k-1}$, $\hat{\mathbf{P}}^{\boldsymbol{\theta}\boldsymbol{\theta}}_{k|k-1} = \sum_{i=1}^{2n_{\boldsymbol{\theta}}+1} W_c^{(i)} \left[\mathcal{V}^{(i)}_{k|k-1} - \hat{\boldsymbol{\theta}}_{k|k-1}\right]\left[\mathcal{V}^{(i)}_{k|k-1} - \hat{\boldsymbol{\theta}}_{k|k-1}\right]^T + \mathbf{Q}_{k-1}$

Updating step:

Propagate each $\mathcal{V}^{(i)}_{k|k-1}$ through the measurement equation: $\mathcal{Y}^{(i)}_k = \mathbf{h}_k\left(\mathcal{V}^{(i)}_{k|k-1}, \mathbf{u}_{1:k}\right)$

Measurement: $\hat{\mathbf{y}}_{k|k-1} = \sum_{i=1}^{2n_{\boldsymbol{\theta}}+1} W_m^{(i)} \mathcal{Y}^{(i)}_k$, $\hat{\mathbf{P}}^{\mathbf{yy}}_{k|k-1} = \sum_{i=1}^{2n_{\boldsymbol{\theta}}+1} W_c^{(i)} \left[\mathcal{Y}^{(i)}_k - \hat{\mathbf{y}}_{k|k-1}\right]\left[\mathcal{Y}^{(i)}_k - \hat{\mathbf{y}}_{k|k-1}\right]^T + \mathbf{R}_k$

Cross-covariance: $\hat{\mathbf{P}}^{\boldsymbol{\theta}\mathbf{y}}_{k|k-1} = \sum_{i=1}^{2n_{\boldsymbol{\theta}}+1} W_c^{(i)} \left[\mathcal{V}^{(i)}_{k|k-1} - \hat{\boldsymbol{\theta}}_{k|k-1}\right]\left[\mathcal{Y}^{(i)}_k - \hat{\mathbf{y}}_{k|k-1}\right]^T$

Kalman gain: $\mathbf{K}_k = \hat{\mathbf{P}}^{\boldsymbol{\theta}\mathbf{y}}_{k|k-1}\left(\hat{\mathbf{P}}^{\mathbf{yy}}_{k|k-1}\right)^{-1}$

Parameter update: $\hat{\boldsymbol{\theta}}_{k|k} = \hat{\boldsymbol{\theta}}_{k|k-1} + \mathbf{K}_k\left(\mathbf{y}_k - \hat{\mathbf{y}}_{k|k-1}\right)$, $\hat{\mathbf{P}}^{\boldsymbol{\theta}\boldsymbol{\theta}}_{k|k} = \hat{\mathbf{P}}^{\boldsymbol{\theta}\boldsymbol{\theta}}_{k|k-1} - \mathbf{K}_k \hat{\mathbf{P}}^{\mathbf{yy}}_{k|k-1} \mathbf{K}_k^T$

2.3.2 Batch Bayesian Parameter Estimation

Batch Bayesian parameter estimation updates the prior PDF $p(\boldsymbol{\theta})$ to the posterior PDF $p(\boldsymbol{\theta} \mid \mathbf{u}_{1:N}, \mathbf{y}_{1:N})$ using all the measurement data $\mathcal{D}$ at once. This batch estimation is performed using the following implementation of Bayes' theorem:

$$\underbrace{p(\boldsymbol{\theta} \mid \mathbf{u}_{1:N}, \mathbf{y}_{1:N})}_{posterior} = \frac{\overbrace{p(\mathbf{y}_{1:N} \mid \mathbf{u}_{1:N}, \boldsymbol{\theta})}^{likelihood} \times \overbrace{p(\boldsymbol{\theta})}^{prior}}{\underbrace{p(\mathbf{y}_{1:N} \mid \mathbf{u}_{1:N})}_{evidence}} \tag{2.5}$$

where $p(\mathbf{y}_{1:N} \mid \mathbf{u}_{1:N}, \boldsymbol{\theta})$ is the likelihood function (also simply referred to as likelihood) which is essentially a goodness of fit of the measurement model (Eq. (2.1) and (2.2)) to the measurement data $\mathcal{D}$ given the values of the unknown parameter vector $\boldsymbol{\theta}$. The PDF $p(\boldsymbol{\theta} \mid \mathbf{u}_{1:N}, \mathbf{y}_{1:N})$ is the posterior distribution of $\boldsymbol{\theta}$ accounting for all measurement data $\mathcal{D}$. The denominator $p(\mathbf{y}_{1:N} \mid \mathbf{u}_{1:N})$ is the evidence. In the context of parameter estimation, the evidence is just viewed as a normalizing constant ensuring that the posterior PDF integrates to one. Thus, equation (2.5) can be written as

$$\underbrace{p(\boldsymbol{\theta} \mid \mathbf{u}_{1:N}, \mathbf{y}_{1:N})}_{posterior} \propto \underbrace{p(\mathbf{y}_{1:N} \mid \mathbf{u}_{1:N}, \boldsymbol{\theta})}_{likelihood} \times \underbrace{p(\boldsymbol{\theta})}_{prior} \tag{2.6}$$

With the measurement model defined in Eq. (2.1) and (2.2), the likelihood function $p(\mathbf{y}_{1:N} \mid \mathbf{u}_{1:N}, \boldsymbol{\theta})$ is given by

$$
\begin{aligned}
p\left(\mathbf{y}_{1:N} \mid \mathbf{u}_{1:N}, \boldsymbol{\theta}\right) &= \prod_{k=1}^{N} p\left(\mathbf{y}_k \mid \mathbf{u}_{1:k}, \boldsymbol{\theta}\right) \\
&= \prod_{k=1}^{N} \frac{1}{\left(2\pi\right)^{n_{\mathbf{y}}/2}} \left|\mathbf{R}\right|^{-1/2} \exp\left\{-\frac{1}{2}\left[\mathbf{y}_k - \mathbf{h}_k\left(\mathbf{u}_{1:k}, \boldsymbol{\theta}\right)\right] \mathbf{R}^{-1} \left[\mathbf{y}_k - \mathbf{h}_k\left(\mathbf{u}_{1:k}, \boldsymbol{\theta}\right)\right]^T\right\} \\
&= \frac{1}{\left(2\pi\right)^{n_{\mathbf{y}}N/2}} \left|\mathbf{R}\right|^{-N/2} \exp\left\{\sum_{k=1}^{N}\left[-\frac{1}{2}\left[\mathbf{y}_k - \mathbf{h}_k\left(\mathbf{u}_{1:k}, \boldsymbol{\theta}\right)\right] \mathbf{R}^{-1} \left[\mathbf{y}_k - \mathbf{h}_k\left(\mathbf{u}_{1:k}, \boldsymbol{\theta}\right)\right]^T\right]\right\}
\end{aligned}
\tag{2.7}
$$

Note that $\mathbf{u}_{1:N}$ and $\mathbf{y}_{1:N}$ in the Eq. (2.7) are the input and output measurement data, respectively. Thus, the likelihood $p\left(\mathbf{y}_{1:N} \mid \mathbf{u}_{1:N}, \boldsymbol{\theta}\right)$ is viewed as only a function of $\boldsymbol{\theta}$ and is denoted by $\mathcal{L}\left(\boldsymbol{\theta}\right)$.

Determining analytically (in explicit form) the joint posterior distribution $p\left(\boldsymbol{\theta} \mid \mathbf{u}_{1:N}, \mathbf{y}_{1:N}\right)$ with the likelihood function given in Eq. (2.7) is not possible. This is mainly due to the fact that evaluating the likelihood function involves running a FE model $\mathbf{h}$ (i.e., a complex numerical model). Numerical approximation methods such as grid-based methods, sampling-based methods (e.g., Markov chain Monte Carlo (MCMC) methods, transitional Markov chain Monte Carlo (TMCMC) method) and variational approximations (e.g., variational inference) have been developed by researchers to obtain the posterior PDF. In this paper, we focus on sampling-based methods (e.g., MCMC and TMCMC), i.e., methods that aim at sampling the joint posterior distribution of the unknown parameter vector $\boldsymbol{\theta}$.

MCMC methods (such as Metropolis-Hastings, Slice sampling, Gibbs sampling and Hamiltonian methods) are applicable in very general settings (non-gaussian prior, nonlinear model, etc.) and hence are widely used in various fields. Theoretically, MCMC can sample any joint PDF known up to a constant. However, in practice, many standard MCMC methods do not perform well (in terms of convergence) in sampling multi-modal PDFs or PDFs with flat

manifolds (Ching and Chen 2007). In addition, MCMC methods are not parallelizable and hence not ideal for model updating of computationally expensive FE models.

The TMCMC algorithm is also very flexible, easy to implement and applicable in general settings. Unlike MCMC methods, TMCMC is inherently parallel. So, it can be used to perform model updating of computationally expensive high-fidelity large-scale nonlinear FE models using high-performance computing (HPC) resources. In addition, TMCMC can effectively sample from multi-modal PDFs and PDFs with flat manifolds (Ching and Chen 2007). TMCMC also computes the model evidence as a by-product, which can then be used for Bayesian model class selection and model averaging (Ching and Chen 2007). To this end, TMCMC is used in this paper for batch Bayesian estimation of the testbed structure.

2.3.2.1 Transitional Markov Chain Monte Carlo

TMCMC method is a simulation-based Bayesian inference technique which sample from the complete joint posterior distribution of the unknown parameter vector $\boldsymbol{\theta}$. In the literature, there are several closely related algorithms such as cascading adaptive transitional metropolis in parallel, sequential Monte Carlo, particle filters, bootstrap filters, condensation algorithm, survival of the fittest and population Monte Carlo algorithms. TMCMC do not require the Gaussian assumption about the prior and posterior PDFs of the unknown parameters, an inherent assumption in Kalman filters and its nonlinear variants.

TMCMC avoids sampling directly the target PDF, but instead constructs a series of easy-to-sample intermediate PDFs that starts from the prior distribution and converges to the target posterior distribution as

$$p\left(\boldsymbol{\theta} \mid \mathbf{u}_{1:N}, \mathbf{y}_{1:N}\right)_j \propto p\left(\mathbf{y}_{1:N} \mid \mathbf{u}_{1:N}, \boldsymbol{\theta}\right)^{\beta_j} \times p\left(\boldsymbol{\theta}\right); \quad j = 0,1,...,m \quad 0 = \beta_0 < \beta_1 < ... < \beta_m = 1 \quad (2.8)$$

where index j denotes the stage number, m denotes the total number of stages and $p(\boldsymbol{\theta}|\mathbf{u}_{1:N},\mathbf{y}_{1:N})_j$ is the intermediate PDF at stage j controlled by parameter β_j. At the initial stage $(j=0)$, parameter $\beta_0=0$ and the intermediate PDF $p(\boldsymbol{\theta}|\mathbf{u}_{1:N},\mathbf{y}_{1:N})_0$ is just the prior PDF $p(\boldsymbol{\theta})$. The TMCMC sampler progresses by monotonically increasing the value of β_j, at each stage j, until it reaches the value of 1. At the final stage $(j=m)$, parameter $\beta_m=1$ and the intermediate PDF $p(\boldsymbol{\theta}|\mathbf{u}_{1:N},\mathbf{y}_{1:N})_m$ is the target posterior PDF $p(\boldsymbol{\theta}|\mathbf{u}_{1:N},\mathbf{y}_{1:N})$. The series of intermediate PDFs is represented as

$$\underbrace{p(\boldsymbol{\theta}|\mathbf{u}_{1:N},\mathbf{y}_{1:N})_0}_{\equiv p(\boldsymbol{\theta})} \rightarrow p(\boldsymbol{\theta}|\mathbf{u}_{1:N},\mathbf{y}_{1:N})_1 \rightarrow \cdots \rightarrow \underbrace{p(\boldsymbol{\theta}|\mathbf{u}_{1:N},\mathbf{y}_{1:N})_m}_{\equiv p(\boldsymbol{\theta}|\mathbf{u}_{1:N},\mathbf{y}_{1:N})} \tag{2.9}$$

TMCMC represents the intermediate PDF at every stage by a set of weighted samples (known as particles). TMCMC approximates the j^{th} stage intermediate PDF $p(\boldsymbol{\theta}|\mathbf{u}_{1:N},\mathbf{y}_{1:N})_j$ by weighting, resampling, and perturbing the particles representing the $(j-1)^{th}$ stage intermediate PDF $p(\boldsymbol{\theta}|\mathbf{u}_{1:N},\mathbf{y}_{1:N})_{j-1}$. In this paper, resampling is performed using random sampling and the perturbation of particles is performed using the MCMC Metropolis-Hastings algorithm. The TMCMC sampler can be thought of as a parallel MCMC algorithm that can effectively sample high-dimensional parameter spaces. The algorithmic details of the process of weighting, resampling and perturbing at each TMCMC stage are provided in Table 2.2 and a schematic representation of a TMCMC stage is shown in Figure 2.1. For more details about the TMCMC algorithm refer to (Ching and Chen 2007; Minson et al. 2013).

Table 2.2: TMCMC algorithm for parameter estimation

Notation: N_p : number of particles ; j : stage number ; $\boldsymbol{\theta}$: unknown parameter vector ;

$\boldsymbol{\theta}_{(j)}^{(i)}$: i^{th} particle of $\boldsymbol{\theta}$ at stage j ; wn_j^i : weight of i^{th} particle of $\boldsymbol{\theta}$ at stage j ;

N_{MCMC} : number of MCMC steps ;

s : scaling factor of proposal covariance in perturbation step ;

$ESS_j \triangleq \dfrac{1}{\sum_{i=1}^{N_p}\left(wn_j^i\right)^2} \in \left[1, N_p\right]$: effective sample size at stage j

Initialize: N_p , $j=0$, $ESS_0 = N_p$, $\beta_0 = 0$, N_{MCMC} , $s=1$

Generate N_p samples $\left\{\boldsymbol{\theta}_{(j=0)}^{(i)},\ i=1,...,N_p\right\}$ from the prior PDF $p(\boldsymbol{\theta})$

while $\beta_j < 1$:

Stage number $j = j+1$

Determine β_j:

find $\tilde{\beta}_j$ such that $ESS_j = 0.95 \times ESS_{j-1}$ (through applying the weighting step below iteratively) ; when converged: $\beta_j = \min\left(\tilde{\beta}_j, 1\right)$

<u>weighting</u>:

$$wn_j^i = \frac{w_j^i}{\sum_{i=1}^{N_p} w_j^i};\quad w_j^i = \frac{p\left(\boldsymbol{\theta}_{(j-1)}^{(i)} \mid \mathbf{u}_{1:N}, \mathbf{y}_{1:N}\right)_j}{p\left(\boldsymbol{\theta}_{(j-1)}^{(i)} \mid \mathbf{u}_{1:N}, \mathbf{y}_{1:N}\right)_{j-1}} = p\left(\mathbf{y}_{1:N} \mid \mathbf{u}_{1:N}, \boldsymbol{\theta}_{(j-1)}^{(i)}\right)^{\beta_j - \beta_{j-1}} \text{ for } i = 1,...,N_p$$

Sample mean of weighted samples: $\bar{\boldsymbol{\theta}}_{(j-1)} = \sum_{i=1}^{N_p} wn_j^i\ \boldsymbol{\theta}_{(j-1)}^{(i)}$

Sample covariance of weighted samples: $\bar{\mathbf{C}}_{(j-1)} = \sum_{i=1}^{N_p} wn_j^i \left[\boldsymbol{\theta}_{(j-1)}^{(i)} - \bar{\boldsymbol{\theta}}_{(j-1)}\right]\left[\boldsymbol{\theta}_{(j-1)}^{(i)} - \bar{\boldsymbol{\theta}}_{(j-1)}\right]^T$

<u>resampling</u>:

$\tilde{\boldsymbol{\theta}}_{(j)}^{(i)}$ $\left(i = 1,\ldots,N_p\right)$ are sampled according to the probability mass function $P\left[\boldsymbol{\theta} = \boldsymbol{\theta}_{(j-1)}^{(k)}\right] = wn_j^k$ $\left(k = 1,\ldots,N_p\right)$

Table 2.2: TMCMC algorithm for parameter estimation (continued)

perturbation:

start an MCMC Metropolis-Hastings chain at $\tilde{\boldsymbol{\theta}}_{(j)}^{(i)}$ and take N_{MCMC} steps with target distribution $p\left(\boldsymbol{\theta}\,|\,\mathbf{u}_{1:N},\mathbf{y}_{1:N}\right)_j$, for each $i=1,...,N_p$. The proposal distribution for the MCMC walks is a Normal distribution with covariance matrix $s^2\,\overline{\mathbf{C}}_{(j-1)}$. Gather the last sample of each MCMC chain to obtain $\left\{\boldsymbol{\theta}_{(j)}^{(i)};\, i=1,...,N_p\right\}$. These samples represent the intermediate PDF $p\left(\boldsymbol{\theta}\,|\,\mathbf{u}_{1:N},\mathbf{y}_{1:N}\right)_j$ (see red particles in Figure 2.1).

Calculate the acceptance rate $R \triangleq \dfrac{\text{total number of accepts}}{\text{total number of proposals}}$ of the perturbation step.

Using R, compute scaling factor for next stage proposal distribution: $s=(1/9)+(8/9)R$. (Minson et al. 2013)

end

save last stage $m=j$

$\left\{\boldsymbol{\theta}_{(m)}^{(i)},\ i=1,...,N_p\right\}$: samples representing the target posterior $p\left(\boldsymbol{\theta}\,|\,\mathbf{u}_{1:N},\mathbf{y}_{1:N}\right)$

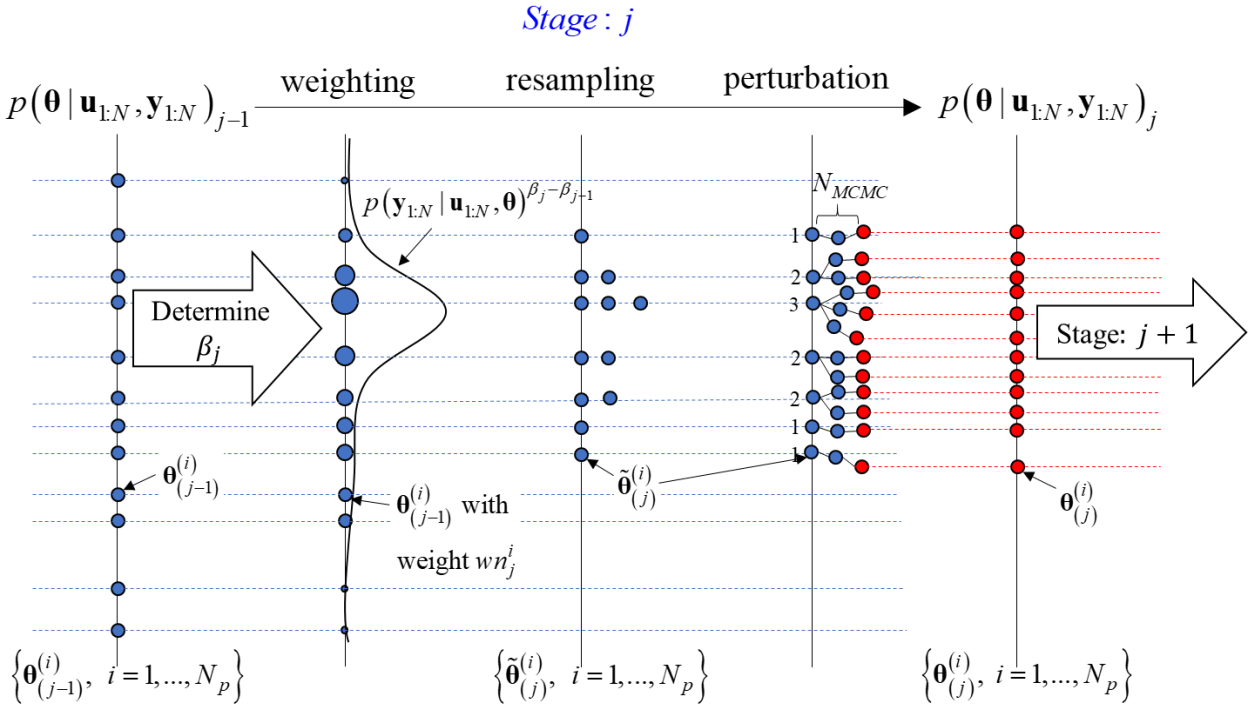

Figure 2.1: A stage in TMCMC algorithm (weighting, resampling, and perturbation). In the above illustration, $\boldsymbol{\theta}$ is a scalar quantity.

2.4 Identifiability

Identifiability is concerned with the possibility of estimating (at least locally) the unknown parameters of a mathematical model (e.g., FE models of civil structural systems) for a given input and output. Under this definition, identifiability is a property of the likelihood function and is the same whether considered classically or from the Bayesian approach (San Martın and González 2010). The problem of model identifiability surfaces in mathematical models of various fields (e.g., ordinary or partial differential equations of biophysical systems, FE models of civil structural systems) while solving a model updating problem. Therefore, it is important to perform some sort of identifiability analysis before solving an actual inverse problem to answer questions such as “which model parameters or parameter combinations can be uniquely estimated from the input-output measurement data?”. This paper mainly concerns the

identifiability of FE models. It is important to note that identifiability is a property of both the model and the input-output measurement data, and not just of the model. Therefore, identifiability analysis is performed given a model and the input-output measurement data considered.

A non-identifiable model parameter indicates that the model output (for a given input) is either insensitive to that parameter or the parameter is part of an identifiable parameter combination (Brouwer and Eisenberg 2018). If the sensitivity of the model output (for a given input) to a parameter is zero or low, then it implies that the measurement input-output data will contain no or little information about that parameter. Such insensitive or poorly sensitive parameter should ideally be eliminated from the inference process by fixing its value anywhere in its range of uncertainty as it has no or little effect on the model output. On the other hand, if a parameter is not identifiable because it is part of an identifiable parameter combination, then the model structure should ideally be changed by replacing the entire identifiable parameter combination with a single parameter. For example, in the model $y=(m_1+m_2)x+c$ with (x,y) pairs as the measurement input-output data, parameter c is identifiable but parameters m_1 and m_2 are not, but the sum (m_1+m_2) is an identifiable parameter combination. There are infinite (m_1,m_2) pairs that explain the measurement data equally well, i.e., parameters m_1 and m_2 compensate each other to explain the measurement data. Thus, this kind of non-identifiability results in non-unique estimates when the inference is performed using approximate inference methods that rely on point estimates such as Kalman filters. If the model is reparametrized as $y=mx+c$, the new model parameters (m and c) are identifiable with (x,y) pairs as measurement input-output data (Brouwer and Eisenberg 2018). However, this requires: (1)

screening the existing model $y=(m_1+m_2)x+c$ to identify compensating parameters (m_1, m_2), (2) obtaining the functional relation between the compensating parameters, m_1+m_2, and (3) restructuring the model by replacing the identifiable parameter combination with a single parameter, $y=mx+c$. Refer to (Eisenberg and Hayashi 2014; Raue et al. 2009) for more information about determining identifiable parameters and/or parameter combinations of mathematical models. In the case of FE models, it is extremely difficult to determine compensating parameters (i.e., parameters with compensating effects) and the functional relation among them (i.e., identifiable parameter combination). Even if found, replacing the identifiable parameter combination with a single parameter would require having access to the FE source code (e.g., OpenSees software). A practical alternative is to fix all the parameters (from the parameter combination) in their range of uncertainty except for one of them and estimate the leftover parameter. In the above example, if m_2 is fixed to a certain value, then m_1 becomes identifiable. The caveat is that when m_2 is fixed to a non-true value, then m_1 will be estimated incorrectly. However, the exact values of m_1 and m_2 may not be required to understand the system behavior. Based on the authors' experience, it is very likely that a nonlinear FE model of a large-scale civil structural system contains non-identifiable parameters (either due to parameter insensitivity or parameter being part of an identifiable parameter combination).

A common distinction in parameter identifiability is global and local identifiability. A parameter of the model is said to be globally identifiable if there exists a unique solution in the parameter space for a given model input-output. On the other hand, if a parameter, say ϕ, of the model has a finite number of solutions in its parameter space for a given model and input-output, but a unique solution in the neighborhood of, say ϕ^*, then the parameter ϕ is said to be locally

identifiable in the neighborhood of ϕ^*. If a parameter of the model has infinitely many solutions in its parameter space for a given model and input-output, then it is said to be non-identifiable or unidentifiable (such as in the simple linear example described above). Another important distinction in model identifiability is structural/theoretical versus practical identifiability. Structural or theoretical identifiability deals with the ability to uniquely determine the unknown parameters of the model assuming ideal conditions (i.e., noise-free input-output measurement data and error-free model) thus revealing identifiability issues related to the model structure of the candidate mathematical model. Therefore, structural identifiability of the model just depends on the model structure (which includes the designation of the input and output) and not on the measurement data (as in the simple linear example described above). Although it is unrealistic to assume these ideal conditions, structural identifiability of the model (i.e., identifiability of all parameters of the error-free model using noise-free input-output measurement data) is a necessary condition for practical identifiability. Practical identifiability deals with the possibility of uniquely estimating the unknown parameters from noisy input-output data using an imperfect model (real world scenario) thus highlighting identifiability issues related to the use of real data. Therefore, practical identifiability of a model is a property of both the model structure and the measurement input-output data (i.e., depends on the quantity, quality and frequency content of the data).

In identifiability analysis, the model should be viewed as the mapping between unknown parameters and the output response (e.g., type, location and number of sensors) for a given input which is considered part of the model. Thus, in the identifiability analysis part of this paper, the model is the mapping between the unknown parameter vector $\boldsymbol{\theta}$ and the FE output response of interest $\mathbf{y}_{1:N}^{FE}$, where $\mathbf{y}_k^{FE} = \mathbf{h}_k\left(\mathbf{u}_{1:k}, \boldsymbol{\theta}\right) \in \mathbb{R}^{n_\mathbf{y}}$. In this regard, practical identifiability analysis

should be performed for several realizations (e.g., different earthquake ground motion records with the same overall intensity but different frequency content) of the input $\mathbf{u}_{1:N}$ to conclude which parameters are practically identifiable for that specific input.

As mentioned above, a practically non-identifiable model parameter indicates that the model output (for a given input) is either insensitive to that parameter or the parameter is part of an identifiable parameter combination (with compensation effects between the parameters of that combination). Sensitivity analysis should be performed to assess the sensitivity of each output to each parameter of the model. Non and low sensitive parameters should be eliminated from the inference as they are not practically identifiable. However, highly sensitive parameters could also be practically non-identifiable, as they can be part of an identifiable parameter combination. In other words, parameter sensitivity is a necessary but not sufficient condition for practical parameter identifiability. Thus, we cannot address practical identifiability without considering sensitivity.

2.4.1 Sensitivity analysis

Sensitivity analysis in the context of parameter estimation is a study of how uncertainty (or variability) in the model output can be apportioned to different sources of uncertainty (or variability) in the model parameters (Saltelli et al. 2007). Sensitivity analysis allows the detection of the parameters or parameter sets that have the greatest influence on the model output(s). Sensitivity analysis has been widely used in numerous fields, such as computational optimization, structural reliability and risk analysis, and economics, and it is instrumental in civil engineering to guide the development and understanding of complex nonlinear FE models of civil infrastructure systems. There are two main approaches to sensitivity analysis: local

sensitivity analysis (LSA) and global sensitivity analysis (GSA). Well known approaches to GSA are derivative-based GSA and variance-based GSA (also known as Sobol' method). Each of these approaches are briefly described below. A schematic representation of these approaches is shown in Figure 2.2.

LSA varies one parameter at a time (in small increments) and determines its effect on the model output. For a model $z = f(\boldsymbol{\theta})$ with scalar output $z \in \mathbb{R}$ and vector parameterization $\boldsymbol{\theta} = \left[\theta_1, \theta_2, ..., \theta_{n_{\boldsymbol{\theta}}}\right] \in \mathbb{R}^{n_{\boldsymbol{\theta}}}$, the derivative $\partial z / \partial \theta_i \big|_{\theta_i = \theta_i^*}$ of scalar output z with respect to parameter θ_i is the local sensitivity metric for sensitivity of z to θ_i at the evaluation point $\theta_i = \theta_i^*$. The derivatives are only informative at the evaluation point θ_i^*; therefore, local sensitivity metrics are only valid in the local region around the evaluation point. This is a major limitation for models with a nonlinear relation between parameters and model output (as is the case of most FE models of civil structural systems). In addition, LSA only varies one parameter at a time thus not revealing the effect of simultaneous changes in model parameters on the model output. Derivatives for LSA can be directly computed by the direct differentiation method (DDM) (Conte et al. 2003). However, the DDM is not implemented in most FE software. Alternatively, local derivates of FE responses can be obtained using the finite difference method or the adjoint method. The FE software used in this paper – *OpenSees* – has DDM response sensitivity capabilities (Scott and Haukaas 2008).

Derivative-based GSA has become popular among researchers in recent years. This metric average local derivatives over the parameter space to produce global sensitivity metric (i.e., a natural extension of LSA). For our previous model $z = f(\boldsymbol{\theta})$, the derivative-based global

sensitivity metrics for some probability distribution over the parameter space, $\rho(\boldsymbol{\theta})$, are defined as

$$\nu_i = \int \left(\frac{\partial z}{\partial \theta_i} \right)^2 \rho(\boldsymbol{\theta}) \, d\boldsymbol{\theta}, \quad i = 1, 2, ..., n_{\boldsymbol{\theta}} \tag{2.10}$$

Evaluating derivative-based global sensitivity metrics is not within the scope of this paper. For more information about derivative-based GSA, refer to (Kucherenko et al. 2009; Kucherenko and Iooss 2017; Sobol' and Kucherenko 2009).

Variance-based GSA (aka Sobol' method) varies all parameters simultaneously (explores the global parameter space) and quantifies the effect on the model output in a rigorous and structured way. In variance-based GSA, sensitivity of each individual parameter is evaluated by varying all parameters simultaneously thus revealing any possible interaction between parameters within a model. Variance-based GSA does not need an evaluation point. Hence, it is a tool for studying the mathematical model rather than its specific solutions (Sobol' 2001). In the context of parameter estimation, the GSA framework is fundamentally rooted in the decomposition of the variance of the model output (for a given input) into contributions of the parameters and their interactions (i.e., sets of parameters). Indices obtained as a result of this decomposition (Sobol' indices) can be directly used as measures of sensitivity.

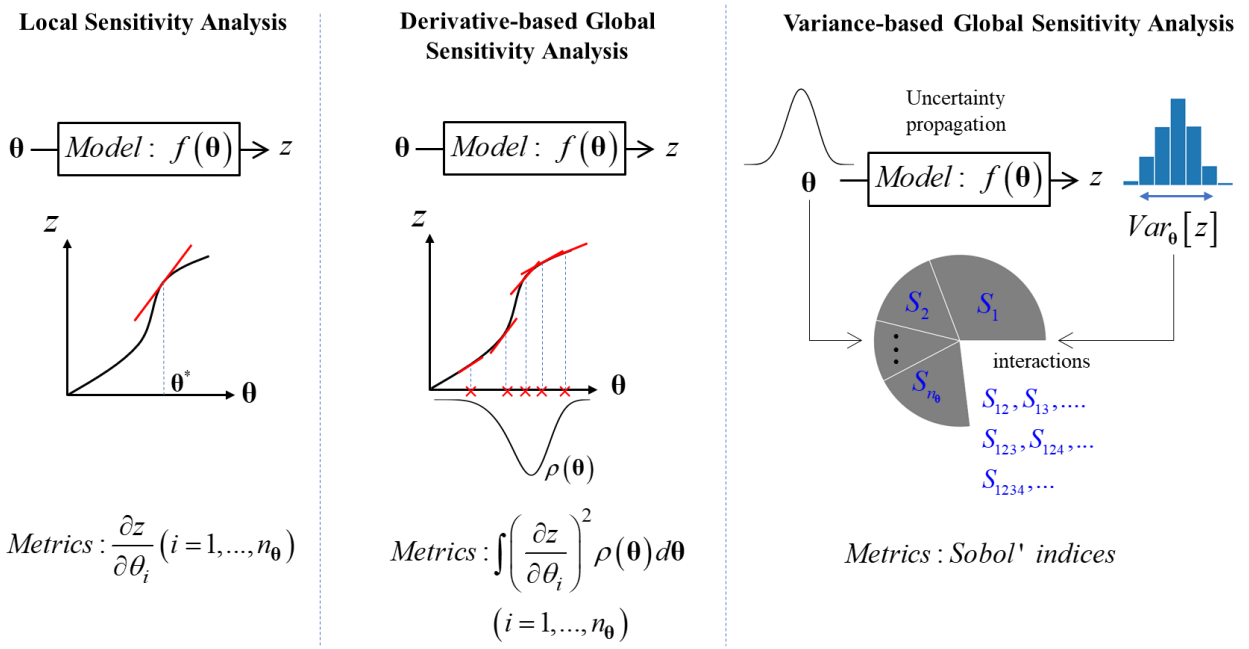

Figure 2.2: Schematic representation of local sensitivity analysis, derivative-based GSA, and variance-based GSA

For a dynamic system (e.g., the testbed structure in Section 2.5), sensitivity metrics/indices (local or global) are obtained as a function of time. Hence, they are referred to as sensitivity functions or sensitivity time histories. Section 2.4.2 focuses on local practical identifiability analysis using Fisher information matrix, which uses local sensitivity results, while Section 2.4.3 deals with the variance-based GSA method as a way to shed light into global identifiability. Note that in nonlinear FE models under dynamic loading, the identifiability/sensitivity of parameters changes with time and with the considered output measurement channel. This aspect is beyond the scope of this paper. This paper focuses on the identifiability/sensitivity analysis of parameters considering only the entire measurement data (i.e., entire time history of all input and output measurement channels) (Bhrushundi et al. 2019; Jung et al. 2021; Karingula et al. 2021).

2.4.2 Local Practical Identifiability Analysis using Fisher Information Matrix

The concept of Fisher information stems from classical estimation theory. Fisher information represents the amount of information that the measurement data $\mathcal{D}$ contain about the unknown parameter vector $\boldsymbol{\theta}$, and is therefore very useful for structural and practical identifiability analysis. In terms of geometric interpretation, Fisher information is closely related to the curvature of the log-likelihood function, as measured by its Hessian. Its sharpness determines how accurately the unknown parameter vector $\boldsymbol{\theta}$ can be estimated from the measurement data $\mathcal{D}$ (Kay 1993).

Recall the measurement equation at time step k (Eq. (2.1) and (2.2))

$$\mathbf{y}_k = \mathbf{h}_k\left(\mathbf{u}_{1:k};\boldsymbol{\theta}\right) + \mathbf{w}_k \quad \text{where} \quad \mathbf{w}_k \sim \mathcal{N}\left(\mathbf{0},\mathbf{R}\right) \tag{2.11}$$

The measurement equation for all time steps ($k = 1,2,...,N$) combinedly can be written as

$$\mathbf{y}_{1:N} = \mathbf{y}_{1:N}^{FE} + \mathbf{w} \quad \text{where} \quad \mathbf{w} \sim \mathcal{N}\left(\mathbf{0},\mathbf{C}\right) \tag{2.12}$$

where $\mathbf{y}_{1:N}^{FE} = \left[\mathbf{y}_1^{FE^T}, \mathbf{y}_2^{FE^T}, ..., \mathbf{y}_N^{FE^T}\right]^T \in \mathbb{R}^{\left(n_{\mathbf{y}} \times N\right) \times 1}$, $\mathbf{y}_k^{FE} = \mathbf{h}_k\left(\mathbf{u}_{1:k},\boldsymbol{\theta}\right) \in \mathbb{R}^{n_{\mathbf{y}}}$ and the error/noise covariance matrix $\mathbf{C}$ is defined in Eq. (2.2). Therefore, the likelihood function is of the form

$$p\left(\mathbf{y}_{1:N} \mid \mathbf{u}_{1:N},\boldsymbol{\theta}\right) = \mathcal{N}\left(\mathbf{y}_{1:N}^{FE}\left(\boldsymbol{\theta}\right),\mathbf{C}\right) \tag{2.13}$$

Note that only the mean of $p\left(\mathbf{y}_{1:N} \mid \mathbf{u}_{1:N},\boldsymbol{\theta}\right)$, $\mathbf{y}_{1:N}^{FE}\left(\boldsymbol{\theta}\right)$, depends on $\boldsymbol{\theta}$. For such cases, the Fisher information matrix (FIM), $\mathbf{I}\left(\boldsymbol{\theta}\right)$, evaluated at any $\boldsymbol{\theta} = \boldsymbol{\theta}^*$, is a symmetric $n_{\boldsymbol{\theta}} \times n_{\boldsymbol{\theta}}$ matrix given by (refer to Section 3.9 of (Kay 1993))

$$\underset{n_{\boldsymbol{\theta}}\times n_{\boldsymbol{\theta}}}{\mathbf{I}\left(\boldsymbol{\theta}^{*}\right)}=\underbrace{\boldsymbol{\chi}\left(\boldsymbol{\theta}^{*}\right)^{T}}_{n_{\boldsymbol{\theta}}\times Nn_{\mathbf{y}}}\underset{Nn_{\mathbf{y}}\times Nn_{\mathbf{y}}}{\mathbf{C}^{-1}}\underset{Nn_{\mathbf{y}}\times n_{\boldsymbol{\theta}}}{\boldsymbol{\chi}\left(\boldsymbol{\theta}^{*}\right)} \tag{2.14}$$

where $\boldsymbol{\chi}\left(\boldsymbol{\theta}^{*}\right)$ is the sensitivity matrix evaluated at $\boldsymbol{\theta}=\boldsymbol{\theta}^{*}$, i.e.,

$$\underset{Nn_{\mathbf{y}}\times n_{\boldsymbol{\theta}}}{\boldsymbol{\chi}\left(\boldsymbol{\theta}\right)}=\frac{\partial\mathbf{y}_{1:N}^{FE}}{\partial\boldsymbol{\theta}}=\begin{pmatrix}\frac{\partial\mathbf{y}_{1:N}^{FE}}{\partial\theta_1} & \cdots & \frac{\partial\mathbf{y}_{1:N}^{FE}}{\partial\theta_{n_{\boldsymbol{\theta}}}}\end{pmatrix}=\begin{pmatrix}\frac{\partial\mathbf{y}_{1}^{FE}}{\partial\theta_1} & \cdots & \frac{\partial\mathbf{y}_{1}^{FE}}{\partial\theta_{n_{\boldsymbol{\theta}}}}\\ \vdots & \ddots & \vdots\\ \frac{\partial\mathbf{y}_{N}^{FE}}{\partial\theta_1} & \cdots & \frac{\partial\mathbf{y}_{N}^{FE}}{\partial\theta_{n_{\boldsymbol{\theta}}}}\end{pmatrix}=\begin{pmatrix}\frac{\partial y_{1,(1)}^{FE}}{\partial\theta_1} & \cdots & \frac{\partial y_{1,(1)}^{FE}}{\partial\theta_{n_{\boldsymbol{\theta}}}}\\ \vdots & \ddots & \vdots\\ \frac{\partial y_{1,(n_{\mathbf{y}})}^{FE}}{\partial\theta_1} & \cdots & \frac{\partial y_{1,(n_{\mathbf{y}})}^{FE}}{\partial\theta_{n_{\boldsymbol{\theta}}}}\\ \vdots & \ddots & \vdots\\ \frac{\partial y_{N,(1)}^{FE}}{\partial\theta_1} & \cdots & \frac{\partial y_{N,(1)}^{FE}}{\partial\theta_{n_{\boldsymbol{\theta}}}}\\ \vdots & \ddots & \vdots\\ \frac{\partial y_{N,(n_{\mathbf{y}})}^{FE}}{\partial\theta_1} & \cdots & \frac{\partial y_{N,(n_{\mathbf{y}})}^{FE}}{\partial\theta_{n_{\boldsymbol{\theta}}}}\end{pmatrix} \tag{2.15}$$

where $\mathbf{y}_{k}^{FE}=\left[y_{k,(1)}^{FE},y_{k,(2)}^{FE},...,y_{k,(n_{\mathbf{y}})}^{FE}\right]^{T}\in\mathbb{R}^{n_{\mathbf{y}}}$ and $y_{k,(i)}^{FE}$ is the FE predicted output response corresponding to the i^{th} measurement channel at time step k. Note that for structural identifiability analysis, the matrix $\mathbf{C}$ in Eq. (2.14) is taken as the identity matrix (Brouwer and Eisenberg 2018).

The FIM evaluated at $\boldsymbol{\theta}=\boldsymbol{\theta}^{*}$, $\mathbf{I}\left(\boldsymbol{\theta}^{*}\right)$, having full rank (i.e., $rank\left(\mathbf{I}\left(\boldsymbol{\theta}^{*}\right)\right)=n_{\boldsymbol{\theta}}$) implies that the parameter vector/set $\boldsymbol{\theta}=\left[\theta_1,\theta_2,...,\theta_{n_{\boldsymbol{\theta}}}\right]^{T}$ is practically locally identifiable in the neighborhood of $\boldsymbol{\theta}=\boldsymbol{\theta}^{*}$. If $\mathbf{I}\left(\boldsymbol{\theta}^{*}\right)$ is rank deficient, then $rank\left(\mathbf{I}\left(\boldsymbol{\theta}^{*}\right)\right)$ gives the number of (practically locally) identifiable parameters. In this case, the model is referred to as partially identifiable since all the parameters of the model are not identifiable. The FIM is a real

symmetric positive semi-definite ((Kay 1993)). The numerical rank of such positive semi-definite matrix is defined as the number of eigenvalues that are larger than some tolerance. The choice of the tolerance depends on both the matrix and the application.

For partially identifiable models, the notion of Cramer-Rao lower bound (CRLB) from classical estimation theory can be used to determine the identifiable parameters in the parameter vector $\boldsymbol{\theta}$. Let $\tilde{\boldsymbol{\theta}}$ be an unbiased estimator of $\boldsymbol{\theta}$. The vector parameter CRLB places a lower bound on the variance of each element $\tilde{\theta}_i$ of $\tilde{\boldsymbol{\theta}}$ (Kay 1993). In other words, there exists no unbiased estimator whose variance is lower than the CRLB. Under certain common assumptions (Kay 1993), the inverse of the FIM provides the CRLB covariance matrix, **CRLBCM**, whose diagonal entries correspond to the CRLB of each parameter estimator $\tilde{\theta}_i$ (i.e., lower bound on the variance of $\tilde{\theta}_i$), denoted as $CRLB\left(\tilde{\theta}_i\right)$. If $CRLB\left(\tilde{\theta}_i\right)$ is very large, then so is the lower bound of the variance of estimator $\tilde{\theta}_i$ and parameter θ_i is probably unidentifiable. Furthermore, if $CRLB\left(\tilde{\theta}_i\right) > CRLB\left(\tilde{\theta}_j\right)$, then θ_j is easier to estimate than θ_i (Kay 1993). Thus, the CRLB can be used to rank the parameters in order of their local identifiability in the neighborhood of $\boldsymbol{\theta} = \boldsymbol{\theta}^*$. Note that for a partially identifiable model, the FIM is singular and therefore the CRLB covariance matrix does not exist; however, the inverse of the FIM can still be calculated numerically as, in this case, the determinant of the FIM is generally extremely low but non-zero. The algorithm for ranking the parameters is shown in Table 2.3. Using this ranking of parameters together with the rank of the FIM (evaluated numerically), an informed decision can be made about which parameters of $\boldsymbol{\theta}$ are practically identifiable locally in the neighborhood of $\boldsymbol{\theta} = \boldsymbol{\theta}^*$.

Table 2.3: Algorithm for ranking and determining practically locally identifiable parameters for parameter estimation

Initialize: parameter vector $\boldsymbol{\theta}^{(1)} = \left[\theta_1, \theta_2, ..., \theta_{n_{\boldsymbol{\theta}}}\right]^T \in \mathbb{R}^{n_{\boldsymbol{\theta}}}$

sensitivity matrix $\boldsymbol{\chi}^{(1)} = \boldsymbol{\chi}\left(\boldsymbol{\theta}^*\right) \in \mathbb{R}^{Nn_{\mathbf{y}} \times n_{\boldsymbol{\theta}}}$ at the evaluation point $\boldsymbol{\theta} = \boldsymbol{\theta}^*$

error/noise covariance matrix $\mathbf{C} \in \mathbb{R}^{Nn_{\mathbf{y}} \times Nn_{\mathbf{y}}}$

Note: In this table, $\boldsymbol{\theta}^{(i)}$ must be viewed as a symbolic parameter vector.

Number of locally identifiable parameters: $n_{\boldsymbol{\theta}}^{ID} = rank\left(\mathbf{I}\left(\boldsymbol{\theta}^*\right)\right)$ (evaluate the rank of matrix $\mathbf{I}\left(\boldsymbol{\theta}^*\right)$ numerically, i.e., the number of eigenvalues of $\mathbf{I}\left(\boldsymbol{\theta}^*\right)$ that are larger than some tolerance)

To rank the parameters in order of their local identifiability in the neighborhood of $\boldsymbol{\theta} = \boldsymbol{\theta}^*$:

for $i = 1, 2, ..., n_{\boldsymbol{\theta}}$

Evaluate the Fisher information matrix: $\mathbf{I}^{(i)}\left(\boldsymbol{\theta}^*\right) = \left(\boldsymbol{\chi}^{(i)}\right)^T \mathbf{C}^{-1} \left(\boldsymbol{\chi}^{(i)}\right)$

Evaluate numerically the CRLB covariance matrix: $\mathbf{CRLBCM}^{(i)} = \left(\mathbf{I}^{(i)}\left(\boldsymbol{\theta}^*\right)\right)^{-1}$

Find index j such that $\left[diag\left(\mathbf{CRLBCM}^{(i)}\right)\right]_j = \max\left(diag\left(\mathbf{CRLBCM}^{(i)}\right)\right)$

Assign rank $n_{\boldsymbol{\theta}} - (i-1)$ to j^{th} element of parameter vector $\boldsymbol{\theta}^{(i)}$

$\boldsymbol{\theta}^{(i+1)}$ = parameter vector $\boldsymbol{\theta}^{(i)}$ with j^{th} element removed

$\boldsymbol{\chi}^{(i+1)}$ = sensitivity matrix $\boldsymbol{\chi}^{(i)}$ with j^{th} column removed

end

Now each element of parameter vector $\left[\theta_1, \theta_2, ..., \theta_{n_{\boldsymbol{\theta}}}\right]^T$ has an assigned rank. The top ranked $n_{\boldsymbol{\theta}}^{ID}$ parameters are the practically locally identifiable parameters around $\boldsymbol{\theta} = \boldsymbol{\theta}^*$

In practice, the parameters in vector $\boldsymbol{\theta}$ are usually of different physical dimensions. In addition, the output responses of the FE model may also be of different physical dimensions.

Therefore, some normalization is performed on the sensitivity matrix for many identifiability tests in practical applications. The following normalization is used in this paper and the normalized sensitivity matrix is used to rank the parameters according to the algorithm presented in Table 2.3.

$$\underset{Nn_{\mathbf{y}}\times n_{\boldsymbol{\theta}}}{\chi'(\boldsymbol{\theta})}=\begin{pmatrix} \frac{\theta_1^{prior}}{yn_{(1)}}\frac{\partial y_{1,(1)}^{FE}}{\partial\theta_1} & \cdots & \frac{\theta_{n_{\boldsymbol{\theta}}}^{prior}}{yn_{(1)}}\frac{\partial y_{1,(1)}^{FE}}{\partial\theta_{n_{\boldsymbol{\theta}}}} \\ \vdots & \ddots & \vdots \\ \frac{\theta_1^{prior}}{yn_{(n_{\mathbf{y}})}}\frac{\partial y_{1,(n_{\mathbf{y}})}^{FE}}{\partial\theta_1} & \cdots & \frac{\theta_{n_{\boldsymbol{\theta}}}^{prior}}{yn_{(n_{\mathbf{y}})}}\frac{\partial y_{1,(n_{\mathbf{y}})}^{FE}}{\partial\theta_{n_{\boldsymbol{\theta}}}} \\ \vdots & \ddots & \vdots \\ \frac{\theta_1^{prior}}{yn_{(1)}}\frac{\partial y_{N,(1)}^{FE}}{\partial\theta_1} & \cdots & \frac{\theta_{n_{\boldsymbol{\theta}}}^{prior}}{yn_{(1)}}\frac{\partial y_{N,(1)}^{FE}}{\partial\theta_{n_{\boldsymbol{\theta}}}} \\ \vdots & \ddots & \vdots \\ \frac{\theta_1^{prior}}{yn_{(n_{\mathbf{y}})}}\frac{\partial y_{N,(n_{\mathbf{y}})}^{FE}}{\partial\theta_1} & \cdots & \frac{\theta_{n_{\boldsymbol{\theta}}}^{prior}}{yn_{(n_{\mathbf{y}})}}\frac{\partial y_{N,(n_{\mathbf{y}})}^{FE}}{\partial\theta_{n_{\boldsymbol{\theta}}}} \end{pmatrix};\quad \begin{aligned} &yn_{(i)}=\max_k\left(abs(y_{k,(i)}^{FE,prior})\right),\\ &i=1,2,...,n_{\mathbf{y}};\ k=1,2,...,N \end{aligned} \tag{2.16}$$

where $\boldsymbol{\theta}^{prior}$ is the mean of the prior PDF $p(\boldsymbol{\theta})$, $\mathbf{y}_k^{FE,prior}=\mathbf{h}_k\left(\mathbf{u}_{1:k};\boldsymbol{\theta}^{prior}\right)\in\mathbb{R}^{n_{\mathbf{y}}}$ is the output response at time step k of the FE model characterized by parameter values $\boldsymbol{\theta}^{prior}$, and $yn_{(i)}$ is the maximum absolute value of the FE output response (characterized by $\boldsymbol{\theta}^{prior}$) corresponding to the i^{th} measurement channel.

2.4.3 Variance-based Global Sensitivity Analysis

Variance-based methods for sensitivity analysis (also referred to as Sobol' method) are fundamentally rooted in the decomposition of the variance of the model output (for a given input) into contributions of the parameters and sets of parameters. Sobol' sensitivity analysis

determines the contribution of each input parameter and their interactions to the variance of the model output. For a model $z = f(\boldsymbol{\theta})$ with scalar output $z \in \mathbb{R}$ and vector input $\boldsymbol{\theta} = \left[\theta_1, \theta_2, ..., \theta_{n_{\boldsymbol{\theta}}}\right] \in \mathbb{R}^{n_{\boldsymbol{\theta}}}$, the variance of the model output $Var_{\boldsymbol{\theta}}[z]$ can be uniquely decomposed (Saltelli et al. 2007) as follows when the parameters θ_i's are mutually statistically independent:

$$Var_{\boldsymbol{\theta}}[z] = \sum_i V_i + \sum_i \sum_{j>i} V_{ij} + \sum_i \sum_{j>i} \sum_{k>j} V_{ijk} + \ldots + V_{123....n_{\boldsymbol{\theta}}} \tag{2.17}$$

where $V_i = Var_{\theta_i}\left[E_{\boldsymbol{\theta}_{-i}|\theta_i}[z \mid \theta_i]\right]$, $V_{ij} = Var_{\theta_i,\theta_j}\left[E_{\boldsymbol{\theta}_{-i,j}|\theta_i,\theta_j}\left[z \mid \theta_i, \theta_j\right]\right] - V_i - V_j$, and so forth. V_i is the variance of the model output explained by θ_i (the first-order effect of θ_i on the model output z). V_{ij} is the variance of the model output explained by the interaction between θ_i and θ_j (i.e., variance contribution of θ_i and θ_j to the model output not expressed in V_i and V_j), and so forth. $\boldsymbol{\theta}_{-i}$ denote all parameters of $\boldsymbol{\theta}$ except θ_i, $\boldsymbol{\theta}_{-i,j}$ denote all parameters of $\boldsymbol{\theta}$ except θ_i and θ_j, and so forth. $Var[.]$ is the variance operator and $E[.|.]$ is the conditional expectation (mean) operator.

Sobol' indices or variance-based sensitivity indices are defined as

$$S_i = \frac{V_i}{Var_{\boldsymbol{\theta}}[z]}, \quad S_{ij} = \frac{V_{ij}}{Var_{\boldsymbol{\theta}}[z]}, \quad ... \tag{2.18}$$

From Eq. (2.17) and Eq. (2.18), the sum of all Sobol' indices is unity

$$\sum_i S_i + \sum_i \sum_{j>i} S_{ij} + \sum_i \sum_{j>i} \sum_{k>j} S_{ijk} + \ldots + S_{123....n_{\boldsymbol{\theta}}} = 1 \tag{2.19}$$

The total number of Sobol' indices, $2^{n_{\boldsymbol{\theta}}}-1$, grows exponentially with the parameter space dimension $n_{\boldsymbol{\theta}}$. Owing to the computational cost and interpretation reasons, researchers usually look at first-order S_i and total-order S_{Ti} indices. The first-order index, S_i, captures the first-order effect of θ_i on the model output z. The total-order index, S_{Ti}, introduced by Saltelli (Saltelli et al. 2007), accounts for all contributions (of all orders) to the variance of the model output due to parameter θ_i, therefore

$$S_{Ti} = S_i + \sum_{j \neq i}^{n} S_{ij} + \ldots + S_{1\ldots i\ldots n} \tag{2.20}$$

From Eq. (2.18), the first-order index S_i is defined as

$$S_i = \frac{Var_{\theta_i}\left[E_{\boldsymbol{\theta}_{-i}|\theta_i}\left[z \mid \theta_i\right]\right]}{Var_{\boldsymbol{\theta}}\left[z\right]} \tag{2.21}$$

Consider the following form of the law of total variance:

$$E_{\theta_i}\left[Var_{\boldsymbol{\theta}_{-i}|\theta_i}\left[z \mid \theta_i\right]\right] + Var_{\theta_i}\left[E_{\boldsymbol{\theta}_{-i}|\theta_i}\left[z \mid \theta_i\right]\right] = Var_{\boldsymbol{\theta}}\left[z\right] \tag{2.22}$$

where $Var\left[.|.\right]$ is the conditional variance operator and $E\left[.\right]$ is the expectation (mean) operator. Note that $E_{\theta_i}\left[Var_{\boldsymbol{\theta}_{-i}|\theta_i}\left[z \mid \theta_i\right]\right]$ is the expected variance of z when only θ_i is fixed. Thus, in Eq. (2.22), $Var_{\theta_i}\left[E_{\boldsymbol{\theta}_{-i}|\theta_i}\left[z \mid \theta_i\right]\right]$ can be interpreted as the expected variance reduction of z when only θ_i is fixed. Now, from Eq. (2.21), the first-order index S_i can be interpreted as the fractional variance reduction of z (on average) when only θ_i is fixed. Thus, the first-order Sobol' indices ($S_i's$) provide guidance for parameter prioritization or experiment prioritization, i.e., first-order indices help identify parameters which, once accurately estimated (by performing

experiments) and fixed (set) at their "true" values, reduce the variance of the model output the most.

Using the following form of the law of total variance:

$$E_{\boldsymbol{\theta}_{-i}}\left[Var_{\theta_i|\boldsymbol{\theta}_{-i}}\left[z\,|\,\boldsymbol{\theta}_{-i}\right]\right]+Var_{\boldsymbol{\theta}_{-i}}\left[E_{\theta_i|\boldsymbol{\theta}_{-i}}\left[z\,|\,\boldsymbol{\theta}_{-i}\right]\right]=Var_{\boldsymbol{\theta}}\left[z\right], \tag{2.23}$$

the total-order index S_{Ti} defined in Eq. (2.20) can be expressed (Saltelli et al. 2007) as

$$S_{Ti}=\frac{E_{\boldsymbol{\theta}_{-i}}\left[Var_{\theta_i|\boldsymbol{\theta}_{-i}}\left[z\,|\,\boldsymbol{\theta}_{-i}\right]\right]}{Var_{\boldsymbol{\theta}}\left[z\right]} \tag{2.24}$$

Note that $E_{\boldsymbol{\theta}_{-i}}\left[Var_{\theta_i|\boldsymbol{\theta}_{-i}}\left[z\,|\,\boldsymbol{\theta}_{-i}\right]\right]$ is the expected variance of z when only $\boldsymbol{\theta}_{-i}$ is fixed (or when only θ_i is released). Therefore, the total-order index S_{Ti} can be interpreted as the fractional variance contribution to z (on average) when only θ_i is released. Thus, the total-order indices (S_{Ti}'s) provide guidance for parameter fixing, i.e., total-order indices help identify parameters that can be fixed anywhere in their range of uncertainty without appreciably affecting the variance of the model output. In this regard, prior to model updating, the total-order Sobol' indices can be used to rank the parameters in order of their sensitivity to model output as the low ranked parameters can then be eliminated from the parameter estimation stage by fixing them anywhere in their range of uncertainty (it is recommended to fix them at their nominal values).

To determine the number of parameters to be included in the estimation phase, sets of parameters can be analyzed (grouped variables – sensitivity analysis). The advantage of variance-based sensitivity analysis methods is that they allow for a concise treatment of sets of parameters. If the parameter vector is split into two groups as $\boldsymbol{\theta}=\left[\boldsymbol{\theta}_{G1}^T,\boldsymbol{\theta}_{G2}^T\right]^T\in\mathbb{R}^{n_{\boldsymbol{\theta}}}$, the uncertainty of the model output z is shared by $\boldsymbol{\theta}_{G1}$,$\boldsymbol{\theta}_{G2}$ and their interactions, therefore

$$S_{G1} + S_{G2} + S_{G1G2} = 1 \tag{2.25}$$

where S_{G1} includes all the first-order terms related to $\boldsymbol{\theta}_{G1}$ and all higher-order terms including only elements of vector $\boldsymbol{\theta}_{G1}$. Likewise, S_{G2} includes all the first-order terms related to $\boldsymbol{\theta}_{G2}$ and all higher-order terms including only elements of vector $\boldsymbol{\theta}_{G2}$. Finally, S_{G1G2} includes all cross-terms not involved in S_{G1} and S_{G2} (Saltelli et al. 2007). Let S_{TG1} and S_{TG2} be the total-order Sobol' indices of $\boldsymbol{\theta}_{G1}$ and $\boldsymbol{\theta}_{G2}$, respectively. Therefore,

$$\begin{aligned} S_{TG1} &= S_{G1} + S_{G1G2} \\ S_{TG2} &= S_{G2} + S_{G1G2} \end{aligned} \tag{2.26}$$

Using Eq. (2.26), Eq. (2.25) can be written as

$$S_{G1} + S_{TG2} = 1 \tag{2.27}$$

The total-order effect of $\boldsymbol{\theta}_{G2}$ on the model output z being close to zero (i.e., $S_{TG2} \approx 0$ or $S_{G1} \approx 1$) implies that all parameters in vector $\boldsymbol{\theta}_{G2}$ can be fixed anywhere in their range of uncertainty without appreciably affecting the variance of the model output. From the parameter estimation viewpoint, the goal is to find the largest number of parameters in parameter vector $\boldsymbol{\theta} = \left[\theta_1, \theta_2, ..., \theta_{n_{\boldsymbol{\theta}}} \right] \in \mathbb{R}^{n_{\boldsymbol{\theta}}}$ to be included in $\boldsymbol{\theta}_{G2}$ such that $S_{TG2} \approx 0$. The parameters $\theta_1, \theta_2, ..., \theta_{n_{\boldsymbol{\theta}}}$ can be ranked according to their individual total-order indices (i.e., S_{Ti}'s), with the bottom ranked parameter having the lowest value of S_{Ti}. Therefore, the problem boils down to finding the largest number of bottom ranked parameters (ranked according to S_{Ti}'s) to be included in $\boldsymbol{\theta}_{G2}$ such that $S_{TG2} < \textit{Threshold}$, where the value of *Threshold* depends on the analyst. This is an optimization problem and the best approach to solve this problem is beyond the scope of this paper. A naive approach is employed in this paper and is presented in Table 2.4.

Note that the parameters that are not in $\boldsymbol{\theta}_{G2}$ will be in $\boldsymbol{\theta}_{G1}$ as $\boldsymbol{\theta} = \left[\boldsymbol{\theta}_{G1}^T, \boldsymbol{\theta}_{G2}^T\right]^T \in \mathbb{R}^{n_{\boldsymbol{\theta}}}$ and every parameter added to $\boldsymbol{\theta}_{G2}$ (or removed from $\boldsymbol{\theta}_{G1}$) increases the value of S_{TG2}.

Table 2.4: Algorithm for determining influent parameters using GSA of individual and groups of parameters for parameter estimation

Model $z = f(\boldsymbol{\theta})$ with scalar output $z \in \mathbb{R}$ and input vector $\boldsymbol{\theta} = \left[\theta_1, \theta_2, ..., \theta_{n_{\boldsymbol{\theta}}}\right] \in \mathbb{R}^{n_{\boldsymbol{\theta}}}$
Compute total-order Sobol' indices ($S_{T1}, S_{T2}, ..., S_{Tn_{\boldsymbol{\theta}}}$) of all parameters $\theta_1, \theta_2, ..., \theta_{n_{\boldsymbol{\theta}}}$ Rank the parameters using S_{Ti}'s : $\left\{\theta_{r1}, \theta_{r2}, ..., \theta_{rn_{\boldsymbol{\theta}}}\right\}$ where parameter θ_{r1} has the largest S_{Ti}. **Initialize**: $\boldsymbol{\theta}_{G2} = \left[\theta_{rn_{\boldsymbol{\theta}}}\right] \in \mathbb{R}^1$ (lowest ranked parameter), $\boldsymbol{\theta}_{G1} = \left[\theta_{r1}, \theta_{r2}, ..., \theta_{r\left(n_{\boldsymbol{\theta}}-1\right)}\right] \in \mathbb{R}^{n_{\boldsymbol{\theta}}-1}$, $S_{TG2} = \min\left(S_{T1}, S_{T2}, ..., S_{Tn_{\boldsymbol{\theta}}}\right)$, set *Threshold* **while** $S_{TG2} < Threshold$ Remove the last element of $\boldsymbol{\theta}_{G1}$ (as it has the lowest S_{Ti} in $\boldsymbol{\theta}_{G1}$) and add it to $\boldsymbol{\theta}_{G2}$ Compute S_{TG2}, i.e., total-order index of $\boldsymbol{\theta}_{G2}$ **end** Remove last parameter added to $\boldsymbol{\theta}_{G2}$ and bring it back to $\boldsymbol{\theta}_{G1}$
$\boldsymbol{\theta}_{G1}$ contains influent parameters and the parameters in $\boldsymbol{\theta}_{G2}$ can be fixed anywhere in their range of uncertainty during model updating as they do not affect the model output appreciably.

The first- and total-order indices (of individual parameters and parameter sets) in Table 2.4 are computed using the methodology described by Saltelli (Saltelli et al. 2010). This algorithm uses Saltelli's sampling scheme (Saltelli 2002), an extension of Sobol' quasi-random sequences (Sobol' 2001) in a way to reduce error rate in the sensitivity index calculations.

The algorithm in Table 2.4 seems extremely computationally expensive as each time a parameter is added to $\boldsymbol{\theta}_{G2}$ (or removed from $\boldsymbol{\theta}_{G1}$), S_{TG2} should be recomputed (see second step inside the while loop in Table 2.4). However, note that the major cost in computing Sobol'

indices is from model evaluations. The model evaluations performed to compute the total-order indices $S_{T1}, S_{T2}, ..., S_{Tn_\theta}$ of individual parameters $\theta_1, \theta_2, ..., \theta_{n_\theta}$ can be reused to compute the total-order indices of parameter sets (e.g., S_{TG2}) (Saltelli 2002; Saltelli et al. 2010; Sobol' 2001). Thus, no additional model evaluations are needed to compute total-order indices of parameter sets.

A dynamic system with multiple output measurement channels (such as the testbed structure in Section 2.5) results in sensitivity time histories (first-order or total-order Sobol' indices) corresponding to each output measurement channel. In this paper, the sensitivity time-histories are averaged over time and over measurement channels and then used for ranking parameters. Let $(S_{Ti})_{k,j}$ denote the total-order sensitivity index of parameter i corresponding to the response at time step k of the j^{th} measurement channel. Therefore, the total-order Sobol' index averaged over time and measurement channels for each individual parameter θ_i $(i = 1, ..., n_\theta)$ is defined as

$$S_{Tai} = \frac{1}{n_y} \sum_{j=1}^{n_y} \left(\frac{1}{N} \sum_{k=1}^{N} \left[(S_{Ti})_{k,j} \right] \right), \quad i = 1, 2, ..., n_\theta \tag{2.28}$$

where N is the total number of time steps, n_y is the number of measurement channels, and n_θ denotes the number of parameters (to be estimated) of the mathematical model.

2.5 Testbed Structure: Pine Flat Concrete Gravity Dam

Pine Flat concrete gravity dam (Figure 2.3a-b) located in the seismic region of Fresno, California is taken as the testbed structure. The 560m wide dam consists on thirty-six 15.2m

wide and one 12.2m wide monoliths (Figure 2.3c) (Rea et al. 1974). The height of the tallest monolith is 122m (Figure 2.3c).

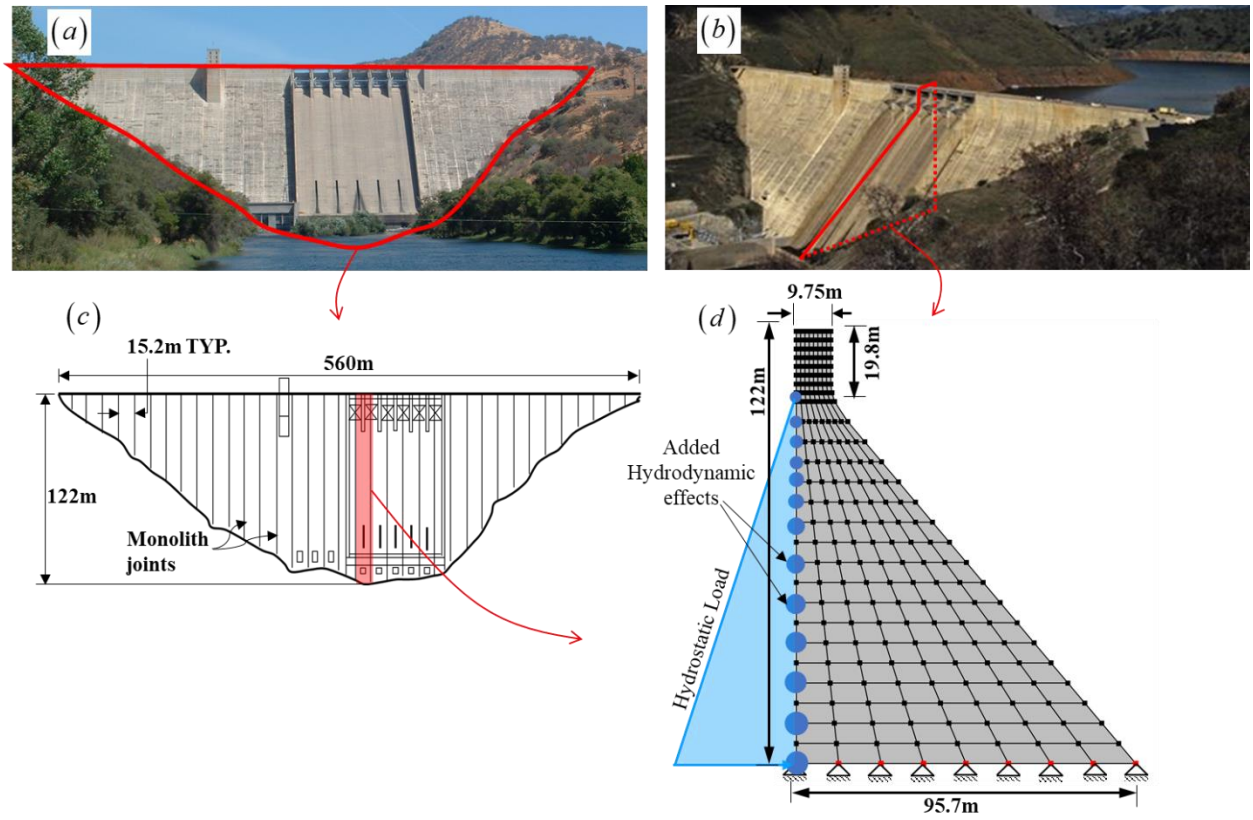

Figure 2.3: (a) Pine Flat concrete gravity Dam, (b) Downstream elevation, and (c) 2D nonlinear FE model

2.5.1 Nonlinear Finite Element (FE) Model

Mathematical modeling of concrete gravity dams is a subject of interest to many researchers. 2D or 3D linear elastic or nonlinear FE models can be used as mathematical models of dams. Each FE modeling approach has a certain range of applicability and represents reality to a certain degree (Brand et al. 2014). Even though 3D nonlinear FE models represent the best (most advanced) available method for modeling dams and simulating their response to various loading conditions, 2D nonlinear FE models achieve a good compromise between computational cost and applicability (Brand et al. 2014). A study conducted by Chopra and his co-workers on

mathematical models of concrete dams subjected to dynamics loads (e.g., earthquakes) states that "a 2D FE model including effects of water in the reservoir appears to be the most appropriate model available for predicting the response of concrete gravity dams to moderate or intense earthquake ground motion" (Rea et al. 1974). Therefore, in this study, a 2D nonlinear FE model of Pine Flat Dam is developed in the FE software framework *OpenSees* (McKenna et al. 2000), by modeling the tallest monolith as a plane section (Figure 2.3d). In the developed FE model, the dam is assumed to be supported on rigid foundation rock, i.e., the boundary conditions at the bottom of the dam are assumed fixed (Figure 2.3d). The hydrostatic load from the water in the reservoir is applied as a triangular load pattern and the additional hydrodynamic effects of water are included using Westergaard masses (Hall and Chopra 1980) added to the upstream face of the dam (Figure 2.3d).

The concrete material of the dam is assumed to be isotropic and homogeneous (i.e., represented by the same material model and the same set of material parameter values) over the entire cross-section of the dam. The FE model hierarchy (i.e., structure, element, and numerical integration point/material level) is shown in Figure 2.4a-c. Each FE is a bilinear quadrilateral element (Figure 2.4b) with material behavior at each integration point governed by the cap plasticity model, a classical 3D non-smooth multi-surface plasticity model (Figure 2.4c) (Hofstetter et al. 1993; Sandler et al. 1976; Simo et al. 1988). The cap plasticity model is a material constitutive model for plain concrete (a quasi-brittle material) addressing three major issues in modeling concrete: (i) the drastic difference in behavior under tension and compression; (ii) the hardening behavior under hydrostatic compression; and (iii) the nonlinear dilatancy behavior. Note that the cap plasticity model is a reasonable model for plain concrete; however, more advanced and accurate constitutive models for concrete have been proposed in the

literature. An advantage of using the cap plasticity model in this study is that the Direct Differentiation Method (DDM) is implemented in OpenSees for this model. The cap plasticity model is characterized by a set of eleven (11) time-invariant material parameters (i.e., material constants) (Simo et al. 1988). Two of these parameters, the shear modulus (G) and the bulk modulus (K), are the linear elastic parameters, while the other nine parameters $(T, X, R, \alpha, \lambda, D, W, \beta \text{ and } \phi)$ characterize the yield surfaces, flow rule and hardening law of the cap plasticity model. The three yield surfaces consist of: (1) an ideal plasticity failure envelope $f_1(\boldsymbol{\sigma}) = 0$ with parameters $\alpha, \lambda, \beta \text{ and } \phi$, (2) a strain hardening elliptical cap $f_2(\boldsymbol{\sigma}, \kappa) = 0$ (κ is the hardening parameter acting as a material history variable or internal state variable) defined by parameters X and R, and (3) an ideal plasticity tensile-cutoff surface $f_3(\boldsymbol{\sigma}) = 0$ defined by the tensile strength (T). Parameters D and W characterize the hardening law. Here, $\boldsymbol{\sigma}$ represents the stress tensor with $\mathbf{s}$ and $(I_1/3)\mathbf{I}$ denoting its deviatoric and volumetric components such that $\boldsymbol{\sigma} = \boldsymbol{s} + (I_1/3)\mathbf{I}$ (I_1 is the first invariant of the stress tensor, and $\mathbf{I}$ denotes the 4th order identity tensor). In this paper, the eleven time-invariant parameters of the cap plasticity material model define the unknown parameter vector $\boldsymbol{\theta}$ as

$$\boldsymbol{\theta} = \left[G, K, X, D, W, R, \lambda, \phi, \beta, \alpha, T\right]^T \in \mathbb{R}^{11\times 1} \tag{2.29}$$

The developed FE model is not an advanced state-of-the-art mechanics-based 3D nonlinear FE model of a dam including dam-reservoir (fluid)-foundation interaction. It cannot capture all the potential failure modes of the dam. However, it has some major ingredients of a more sophisticated FE dam model as far as nonlinear FE model updating and identifiability assessment is concerned in the context of SHM/DP.

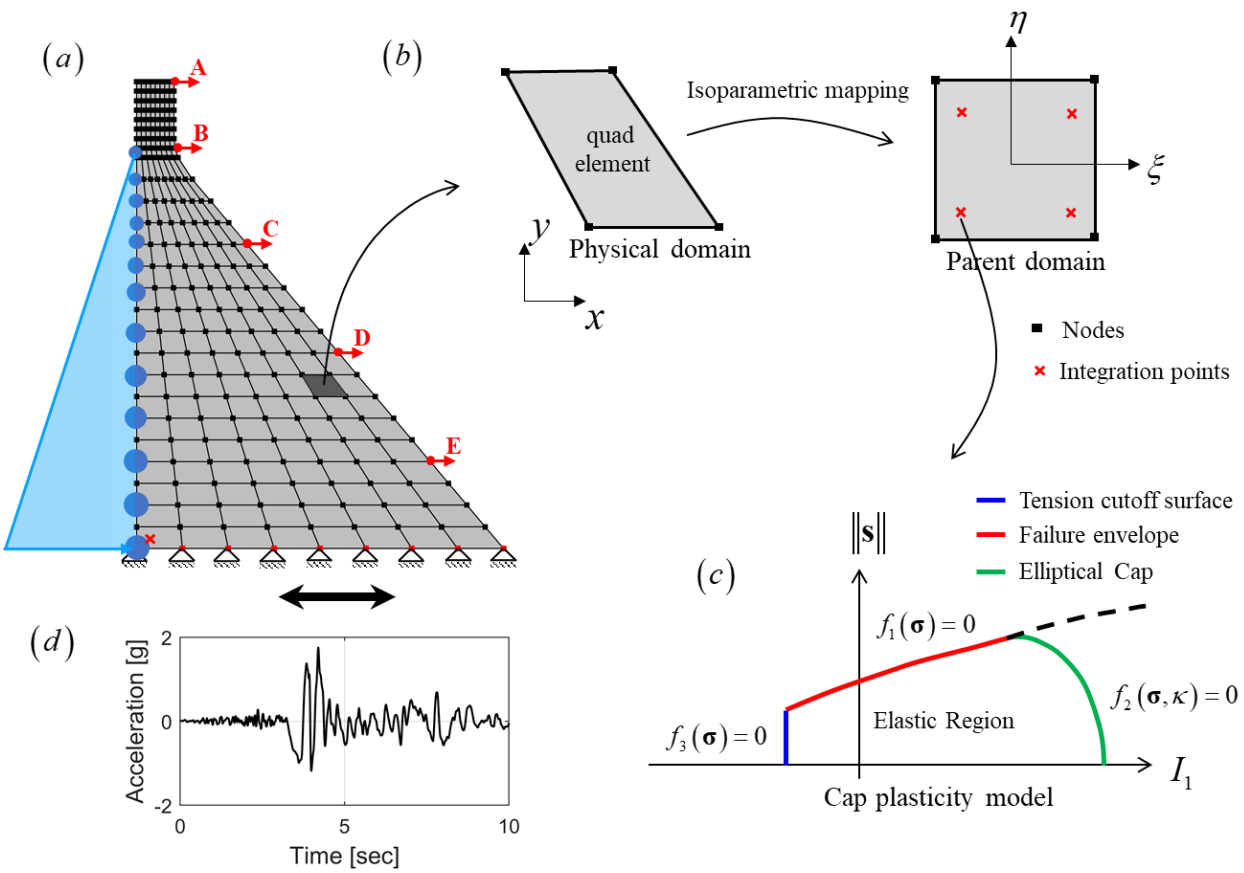

Figure 2.4: FE model hierarchy: (a) Structure level, (b) Element level, and (c) Material level; (d) Input ground motion

2.5.2 FE Model Updating of Testbed Structure

2.5.2.1 Sensors, Data Simulation, and Prior

The numerically simulated seismic response data with added Gaussian white noise (to simulate the measurement noise) is assumed to represent the data measured from a real-world dam and is used as measurement data $\mathcal{D}$ in this paper. In simulating such measurement data, sensors measuring absolute acceleration and relative displacement (with respect to the base of the dam) response time histories are assumed to be installed at locations A through E on the downstream face of the dam as shown in Figure 2.4a. For measurement data generation (simulation), the 2D FE model of the dam (Figure 2.3d) is characterized by a realistic set of

material parameter values (Simo et al. 1988) which were obtained by calibrating the cap plasticity model to the Colorado concrete test data (uniaxial compressive strength of 27.6 MPa) at the material level. This set of "true" material parameter values are referred to herein as $\boldsymbol{\theta}^{true}$ and are reported in Eq. (2.30).

$$\underset{11\times 1}{\boldsymbol{\theta}^{true}} = \begin{bmatrix} 11721.1\ \text{MPa},\ 14479\ \text{MPa},\ 4.6\times 10^{-4}\ \text{MPa}^{-1},\ 0.42, 110.32\ \text{MPa},\ 4.43, \\ 8\ \text{MPa},\ 0.064\ \text{MPa}^{-1},\ 0.11,\ 26.61\,\text{MPa},\ -2.07\ \text{MPa} \end{bmatrix}^T \quad (2.30)$$

No additional damping (beyond the material hysteretic damping) is considered in this case study. The developed FE model $\mathbf{h}$ characterized by $\boldsymbol{\theta}^{true}$ is subjected to seismic input time history, the first 10 sec of the 360^0 horizontal component of the 1994 Northridge earthquake (M6.7) recorded at Sylmar Hospital station. The absolute acceleration and relative displacement response time histories at locations A through E are obtained from the dynamic seismic response analysis performed in *OpenSees*. This analysis takes 10 sec to run on an Intel Xeon W-2155 @ 3.30 GHz CPU with 10 cores / 20 threads and 128 GB RAM workstation. The computed output response data $\mathbf{y}^{true}$ (referred to as true output response measurement) are then polluted with additive Gaussian white noise of root mean square (RMS) 1.0%g and 1.9mm for the acceleration and displacement responses, respectively, to simulate the output measurement noise. This polluted output response is used as the output measurement data $\mathbf{y}_{1:N}$, thus $\mathbf{y}_k = \left[a_k^A, a_k^B, \ldots a_k^E, d_k^A, d_k^B, \ldots d_k^E \right]^T \in \mathbb{R}^{10}$ where a_k^i and d_k^i denote the polluted absolute acceleration and relative displacement response, respectively, at time step $k \in [1, 2, \ldots, N]$ at location $i \in [A, B, \ldots, E]$. The seismic input (ground motion record considered as true seismic input) is also polluted with 1.0%g RMS additive Gaussian white noise to simulate the input measurement noise. This polluted input is used as the input measurement data $\mathbf{u}_{1:N}$. Note that the

input measurement noise is filtered (together with the true seismic input) through the dam nonlinear FE model and therefore appears as transformed (filtered) input noise in the system output. Therefore, the total noise associated with each output measurement channel comprises the transformed input measurement noise and added output measurement noise.

The response of the developed FE model $\mathbf{h}$ characterized by the parameter vector $\boldsymbol{\theta}$ and subjected to the measurement input $\mathbf{u}_{1:k}$ is given by $\mathbf{y}_k^{FE} = \left[a_k^{A,FE}, a_k^{B,FE}, \ldots a_k^{E,FE}, d_k^{A,FE}, d_k^{B,FE}, \ldots d_k^{E,FE} \right]^T \in \mathbb{R}^{10}$ where $a_k^{i,FE}$ and $d_k^{i,FE}$ are the absolute acceleration and relative displacement responses, respectively, of the FE model at time step $k \in [1, 2, \ldots, N]$ and at location $i \in [A, B, \ldots, E]$.

In this paper, the prior PDF $p(\boldsymbol{\theta})$ is assumed Gaussian $\mathcal{N}\left(\boldsymbol{\theta}^{prior}, \boldsymbol{\Sigma}^{prior}\right)$ with

$$\begin{aligned} \underset{11\times 1}{\boldsymbol{\theta}^{prior}} &= [1.40, 0.55, 0.85, 1.20, 0.80, 0.80, 1.15, 1.05, 0.95, 0.80, 0.60\ ]^T \odot \boldsymbol{\theta}^{true} \\ \underset{11\times 11}{\boldsymbol{\Sigma}^{prior}} &= \left[diag\left([0.30,\ 0.30,\ 0.20,\ 0.20,\ 0.20,\ 0.20,\ 0.20,\ 0.20,\ 0.20,\ 0.20,\ 0.20]^T \odot \left(\boldsymbol{\theta}^{prior}\right) \right) \right]^2 \end{aligned} \tag{2.31}$$

where $\odot$ represents the element-wise vector multiplication operator, $\boldsymbol{\theta}^{prior}$ is the prior mean vector. Prior covariance matrix $\boldsymbol{\Sigma}^{prior}$ is a diagonal matrix with coefficient of variation of 0.30 for the linear elastic parameters (G and K) and 0.20 for the other parameters ($X, D, W, R, \lambda, \phi, \beta, \alpha,$ and T).

For the initial condition/state of the testbed structure, both in both data simulation and model updating, the dam is assumed to be perfectly healthy (linear elastic with no damage).

2.5.2.2 FE Model Updating using Unscented Kalman Filtering

FE model updating of the testbed structure is performed using the UKF algorithm provided in Table 2.1 together with simulated input-output measurement data. With the prior PDF $p(\boldsymbol{\theta})$ defined in Eq. (2.31), the initialization step in Table 2.1 is $\hat{\boldsymbol{\theta}}_{0|0} = \boldsymbol{\theta}^{prior}$ and $\hat{\mathbf{P}}^{\boldsymbol{\theta}\boldsymbol{\theta}}_{0|0} = \boldsymbol{\Sigma}^{prior}$. The process noise covariance matrix $\mathbf{Q}$ is taken as $\mathbf{Q} = diag\left(10^{-3} \times \hat{\boldsymbol{\theta}}_{0|0}\right)$. $\mathbf{Q}$ governs the convergence and tracking performance of the UKF; the choice of $\mathbf{Q}$ used in this study is based on the existing literature and experience of the authors in solving this type of problems. A standard deviation of 1.3%g and 0.25mm for the acceleration and displacement output measurement channels, respectively, is used to construct measurement noise covariance matrix $\mathbf{R}$. For data recorded in the real world, the variance (or standard deviation) of the measurement noise corresponding to each measurement channel should be first estimated based on the noise sources, experience, and engineering judgment and then used to construct $\mathbf{R}$.

Figure 2.6 shows the time histories of the posterior mean estimates ($\hat{\boldsymbol{\theta}}_{k|k}$, $k = 1, 2, ..., N$), normalized with respect to their corresponding true values ($\boldsymbol{\theta}^{true}$),of all eleven time-invariant parameters $\boldsymbol{\theta}$ of the testbed structure obtained using the UKF. Note that the length of these time histories is 10 sec corresponding to the length of the input ground motion (Figure 2.4d). The blue solid line in each plot represents the time history of the normalized mean parameter estimate ($\hat{\boldsymbol{\theta}}_{k|k}$, $k = 1, 2, ..., N$), the grey shaded area represents the parameter estimation uncertainty shown in terms of mean ± two standard deviations (with standard deviation obtained from $\hat{\mathbf{P}}^{\boldsymbol{\theta}\boldsymbol{\theta}}_{k|k}$, $k = 1, 2, ..., N$), and the red dashed line represents the normalized true parameter value. From the dynamic response history analysis performed during data simulation (Section 2.5.2.1), it is observed that the dam is in its linear elastic regime at the beginning of the earthquake

excitation $[0-1\,\text{sec}]$. Thus, the output measurement data only contains information about the concrete material parameters governing the linear elastic response of the system. And since the correlation between all parameters is assumed to be zero in the prior (Eq. (2.31)), only the linear elastic material parameters (G and K) start getting updated in the $[0-1\,\text{sec}]$ time window (Figure 2.6). After 1 sec, the structure is still predominantly in its linear elastic regime along with some tensile cracking at the heel of the dam until 3.5 sec. Hence, the tensile strength of concrete (parameter T) starts to update at around 1 sec. At 3.5 sec, the large pulse in the input ground motion (Figure 2.4d) drives the dam into its nonlinear regime (Figure 2.5 shows the stress-path at the heel and neck of the dam displaying the level of nonlinearity). Thus, other parameters governing the nonlinear material response of the dam are being updated. The mean estimates of the linear elastic parameters G and K and the nonlinear parameter T converge to their corresponding true values and their estimation uncertainty decrease asymptotically as information about these parameters is assimilated step by step from the measurement data. The estimates of parameters $X, D, W, R, \lambda, \beta,$ and α do not converge to their corresponding true values. The estimate of parameter ϕ is unchanged (from its prior estimate) most likely because it is not identifiable (the data may not contain any information about this parameter). Ideally, parameters such as ϕ should be detected and removed from the estimation process; more on this in Section 2.5.3.

The response predicted by the FE model (characterized by the mean estimates of the parameters $\boldsymbol{\theta}$) is compared with the true output response using the relative root mean square (RRMS) error as the metric for comparison. For the first measurement channel $\mathbf{a}^A$, we have

$a_k^{A,FE}, k=1,2,...,N$ for the FE predicted response and $a_k^{A,true}, k=1,2,...,N$ for the true response.. The RRMS error for this measurement channel is given by

$$\text{RRMS error} = \frac{\sqrt{\left[\frac{1}{N}\sum_{k=1}^{N}\left(a_k^{A,true} - a_k^{A,FE}\right)^2\right]}}{\sqrt{\left[\frac{1}{N}\sum_{k=1}^{N}\left(a_k^{A,true}\right)^2\right]}} \times 100(\%) \tag{2.32}$$

The evolution of the RRMS error of each measurement channel $\left(\mathbf{a}^A, \mathbf{a}^B, ..., \mathbf{a}^E, \mathbf{d}^A, \mathbf{d}^B, ..., \mathbf{d}^E\right)$ during the unscented Kalman filtering is depicted in Figure 2.7. The RRMS error at each time step k is computed between the response predicted by the FE model characterized by the updated mean parameter estimates at time step k (i.e., $\mathbf{h}\left(\mathbf{u}_{1:N}; \hat{\boldsymbol{\theta}}_{k|k}\right)$) and the true output measurement response $\mathbf{y}^{true}$. As expected, the error between the FE predicted response and the true response is very high (RRMS error > 100%) before filtering (at 0 sec). During filtering, the RRMS error progressively decreases and the rate of decrease depends on the amount of information about parameters $\boldsymbol{\theta}$ assimilated from the measurement data. Intuitively, the UKF adjusts the parameter estimates during filtering to decrease the error between the FE predicted response and the output measurement response. Note that although estimates of some parameters did not converge to their corresponding true values, the error between the FE predicted and true responses is very small for all measurement channels at the end of filtering (RRMS errors lower than 5% and 3% for acceleration and displacement sensors, respectively). In other words, the filter finds a different set of parameter values (non-true) yielding a very good match between FE predicted and measured output. This issue is resolved by including only identifiable parameters in the estimation process (Section 2.5.4). The runtime of this FE model updating using unscented Kalman filtering for eleven parameters is 6.4 hours on an Intel Xeon

W-2155 @ 3.30 GHz CPU with 10 cores / 20 threads and 128 GB RAM workstation. Parallel computing was exploited to propagate the SPs though the measurement equation.

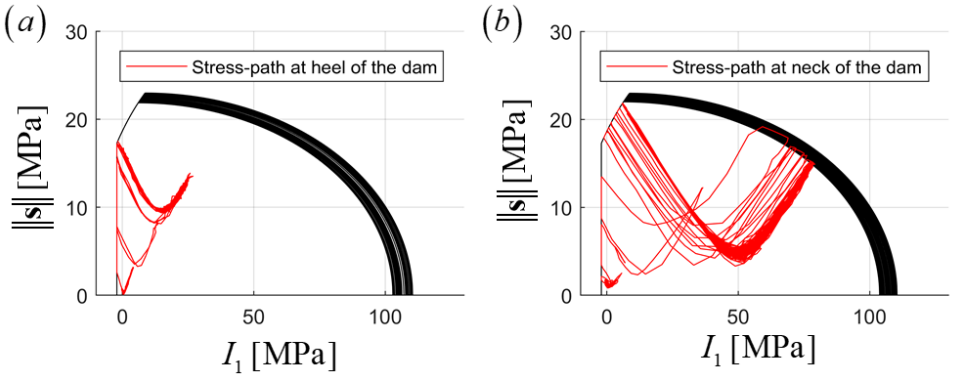

Figure 2.5: Stress-path in the $I_1 - \|\mathbf{s}\|$ space at (a) heel of the dam, and (b) neck of the dam

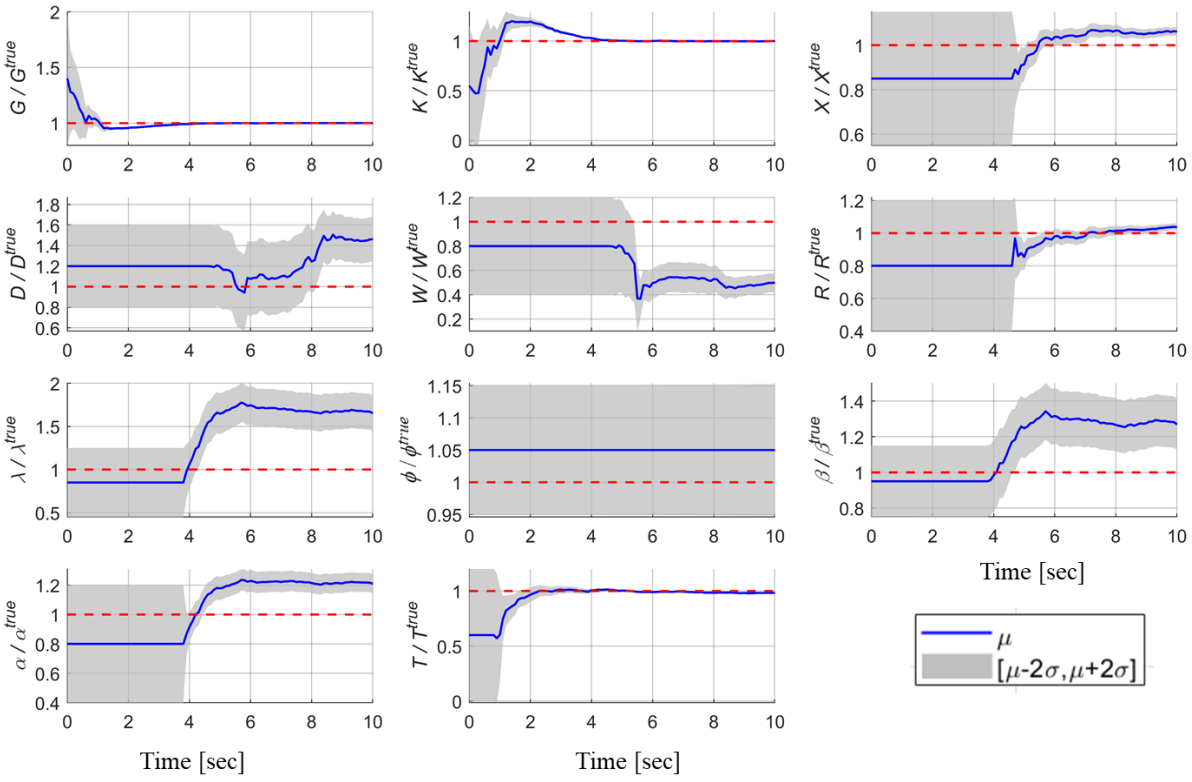

Figure 2.6: Time histories of the posterior mean estimates, normalized with respect to their corresponding true values, of all eleven time-invariant parameters $\boldsymbol{\theta}$ obtained using the UKF.

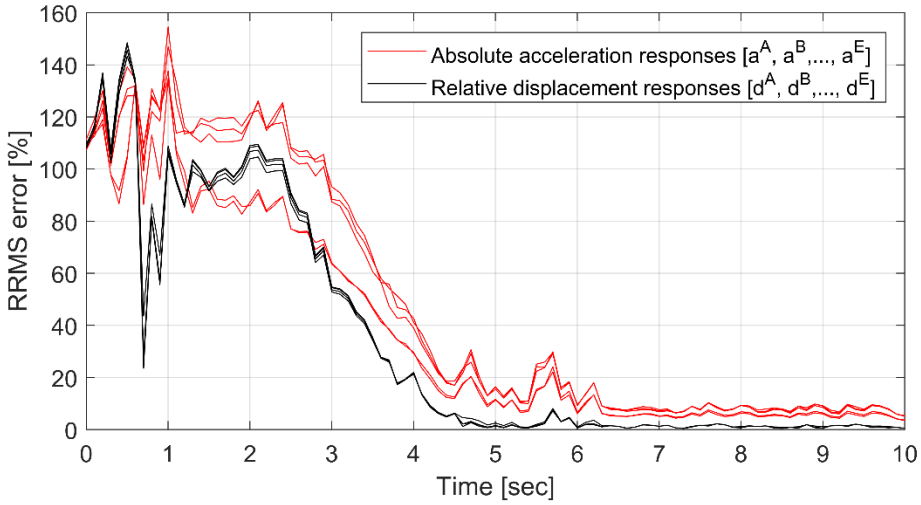

Figure 2.7: Evolution of RRMS error for all measurement channels during unscented Kalman filtering

2.5.2.3 FE Model Updating using Transitional Markov chain Monte Carlo

FE model updating of the testbed structure is performed using the TMCMC algorithm defined in Table 2.2 together with simulated input-output measurement data. For the algorithm initialization, the prior PDF $p(\boldsymbol{\theta})$ is given in Eq. (2.31). At every TMCMC stage, $N_p = 1500$ particles are used to approximate the intermediate joint PDF. The number of MCMC steps in the perturbation stage of each TMCMC stage (Figure 2.1) is set to 15 (i.e., $N_{MCMC} = 15$).

The "pairs plot" (scatter plots of the pairs of parameters) of all eleven time-invariant material parameters of the testbed structure obtained using the posterior samples (normalized with respect to $\boldsymbol{\theta}^{true}$) generated by TMCMC is shown in Figure 2.8. In this Figure, G' denotes G/G^{true}, K' denotes K/K^{true} and so on. The plots along the diagonal show the histograms and kernel density estimates of the marginal posterior PDFs of the eleven parameters. The coefficient of variation (δ) conveys the sharpness of the marginal posterior PDF, an indicator of the remaining estimation uncertainty after model updating. The marginal posterior PDFs of the linear elastic material parameters (G and K) are extremely sharp (as indicated by very small

values of δ on the order of 10^{-4}). The plots above the diagonal show the posterior samples (normalized with respect to $\boldsymbol{\theta}^{true}$) in the space of each pair of parameters (each sample point is surrounded by a white circle) and the plots below the diagonal depict the contour plots of the corresponding bi-variate kernel density estimates where r denotes the Pearson correlation coefficient. Highly correlated parameters can compensate each other to explain the measurement data equally well (see Section 2.5.2.4 for more details). The prior and posterior coefficients of variation (δ) of the parameters are compared in Table 2.5. The reduction in δ (from prior to posterior) of each parameter can be directly attributed to its identifiability. The linear elastic parameters G and K experience the largest reduction in δ, while the δ of parameters D and W barely decreases. The small increase in δ for parameter ϕ can be due to numerical approximation errors.

The runtime of this FE model updating using TMCMC for eleven parameters is 93.7 hours on an Intel Xeon W-2155 @ 3.30 GHz CPU with 10 cores / 20 threads and 128 GB RAM workstation. Parallel computing was exploited in the weighting and perturbation steps of each TMCMC stage.

Table 2.5: Comparison of prior and posterior (obtained using TMCMC) coefficients of variation for all parameters

Parameter	G	K	X	D	W	R
Prior δ	3.0×10^{-1}	3.0×10^{-1}	2.0×10^{-1}	2.0×10^{-1}	2.0×10^{-1}	2.0×10^{-1}
Posterior δ	7.3×10^{-5}	2.1×10^{-4}	4.8×10^{-3}	1.9×10^{-1}	1.8×10^{-1}	4.6×10^{-3}
Parameter	λ	ϕ	β	α	T	
Prior δ	2.0×10^{-1}	2.0×10^{-1}	2.0×10^{-1}	2.0×10^{-1}	2.0×10^{-1}	
Posterior δ	1.3×10^{-1}	2.2×10^{-1}	7.3×10^{-2}	3.3×10^{-2}	3.9×10^{-2}	

Figure 2.8: Pairs plot of eleven parameters of testbed structure obtained using posterior samples generated by TMCMC.

2.5.2.4 Consistency between UKF and TMCMC Parameter Estimation Results

In this section, the parameter estimation results obtained using the UKF, an approximate Bayesian inference technique that operates using point estimates, are compared with the results obtained by the TMCMC, a "full distribution" Bayesian method. Note that high correlation ($r > 0.80$ or $r < -0.80$) is observed for the parameter pairs $(G,K), (D,W), (X,R), (\lambda,\phi), (\lambda,\beta), (\lambda,\alpha), (\phi,\alpha),$ and (β,α) using TMCMC (Figure 2.8). Highly correlated parameters compensate each other to explain the measurement data equally well. For example, as the estimates of parameters D and W are extremely highly correlated ($r = 0.97$), there exist many pairs of (D,W) values that explain the measurement data equally well. To illustrate this, the unscented Kalman filtering is performed for seven cases, in each case

fixing parameter W to a non-true value ($W/W^{true} = [0.8, 0.9, 1.0, 1.1, 1.2, 1.3, 1.4]$) and estimating parameter D only. For this exercise, the remaining nine parameters ($G, K, X, R, \lambda, \phi, \beta, \alpha,$ and T) are not updated and fixed to their corresponding true values. The mean estimate of D, normalized with D^{true}, from the last UKF update step for each case ($W' \equiv W/W^{true} = [0.8, 0.9, 1.0, 1.1, 1.2, 1.3, 1.4]$) is shown in Figure 2.9. The UKF mean parameter estimates are overlaid on the contour plot of the kernel density estimate of D and W constructed using the TMCMC posterior samples of parameters D and W. Thus, Bayesian inference when performed using methods that focus on point estimates (e.g., Kalman filter and its variants) can end up finding non-true sets of parameter estimates which explain the measurement response equally well. This motivates the need to look at identifiability of the unknown parameters of the model given the model and measurement data before solving the model updating problem.

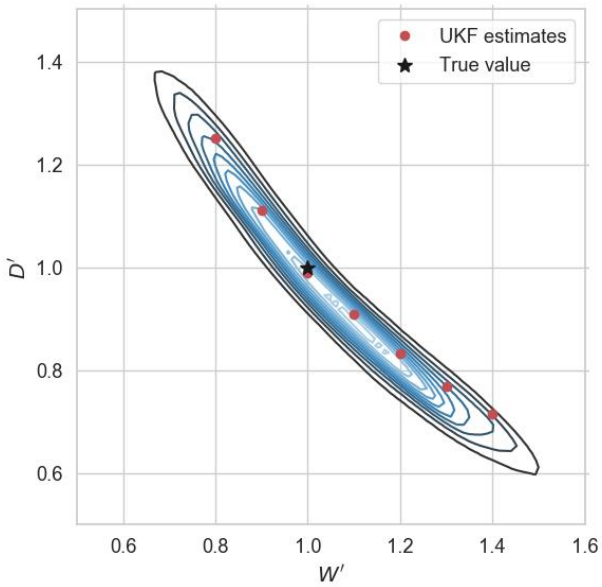

Figure 2.9: Consistency between UKF estimates and TMCMC posterior for parameters D and W

2.5.3 Identifiability and Sensitivity Analysis of Testbed Structure

2.5.3.1 Local Practical Identifiability Analysis using Fisher Information Matrix

Local practical identifiability analysis of the testbed structure is performed using the algorithm presented in Table 2.3. The local sensitivity analysis of the testbed structure is performed using the direct differentiation method within the sensitivity analysis framework in *OpenSees*. Since, in a real world application, the true values of parameters $\boldsymbol{\theta}$ are unknown, the LSA is performed here at $\boldsymbol{\theta}^{prior}$ (i.e., the evaluation point $\boldsymbol{\theta}^{*}$ in Table 2.3 is $\boldsymbol{\theta}^{prior}$). The time histories of the FE response sensitivities with respect to all eleven time-invariant material parameters $(G, K, X, D, W, R, \lambda, \theta, \beta, \alpha, T)$ for all ten measurement channels $\left(\mathbf{a}^{A}, \mathbf{a}^{B}, ..., \mathbf{a}^{E}, \mathbf{d}^{A}, \mathbf{d}^{B}, ..., \mathbf{d}^{E}\right)$ are used to construct the normalized sensitivity matrix $\chi'\left(\boldsymbol{\theta}^{prior}\right)$ using Eq. (2.16). For illustration purposes, the normalized sensitivity time histories of a measurement channel, the acceleration at the top of the dam ($\mathbf{a}^{A}$), with respect to all parameters $\boldsymbol{\theta}$ are displayed in Figure 2.10. The FE acceleration response at the top of the dam is highly sensitive to the linear elastic parameters (G and K) and considerably less sensitive to the material constitutive parameters that govern the nonlinear behavior of the dam.

The FIM evaluated at $\boldsymbol{\theta}^{prior}$ (i.e., $\mathbf{I}\left(\boldsymbol{\theta}^{prior}\right) = \boldsymbol{\chi}'\left(\boldsymbol{\theta}^{prior}\right)^{T} \mathbf{C}^{-1} \boldsymbol{\chi}'\left(\boldsymbol{\theta}^{prior}\right)$) is represented as a 3D bar plot in Figure 2.11a and its diagonal elements are shown as a bar plot in Figure 2.11b. A standard deviation of 1.3%g and 0.25mm for the acceleration and displacement measurement channels, respectively, is used to construct the measurement noise covariance matrix $\mathbf{R}$. The matrix $\mathbf{R}$ is then used to construct matrix $\mathbf{C}$, see Eq. (2.2), for evaluating $\mathbf{I}\left(\boldsymbol{\theta}^{prior}\right)$. From Figure 2.11a and Figure 2.11b (notice the logarithmic scale on the vertical axis), it is observed

that the measurement data contains much more information about the linear elastic parameters (G and K) than about the parameters that govern the nonlinear behavior of the dam. The blue lines in Figure 2.11c show the eigenvalues of $\mathbf{I}\left(\boldsymbol{\theta}^{prior}\right)$. The numerical rank of the FIM $\mathbf{I}\left(\boldsymbol{\theta}^{prior}\right)$ is 6 with a specified tolerance of 1.0 (see red line in Figure 2.11c). Note that the numerical rank of a positive semi-definite matrix is the number of eigenvalues that are larger than the tolerance.

The algorithm presented in Table 2.3 is now used to rank the parameters based on their local identifiability around $\boldsymbol{\theta}^{prior}$ and to determine the locally practically identifiable parameters. The ranking of the parameters $\boldsymbol{\theta}$ using this algorithm is reported in Table 2.6. Since the rank of the FIM is identified as 6 (with tolerance = 1.0), it can be concluded that the parameters $G, K, \alpha, X, T,$ and R are locally practically identifiable in the neighborhood of $\boldsymbol{\theta}^{prior}$.

In Table 2.6, parameter α is ranked better than parameter T. However, from the UKF results (Figure 2.6), it is observed that α converges to an incorrect value, while T converges to its true value. The convergence of α to an incorrect value can be attributed to its compensation with parameters β, ϕ and λ (see the pairwise correlations between these four parameters in Figure 2.8).

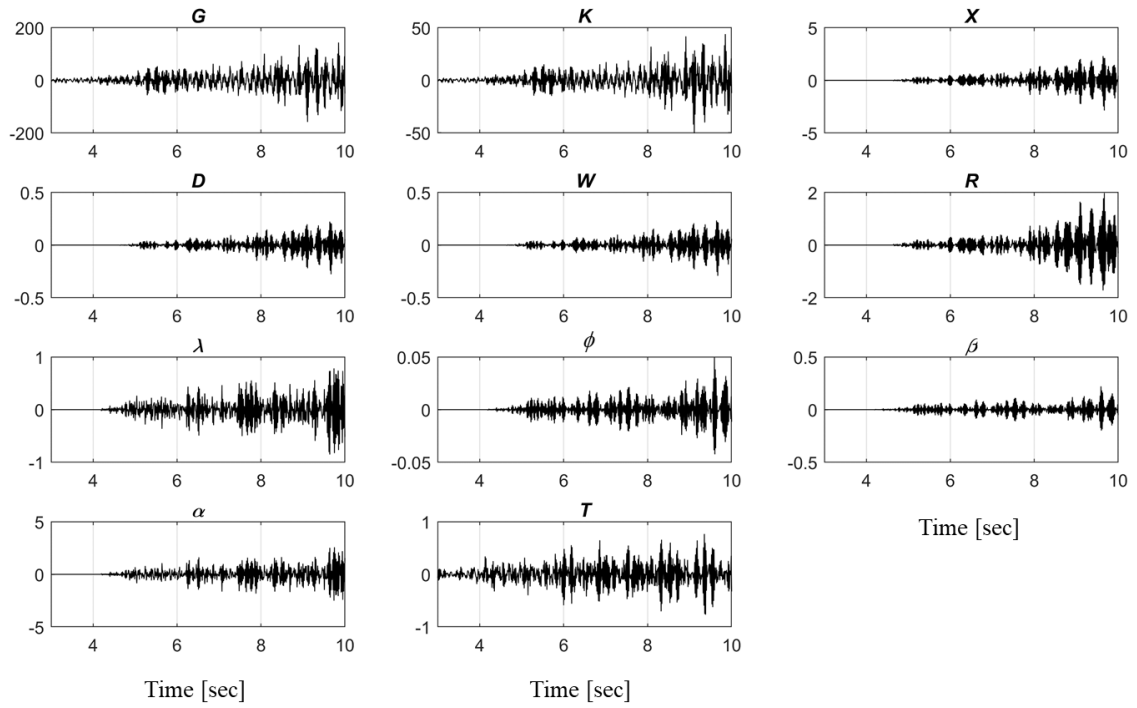

Figure 2.10: Normalized sensitivities of acceleration response at the top of the dam $\mathbf{a}^A$

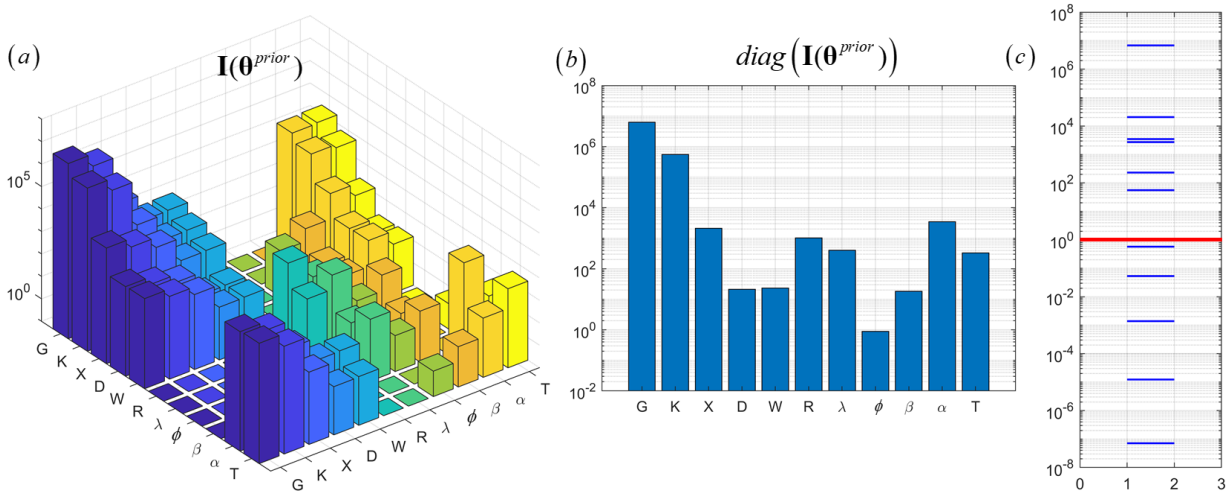

Figure 2.11: (a) Fisher information matrix of the testbed structure evaluated at $\boldsymbol{\theta}^{prior}$, (b) its diagonal elements, and (c) its eigenvalues

Table 2.6: Parameters of testbed structure ranked using algorithm in Table 2.3

Rank	1	2	3	4	5	6	7	8	9	10	11
Parameter	*G*	*K*	α	*X*	*T*	*R*	λ	*W*	β	ϕ	*D*

2.5.3.2 Variance-based Global Sensitivity Analysis (GSA)

Variance-based GSA of the testbed structure is performed according to the algorithm described in Section 2.4.3 and summarized in Table 2.4 to determine the influent parameters. To compute the sensitivity indices, the eleven unknown model parameters are assumed statistically independent. Computing variance-based global sensitivities for statistically dependent parameters is beyond the scope of this paper (refer to (Hu and Mahadevan 2019) for such analysis). To evaluate the first- and total-order Sobol' indices, the base sample size is set to 5000. As there are eleven parameters, the total number of FE model runs required is 65000 ($=5000\times(11+2)$). Refer to (Saltelli 2002; Saltelli et al. 2010) for more details about this computation. The runtime to compute the first- and total-order Sobol' indices for the eleven parameters is 18.05 hours on an Intel Xeon W-2155 @ 3.30 GHz CPU with 10 cores / 20 threads and 128 GB RAM workstation. Parallel computing was exploited for FE model evaluations.

For illustration purposes, Figure 2.12 shows the time histories of the total-order sensitivity indices of a measurement channel, the acceleration at the top of the dam $\mathbf{a}^A$, with respect to all parameters. The blue line in each plot represents the total-order sensitivity index time history, while the grey region denotes its 95% confidence interval. Figure 2.13 shows the bar plot of the averaged (according to Eq. (2.28)) total-order Sobol' indices of all parameters. The ranking of the parameters based on these averaged sensitivity indices is reported in Table 2.7.

Now the ranked parameters are separated into two groups (influent parameters $\boldsymbol{\theta}_{G1}$ and non-influent parameters $\boldsymbol{\theta}_{G2}$) using the algorithm in Table 2.4 with $Threshold = 0.1$. The top ranked six parameters $\boldsymbol{\theta}_{G1} = \left[G, K, \alpha, X, R, T\right]^T$ are identified as influent parameters and the

remaining five parameters $\boldsymbol{\theta}_{G2} = [\lambda, D, W, \phi, \beta]^T$ as non-influent. The first- and total-order Sobol' indices time histories averaged over the measurement channels of the influent and non-influent parameter groups, $\boldsymbol{\theta}_{G1}$ and $\boldsymbol{\theta}_{G2}$, respectively, are plotted in Figure 2.14a. It is observed that the total-order sensitivity index of group $\boldsymbol{\theta}_{G1}$ is close to 1.0 throughout the duration of the input ground motion (0-10 sec), thus confirming that parameters $\boldsymbol{\theta}_{G1} = [G, K, \alpha, X, R, T]^T$ are influent parameters. The total-order index of group $\boldsymbol{\theta}_{G2}$ is negligible (close to 0) except at around 4 sec. At around 4 sec, the first- and total-order index of group $\boldsymbol{\theta}_{G2}$ is negligible and non-negligible, respectively. This implies that the parameters of group $\boldsymbol{\theta}_{G1}$ are interacting with the parameters of group $\boldsymbol{\theta}_{G2}$ at around 4 sec. This phenomenon is also observed in the first-order sensitivity time history of parameter group $\boldsymbol{\theta}_{G1}$ (observe the dip at around 4 sec). Note that the input ground motion has a large pulse at from 3.5 – 4.5 sec (Figure 2.4d). The averaged (using Eq. (2.28)) first- and total-order sensitivity indices of the influent and non-influent parameter groups, $\boldsymbol{\theta}_{G1}$ and $\boldsymbol{\theta}_{G2}$, respectively, are shown in Figure 2.14b.

Table 2.7: Parameters of testbed structure ranked based on averaged total-order Sobol' indices

Rank	1	2	3	4	5	6	7	8	9	10	11
Parameter	G	K	α	X	R	T	λ	D	W	ϕ	β

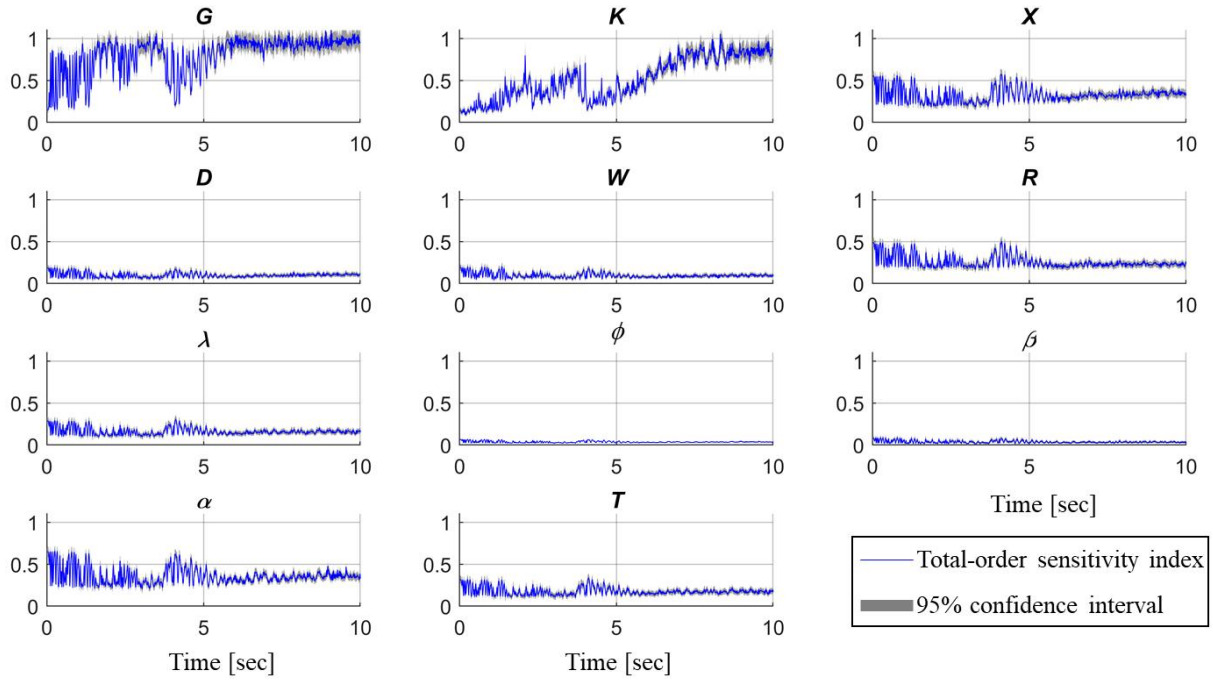

Figure 2.12: Total-order sensitivity index time histories for the acceleration at the top of the dam $\mathbf{a}^A$

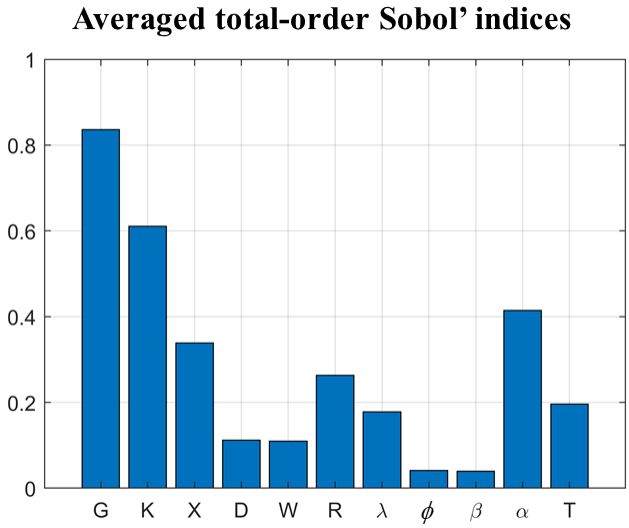

Figure 2.13: Averaged total-order Sobol' indices of parameters of the testbed structure

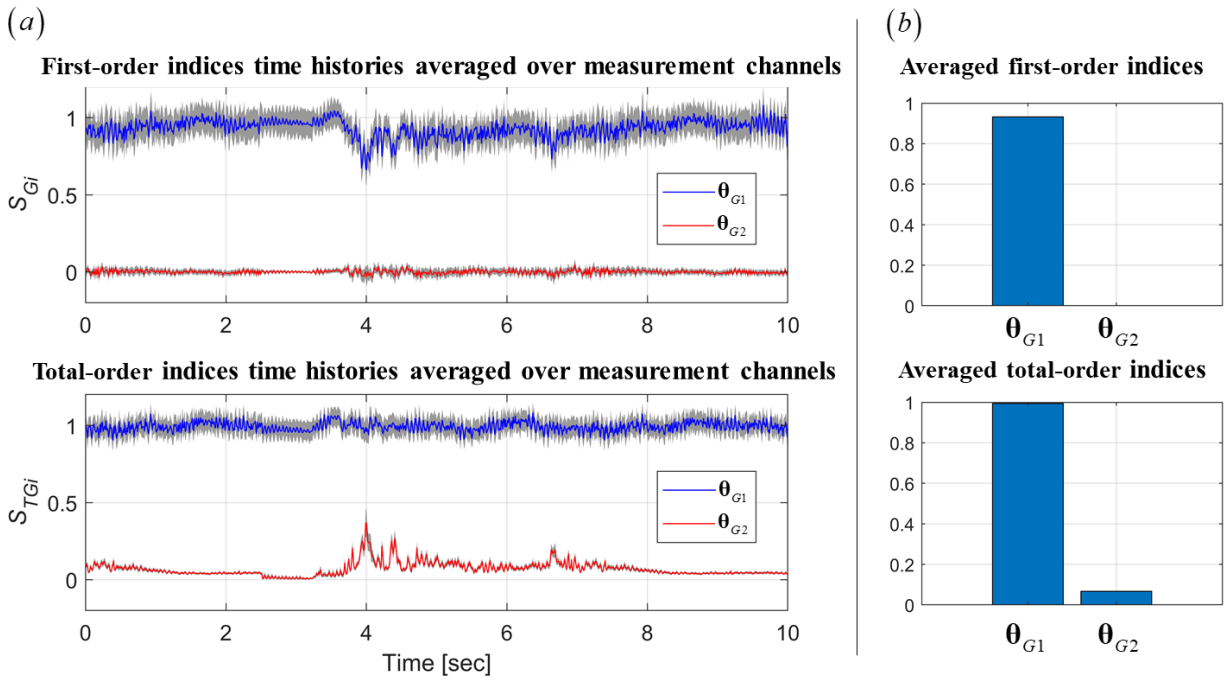

Figure 2.14: (a) first- and total-order Sobol' indices time histories averaged over measurement channels, (b) first- and total-order Sobol' indices averaged over time and measurement channels, for parameter groups

2.5.4 Revisiting Unscented Kalman Filter

From the local practical identifiability analysis using FIM and variance-based GSA, parameters $G, K, X, R, \alpha,$ and T are determined to be locally identifiable and influent parameters, respectively. Note that for the considered case study, the influent parameters identified using GSA and locally identifiable parameters determined using FIM happen to be the same. But it is quite possible that they could be different for other systems or with different measurement data. It is then the choice of the analyst to perform either of the two analyses and choose a parameter set to be included in the estimation stage. In this section, only these influent or locally identifiable parameters are estimated using the UKF, an approximate Bayesian inference technique that rely on point estimates, while fixing the other parameters to their corresponding mean value of their prior PDF (Eq. (2.31)). Instead of setting the non-influent or

non-identifiable parameters at a certain value, their uncertainty can be "considered" while updating only the influent or identifiable parameters using techniques such as the Consider Kalman filter (Woodbury and Junkins 2010). However, this is beyond the scope of this paper.

Figure 2.15 shows the time histories of the posterior mean parameter estimates, normalized with respect to their corresponding true values $\boldsymbol{\theta}^{true}$, obtained using the UKF for the influent or locally identifiable parameters of the testbed structure. The blue solid line in each plot represents the time history of the normalized mean parameter estimate ($\hat{\boldsymbol{\theta}}_{k|k},\ k=1,2,...,N$), the grey shaded region represents the corresponding estimation uncertainty as the mean ± two standard deviations (obtained from $\hat{\mathbf{P}}^{\boldsymbol{\theta\theta}}_{k|k},\ k=1,2,...,N$) interval, and the red dashed line denotes the normalized true parameter value. Estimates of parameters $G, K, X, R,$ and T converge to their corresponding true values while parameter α converges to a non-true value. It was observed that the parameter α also converges to its true value when the UKF is performed by setting the non-identifiable or non-influent parameters to their true values. Thus, the convergence of parameter α to a nontrue value can be attributed to compensation effects with non-identifiable or non-influent parameters. For example, in the model $y=(m_1+m_2)x+c$ with (x,y) pairs as the measurement input-output data, parameter c is identifiable and fixing parameter m_1 renders m_2 identifiable and vice-versa. However, if m_1 is fixed at an incorrect value then m_2 will be estimated incorrectly due to its compensation with m_1 and vice-versa, whereas c will be estimated correctly. The runtime of this FE model updating using the UKF for the six influent parameters is 3.6 hours on Intel Xeon W-2155 @ 3.30 GHz CPU with 10 cores / 20 threads and 128 GB RAM workstation. Recall that it took 6.4 hours to run the UKF to estimate all eleven parameters (Section 2.5.2.2). In summary, removing non-identifiable parameters when using

approximate Bayesian inference methods that rely on point estimates improves significantly the estimation results and computational time.

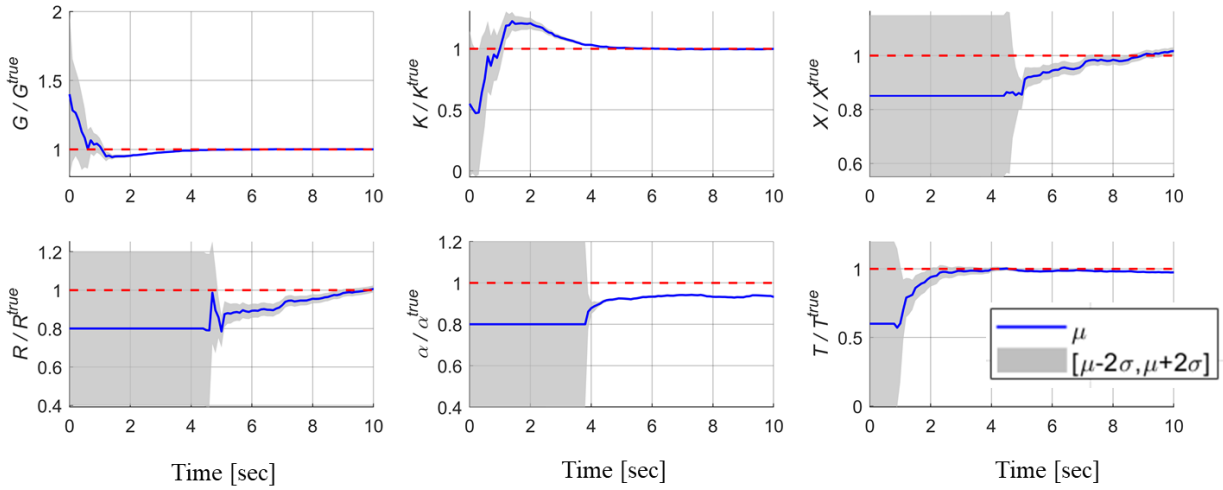

Figure 2.15: Time histories of the posterior mean estimates, normalized with respect to their corresponding true values, of the influent or locally identifiable parameters obtained using the UKF

2.6 Conclusions

This paper focuses on Bayesian model updating/calibration and identifiability analysis of nonlinear finite element (FE) models with an eye towards large-scale civil structural systems. The problem is challenging in terms of computational cost and identifiability issues arising in such FE models. Pine Flat concrete gravity dam is used as the testbed structure. The parameters of a mechanics-based materially-nonlinear FE model of Pine Flat dam are estimated/updated/calibrated in recursive mode using the unscented Kalman filter (UKF), an approximate Bayesian inference method that relies on point estimates, and in batch mode using transitional Markov chain Monte Carlo (TMCMC), a "full distribution" Bayesian method, using simulated noisy input-output seismic measurement data. The consistency in estimation results obtained from these two approaches is examined. It is shown that for precise and accurate

inference to be possible, the selected FE model must be identifiable. Although Bayesian calibration is theoretically robust against model non-identifiability, many numerical approximate methods of Bayesian inference do not perform well in case of non-identifiability. It is also shown that the non-identifiable model parameters can result in undesirable non-uniqueness in the parameter estimates when the inference is performed using methods that rely on point estimates (e.g., Kalman filter and its variants) motivating the need for model identifiability analysis prior to model updating in practice.

Local and global sensitivity and identifiability analysis methods are described in this paper, especially focusing on their applicability to nonlinear FE models, a topic scarcely addressed in the literature. A local practical identifiability analysis method based on the Fisher information matrix is used in this paper to assess the practical identifiability of the unknown parameter vector of the FE model at a certain local region in the parameter space. The analysis results are used to choose the parameters to be included in the model updating stage. Due to the lack of a method to assess global practical identifiability, global sensitivity analysis based on Sobol's method is used herein. Note however that Sobol's method can only determine (globally) influent parameters but not globally identifiable ones. Total-order Sobol' indices of individual parameters and parameter groups are used to select the influent parameters to be included in the model updating stage. It is demonstrated that removing non-identifiable and/or non-influent parameters resulted in better estimation results in terms of convergence and reduced the computational time.

The emphasis of this paper is on updating nonlinear FE models of civil structural systems. However, the updating and identifiability methodologies described in the paper are general and applicable to any mathematical model. This paper paves the way to FE model

updating of large-scale nonlinear systems using real measurement data for structural health monitoring and damage prognosis purposes. Additional research is needed to (i) improve model identifiability by adding more sensors (measurement responses, e.g., long-gauge fiber optic sensors, rotational accelerometers), (ii) investigate the identifiability of parameters of nonlinear dynamic systems as a function of time, (iii) determine identifiable parameter combinations of an FE model, and (iv) develop methods for global practical identifiability analysis of FE models. There is also a pressing need to develop methods to accurately account for modeling uncertainty (or model form error) in dynamic (linear and nonlinear) systems to estimate physical parameters as such and not as tuning parameters.

2.7 Acknowledgements

Funding for this work by the U.S. Army Corps of Engineers through the U.S. Army Engineer Research and Development Center Research Cooperative Agreement W912HZ-17-2-0024 is gratefully acknowledged. Chapter 2, in part, is a reprint of the material as it appears in the following papers (the dissertation author is the first author of these paper):

Ramancha, M. K., Astroza, R., Madarshahian, R., and Conte, J. P. (2022). "Bayesian updating and identifiability assessment of nonlinear finite element models." *Mechanical Systems and Signal Processing*, 167, 108517. https://doi.org/10.1016/j.ymssp.2021.108517

Ramancha, M. K., Madarshahian, R., Astroza, R., and Conte, J. P. (2020). "Non-unique Estimates in Material Parameter Identification of Nonlinear FE Models Governed by Multiaxial Material Models Using Unscented Kalman Filtering." *Conference Proceedings of the Society for Experimental Mechanics Series*, 257–265. https://doi.org/10.1007/978-3-030-12075-7_29

2.8 Preview to Chapter 3

As mentioned in Section 2.3, assuming the noise process to have zero-mean and time-invariant diagonal covariance matrix (as in Eq. (2.2)) may not be sufficiently accurate especially in the presence of model-form error. Chapter 3 extends the framework presented in Section 2.3 to accurately account for the model form uncertainty in Bayesian calibration focusing on linear dynamic systems.

3 Accounting for Model Form Uncertainty in Bayesian Calibration of Linear Dynamic Systems

3.1 Abstract

Accounting for model form uncertainty is one of the key challenges in the model calibration of physical systems. It has been traditionally ignored (or not properly accounted for) in the model calibration of structural systems. The state-of-the-art Kennedy and O'Hagan (KOH) approach to account for model form uncertainty has only been applied for calibration of systems under static or quasi-static loading. This paper proposes an extension of the KOH approach to account for model form uncertainty in the calibration of linear systems (i.e., estimating their physical parameters) subject to dynamic loading. A novel power spectral density – covariance function pair based on the theory of random vibrations is proposed that can potentially represent model form uncertainty arising in linear dynamic systems. The proposed methodology is illustrated and validated by calibrating structural engineering benchmark problems (single- and multi-degree-of-freedom systems) in the presence of model form uncertainty subject to dynamic loading (wind and earthquake loading). A bias in estimates of physical parameters is observed when the calibration is performed without properly accounting for model form uncertainty. This bias is eliminated when the calibration is performed using the proposed methodology.

Keywords: Bayesian model calibration, parameter estimation, physical parameters, Kennedy and O'Hagan approach, spectral kernel, linear dynamic systems, spectral kernel mixture, fully Bayesian approach.

3.2 Introduction

Physics-based mathematical models are used in engineering to understand and predict the behavior of many systems. Such models often contain parameters that are entirely unknown or only partially constrained, combinedly referred to as unknown parameters in this paper, and need to be calibrated using measurement data. These parameters can be broadly categorized into physical parameters (e.g., inertial parameters such as floor mass, stiffness-related parameters such as story stiffness), non-physical tuning parameters, and semi-physical parameters. Physical parameters are ubiquitous in models of structural systems and maintaining their physical interpretation during calibration is critical for understanding the underlying system and making accurate response predictions (Brynjarsdóttir and O'Hagan 2014).

Model calibration involves learning the unknown parameters of the mathematical model using measurement data (Kennedy and O'Hagan 2001). The data are typically not sufficient to completely constrain the parameters however, and several sources of uncertainty (Chatfield 1995; Kennedy and O'Hagan 2001) need to be accounted for in the calibration process. Model form uncertainty arising from model inadequacies due to simplifying assumptions, hypotheses, and unmodeled physics is a major source of uncertainty in model calibration (Brynjarsdóttir and O'Hagan 2014; Kennedy and O'Hagan 2001; Plumlee 2017; Sargsyan et al. 2015). In the literature, model form uncertainty is also referred to as modeling uncertainty, model discrepancy, model bias, or uncertainty about the model structure. Accounting for model form uncertainty is challenging, especially in structural systems due to abundant possible modeling errors, including approximations about geometries, boundary and loading conditions, energy dissipation mechanisms, non-structural components, material properties, and constitutive equations. Hence, its formal treatment is traditionally ignored in the model calibration of structural systems,

despite its importance in maintaining the meaning of physical model parameters. Accounting for model form uncertainty is an important aspect of model verification, validation, calibration, and uncertainty quantification and must not be ignored, despite the difficulty of its treatment. In recent years, there has therefore been an increased interest in accounting for model form uncertainty in structural systems (Astroza et al. 2019a; Behmanesh et al. 2015; Goulet et al. 2014; Goulet and Smith 2013).

The Bayesian approach to model calibration (Tarantola 2005; Yuen 2010) is considered in this paper. Traditionally, the error between the output measurement response and the response predicted through the mathematical model has been modeled as Gaussian white noise (Ramancha et al. 2020a; Yuen 2010), but this statistical assumption is inaccurate in the presence of model form uncertainty. As a result, the physical parameters act as tuning parameters that contort the model to fit the measurement data at the expense of losing their physical interpretation (Brynjarsdóttir and O'Hagan 2014). However, it is possible to retain the physical meaning of the parameters after calibration if all the uncertainty sources are precisely accounted for (including model form uncertainty) in the model calibration process. This will be demonstrated in this paper in the context of linear dynamic structural models.

To the best of the author's knowledge, there are three approaches to account for model form uncertainty in the Bayesian framework: Kennedy and O'Hagan (KOH) approach (Kennedy and O'Hagan 2001), hierarchical Bayesian approach (Behmanesh et al. 2015), and embedded model form error approach (Sargsyan et al. 2019). In the KOH approach, a discrepancy model (referred to as the delta term in this paper) is added to the mathematical model to account for the model form uncertainty. The hierarchical Bayesian approach for model calibration (Behmanesh et al. 2015) considers the unknown physical parameters as random variables with underlying

probability distribution owing to model form uncertainty. Multiple sets of measurement data are then used to quantify the model form error. Obtaining these multiple data sets might be difficult, if not impossible, in the real world. The embedded model form error approach (Sargsyan et al. 2019) is a newer method that is applicable if the source of modeling error is known and can be embedded inside the mathematical model. The KOH approach is considered here because it does not rely on multiple data sets and is more flexible than the embedded approach when error sources are not known precisely.

The KOH approach proposed in (Kennedy and O'Hagan 2001) is directly applicable for estimating the physical parameters of systems under static loading or quasi-static loading. For dynamic loading scenarios, the difficulty lies in modeling the delta term to accurately represent model form uncertainties. This paper proposes an extension of the KOH approach to account for model form uncertainty in the calibration of linear systems subject to dynamic loading. Like in the KOH approach, the delta term is modeled using a Gaussian process, but a novel power spectral density – covariance function pair based on the theory of random vibrations is proposed to model the covariance kernel of the delta term to accurately represent common model form uncertainties arising in linear dynamic systems. The proposed methodology is illustrated by calibrating structural engineering benchmark problems (single- and multi-degree-of-freedom systems) with dynamic loading (wind and earthquake loading). A comparison of calibration with and without delta term is performed. When model form uncertainty is not accurately accounted for, the support of the posterior probability distribution of physical parameters does not contain the true parameter values (biased estimates). This bias persists/worsens with the increase in input-output measurement data. On the other hand, accounting for this uncertainty using the proposed approach results in a posterior distribution of physical parameters whose support

contains the corresponding true values. The impacts of different sampling rates and sampling durations of measurement data are studied, and the general applicability of the approach is discussed.

3.3 Bayesian Model Calibration with Model Form Error

Model calibration is a process of learning unknown parameters of the mathematical model using measurement data from the system of interest. At the discrete-time t_k (or time step k), let $\mathbf{u}_k \in \mathbb{R}^{n_\mathbf{u}}$ and $y_k \in \mathbb{R}$ be the measured input and output, respectively, where $n_\mathbf{u}$ denotes the number of input measurement channels. For illustration purposes, a single output measurement channel is first considered (up to and including Section 3.3.2). Multi output measurement channels are considered in Section 3.3.3. Mathematically, the case of multiple output measurement channels is no different from the case of single output channel, just the equations become more cumbersome. Assuming the measurements are obtained for N time steps, the input and output measurement data in vector form are $\mathbf{u}_{1:N} = \left[\mathbf{u}_1^T, \mathbf{u}_2^T, ..., \mathbf{u}_N^T\right]^T \in \mathbb{R}^{n_\mathbf{u} N}$ and $\mathbf{y}_{1:N} = \left[y_1, y_2, ..., y_N\right]^T \in \mathbb{R}^N$, respectively. Thus, the entire input-output measurement dataset is $\mathcal{D} = \left\{\left(\mathbf{u}_i, y_i\right)\right\}_{i=1:N} \equiv \left(\mathbf{u}_{1:N}, \mathbf{y}_{1:N}\right)$. These measurements are obtained using the sensor array deployed on the structural system of interest.

Let h denote the physics-based mathematical model of the system developed from design or as-built drawings and using explicitly formulated assumptions and hypotheses. Often, such models contain unknown parameters that need to be calibrated using measurement data. Let $h\left(t_k, \mathbf{u}_{1:k}; \boldsymbol{\theta}\right) \in \mathbb{R}$ be the response of the model h at time step k when subjected to measurement

input time history $\mathbf{u}_{1:k} = \left[\mathbf{u}_1^T, \mathbf{u}_2^T, ..., \mathbf{u}_k^T\right]^T \in \mathbb{R}^{n_\mathbf{u} k}$. Model h is parameterized by an unknown time-invariant parameter vector $\boldsymbol{\theta} \in \mathbb{R}^{n_\boldsymbol{\theta}}$, where $n_\boldsymbol{\theta}$ denotes the number of unknown parameters. Usually, many parameters in physics-based models of structural systems are physical parameters, i.e., parameters with physical meaning (e.g., floor mass, story stiffness). Note that physics-based models can also contain non-physical or semi-physical parameters, however their estimation is not the focus of this paper. Also, model calibration of linear dynamic systems, i.e., estimating the system unknown parameters, can be performed to match: (1) the measured output response time histories (time domain data), (2) the transfer functions between measured input and output data (frequency domain data), or (3) the modal properties of the system observed/identified from the measured input and output data; we focus on (1) in this paper. Hence, this methodology can be extended to nonlinear dynamic systems.

The discrepancy between measured output y_k and model response $h\left(t_k, \mathbf{u}_{1:k}; \boldsymbol{\theta}\right)$ can be attributed to numerous uncertainties encountered in the real world. For structural systems, these include: (1) uncertainty in the measured input and output due to sensor measurement noise, (2) uncertainty about the structure/form of the model or model form uncertainty, i.e., the selected model class cannot exactly represent the real system, (3) uncertainty about the parameters of the model for a given model structure/form, and so on. Of all the uncertainties, model form uncertainty is a major source of uncertainty in model calibration and uncertainty quantification of structural systems. The intent of this paper is to accurately account for it in linear dynamic systems. The objective of model calibration is to learn the unknown physical parameters $\boldsymbol{\theta}$ of the model h using measurement data $\mathcal{D}$ accounting for all pertinent sources of uncertainty. The Bayesian approach to model updating is attractive because it provides the framework to (1) account explicitly for the various uncertainties observed in the real-world during the estimation

process of unknown parameters and (2) characterize probabilistically the uncertainty in the parameter estimates (e.g., estimation uncertainty due to finite data, uncertainty due to model form error) (Stuart 2010; Tarantola 2005; Yuen 2010). The Bayesian approach models the unknown parameter vector $\boldsymbol{\theta}$ as a random vector.

Three main ingredients are required to perform Bayesian model calibration: (1) measurement data $\mathcal{D}$, (2) the prior probability distribution $p(\boldsymbol{\theta})$ of the unknown parameters $\boldsymbol{\theta}$ that encode prior beliefs about them, and (3) a measurement equation (i.e., model of the measurement process). The primary objective of Bayesian model calibration is to obtain $p(\boldsymbol{\theta} \mid \mathcal{D}) \equiv p\left(\boldsymbol{\theta} \mid \mathbf{u}_{1:N}, \mathbf{y}_{1:N}\right)$, referred to as posterior/updated probability distribution of $\boldsymbol{\theta}$. This posterior distribution of $\boldsymbol{\theta}$ accounts for both the prior knowledge $p(\boldsymbol{\theta})$ and the measurement data $\mathcal{D}$. After calibration, the predictions of the system response can be made using the posterior predictive distribution.

3.3.1 Measurement Equation

Measurement equation (i.e., a model of the measurement process) formulation is a crucial step of Bayesian model calibration as it leads to the likelihood function. The measurement equation is a joint physical-statistical model that relates the physical parameters $\boldsymbol{\theta}$ of the model h to measurements $\mathcal{D} \equiv \left(\mathbf{u}_{1:N}, \mathbf{y}_{1:N}\right)$. Traditionally, the following measurement equation is used in the Bayesian model calibration of structural systems:

$$\text{At time step } k: \quad y_k = \underbrace{h\left(t_k, \mathbf{u}_{1:k}; \boldsymbol{\theta}\right)}_{\text{mathematical model}} + \underset{\text{error/ noise}}{w\left(t_k\right)} \;; \quad k \in [1, 2, ..., N] \tag{3.1}$$

In Eq. (3.1), at each time step k, the measured output y_k is expressed as a summation of the model response $h(t_k, \mathbf{u}_{1:k}; \boldsymbol{\theta})$ and an error/noise term $w(t_k) \in \mathbb{R}$. The mathematical model primarily considered in this paper is an ordinary differential equation shown in Eq. (3.28) (equation of motion of an n-degree-of-freedom linear system with classical damping). With the measurement equation shown in Eq. (3.1), all the sources of real-world uncertainties are lumped and accounted for in the noise term. The accurate stochastic and statistical description of the noise process $w(t)$ is therefore crucial for accurate model calibration. The noise process $w(t)$ is traditionally modeled as a zero-mean Gaussian white noise, i.e., random variables $w(t_k)$ and $w(t_l)$ are statistically independent for every pair of distinct time steps k and l, and identically distributed with $w(t) \sim \mathcal{N}(0, \sigma^2)$ where $\mathcal{N}(\boldsymbol{\mu}, \boldsymbol{\Sigma})$ denotes a joint Gaussian distribution with mean vector $\boldsymbol{\mu}$ and covariance matrix $\boldsymbol{\Sigma}$. Hence, σ^2 is the variance of the noise process $w(t)$. This statistical description of the noise process is inaccurate in the presence of model form uncertainty (Brynjarsdóttir and O'Hagan 2014; Kennedy and O'Hagan 2001; Simoen et al. 2013). With Eq. (3.1), the main objective is to obtain $\boldsymbol{\theta}$ that best fits $y_{1:N}$ in presence of zero-mean noise. This causes the physical parameters to act as tuning parameters in model calibration thus leading to inaccurate parameter estimates and biased model response predictions (Section 3.5.1).

The measurement equation proposed by Kennedy and O'Hagan (KOH) is appropriate for model calibration in the presence of model form uncertainty (Kennedy and O'Hagan 2001). The central idea of the KOH approach is to include an additional term, referred to as delta term in this paper, in the measurement equation given in Eq. (3.1) to explicitly account for the model form uncertainty. However, the KOH approach introduced in (Kennedy and O'Hagan 2001) only

considers model calibration of systems subjected to static loading. For systems subjected to dynamic loads, the measurement equation proposed by KOH can be adapted accordingly as

$$\text{At time step } k: \quad y_k = \underbrace{h\left(t_k, \mathbf{u}_{1:k}; \boldsymbol{\theta}\right)}_{\text{mathematical model}} + \underset{\text{delta}}{\delta\left(\mathbf{x}_k\right)} + \underset{\text{error/ noise}}{w\left(t_k\right)} \; ; \quad k \in \left[1, 2, ..., N\right] \tag{3.2}$$

In Eq. (3.2), at each time step k, the measured output y_k is expressed as a summation of model response $h\left(t_k, \mathbf{u}_{1:k}; \boldsymbol{\theta}\right)$, delta term $\delta\left(\mathbf{x}_k\right) \in \mathbb{R}$, and an error/noise term $w\left(t_k\right) \in \mathbb{R}$. $\mathbf{x} \in \mathbb{R}^{n_\mathbf{x}}$ denotes the input of the delta process $\delta\left(\mathbf{x}\right)$ similar to time t being the input of the noise process $w\left(t\right)$. In this paper, only time is considered as the input of the delta process, i.e., $\mathbf{x}_k = \left[t_k\right]$, for the reasons mentioned at the beginning of Section 3.4. In the literature, the delta term is also referred to as the model inadequacy function or discrepancy model.

The goal is to account for all uncertainties using both the delta and noise terms with the delta term exclusively accounting for the model form uncertainty. The delta term should explain that part of the true system response that cannot be explained by the mathematical model due to the model form uncertainty. The delta term adds flexibility to the measurement equation to fit measurement data allowing the calibrated physical parameters to retain their physical meaning and not act like tuning parameters when calibrating models with model form uncertainty (Section 3.5.1).

Both the noise and delta processes are modeled as stochastic processes. As in the previous case, the noise process $w\left(t\right)$ is modeled as a zero-mean Gaussian white noise with $w\left(t\right) \sim \mathcal{N}\left(0, \sigma^2\right)$. Following the KOH approach, the delta process is modeled using a Gaussian process model with zero-mean and is denoted as $\delta\left(\mathbf{x}\right) \sim \mathcal{GP}\left(0, k\left(\mathbf{x}, \mathbf{x}'; \boldsymbol{\beta}\right)\right)$, where $k\left(\mathbf{x}, \mathbf{x}'; \boldsymbol{\beta}\right) \in \mathbb{R}$ is the covariance function/kernel parameterized by parameter vector $\boldsymbol{\beta}$. Hence, $E\left[\delta\left(\mathbf{x}\right)\right] = 0$ and

$k(\mathbf{x},\mathbf{x}') = E\left[\delta(\mathbf{x})\delta(\mathbf{x}')\right]$, where $E[.]$ is the expectation operator. The covariance function $k(\mathbf{x},\mathbf{x}')$ can be interpreted as a measure of the correlation between $\delta(\mathbf{x})$ and $\delta(\mathbf{x}')$. Hence, the covariance function $k(\mathbf{x},\mathbf{x}')$ is used to model the smoothness of $\delta(\mathbf{x})$. The challenging aspect for accurate model calibration of dynamic systems is choosing the appropriate covariance function $k(\mathbf{x},\mathbf{x}';\boldsymbol{\beta})$ and choosing the appropriate input $\mathbf{x}$ of the delta term $\delta(\mathbf{x})$. These aspects are focused in Section 3.4.

Gaussian processes are non-parametric probabilistic models (Rasmussen and Williams 2005). Compared to parametric models, non-parametric models like Gaussian processes require fewer (or weak) assumptions about the underlying process – ideal for modeling model form uncertainty. Gaussian processes also allow to incorporate prior knowledge about the underlying process (i.e., model form error in this case). Other machine learning techniques such as artificial neural networks and autoregressive-moving-average (ARMA) models can also be used to model the delta term (Lei et al. 2020; Yucesan et al. 2020). Note that Eq. (3.2) describes a case of fusing physics-based models h with machine learning models δ to explain the measurement data. The machine learning model δ addresses the part of the true system response that cannot be explained by the physics-based model h, due to model form uncertainty. This is an extremely powerful and influential equation that can be used in various scientific fields for forecasting and predictions.

3.3.2 Estimating Physical Parameters using Bayesian inference

This section focuses on the estimation of the physical parameters $\boldsymbol{\theta}$ of the model h using Bayesian inference considering both measurement equations defined in Section 3.3.1. In this

paper, Eqs. (3.1) and (3.2) are referred to as measurement equation without and with delta term, respectively. The primary objective of Bayesian model calibration is to obtain the posterior distribution of $\boldsymbol{\theta}$, $p(\boldsymbol{\theta} | \mathbf{u}_{1:N}, \mathbf{y}_{1:N})$. Model calibration using the measurement equation with delta term (i.e., Eq. (3.2)) is primarily described in this section. This methodology can be adapted accordingly for model calibration using the measurement equation without delta term (i.e., Eq. (3.1)).

In Eq. (3.2), the total unknown parameters $\{\boldsymbol{\theta}, \boldsymbol{\beta}, \sigma\}$ comprise the physical parameters $\boldsymbol{\theta}$, and hyperparameters $\boldsymbol{\beta}$ (covariance function parameters) and σ (standard deviation of the noise process). There are various approaches to obtain the posterior distribution $p(\boldsymbol{\theta} | \mathbf{u}_{1:N}, \mathbf{y}_{1:N})$ such as fully Bayesian approach, integrated likelihood approach (Wolpert et al. 1999), and modular Bayesian approach (Kennedy and O'Hagan 2001). Fully Bayesian analysis (Section 3.3.2.1) fully accounts for all sources of uncertainty consistently and rigorously and is therefore employed in this paper for model calibration. However, the fully Bayesian analysis is computationally expensive, might not be always practical, and requires careful consideration of prior knowledge of the hyperparameters (refer to Section 4.5 of (Kennedy and O'Hagan 2001)). Practical approaches such as the integrated likelihood approach and modular Bayesian approach are briefly described in Appendix B in the context of Bayesian model calibration accounting for model form error.

3.3.2.1 Fully Bayesian Approach

A fully Bayesian approach for model calibration requires first obtaining the joint posterior distribution of the physical parameters and hyperparameters $p(\boldsymbol{\theta}, \boldsymbol{\beta}, \sigma | \mathbf{u}_{1:N}, \mathbf{y}_{1:N})$.

Then, the posterior distribution $p(\boldsymbol{\theta}\,|\,\mathbf{u}_{1:N},\mathbf{y}_{1:N})$ is obtained by integrating out the hyperparameters $\{\boldsymbol{\beta},\sigma\}$. This accomplishes model calibration. The posterior predictive distribution is then obtained for response predictions.

The joint posterior of all unknown parameters $p(\boldsymbol{\theta},\boldsymbol{\beta},\sigma\,|\,\mathbf{u}_{1:N},\mathbf{y}_{1:N})$ can be obtained by the following implementation of Bayes' rule (a central equation in Bayesian inference)

$$p(\boldsymbol{\theta},\boldsymbol{\beta},\sigma\,|\,\mathbf{u}_{1:N},\mathbf{y}_{1:N})=\frac{p(\mathbf{y}_{1:N}\,|\,\mathbf{u}_{1:N},\boldsymbol{\theta},\boldsymbol{\beta},\sigma)\times p(\boldsymbol{\theta},\boldsymbol{\beta},\sigma)}{p(\mathbf{y}_{1:N}\,|\,\mathbf{u}_{1:N})} \tag{3.3}$$

where $p(\mathbf{y}_{1:N}\,|\,\mathbf{u}_{1:N},\boldsymbol{\theta},\boldsymbol{\beta},\sigma)$ is the likelihood function which measures the goodness of fit of the measurement equation to the measurement data $(\mathbf{u}_{1:N},\mathbf{y}_{1:N})$ given the values of all the unknown parameters $\{\boldsymbol{\theta},\boldsymbol{\beta},\sigma\}$. $p(\boldsymbol{\theta},\boldsymbol{\beta},\sigma)$ is the joint prior distribution of all the unknown parameters. It is reasonable to assume the prior distributions of the physical parameters $\boldsymbol{\theta}$, and hyperparameters $\boldsymbol{\beta}$ and σ to be statistically independent, thus $p(\boldsymbol{\theta},\boldsymbol{\beta},\sigma)=p(\boldsymbol{\theta})\,p(\boldsymbol{\beta})\,p(\sigma)$. The denominator $p(\mathbf{y}_{1:N}\,|\,\mathbf{u}_{1:N})$ is a normalizing constant ensuring that $p(\boldsymbol{\theta},\boldsymbol{\beta},\sigma\,|\,\mathbf{u}_{1:N},\mathbf{y}_{1:N})$ integrates to one. Eq. (3.3) can now be written as

$$p(\boldsymbol{\theta},\boldsymbol{\beta},\sigma\,|\,\mathbf{u}_{1:N},\mathbf{y}_{1:N})\propto p(\mathbf{y}_{1:N}\,|\,\mathbf{u}_{1:N},\boldsymbol{\theta},\boldsymbol{\beta},\sigma)\times p(\boldsymbol{\theta})\,p(\boldsymbol{\beta})\,p(\sigma) \tag{3.4}$$

To obtain the likelihood function $p(\mathbf{y}_{1:N}\,|\,\mathbf{u}_{1:N},\boldsymbol{\theta},\boldsymbol{\beta},\sigma)$, the measurement equation defined in Eq. (3.2) is expanded for all time steps $1{:}\,N$ and is written in the following vector form

$$\mathbf{y}_{1:N}=\bar{\mathbf{h}}(\mathbf{u}_{1:N};\boldsymbol{\theta})+\boldsymbol{\delta}(\mathbf{x}_{1:N})+\mathbf{w}(t_{1:N}) \tag{3.5}$$

where $\bar{\mathbf{h}}(\mathbf{u}_{1:N};\boldsymbol{\theta}) = \left[h(t_1,\mathbf{u}_1;\boldsymbol{\theta}), h(t_2,\mathbf{u}_{1:2};\boldsymbol{\theta}),\ldots, h(t_N,\mathbf{u}_{1:N};\boldsymbol{\theta})\right]^T \in \mathbb{R}^N$ is the response time history of the mathematical model, $\boldsymbol{\delta}(\mathbf{x}_{1:N}) = \left[\delta(\mathbf{x}_1), \delta(\mathbf{x}_2),\ldots,\delta(\mathbf{x}_N)\right]^T \in \mathbb{R}^N$ is the time history of the delta process, and $\mathbf{w}(t_{1:N}) = \left[w(t_1), w(t_2),\ldots w(t_N)\right]^T \in \mathbb{R}^N$ is the time history of the noise process.

As the delta process is modeled as a zero-mean Gaussian process, i.e., $\delta(\mathbf{x}) \sim \mathcal{GP}\left(0, k(\mathbf{x},\mathbf{x}';\boldsymbol{\beta})\right)$, the probability distribution of $\boldsymbol{\delta}(\mathbf{x}_{1:N}) \in \mathbb{R}^N$ is a multi-variate zero-mean Gaussian distribution as

$$\begin{aligned} &\boldsymbol{\delta}(\mathbf{x}_{1:N}) \sim \mathcal{N}\left(\mathbf{0}, \mathbf{K}(\mathbf{x}_{1:N},\mathbf{x}_{1:N};\boldsymbol{\beta})\right); \\ &\mathbf{K}(\mathbf{x}_{1:N},\mathbf{x}_{1:N};\boldsymbol{\beta}) = \begin{pmatrix} k(\mathbf{x}_1,\mathbf{x}_1;\boldsymbol{\beta}) & \cdots & k(\mathbf{x}_1,\mathbf{x}_N;\boldsymbol{\beta}) \\ \vdots & \ddots & \vdots \\ k(\mathbf{x}_N,\mathbf{x}_1;\boldsymbol{\beta}) & \cdots & k(\mathbf{x}_N,\mathbf{x}_N;\boldsymbol{\beta}) \end{pmatrix} \in \mathbb{R}^{N\times N} \end{aligned} \tag{3.6}$$

Note that choosing the appropriate covariance function $k(\mathbf{x},\mathbf{x}';\boldsymbol{\beta})$ and choosing the appropriate input $\mathbf{x}$ of the delta term $\delta(\mathbf{x})$ are discussed in Section 3.4. Since the noise process is modeled as a zero-mean Gaussian white noise, the probability distribution of $\mathbf{w}(t_{1:N}) \in \mathbb{R}^N$ is a multi-variate zero-mean Gaussian distribution as

$$\mathbf{w}_{1:N} \sim \mathcal{N}\left(\mathbf{0}, \sigma^2\mathbf{I}_N\right) \tag{3.7}$$

where $\mathbf{I}_N \in \mathbb{R}^{N\times N}$ denotes an identity matrix of size N.

Now using Eqs. (3.5)-(3.7), the likelihood function $p(\mathbf{y}_{1:N} \mid \mathbf{u}_{1:N},\boldsymbol{\theta},\boldsymbol{\beta},\sigma)$ is given by

$$p(\mathbf{y}_{1:N} \mid \mathbf{u}_{1:N},\boldsymbol{\theta},\boldsymbol{\beta},\sigma) = \mathcal{N}\left(\bar{\mathbf{h}}(\mathbf{u}_{1:N};\boldsymbol{\theta}), \mathbf{K}(\mathbf{x}_{1:N},\mathbf{x}_{1:N};\boldsymbol{\beta}) + \sigma^2\mathbf{I}_N\right) \tag{3.8}$$

The response time history of the mathematical model $\bar{\mathbf{h}}(\mathbf{u}_{1:N};\boldsymbol{\theta})$ is the mean vector of the likelihood function $p(\mathbf{y}_{1:N}\,|\,\mathbf{u}_{1:N},\boldsymbol{\theta},\boldsymbol{\beta},\sigma)$. The posterior distribution $p(\boldsymbol{\theta}\,|\,\mathbf{u}_{1:N},\mathbf{y}_{1:N})$ can now be obtained by integrating out the hyperparameters $\{\boldsymbol{\beta},\sigma\}$ from the joint posterior $p(\boldsymbol{\theta},\boldsymbol{\beta},\sigma\,|\,\mathbf{u}_{1:N},\mathbf{y}_{1:N})$ as

$$p(\boldsymbol{\theta}\,|\,\mathbf{u}_{1:N},\mathbf{y}_{1:N}) = \int_{\boldsymbol{\beta}}\int_{\sigma} p(\boldsymbol{\theta},\boldsymbol{\beta},\sigma\,|\,\mathbf{u}_{1:N},\mathbf{y}_{1:N})\,d\sigma\,d\boldsymbol{\beta} \tag{3.9}$$

After model calibration, predicting the response of the system y_j^* (at a certain time step j) with a new measured input time history $\mathbf{u}_{1:j}^*$ conditioned on the entire measurement data $\mathcal{D}$ can be achieved using the following distribution

$$\underbrace{p(y_j^*\,|\,\mathbf{u}_{1:j}^*,\mathcal{D})}_{\text{posterior predictive}} = \int_{\sigma}\int_{\boldsymbol{\beta}}\int_{\boldsymbol{\theta}} p(y_j^*\,|\,\mathbf{u}_{1:j}^*,\boldsymbol{\theta},\boldsymbol{\beta},\sigma,\mathcal{D}) \times \underbrace{p(\boldsymbol{\theta},\boldsymbol{\beta},\sigma\,|\,\mathcal{D})}_{\text{joint posterior}}\,d\boldsymbol{\theta}\,d\boldsymbol{\beta}\,d\sigma \tag{3.10}$$

The posterior predictive distribution $p(y_j^*\,|\,\mathbf{u}_{1:j}^*,\mathcal{D})$ allows the prediction of the response of the system given all the information available in the measurement data $\mathcal{D}$. Using the measurement equation with delta term, $p(y_j^*\,|\,\mathbf{u}_{1:j}^*,\boldsymbol{\theta},\boldsymbol{\beta},\sigma)$ is given by

$$p(y_j^*\,|\,\mathbf{u}_{1:j}^*,\boldsymbol{\theta},\boldsymbol{\beta},\sigma) = \mathcal{N}\left(h(t_j,\mathbf{u}_{1:j}^*;\boldsymbol{\theta}),\; k(\mathbf{x}_j^*,\mathbf{x}_j^*;\boldsymbol{\beta}) + \sigma^2\right) \tag{3.11}$$

where $\mathbf{x}_j^*$ denotes the input of the delta process at time step j. The distribution $p(y_j^*\,|\,\mathbf{u}_{1:j}^*,\boldsymbol{\theta},\boldsymbol{\beta},\sigma,\mathcal{D})$ on the right-hand side in Eq. (3.10) is given by

$$\begin{aligned}
&p(y_j^*\,|\,\mathbf{u}_{1:j}^*,\boldsymbol{\theta},\boldsymbol{\beta},\sigma,\mathcal{D}) = \mathcal{N}\left(\tilde{h}(t_j,\mathbf{u}_{1:j}^*;\boldsymbol{\theta},\boldsymbol{\beta},\sigma),\; \tilde{k}(\mathbf{x}_j^*,\mathbf{x}_j^*;\boldsymbol{\beta},\sigma) + \sigma^2\right);\\
&\tilde{h}(t_j,\mathbf{u}_{1:j}^*;\boldsymbol{\theta},\boldsymbol{\beta},\sigma) = h(t_j,\mathbf{u}_{1:j}^*;\boldsymbol{\theta}) + \mathbf{K}(\mathbf{x}_j^*,\mathbf{x}_{1:N};\boldsymbol{\beta})\left(\mathbf{K}(\mathbf{x}_{1:N},\mathbf{x}_{1:N};\boldsymbol{\beta}) + \sigma^2\mathbf{I}_N\right)^{-1}\left(\mathbf{y}_{1:N} - \bar{\mathbf{h}}(\mathbf{u}_{1:N};\boldsymbol{\theta})\right)\\
&\tilde{k}(\mathbf{x}_j^*,\mathbf{x}_j^*;\boldsymbol{\beta},\sigma) = k(\mathbf{x}_j^*,\mathbf{x}_j^*;\boldsymbol{\beta}) - \mathbf{K}(\mathbf{x}_j^*,\mathbf{x}_{1:N};\boldsymbol{\beta})\left(\mathbf{K}(\mathbf{x}_{1:N},\mathbf{x}_{1:N};\boldsymbol{\beta}) + \sigma^2\mathbf{I}_N\right)^{-1}\mathbf{K}(\mathbf{x}_{1:N},\mathbf{x}_j^*;\boldsymbol{\beta})
\end{aligned} \tag{3.12}$$

where $\mathbf{K}\left(\mathbf{x}_j^*, \mathbf{x}_{1:N}; \boldsymbol{\beta}\right) = \mathbf{K}\left(\mathbf{x}_{1:N}, \mathbf{x}_j^*; \boldsymbol{\beta}\right)^T = \left[k\left(\mathbf{x}_j^*, \mathbf{x}_1; \boldsymbol{\beta}\right) \quad \cdots \quad k\left(\mathbf{x}_j^*, \mathbf{x}_N; \boldsymbol{\beta}\right)\right] \in \mathbb{R}^{1\times N}$. For more details on the derivation of Eq. (12), see Section 2.2 of (Rasmussen and Williams 2005).

The posterior and posterior predictive probability distributions presented in this section can be derived accordingly for model calibration using the measurement equation without the delta term (i.e., Eq. (3.1)). For this case, the total unknown parameters $\{\boldsymbol{\theta}, \sigma\}$ comprise the physical parameters $\boldsymbol{\theta}$ and hyperparameter σ (standard deviation of the noise process). The posterior and posterior predictive distributions for model calibration without and with delta term are compared in Table 3.1. A major disparity in the comparison is in the posterior predictive distribution. The posterior predictive distribution $p\left(y_j^* \mid \mathbf{u}_{1:j}^*, \mathcal{D}\right)$ based on the measurement equation without delta term is given by

$$p\left(y_j^* \mid \mathbf{u}_{1:j}^*, \mathcal{D}\right) = \int_{\sigma}\int_{\boldsymbol{\theta}} p\left(y_j^* \mid \mathbf{u}_{1:j}^*, \boldsymbol{\theta}, \sigma\right) \times p\left(\boldsymbol{\theta}, \sigma \mid \mathcal{D}\right) d\boldsymbol{\theta}\, d\sigma \tag{3.13}$$

Since the measurement equation without delta term is parametric, the following relation holds (Ghahramani 2013):

$$p\left(y_j^* \mid \mathbf{u}_{1:j}^*, \boldsymbol{\theta}, \sigma, \mathcal{D}\right) = p\left(y_j^* \mid \mathbf{u}_{1:j}^*, \boldsymbol{\theta}, \sigma\right) \tag{3.14}$$

$p\left(y_j^* \mid \mathbf{u}_{1:j}^*, \boldsymbol{\theta}, \sigma\right)$ can then be obtained from the measurement equation without delta term as

$$p\left(y_j^* \mid \mathbf{u}_{1:j}^*, \boldsymbol{\theta}, \sigma\right) = \mathcal{N}\left(h\left(t_j, \mathbf{u}_{1:j}^*; \boldsymbol{\theta}\right), \sigma^2\right) \tag{3.15}$$

Note that the measurement model with delta term is non-parametric since the delta term is modeled as a Gaussian process, a non-parametric model. Thus, Eq. (3.14) is not applicable (Ghahramani 2013).

Table 3.1: Overview of model calibration using measurement equation without and with delta term (fully Bayesian approach)

Model calibration without delta term	**Model calibration with delta term**
Measurement equation at time step k	
$y_k = \underbrace{h(t_k, \mathbf{u}_{1:k}; \boldsymbol{\theta})}_{\text{mathematical model}} + \underbrace{w(t_k)}_{\text{error/ noise}}$ $w(t) \sim \mathcal{N}(0, \sigma^2)$	$y_k = \underbrace{h(t_k, \mathbf{u}_{1:k}; \boldsymbol{\theta})}_{\text{mathematical model}} + \underbrace{\delta(\mathbf{x}_k)}_{\text{delta}} + \underbrace{w(t_k)}_{\text{error/ noise}}$ $w(t) \sim \mathcal{N}(0, \sigma^2) \quad \delta(\mathbf{x}) \sim \mathcal{GP}(0, k(\mathbf{x}, \mathbf{x}'; \boldsymbol{\beta}))$
Total unknown parameters	
$\{\boldsymbol{\theta}, \sigma\}$	$\{\boldsymbol{\theta}, \boldsymbol{\beta}, \sigma\}$
Joint posterior of physical parameters and hyperparameters	
$p(\boldsymbol{\theta}, \sigma \mid \mathbf{u}_{1:N}, \mathbf{y}_{1:N})$ $\propto p(\mathbf{y}_{1:N} \mid \mathbf{u}_{1:N}, \boldsymbol{\theta}, \sigma) \times p(\boldsymbol{\theta})\, p(\sigma)$	$p(\boldsymbol{\theta}, \boldsymbol{\beta}, \sigma \mid \mathbf{u}_{1:N}, \mathbf{y}_{1:N})$ $\propto p(\mathbf{y}_{1:N} \mid \mathbf{u}_{1:N}, \boldsymbol{\theta}, \boldsymbol{\beta}, \sigma) \times p(\boldsymbol{\theta})\, p(\boldsymbol{\beta})\, p(\sigma)$
Likelihood function	
$p(\mathbf{y}_{1:N} \mid \mathbf{u}_{1:N}, \boldsymbol{\theta}, \sigma)$ $= \mathcal{N}(\bar{\mathbf{h}}(\mathbf{u}_{1:N}; \boldsymbol{\theta}), \sigma^2 \mathbf{I}_N)$	$p(\mathbf{y}_{1:N} \mid \mathbf{u}_{1:N}, \boldsymbol{\theta}, \boldsymbol{\beta}, \sigma)$ $= \mathcal{N}(\bar{\mathbf{h}}(\mathbf{u}_{1:N}; \boldsymbol{\theta}), \mathbf{K}(\mathbf{x}_{1:N}, \mathbf{x}_{1:N}; \boldsymbol{\beta}) + \sigma^2 \mathbf{I}_N)$
Posterior distribution of physical parameters $p(\boldsymbol{\theta} \mid \mathbf{u}_{1:N}, \mathbf{y}_{1:N})$	
$= \int_{\sigma} p(\boldsymbol{\theta}, \sigma \mid \mathbf{u}_{1:N}, \mathbf{y}_{1:N})\, d\sigma$	$= \int_{\boldsymbol{\beta}} \int_{\sigma} p(\boldsymbol{\theta}, \boldsymbol{\beta}, \sigma \mid \mathbf{u}_{1:N}, \mathbf{y}_{1:N})\, d\sigma\, d\boldsymbol{\beta}$
Posterior predictive distribution $p(y_j^* \mid \mathbf{u}_{1:j}^*, \mathcal{D})$	
$= \int_{\sigma} \int_{\boldsymbol{\theta}} p(y_j^* \mid \mathbf{u}_{1:j}^*, \boldsymbol{\theta}, \sigma, \mathcal{D}) \times p(\boldsymbol{\theta}, \sigma \mid \mathcal{D})\, d\boldsymbol{\theta}\, d\sigma$ where $p(y_j^* \mid \mathbf{u}_{1:j}^*, \boldsymbol{\theta}, \sigma, \mathcal{D}) = p(y_j^* \mid \mathbf{u}_{1:j}^*, \boldsymbol{\theta}, \sigma)$ $= \mathcal{N}(h(t_j, \mathbf{u}_{1:j}^*; \boldsymbol{\theta}), \sigma^2)$ Refer to Eqs. (3.14), (3.15)	$= \int_{\sigma} \int_{\boldsymbol{\beta}} \int_{\boldsymbol{\theta}} p(y_j^* \mid \mathbf{u}_{1:j}^*, \boldsymbol{\theta}, \boldsymbol{\beta}, \sigma, \mathcal{D}) \times p(\boldsymbol{\theta}, \boldsymbol{\beta}, \sigma \mid \mathcal{D})\, d\boldsymbol{\theta}\, d\boldsymbol{\beta}\, d\sigma$ where $p(y_j^* \mid \mathbf{u}_{1:j}^*, \boldsymbol{\theta}, \boldsymbol{\beta}, \sigma, \mathcal{D})$ $= \mathcal{N}(\tilde{h}(t_j, \mathbf{u}_{1:j}^*; \boldsymbol{\theta}, \boldsymbol{\beta}, \sigma), \tilde{k}(\mathbf{x}_j^*, \mathbf{x}_j^*; \boldsymbol{\beta}, \sigma) + \sigma^2)$ Refer to Eq. (3.12)

3.3.2.2 Sampling Posterior and Posterior Predictive Distributions

Computing the joint posterior distribution of all unknown parameters is often analytically intractable. Therefore, obtaining the posterior predictive distribution analytically is also not possible. Obtaining these distributions involves computing multi-dimensional integrals that are intractable. Simulation-based approaches can be used to generate samples from the target distribution (Bishop 2006). These include rejection sampling, importance sampling, Markov chain Monte Carlo (MCMC) sampling, and Transitional Markov chain Monte Carlo (TMCMC) sampling. In this paper, TMCMC sampling is used to sample from the joint posterior distribution of all unknown parameters. The TMCMC algorithm is very flexible, easy to implement, and applicable in general settings. TMCMC sampling is also inherently parallel. So, it can be used to perform model calibration of computationally expensive mathematical models using high-performance computing resources. Refer to (Ching and Chen 2007; Minson et al. 2013) for the theory behind the TMCMC algorithm and refer to Table 2 of (Ramancha et al. 2022) for the TMCMC algorithm used in this paper.

Sampling of the joint posterior $p\left(\boldsymbol{\theta},\boldsymbol{\beta},\sigma \mid \mathbf{u}_{1:N},\mathbf{y}_{1:N}\right)$ and posterior predictive $p\left(y_j^* \mid \mathbf{u}_{1:j}^*,\mathcal{D}\right)$ distributions for the case of the measurement equation with delta term is presented in this section. This can be adapted accordingly for the case of the measurement equation without the delta term. Let $\left\{\boldsymbol{\theta}^{(i)},\boldsymbol{\beta}^{(i)},\sigma^{(i)}\right\}_{i=1:N_p}$ be the samples of the joint posterior distribution $p\left(\boldsymbol{\theta},\boldsymbol{\beta},\sigma \mid \mathbf{u}_{1:N},\mathbf{y}_{1:N}\right)$ generated by any simulation-based approach, where N_p denotes the number of samples. Thus, $\left\{\boldsymbol{\theta}^{(i)}\right\}_{i=1:N_p}$ are the samples of the posterior distribution

$p\left(\boldsymbol{\theta} \mid \mathbf{u}_{1:N}, \mathbf{y}_{1:N}\right)$. The posterior predictive distribution shown in Eq. (3.10) can be approximated using Monte Carlo integration as

$$p\left(y_j^* \mid \mathbf{u}_{1:j}^*, \mathcal{D}\right) \approx \frac{1}{N_p} \sum_{i=1}^{N_p} p\left(y_j^* \mid \mathbf{u}_{1:j}^*, \boldsymbol{\theta}^{(i)}, \boldsymbol{\beta}^{(i)}, \sigma^{(i)}, \mathcal{D}\right) \tag{3.16}$$

Using Eq. (3.12), Eq. (3.16) reduces to

$$p\left(y_j^* \mid \mathbf{u}_{1:j}^*, \mathcal{D}\right) \approx \frac{1}{N_p} \sum_{i=1}^{N_p} \mathcal{N}\left(\tilde{h}\left(t_j, \mathbf{u}_{1:j}^*; \boldsymbol{\theta}^{(i)}, \boldsymbol{\beta}^{(i)}, \sigma^{(i)}\right), \tilde{k}\left(\mathbf{x}_j^*, \mathbf{x}_j^*; \boldsymbol{\beta}^{(i)}, \sigma^{(i)}\right) + \left(\sigma^{(i)}\right)^2\right) \tag{3.17}$$

Eq. (3.17) is a Gaussian mixture model of N_p components with equal weights. Thus, sampling from the Monte Carlo approximated posterior predictive distribution is the same as sampling from the Gaussian mixture model. Sampling from a mixture distribution is well established in the literature.

3.3.3 Multi-Output Measurement Channels

The model calibration methodology shown until now in this Section 3.3 focused on a single output measurement channel, i.e., $y_k \in \mathbb{R} \ \forall k$. However, in structural systems, there are typically multiple output measurement channels. Let $n_{\mathbf{y}} \in \mathbb{N}$ be the number of output measurement channels and $\mathbf{y}_k \in \mathbb{R}^{n_{\mathbf{y}}}$ be the measured output at time step k. The measurement equation (with delta term) in Eq. (3.2) can be adapted for multi-output measurement channels as

$$\text{At time step } k: \quad \mathbf{y}_k = \underbrace{\mathbf{h}\left(t_k, \mathbf{u}_{1:k}; \boldsymbol{\theta}\right)}_{\text{mathematical model}} + \underbrace{\boldsymbol{\delta}\left(\mathbf{x}_k\right)}_{\text{delta}} + \underbrace{\mathbf{w}\left(t_k\right)}_{\text{error/ noise}} ; \quad k \in \left[1, 2, ..., N\right] \tag{3.18}$$

At each time step k, the measured output $\mathbf{y}_k = \begin{bmatrix} y_k^{(1)} & \cdots & y_k^{(n_y)} \end{bmatrix}^T \in \mathbb{R}^{n_{\mathbf{y}}}$ is expressed as the summation of the model response

$\mathbf{h}\left(t_k,\mathbf{u}_{1:k};\boldsymbol{\theta}\right)=\left[\begin{array}{ccc} h^{(1)}\left(t_k,\mathbf{u}_{1:k};\boldsymbol{\theta}\right) & \cdots & h^{(n_y)}\left(t_k,\mathbf{u}_{1:k};\boldsymbol{\theta}\right)\end{array}\right]^T\in\mathbb{R}^{n_\mathbf{y}}$, delta term $\boldsymbol{\delta}\left(\mathbf{x}_k\right)=\left[\begin{array}{ccc}\delta^{(1)}\left(\mathbf{x}_k\right) & \cdots & \delta^{(n_y)}\left(\mathbf{x}_k\right)\end{array}\right]^T\in\mathbb{R}^{n_\mathbf{y}}$, and an error/noise term $\mathbf{w}\left(t_k\right)=\left[\begin{array}{ccc} w^{(1)}\left(t_k\right) & \cdots & w^{(n_y)}\left(t_k\right)\end{array}\right]^T\in\mathbb{R}^{n_\mathbf{y}}$. The superscript $\left(j\right)$ indicates the measurement channel j. Note that measurement input $\left\{\mathbf{u}_k\in\mathbb{R}^{n_\mathbf{u}},\, k=1{:}\,N\right\}$ can also be a multi-variable (vector) excitation (i.e., $n_\mathbf{u}\geq 1$). In this paper, the noise term $\mathbf{w}\left(t_k\right)$ is modeled as a Gaussian white noise vector with statistically independent components (i.e., statistical independence across measurement channels). Thus,

$$\mathbf{w}\left(t_k\right)\sim\mathcal{N}\left(\underset{n_\mathbf{y}\times 1}{\mathbf{0}}\,,\mathbf{R}=\left(\begin{array}{cccc}\sigma_1^2 & 0 & \cdots & 0\\ 0 & \sigma_2^2 & \cdots & 0\\ \vdots & \vdots & \ddots & \vdots\\ 0 & 0 & \cdots & \sigma_{n_\mathbf{y}}^2\end{array}\right)_{n_\mathbf{y}\times n_\mathbf{y}}\right) \tag{3.19}$$

where σ_j^2 denotes the variance of the measurement noise process corresponding to the $j-th$ measurement channel. Following the KOH approach, the delta term is modeled as a zero-mean vector-valued Gaussian process $\boldsymbol{\delta}\left(\mathbf{x}\right)\sim\mathcal{GP}\left(\mathbf{0},\mathbf{k}\left(\mathbf{x},\mathbf{x}';\boldsymbol{\beta}\right)\right)$, where $\mathbf{k}\left(\mathbf{x},\mathbf{x}';\boldsymbol{\beta}\right)=E\left[\boldsymbol{\delta}\left(\mathbf{x}\right)\boldsymbol{\delta}\left(\mathbf{x}'\right)^T\right]\in\mathbb{R}^{n_\mathbf{y}\times n_\mathbf{y}}$ is a matrix-valued covariance function given by

$$\mathbf{k}\left(\mathbf{x},\mathbf{x}';\boldsymbol{\beta}\right)=\left(\begin{array}{ccc}k^{(1,1)}\left(\mathbf{x},\mathbf{x}'\right) & \cdots & k^{(1,n_\mathbf{y})}\left(\mathbf{x},\mathbf{x}'\right)\\ \vdots & \ddots & \vdots\\ k^{(n_\mathbf{y},1)}\left(\mathbf{x},\mathbf{x}'\right) & \cdots & k^{(n_\mathbf{y},n_\mathbf{y})}\left(\mathbf{x},\mathbf{x}'\right)\end{array}\right)\in\mathbb{R}^{n_\mathbf{y}\times n_\mathbf{y}} \tag{3.20}$$

where $k^{(j,j)}(\mathbf{x},\mathbf{x}')$ is the autocovariance function of $\delta^{(j)}(\mathbf{x})$ and $k^{(j,l)}(\mathbf{x},\mathbf{x}')$, $j \neq l$ is the cross-covariance function between $\delta^{(j)}(\mathbf{x})$ and $\delta^{(l)}(\mathbf{x}')$. Estimating physical parameters described in Section 3.3.2 can now be adapted accordingly for the case of multi-output measurement channels.

3.4 Modeling the Delta Term in Linear Dynamic Systems

First consider the case of single output measurement channel; the delta term in Eq. (3.2) is modeled as a zero-mean Gaussian process $\delta(\mathbf{x}) \sim \mathcal{GP}(0, k(\mathbf{x},\mathbf{x}';\boldsymbol{\beta}))$. Ideally, at each time step k, the input of the delta process $\mathbf{x}_k$ should be the same as the input $(t_k, \mathbf{u}_{1:k})$ to the mathematical model of the dynamic system, i.e., $\mathbf{x}_k = \left[t_k, \mathbf{u}_{1:k}{}^T\right]^T \in \mathbb{R}^{n_\mathbf{u}k+1}$. In such a case, the dimension of the input $\mathbf{x}_k$ $(= n_\mathbf{u}k+1)$) of the delta process grows linearly with the time step k. This is very difficult, if not impossible, to handle when the delta process is modeled using a Gaussian process. For analytical and therefore computational tractability purposes, the input size of the delta process should be kept constant. In this paper, only time is considered as the input of the delta process, i.e., $\mathbf{x}_k = [t_k]$. A covariance function based on the theory of random vibrations is proposed to model the covariance kernel $k(t,t';\boldsymbol{\beta})$ for accurately capturing the model discrepancy time history using the delta process $\delta(t)$. True model discrepancy time history is defined as the error between the response of the true system and the mathematical model parameterized with the true parameter values (see Section 3.5 for more details).

Consider the following stationary covariance function from the theory of random vibrations:

$$k_{\text{SDOF}}\left(t,t';\boldsymbol{\beta}\right)=\underbrace{\frac{\pi\phi_0^{GP}}{2\xi^{GP}\left(\omega_0^{GP}\right)^3}}_{=\nu^{GP}}e^{-\xi^{GP}\omega_0^{GP}\left|t-t'\right|}\left[\cos\left(\omega_D^{GP}\left|t-t'\right|\right)+\frac{\xi^{GP}}{\sqrt{1-\left(\xi^{GP}\right)^2}}\sin\left(\omega_D^{GP}\left|t-t'\right|\right)\right] \tag{3.21}$$

with $\omega_D^{GP}=\omega_0^{GP}\sqrt{1-\left(\xi^{GP}\right)^2}$

The parameters of the covariance kernel $k_{\text{SDOF}}\left(t,t';\boldsymbol{\beta}\right)$ are $\boldsymbol{\beta}=\left[\nu^{GP},\omega_0^{GP},\xi^{GP}\right]^T\in\mathbb{R}^3$. This covariance function has the following power spectral density:

$$\phi_{\text{SDOF}}\left(\omega;\boldsymbol{\beta}\right)=\frac{\phi_0^{GP}}{\left[\left(\left(\omega_0^{GP}\right)^2-\omega^2\right)^2+4\left(\xi^{GP}\right)^2\left(\omega_0^{GP}\right)^2\omega^2\right]} \tag{3.22}$$

Note that the covariance function and power spectral density of a stationary random process form a Fourier transform pair (Lutes and Sarkani 2004). Knowledge of the power spectral density and knowledge of the stationary covariance function are equivalent since one can be deduced from the other via the Wiener-Khinchin theorem. In the context of structural dynamics, the power spectral density is a more intuitive and insightful description of the random process than the covariance function. In random vibrations, this covariance function – power spectral density pair characterizes the relative displacement response of a linear elastic SDOF system subjected to white noise excitation after the response has reached stationarity. The reasons for using this kernel over the standard kernels used in Gaussian process literature are discussed in Remark 3.

A schematic representation of the power spectral density (Eq. (3.22)) and covariance kernel (Eq. (3.21)) is shown in Figure 3.1a and Figure 3.1b, respectively. Both plots are only shown on the positive axis as the power spectral density and covariance kernel are symmetric about the origin. The parameters ν^{GP} and ω_0^{GP} represent the variance (or mean-square value)

and predominant frequency of the underlying random process. The full width of the power spectral density at half maximum height is given by $2\xi^{GP}\omega_0^{GP}$ (Figure 3.1a). The hyperparameter $\xi^{GP} \in (0,1)$ controls the bandwidth of the underlying random process, with a small value of ξ^{GP} representing a narrowband process and a large value of ξ^{GP} representing a broadband process. As ξ^{GP} approaches zero, the covariance function reduces to $v^{GP}\cos\left(\omega_0^{GP}|t-t'|\right)$ and the underlying random process is periodic with frequency ω_0^{GP} and variance v^{GP} (i.e., single random harmonic component).

Figure 3.2 shows the power spectral density, covariance function, and a realization of the random process for different values of v^{GP}, ω_0^{GP}, and ξ^{GP}. With a very small value of ξ^{GP} in Figure 3.2b, the random process realization is quasi-periodic. An increase in ξ^{GP} from Figure 3.2a to Figure 3.2d causes an increase in bandwidth of the power spectral density which results in a realization that is more irregular (Figure 3.2d) as it contains more random harmonic components. An increase in v^{GP} from Figure 3.2a to Figure 3.2c results in a higher amplitude realization of the random process as v^{GP} controls the variance of the underlying process. The physical interpretation of the hyperparameters v^{GP}, ω_0^{GP}, and ξ^{GP} is extremely useful to set their prior distribution in Bayesian calibration. Also, the calibrated values of the hyperparameters can provide insights into the sources and level of model form uncertainty. The covariance function $k_{\text{SDOF}}(t,t';\boldsymbol{\beta})$ can be used to model any narrowband or broadband stationary process with a single predominant frequency.

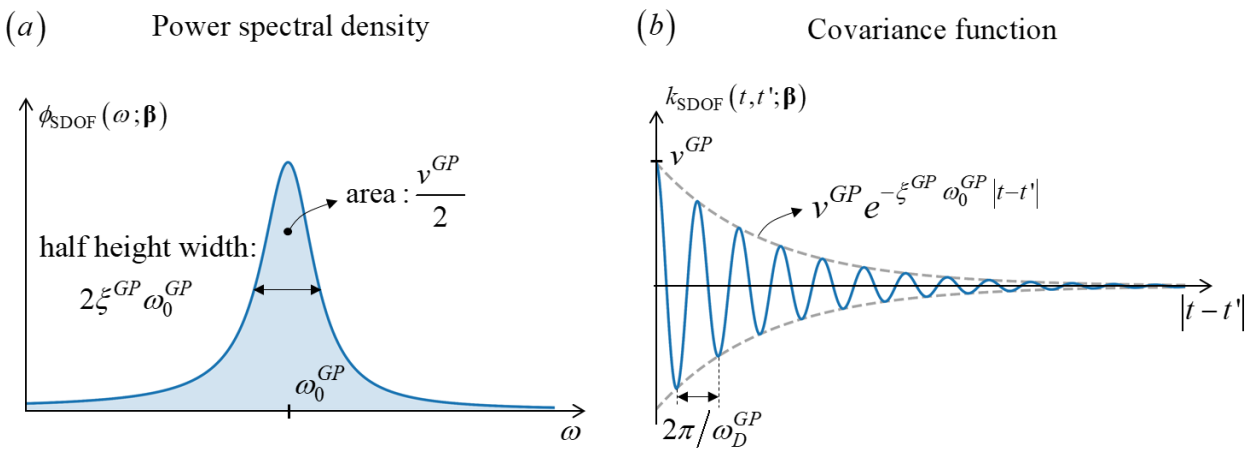

Figure 3.1: Schematic representation of (a) power spectral density (Eq. (3.22)) and (b) covariance function (Eq. (3.21))

Remark 1: the rationale behind using the covariance function $k_{\text{SDOF}}(t,t';\boldsymbol{\beta})$

The kernel $k_{\text{SDOF}}(t,t';\boldsymbol{\beta})$ is the covariance function of the displacement response of an SDOF system (with natural frequency ω_0^{GP} and damping ratio ξ^{GP}) subjected to white noise (of mean square ϕ_0^{GP}) base excitation (Lutes and Sarkani 2004). The idea is to consider the model discrepancy time history as an output response of a fictitious linear dynamic system excited by a fictitious stochastic excitation. The simplest stochastic excitation is a zero-mean Gaussian white noise and it allows for the computation of the covariance function of the response of any linear dynamic system in closed form. Also, the output response of any linear dynamic system subjected to a zero-mean Gaussian white noise is a zero-mean Gaussian process. This perfectly aligns with the KOH approach since it also models the delta process using a zero-mean Gaussian process. In summary, modeling the delta process as a zero-mean Gaussian process with the kernel given in Eq. (3.21) is equivalent to modeling the delta process as an output response of a fictitious SDOF system (with natural frequency ω_0^{GP} and damping ratio ξ^{GP}) subjected to a fictitious zero-mean Gaussian white noise (of mean square ϕ_0^{GP}) base excitation (acceleration).

The kernel $k_{\text{SDOF}}(t,t';\boldsymbol{\beta})$ can be used if the true model discrepancy is known/believed/assumed to be a stationary process (narrowband or broadband) with a single predominant frequency. In linear Multi-DOF (MDOF) systems, the output responses are usually characterized by multiple dominant frequencies (corresponding to the natural frequencies of vibration modes contributing significantly to the output responses). Hence, it can be argued that the model discrepancy time histories in such systems can also contain multiple dominant frequencies. Two different approaches to obtain a covariance function appropriate to model stationary processes with multiple dominant frequencies are presented next. They are referred to as the "MDOF covariance function" approach and the "mixture of SDOF covariance functions" approach, respectively. The single output measurement channel case is considered in Section 3.4.1 to introduce these two approaches and then extended for the multiple-output measurement channels case in Section 3.4.2.

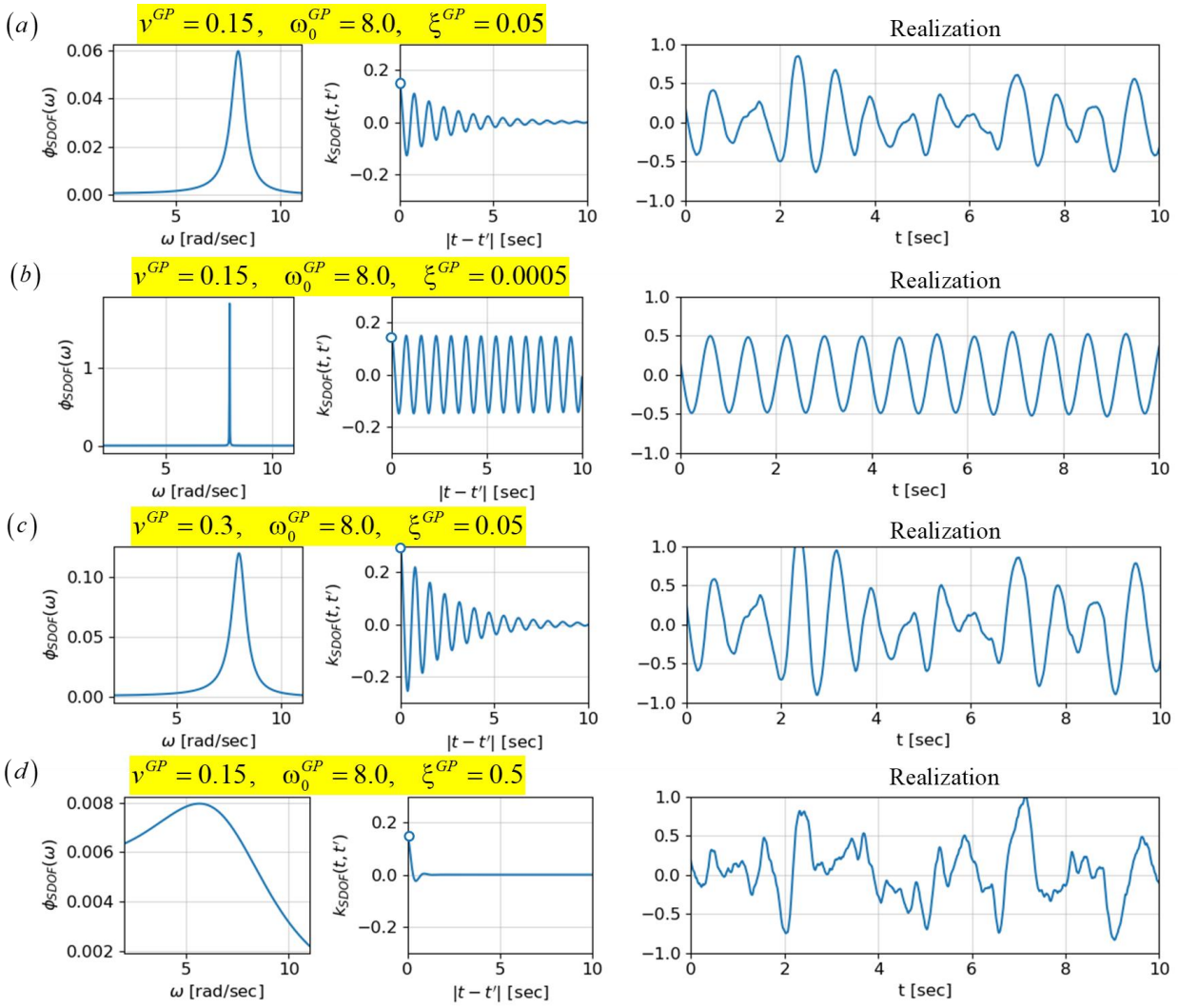

Figure 3.2: Power spectral density, covariance function, and a realization of the random process for different values of ν^{GP}, ω_0^{GP}, and ξ^{GP}.

3.4.1 Single Output Measurement Channel

3.4.1.1 MDOF Covariance Function Approach

This approach is based on "Remark 1: the rationale behind using the covariance function $k_{\text{SDOF}}(t,t';\boldsymbol{\beta})$". The idea is to consider the model discrepancy time history (arising in MDOF systems) as an output response of a fictitious MDOF system subjected to a fictitious excitation. There exist numerous possible choices to construct a fictitious MDOF system for this purpose.

The first thought that comes to mind is to assume the fictitious MDOF system to be the mathematical model h (of the dynamic system to be calibrated) with fictitious parameterization $\boldsymbol{\theta}^{GP}$. That is, the fictitious MDOF system is assumed to have the same geometric and kinematic constraints as the mathematical model h. Regarding the fictitious excitation, we chose a univariate zero-mean Gaussian white noise excitation herein for the reasons mentioned at the end of this subsection. These assumptions may be too restrictive and limit the subset of stationary processes that can be represented by this approach – a significant limitation (see Remark 2 in next section). In summary, the model discrepancy time history in this approach is assumed an output response of a mathematical model h with fictitious parameterizations $\boldsymbol{\theta}^{GP}$ excited by a fictitious univariate zero-mean Gaussian white noise. The parameters $\boldsymbol{\theta}$ of the mathematical model h of the actual dynamic system considered here and parameters $\boldsymbol{\theta}^{GP}$ of the fictitious mathematical model are distinguished using the superscript GP.

Let $k_{\text{MDOF}}\left(t,t';\boldsymbol{\beta}\right)$ denote the covariance function of the displacement response at the DOF corresponding to the output measurement channel of the mathematical model h with fictitious parameterizations $\boldsymbol{\theta}^{GP}$ and excited by a fictitious univariate zero-mean Gaussian white noise (of mean square ϕ_0^{GP}) forcing function. The hyperparameters of the covariance function $k_{\text{MDOF}}\left(t,t';\boldsymbol{\beta}\right)$ are $\boldsymbol{\beta}=\left[\phi_0^{GP},\left(\boldsymbol{\theta}^{GP}\right)^T\right]^T\in\mathbb{R}^{n_{\boldsymbol{\theta}}+1}$. The power spectral density matrix and auto/cross-correlation matrix of the displacement responses at all degrees of freedom of an MDOF system subjected to white noise excitation can be obtained in closed-form and are presented in Appendix A.

The covariance function $k_{\text{MDOF}}(t,t';\boldsymbol{\beta})$ is the diagonal term (at the DOF corresponding to the single output measurement channel) of the auto/cross-correlation matrix. $k_{\text{MDOF}}(t,t';\boldsymbol{\beta})$ is used to model the kernel of the delta process in the measurement equation.

In summary, modeling the delta process as a zero-mean Gaussian process with the kernel $k_{\text{MDOF}}(t,t';\boldsymbol{\beta})$ is equivalent to modeling the delta process as an output response of a fictitious mathematical model h (i.e., with fictitious parameterizations $\boldsymbol{\theta}^{GP}$) subjected to a fictitious univariate zero-mean Gaussian white noise (of mean square ϕ_0^{GP}) base excitation.

Note that the fictitious excitation used in this paper is taken as a univariate zero-mean Gaussian white noise base excitation so that it is feasible to compute in closed form the power spectral density matrix and auto/cross-correlation matrix of the output responses of an MDOF system (Appendix A). In addition, the illustration examples (Section 3.5 and 3.6) considered in this paper are characterized by a univariate excitation. However, for the case in which the actual system is subjected to multiple excitations (e.g., three-component earthquake base excitation), this approach can be directly applied/adapted by considering a multi-variate fictitious excitation (e.g., set of statistically independent white-noise processes). Moreover, other forms of fictitious excitations (including non-white excitations, but for which closed form solutions may not be available) can also be considered in this approach. Section 3.4.1.2 presents a more general approach which does not need any assumptions on the fictitious MDOF system or on the fictitious input excitation. The approach presented in Section 3.4.1.2 is also directly applicable to the case of multiple excitations.

3.4.1.2 Mixture of SDOF Covariance Functions Approach

The covariance function $k_{\text{SDOF}}(t,t';\boldsymbol{\beta})$ – power spectral density $\phi_{\text{SDOF}}(\omega;\boldsymbol{\beta})$ pair described earlier is only ideal to model stationary processes with a single dominant frequency. However, a mixture of power spectral densities $\phi_{\text{SDOF}}(\omega;\boldsymbol{\beta}_i)$ with different hyperparameters $\boldsymbol{\beta}_i$ can be used to model stationary processes with multiple dominant frequencies (Shen 2019; Wilson and Adams 2013). Let $\phi_{\text{Mix-SDOF}}(\omega;\boldsymbol{\beta})$ denote a mixture power spectral density with $m \in \mathbb{N}$ components and $k_{\text{Mix-SDOF}}(t,t';\boldsymbol{\beta})$ be its Fourier dual (inverse Fourier transform), then

$$\begin{aligned} \phi_{\text{Mix-SDOF}}(\omega;\boldsymbol{\beta}) &= \sum_{i=1}^{m} \phi_{\text{SDOF}}(\omega;\boldsymbol{\beta}_i) \\ k_{\text{Mix-SDOF}}(t,t';\boldsymbol{\beta}) &= \sum_{i=1}^{m} k_{\text{SDOF}}(t,t';\boldsymbol{\beta}_i) \end{aligned} \tag{3.23}$$

where $\boldsymbol{\beta}_i = \left[v_i^{GP}, \omega_{0,i}^{GP}, \xi_i^{GP} \right]^T \in \mathbb{R}^3$ and $\boldsymbol{\beta} = \left[\boldsymbol{\beta}_1^T, \boldsymbol{\beta}_2^T, \ldots, \boldsymbol{\beta}_m^T \right]^T \in \mathbb{R}^{3m}$. The hyperparameter v_i^{GP} denotes the variance of component i (also indicates the relative contribution of component i to the total variance of the underlying delta process), $\omega_{0,i}^{GP}$ denotes the dominant frequency of component i, and ξ_i^{GP} controls the bandwidth of component i. The mixture covariance function $k_{\text{Mix-SDOF}}(t,t';\boldsymbol{\beta})$ can be used to model the kernel of the delta process $\delta(t)$ if the model discrepancy time history is known/believed/assumed to contain m dominant frequencies. Besides, the mixture power spectral density $\phi_{\text{Mix-SDOF}}(\omega;\boldsymbol{\beta})$ can approximate the power spectral density of any stationary process given enough mixture components (Wilson and Adams 2013).

Recall that $k_{\text{SDOF}}(t,t';\boldsymbol{\beta}_i)$ is the covariance function of the displacement response of an SDOF system subjected to white noise excitation. Thus, $k_{\text{Mix-SDOF}}(t,t';\boldsymbol{\beta})$ is the covariance

function of the sum of statistically independent displacement responses of multiple white noise excited SDOF systems. This comes from the fact that the covariance function of the sum of statistically independent random processes is the sum of the covariance functions of the individual random process.

Note that the output response of structural systems is typically dominated by a few modes. Hence, it is reasonable to assume that the true model discrepancy time history arising in MDOF systems contains few dominant frequencies as well. Based on this analogy, only a relatively small number of mixture components can be used to model the kernel of the delta process to accurately capture the true model discrepancy time history arising in most structural systems. Thus, we propose that m (number of mixture components of the mixture covariance function) be the same as the number of modes needed to typically characterize the output response of the system at hand.

A schematic representation of a mixture power spectral density and mixture covariance function with 3 mixture components is shown in Figure 3.3a and Figure 3.3b, respectively.

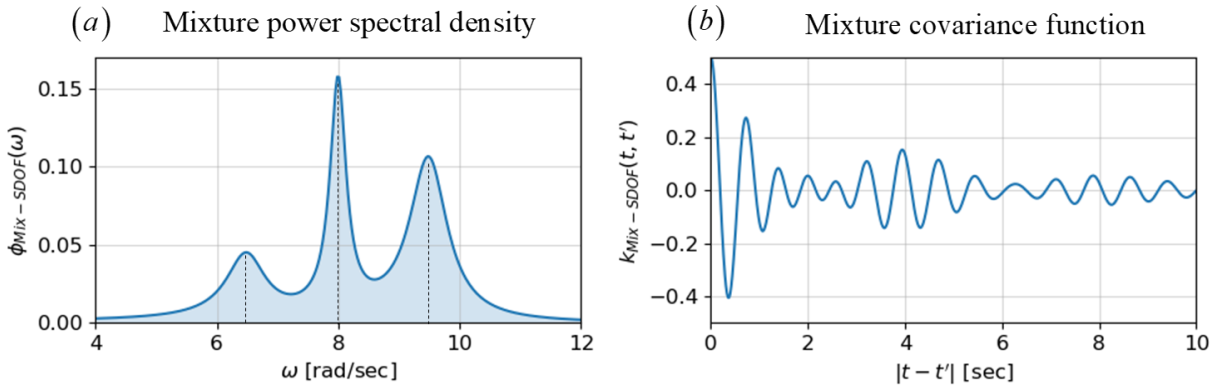

Figure 3.3: Schematic representation of (a) mixture power spectral density and (b) mixture covariance function defined in Eq. (3.23) with 3 mixture components

Remark 2: Comparison of $k_{\text{Mix-SDOF}}(t,t';\boldsymbol{\beta})$ and $k_{\text{MDOF}}(t,t';\boldsymbol{\beta})$ covariance functions

The geometric and kinematic constraints used to construct the covariance function $k_{\text{MDOF}}(t,t';\boldsymbol{\beta})$ limits the set of stationary processes that can be represented. While the covariance function $k_{\text{Mix-SDOF}}(t,t';\boldsymbol{\beta})$ has no such restrictions and can represent any stationary process (given enough mixture components). Thus, $k_{\text{Mix-SDOF}}(t,t';\boldsymbol{\beta})$ can represent a broader subset of stationary processes than the $k_{\text{MDOF}}(t,t';\boldsymbol{\beta})$ covariance function. Also, in contrast to the $k_{\text{MDOF}}(t,t';\boldsymbol{\beta})$ covariance function, the subset of stationary processes represented by $k_{\text{Mix-SDOF}}(t,t';\boldsymbol{\beta})$ can be enlarged by increasing the value of m (i.e., the number of mixture components). In fact, given enough mixture components, $k_{\text{Mix-SDOF}}(t,t';\boldsymbol{\beta})$ can represent any stationary process.

Remark 3: Standard vs random vibration based covariance kernel to model the delta term?

In the approach proposed in this paper, the power spectral density $k_{\text{SDOF}}(t,t';\boldsymbol{\beta})$ – covariance function $\phi_{\text{SDOF}}(\omega;\boldsymbol{\beta})$ pair is a building block used to construct the covariance kernel of the delta term to account for model form uncertainty arising in linear MDOF dynamic systems. The power spectral density of any response quantity of a linear dynamic system subjected to stochastic excitation typically looks like a mixture of bell-shaped functions (the location of each bell curve is around a significant mode of the system). If the input excitation is white noise, each bell-shaped function is of the form given by $\phi_{\text{SDOF}}(\omega;\boldsymbol{\beta})$.

The power spectral density of standard kernels, such as squared exponential kernel, are centered at zero. Thus, these standard kernels are not ideal for modeling response time histories (e.g., model discrepancy time histories) arising when dealing with linear dynamic systems since

their power spectral densities are centered around the dominant non-zero natural frequencies. In addition, unlike the mixture of SDOF covariance functions, the mixture of squared exponential kernels can only represent a small subset of possible stationary processes.

Unlike standard periodic kernels, $k_{\text{SDOF}}(t,t';\boldsymbol{\beta})$ has negative correlations. $k_{\text{SDOF}}(t,t';\boldsymbol{\beta})$ is also more apt to capture the correlation structure seen in the real world because it is rooted in a physical understanding of the system and thus has more structure than the standard periodic kernels. The parameters of $k_{\text{SDOF}}(t,t';\boldsymbol{\beta})$ have a physical meaning which is extremely useful to set their prior distribution. We believe that this random vibration-based covariance function $k_{\text{SDOF}}(t,t';\boldsymbol{\beta})$ will be a valuable addition to the existing set of standard kernels for Gaussian process regression which can be used to model any stationary processes (narrow or wide band) with a single dominant frequency and the mixture covariance function $k_{\text{Mix-SDOF}}(t,t';\boldsymbol{\beta})$ can be used to model any stationary process, including processes with multiple dominant/natural frequencies.

3.4.2 Multi-Output Measurement Channels

As described earlier, time t is considered as the input $\mathbf{x}$ of the delta vector process $\boldsymbol{\delta}(\mathbf{x})$. Thus, $\boldsymbol{\delta}(t) \sim \mathcal{GP}(\mathbf{0}, \mathbf{k}(t,t';\boldsymbol{\beta}))$. Knowledge about the cross-covariance function (across measurement channels) between $\delta^{(j)}(t)$ and $\delta^{(l)}(t)$, i.e., $k^{(j,l)}(t,t')$ $j \neq l$, is seldom available. The simplest approach is to model the delta random process corresponding to each measurement channel as statistically independent from the others and treat them separately. We have found that sufficiently accurate results are obtained with this assumption. Thus, the random processes

$\left\{\delta^{(j)}(t)\right\}$ and $\left\{\delta^{(l)}(t)\right\}$ are statistically independent for all $j \neq l$ (i.e., random variables $\delta^{(j)}(t)$ and $\delta^{(l)}(t')$ are statistically independent for all t, t' and for all $j \neq l$). This is equivalent to modeling the non-diagonal terms of the matrix $\mathbf{k}(t,t';\boldsymbol{\beta})$ as 0, i.e., $k^{(j,l)}(t,t') = 0, \forall\, j \neq l$. Thus,

$$\mathbf{k}(t,t';\boldsymbol{\beta}) = \begin{pmatrix} \ddots & & 0 \\ & k^{(j,j)}(t,t') & \\ 0 & & \ddots \end{pmatrix} \in \mathbb{R}^{n_{\mathbf{y}} \times n_{\mathbf{y}}} \tag{3.24}$$

If the output measurement channels are closely spaced, then it might be useful to model the cross-correlation between the delta processes corresponding to the output measurement channels. The Gaussian process framework can easily handle this (see Section 9.1 of (Rasmussen and Williams 2005)). However, this is beyond the scope of this paper.

3.4.2.1 MDOF Covariance Function Approach

The MDOF covariance approach presented in Section 3.4.1.1 is extended here for multiple output measurement channels. The matrix-valued covariance function constructed using this approach is referred to as $\mathbf{k}_{\text{MDOF}}(t,t';\boldsymbol{\beta})$. The $j-th$ diagonal element of the matrix $\mathbf{k}_{\text{MDOF}}(t,t';\boldsymbol{\beta})$ (shown in Eq. (3.24)) is modeled using $k_{\text{MDOF}}^{(j,j)}(t,t';\boldsymbol{\beta})$ where $k_{\text{MDOF}}^{(j,j)}(t,t';\boldsymbol{\beta})$ denotes the diagonal element, at the DOF corresponding to the $j-th$ measurement channel, of the auto/cross-correlation matrix shown in Appendix A. In this approach, the hyperparameters are $\boldsymbol{\beta} = \left[\phi_0^{GP}, \left(\boldsymbol{\theta}^{GP}\right)^T\right]^T \in \mathbb{R}^{n_{\boldsymbol{\theta}}+1}$.

3.4.2.2 Mixture of SDOF Covariance Functions Approach

The mixture of SDOF covariance functions approach presented in Section 3.4.1.2 is extended here for multiple output measurement channels. The matrix-valued covariance function constructed using this approach is referred to as $\mathbf{k}_{\text{Mix-SDOF}}(t,t';\boldsymbol{\beta})$. The diagonal elements of the matrix $\mathbf{k}_{\text{Mix-SDOF}}(t,t';\boldsymbol{\beta})$ (shown in Eq. (3.24)) are modeled as the mixture of SDOF covariance functions described in Section 3.4.1.2. Thus, the $j-th$ diagonal element of the matrix $\mathbf{k}(t,t';\boldsymbol{\beta})$ is defined by $k^{(j,j)}_{\text{Mix-SDOF}}\left(t,t';\boldsymbol{\beta}^{(j)}\right)$ where

$$k^{(j,j)}_{\text{Mix-SDOF}}\left(t,t';\boldsymbol{\beta}^{(j)}\right)=\sum_{i=1}^{m}k_{\text{SDOF}}\left(t,t';\boldsymbol{\beta}_i^{(j)}\right) \tag{3.25}$$

in which $\boldsymbol{\beta}_i^{(j)}==\left[\nu_i^{GP^{(j)}},\omega_{0,i}^{GP^{(j)}},\xi_i^{GP^{(j)}}\right]^T\in\mathbb{R}^3$ are the hyperparameters characterizing the $i-th$ component of the mixture. It is physically reasonable to assume the hyperparameters $\omega_{0,i}^{GP^{(j)}},\xi_i^{GP^{(j)}}$ of the $i-th$ component of the mixture to be the same for all output channels. In other words, the delta processes at different channels (i.e., $\delta^{(j)}(t),\ j=1:n_y$) are modeled as the sum of identical fictitious SDOF ($\omega_{0,i}^{GP},\xi_i^{GP};\ i=1:m$) responses but with different relative contributions ($\nu_i^{GP^{(j)}}$). Hence, $\boldsymbol{\beta}_i^{(j)}==\left[\nu_i^{GP^{(j)}},\omega_{0,i}^{GP},\xi_i^{GP}\right]^T\in\mathbb{R}^3$ (superscript (j) is dropped for $\omega_{0,i}^{GP}$ and ξ_i^{GP}). This assumption is motivated by the fact that, according to modal analysis, the response of any MDOF system at two different degrees of freedom can be written as the sum of responses of identical SDOF systems (i.e., with the same natural frequency and damping ratio) but with different relative contributions. If there are n_y measurement channels and m

components are used in the mixture, the size of the total hyperparameter vector $\boldsymbol{\beta}$ characterizing the matrix-valued covariance function $\mathbf{k}(t,t';\boldsymbol{\beta})$ is $\left(n_{\mathbf{y}}m+2m\right)$.

3.5 Illustration Example 1: Linear SDOF System

Consider a water tower structure subjected to wind excitation along one horizontal direction. The structure can be represented as an equivalent linear single-degree-of-freedom (SDOF) oscillator with appropriate mass, stiffness, and damping ratio. In this illustrative example, an SDOF system with mass $m^{\text{true}}=3630\,kN\cdot s^2/m$, stiffness $k^{\text{true}}=22\times10^4\,kN/m$, and damping ratio $\xi^{\text{true}}=0.10$ is assumed to perfectly represent the real system thus referred to as the true system. This true system has a natural period of 0.8sec. A different SDOF model, parameterized by an unknown mass m and stiffness k, and with the damping ratio $\xi^{\text{model}}=0.05$ is considered as the mathematical model h of the system. Thus, the unknown parameter vector is $\boldsymbol{\theta}=\left[m,k\right]^T$. Both m and k are parameters with physical meaning representing the effective mass and stiffness of the water tower structure, respectively. Note that in this illustration/application example, the modeling error is mimicked (represented) by the incorrect damping parameter value (damping is a prevalent source of modeling error in structural systems).

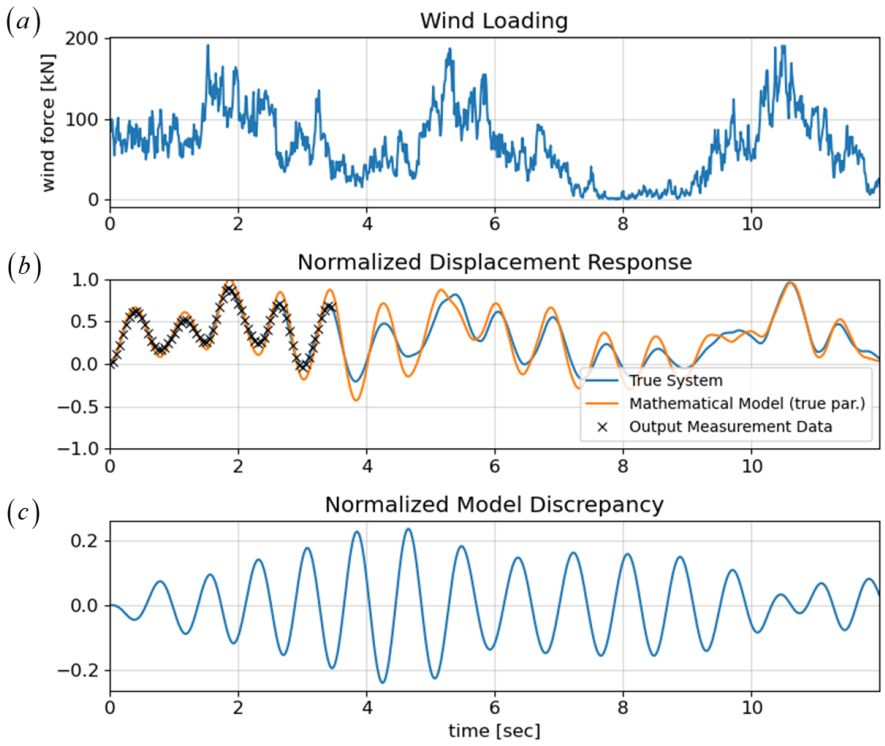

Figure 3.4: Loading, displacement, and model discrepancy time history of the linear SDOF illustrative example

The wind force time history shown in Figure 3.4a is simulated based on the Davenport wind velocity spectrum – velocity is converted to pressure using Bernoulli's principle and then to force by multiplying with the effective area of the structure. This wind force time history is assumed to represent the measured input time history $\mathbf{u}$. The displacement response time histories of the true system and the mathematical model parameterized with true parameter values (i.e. $\boldsymbol{\theta}^{\text{true}} = \left[m^{\text{true}}, k^{\text{true}} \right]^T$) subjected to the wind loading are shown in Figure 3.4b. The difference between these two responses represents the true model discrepancy time history and is shown in Figure 3.4c. All the time histories are normalized with respect to the maximum absolute displacement response of the mathematical model with true parameters. To simulate the output measurement data y, it is assumed that the displacement measurements are obtained every 0.05sec until 3.5sec. These measurements are obtained by polluting the true system

displacement response with Gaussian white noise of root mean square (RMS) 1.0mm to simulate the output measurement noise (see crosses in Figure 3.4b).

The output measurement noise and model form uncertainty are the only sources of uncertainty considered in this application example. Under this setting, the unknown physical parameters $\boldsymbol{\theta} = [m, k]^T$ will be correctly estimated when using the measurement equation with delta term (i.e., Eq. (3.2)), if the delta process $\delta(t)$ captures the true model discrepancy time history (Figure 3.4c) and the noise process $w(t)$ accounts for the added Gaussian white output noise of RMS 1.0mm.

3.5.1 Results and Discussions

This section shows and compares the model calibration and prediction results of the linear SDOF illustration example by considering the measurement equations without and with delta term. In the case of the measurement equation with delta term, the kernel of the delta process is modeled using the covariance function shown in Eq. (3.21). The unknown physical parameter vector is taken as $\boldsymbol{\theta} = [m, k]^T$.

3.5.1.1 Prior distribution of unknown physical parameters and hyperparameters

To construct the prior distribution $p(\boldsymbol{\theta})$, the physical parameters m and k are assumed statistically independent. This independent assumption is not necessary, if one has prior knowledge about the correlation of these physical parameters, it can be easily incorporated into the prior. $\mathcal{N}\left(0.76m^{\text{true}}, \left(0.38m^{\text{true}}\right)^2\right)$ and $\mathcal{N}\left(0.78k^{\text{true}}, \left(0.40k^{\text{true}}\right)^2\right)$ are selected as the prior for the physical parameters m and k, respectively. Since m and k are positive definite, both

the prior distributions are truncated at zero (see Figure 3.5 where the red line indicates the true parameter value).

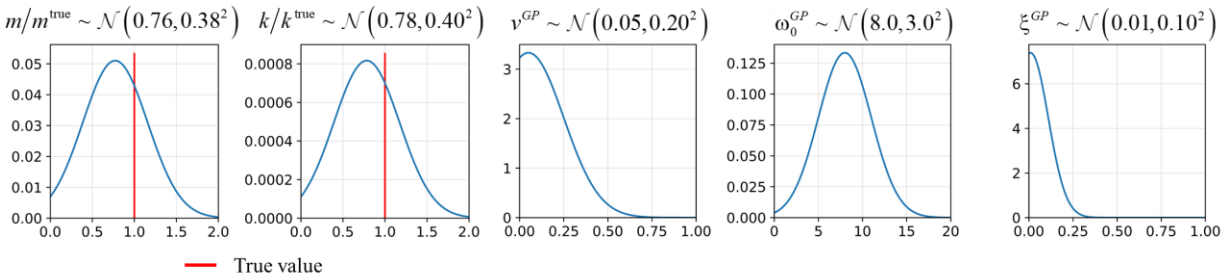

Figure 3.5: Prior distribution of unknown physical parameters and hyperparameters

For model calibration using the measurement equation without delta term, the noise process $w(t) \sim \mathcal{N}(0, \sigma^2)$ accounts for both model discrepancy and measurement noise. $\mathcal{N}(0, 1^2)$ truncated at zero is used as prior $p(\sigma)$. For model calibration using the measurement equation with delta term, the delta process $\delta(t) \sim \mathcal{GP}(0, k_{SDOF}(t, t'; \boldsymbol{\beta}))$ should ideally account for the model discrepancy while the noise process $w(t) \sim \mathcal{N}(0, \sigma^2)$ should account for the measurement noise. To construct the prior $p(\boldsymbol{\beta})$, statistical independence is assumed between parameters v^{GP}, ω_0^{GP}, and ξ^{GP}. $\mathcal{N}(0.05, 0.20^2)$, $\mathcal{N}(8.0, 3.0^2)$, and $\mathcal{N}(0.01, 0.10^2)$ distributions truncated at zero are assumed as prior distributions for v^{GP}, ω_0^{GP}, and ξ^{GP}, respectively (see Figure 3.5). $\mathcal{N}(0, 1^2)$ truncated at zero is used as prior $p(\sigma)$. Note that fully Bayesian approach requires careful consideration of prior knowledge of the hyperparameters.

3.5.1.2 Posterior distribution

The joint posterior distribution of all unknown parameters (defined in Section 3.3.2.1 – fully Bayesian approach) considering the measurement equation without and with delta term is

sampled using the TMCMC algorithm. 250 particles are used to approximate the joint posterior distribution of all unknown parameters in each case.

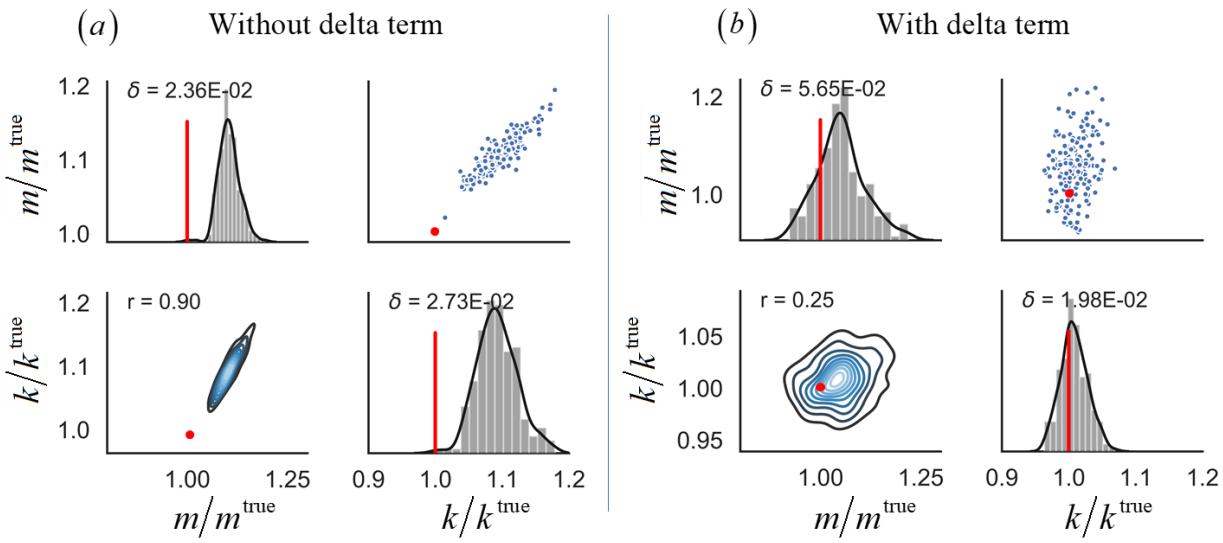

Figure 3.6: Pairs plot of physical parameters constructed from the posterior samples obtained using the measurement equation (a) without delta term and (b) with delta term (red lines and dots indicate true parameter values)

Figure 3.6a and Figure 3.6b show the "pairs plot" of the physical parameters $\boldsymbol{\theta} = [m, k]^T$ constructed from the posterior samples $\{\boldsymbol{\theta}^{(i)}\}_{i=1:250}$ obtained using the measurement equation without and with delta term, respectively. A pairs plot is a grid of scatter plots of pairs of parameters. The plots along the diagonal show the histograms and kernel density estimates of the marginal distributions and the red line indicates the true parameter value. The coefficient of variation (δ) conveys the sharpness (or width) of the marginal distributions, an indicator of the remaining estimation uncertainty after model calibration. The plots above the diagonal show the posterior samples in the space of each pair of parameters, the plots below the diagonal depict the contour plots of the corresponding bivariate kernel density estimates where r denotes the Pearson correlation coefficient, and the red dot indicates the true parameter values. In Figure 3.6a, the supports of the marginal posteriors of both parameters do not enclose the true parameter

values. Thus, model calibration performed using the measurement equation without delta term resulted in biased estimates of the physical parameters. On the other hand, the support of the marginal posterior of each parameter encloses the corresponding true parameter value in Figure 3.6b. Thus, adding the delta term in the measurement equation and modeling the kernel of the delta term using $k_{\mathrm{SDOF}}\left(t,t';\boldsymbol{\beta}\right)$ resulted in improved estimates of the physical parameters.

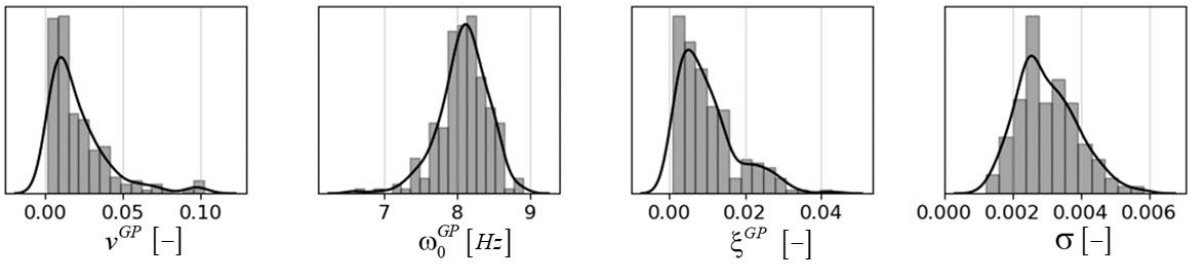

Figure 3.7: Posterior marginal distributions of hyperparameters for the case of model calibration with delta term

Figure 3.7 shows the posterior marginal distribution of all hyperparameters after model calibration with the delta term. When dealing with real-world structures with real measurement data, the calibrated values of the hyperparameters can provide insights into the sources and level of model form uncertainty. For example, the results presented in Figure 3.7 show that the predominant frequency of the model discrepancy time history, as indicated by maximum a posteriori (MAP) value of ω_0^{GP} approximately equal to 8.1 Hz, is slightly above the true natural frequency (7.85 Hz) of the SDOF system. They also indicate that the bandwidth of the model discrepancy time history is very narrow (MAP value of ξ^{GP} approximately equal to 0.5%) and the mean-square value of the normalized model discrepancy time history is 0.02 (MAP value of v^{GP}).

3.5.1.3 Model Response

The samples, $\left\{\boldsymbol{\theta}^{(i)}\right\}_{i=1:250}$, defining the posterior distribution of the unknown physical parameters $\boldsymbol{\theta}$, shown in Figure 3.6a and Figure 3.6b are propagated through the mathematical model h of the dynamic system (by using the same input excitation as the one used for model calibration, see Figure 3.4a) and the corresponding response time histories are shown in Figure 3.8a and Figure 3.8b, respectively. Each plot provides the true dynamic response (black line), output measurement data used for model calibration (black crosses), and the ensemble responses (corresponding to the samples $\left\{\boldsymbol{\theta}^{(i)}\right\}_{i=1:250}$) of the mathematical model (red lines). Note that the measurement data is only available until 3.5sec, however, the predictions are made for the entire 0-12sec range. Since model calibration, when performed using the measurement equation without delta term, resulted in biased estimates of the physical parameters (Figure 3.6a), the ensemble of model response time histories does not enclose the true response (Figure 3.8a). However, the ensemble of model predictions encloses the true response (Figure 3.8b) when model calibration is performed using the measurement equation with delta term.

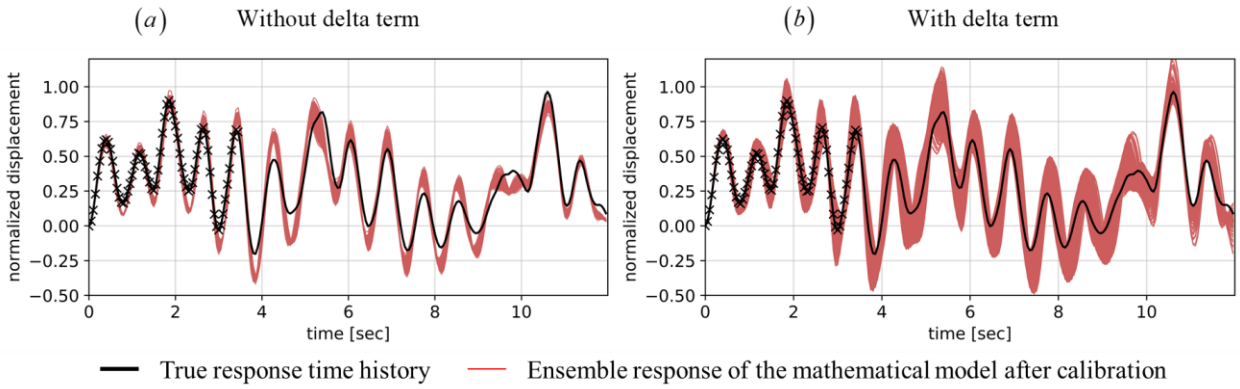

Figure 3.8: Model response time histories after model calibration performed using the measurement equation (a) without delta term and (b) with delta term

3.5.1.4 Posterior Predictive Distribution

The posterior predictive distribution $p\left(y_j^* \mid \mathbf{u}_{1:j}^*, \mathcal{D}\right)$, at discrete-time t_j from 0 to 12sec, is sampled and these ensemble response time histories (grey lines) are shown in Figure 3.9a and Figure 3.9b for the measurement equation without and with delta term, respectively. The posterior predictive distribution for each measurement equation is given in Table 3.1 and its sampling is described in Section 3.3.2.2. In Figure 3.9, the ensemble of predictive response time histories (grey lines) enclose the true response time history (black line) in both plots. This indicates that the Bayesian model calibration is doing its job in both cases. However, note that the predictions without the delta term are much more irregular than the predictions made with the delta term. This is a result of the additive white noise trying to capture the model discrepancy when there is no delta term. The realizations with the delta term are more representative of reality.

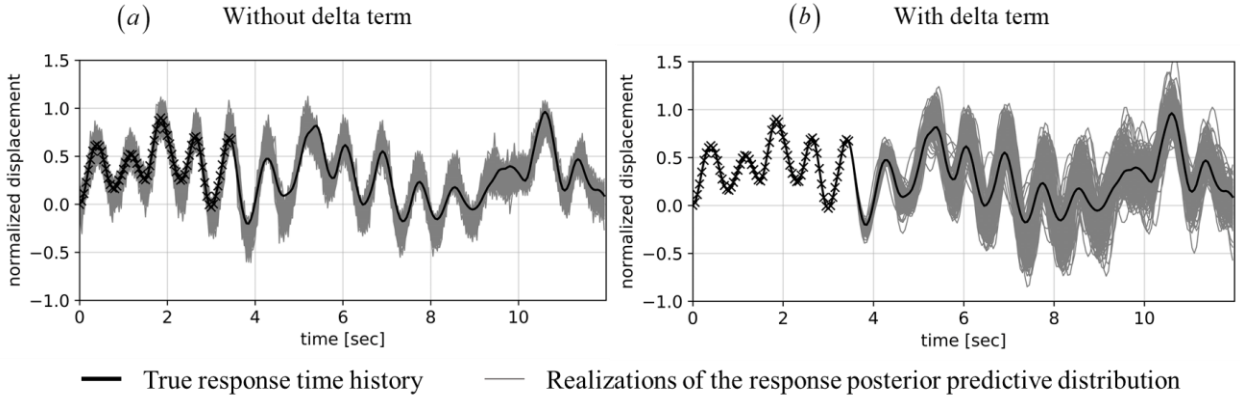

Figure 3.9: Realizations of the response posterior predictive distribution when model calibration is performed using the measurement equation (a) without delta term and (b) with delta term

3.5.1.5 Delta term

Figure 3.10 compares the true model discrepancy (black line) time history with the ensemble of predicted model discrepancy time histories (grey lines) for the case of model

calibration with delta term. The true model discrepancy is defined as the difference between the true response (i.e., response of the true dynamic system parameterized by $\boldsymbol{\theta}^{\text{true}}$) and the response of the mathematical model h parameterized by $\boldsymbol{\theta}^{\text{true}}$ - black line in Figure 3.10. The predicted model discrepancy is defined as the difference between the true response and mathematical model response parameterized by $\boldsymbol{\theta}^{(i)}$, where $\boldsymbol{\theta}^{(i)}$ denotes the i^{th} sample of the estimated posterior distribution $p\left(\boldsymbol{\theta} \mid \mathbf{u}_{1:N}, \mathbf{y}_{1:N}\right)$ - grey lines in Figure 3.10. All the time histories are normalized with the same criteria described in the beginning of Section 3.5. It can be observed that the ensemble of time histories of the predicted model discrepancy (which can be viewed as approximate posterior realizations of the delta process when the measurement noise is small relative to the measured response) enclose the true model discrepancy time history. Thus modeling the delta term with the covariance kernel $k_{\text{SDOF}}\left(t, t'; \boldsymbol{\beta}\right)$ allows the true model discrepancy to be captured well. Note that, in real world applications, one does not know the true response, hence such plots cannot be made to evaluate the working of the covariance kernel.

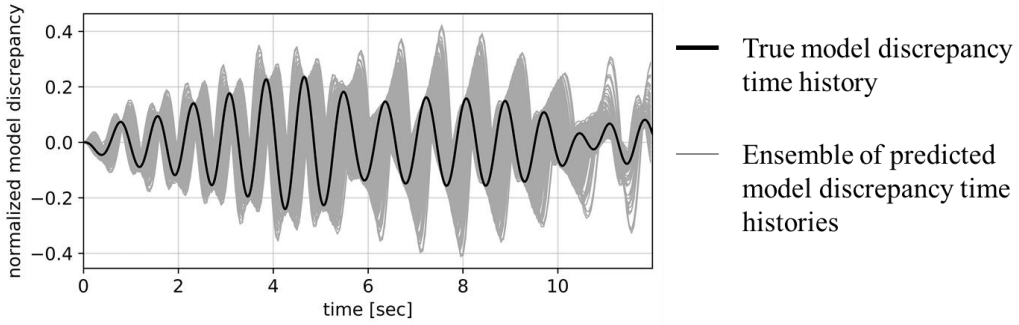

Figure 3.10: A comparison of the true and predicted model discrepancy time histories for the case of model calibration with delta term

3.5.1.6 Effect of the sampling rate of the measurement data on the posterior distribution

This section illustrates the effect of the sampling rate of the input-output measurement data on the posterior distribution of the unknown physical parameters. Three sampling rates (20

Hz, 25 Hz, 33.33 Hz) from 0. to 5.0 sec are considered for the input-output datasets, corresponding to sampling time steps of 0.05 sec, 0.04 sec and 0.03 sec, respectively.

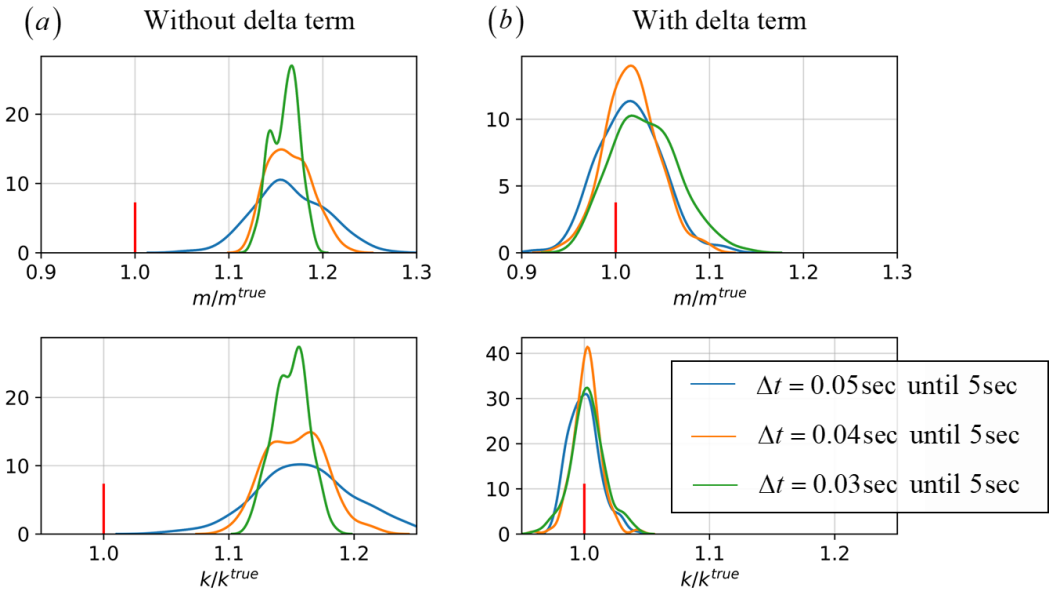

Figure 3.11: Effect of the sampling rate of the input-output measurement data on the posterior distribution of the unknown physical parameters (red line indicates the true parameter value)

Figure 3.11a and Figure 3.11b show the marginal posterior distributions of the physical parameters obtained when using the measurement model without and with delta term, respectively. Each plot shows the marginal kernel density estimate of the posterior distribution based on samples of the latter obtained from model calibration using each dataset considered in this section (and the red line represents the true parameter value). In the case of model calibration without delta term, as the sampling rate of the measurement data increases, the posterior is getting narrower at an incorrect parameter value for both parameters. On the other hand, in the case of model calibration with delta term, the posterior does not change much and its support encloses the true parameter value. Since increasing the sampling rate (beyond a certain level) adds no new information about the physical parameters, the posterior is expected to not change significantly as in the case of model calibration with delta term (see Figure 3.11b). Note

that in the case of model calibration without delta term, the posterior distribution gets narrower with the increase in sampling rate and would converge to a Dirac delta function at incorrect values of the physical parameters – a serious issue in the model calibration of systems under dynamic loading. This problem is eliminated by incorporating the delta term in the model calibration process.

3.5.1.7 Effect of the duration of the measurement data on the posterior distribution

This section illustrates the effect of the duration of the input-output measurement data on the posterior distribution of the unknown physical parameters. Three input-output measurement datasets are considered corresponding to a sampling frequency of 20Hz (time step of 0.05sec) for a duration of 3.5sec, 5.0sec, and 7.0sec. Figure 3.12a and Figure 3.12b show the marginal posterior distributions of the physical parameters obtained when using the measurement model without and with delta term, respectively. Each plot shows the marginal kernel density estimate of the posterior distribution using samples of the latter obtained from model calibration using each dataset considered in this section (and the red line represents the true parameter value). In the case of model calibration without delta term, as the duration of the measurement data increases, the mode of the posterior distribution (or maximum a posteriori estimate) is away from the true parameter value for both parameters (i.e., bias persists). On the other hand, in the case of model calibration with delta term, the posterior distribution is getting narrower and most importantly its support encloses the true parameter value. Since increasing the duration of the measurement data may contribute to an increase in information about the physical parameters, the posterior is expected to become narrower or not change significantly as in the case of model calibration with delta term (see Figure 3.12b).

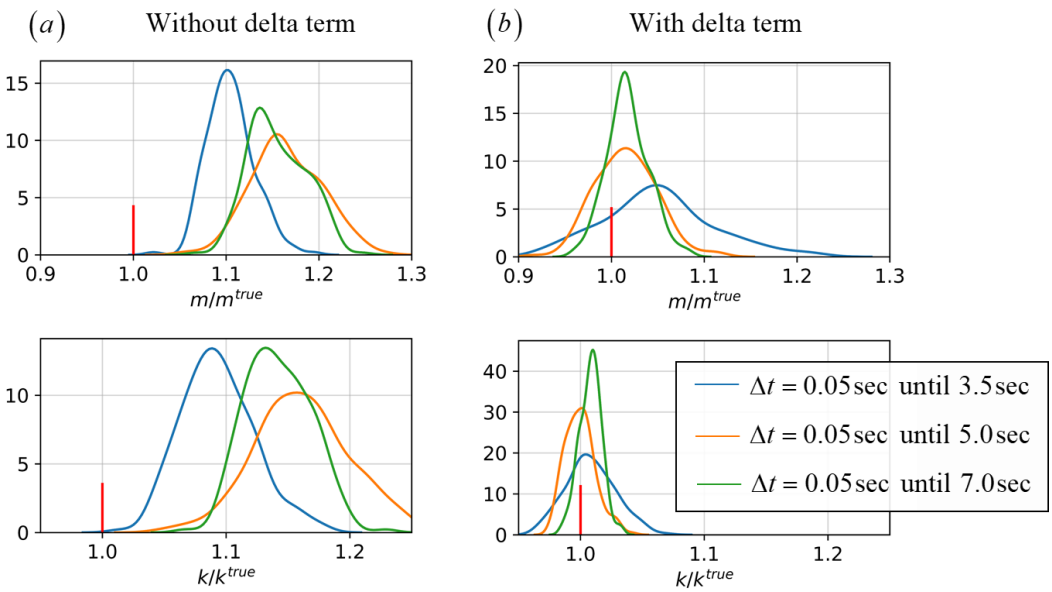

Figure 3.12: Effect of the duration of the input-output measurement data on the posterior distribution of the unknown physical parameters (red line indicates the true parameter value)

True system, true model discrepancy, and true parameter values do not exist when dealing with model calibration of real-world structures using real measurement data. Since this paper considers simulated measurement data, the underlying true model and true parameter values are known and help assess the working of the proposed approach. In a real-world situation, the best we can do is to compare the measurement data with an ensemble of posterior predictive responses (e.g., Figure 3.9 with the black line replaced by the measured response time history).

3.6 Illustration Example 2: Linear 2-DOF System

Consider a linear 2-DOF system (Figure 3.13a) subjected to earthquake base acceleration. In this system, two one-story structures with masses m_1 and m_2, story stiffnesses k_1 and k_2 are connected by a spring of stiffness k. The damping ratios are ξ_1 and ξ_2 for modes 1 and 2, respectively. The 2-DOF system with parameters $m_1 = m_2 = 46\ kN \cdot s^2/m$, $k_1^{\text{true}} = 17 \times 10^3\ kN/m$,

$k_2^{\text{true}} = 42\times10^3\, kN/m$, $k = 8.5\times10^3\, kN/m$, and $\xi_1 = \xi_2 = 0.05$ is considered as the true system which is used to simulate/generate the measurement data used for model calibration. The two natural frequencies (periods) of the system are $22.5\, rad/\text{sec}$ and $36.5\, rad/\text{sec}$ (0.28 *sec* and 0.17 *sec*).

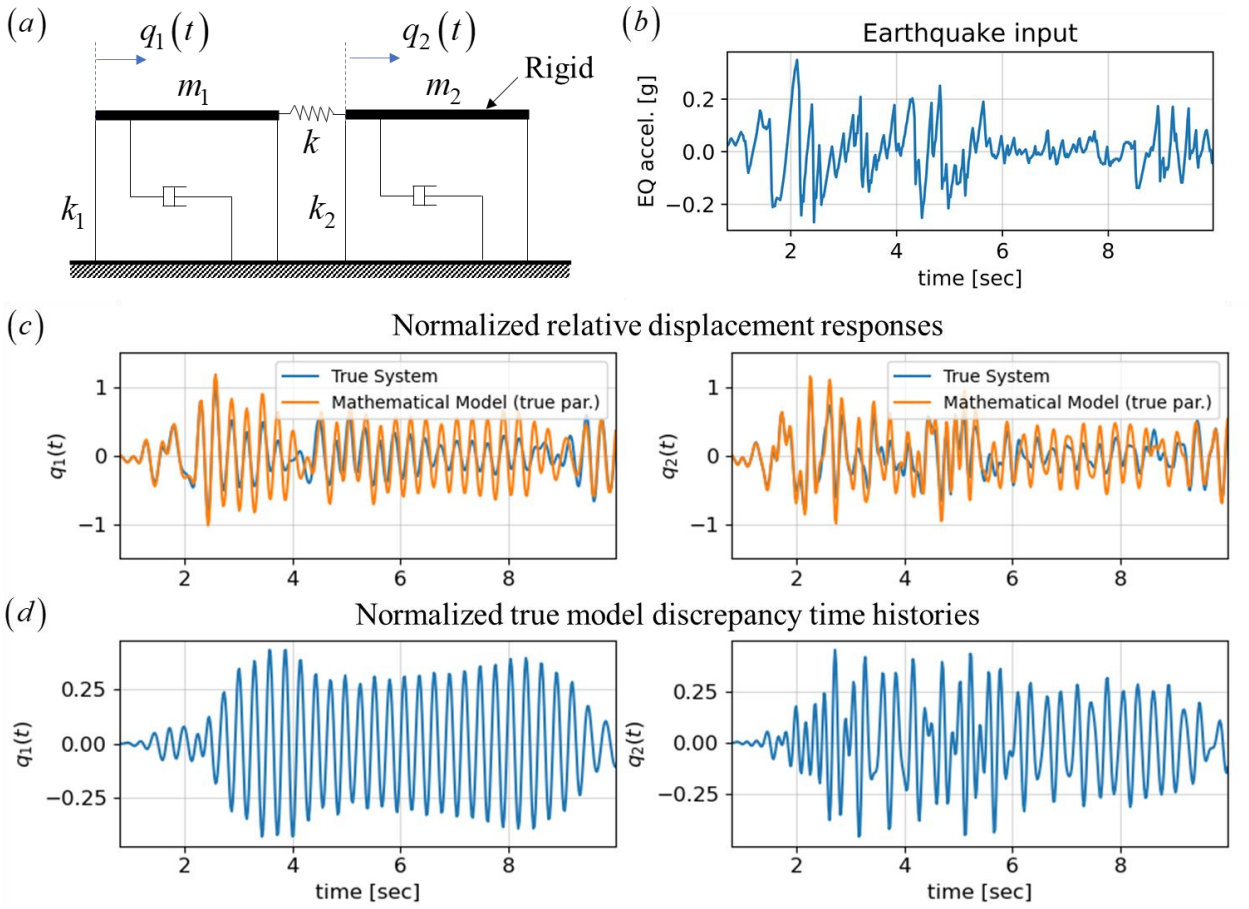

Figure 3.13: (a) 2-DOF system, (b) input earthquake excitation, (c) normalized relative displacement response time histories, and (d) normalized true model discrepancy time histories

In the mathematical model h of the system, the story stiffnesses k_1 and k_2 are considered unknown and need to be estimated using the measurement data. Thus, the unknown parameter vector is $\boldsymbol{\theta} = [k_1, k_2]^T$. In the mathematical model used to estimate the unknown parameters, the damping ratios are set to $\xi_1 = \xi_2 = 0.015$. The other parameters m_1, m_2, and k of the

mathematical model are considered to be the same as in the true system. Thus, the modeling error is mimicked (represented) by the incorrect damping (damping is a prevalent source of modeling error in structural systems).

The 1940 El Centro ground motion acceleration time history shown in Figure 3.13b is taken as the measured input time history $\mathbf{u}$. The relative displacement response time histories of the true system and of the mathematical model parameterized with the true parameter values, i.e., $\boldsymbol{\theta}^{\text{true}} = \left[k_1^{\text{true}}, k_2^{\text{true}} \right]^T$, when subjected to the El Centro ground motion are shown in Figure 3.13c. The differences between these two responses represent the true model discrepancy time histories shown in Figure 3.13d. All the displacement response time histories are normalized with respect to the maximum displacement response (of the corresponding DOF) of the mathematical model parameterized with the true parameter values. To simulate the output measurement data $\mathbf{y}$, it is assumed that the displacement measurements at both DOFs are recorded every 0.02sec until 6.0sec. These measurements are obtained by polluting the true system displacement responses with zero-mean Gaussian white noise of root mean square 1.0mm to simulate the output measurement noise (Diakonikolas et al. 2019; Kane et al. 2019; Karingula and Lovett 2020).

3.6.1 Single Output Measurement Channel

Model calibration is first performed by utilizing only the output measurement data corresponding to the second DOF displacement response (relative to the ground). This is the case of model calibration of linear MDOF systems with a single output measurement channel (Section 3.4.1). The joint posterior distribution of the physical parameters and hyperparameters (see Section 3.3.2.1 – fully Bayesian approach) considering the measurement equation without and with delta term is sampled (approximated) using the TMCMC algorithm with 250 particles in

each case. Figure 3.14 shows the histograms and kernel density estimates of the posterior marginal distributions of the unknown physical parameters $\boldsymbol{\theta} = \left[k_1, k_2\right]^T$ with the red line indicating the true parameter value.

Figure 3.14a compares the posterior marginal distributions of the physical parameters with the corresponding true parameter values when the calibration is performed without delta term. The support of the posterior marginal distribution of each parameter does not enclose the true parameter value. Thus, model calibration performed using the measurement equation without delta term results in biased estimates of the physical parameters. Figure 3.14b and Figure 3.14c show the posterior marginal distributions of the physical parameters when the calibration is performed with the delta term using the covariance kernel $k_{\text{MDOF}}\left(t,t';\boldsymbol{\beta}\right)$ (Section 3.4.1.1) and $k_{\text{Mix-SDOF}}\left(t,t';\boldsymbol{\beta}\right)$ (Section 3.4.1.2) with 2 mixture components, respectively. The support of the posterior marginal distribution of each parameter encloses the corresponding true parameter value in both figures. Thus, adding the delta term to the measurement equation and modeling the kernel of the delta term with either $k_{\text{MDOF}}\left(t,t';\boldsymbol{\beta}\right)$ or $k_{\text{Mix-SDOF}}\left(t,t';\boldsymbol{\beta}\right)$ results in improved estimates of the physical parameters, which can now be estimated as physical parameters and not tuning parameters.

3.6.2 Multi-Output Measurement Channels

Model calibration is now performed utilizing the output measurement data corresponding to both DOF relative displacement responses. This is the case of model calibration of linear MDOF systems with multiple output measurement channels (Section 3.4.2). The joint posterior distribution of all physical parameters and hyperparameters is sampled (approximated) using the

TMCMC algorithm with 250 particles. Figure 3.14d compares the posterior marginal distributions of the physical parameters with the corresponding true parameter values when the calibration is performed without the delta term. The support of the posterior marginal distribution of each parameter does not enclose the true parameter value. Figure 3.14e and Figure 3.14f show the posterior marginal distributions of the physical parameters when the calibration is performed with the delta term using the random vibration based matrix-valued covariance function $\mathbf{k}_{\text{MDOF}}(t,t';\boldsymbol{\beta})$ and $\mathbf{k}_{\text{Mix-SDOF}}(t,t';\boldsymbol{\beta})$ (with 2 mixture components), respectively. The support of the posterior marginal distribution of each parameter encloses its corresponding true value in both cases. However, the true parameter values are near the tails of the posterior marginals in Figure 3.14e. Note that the covariance kernel derived using the "MDOF Covariance Function Approach" is too restrictive (i.e., over-constrained) to capture all kinds of stationary model discrepancy time histories (as discussed in Remark 2), thus resulting in biased parameter estimates in some cases. However, the covariance kernel derived using "A Mixture of SDOF Covariance Functions Approach" can capture any stationary model discrepancy time histories given enough mixture components.

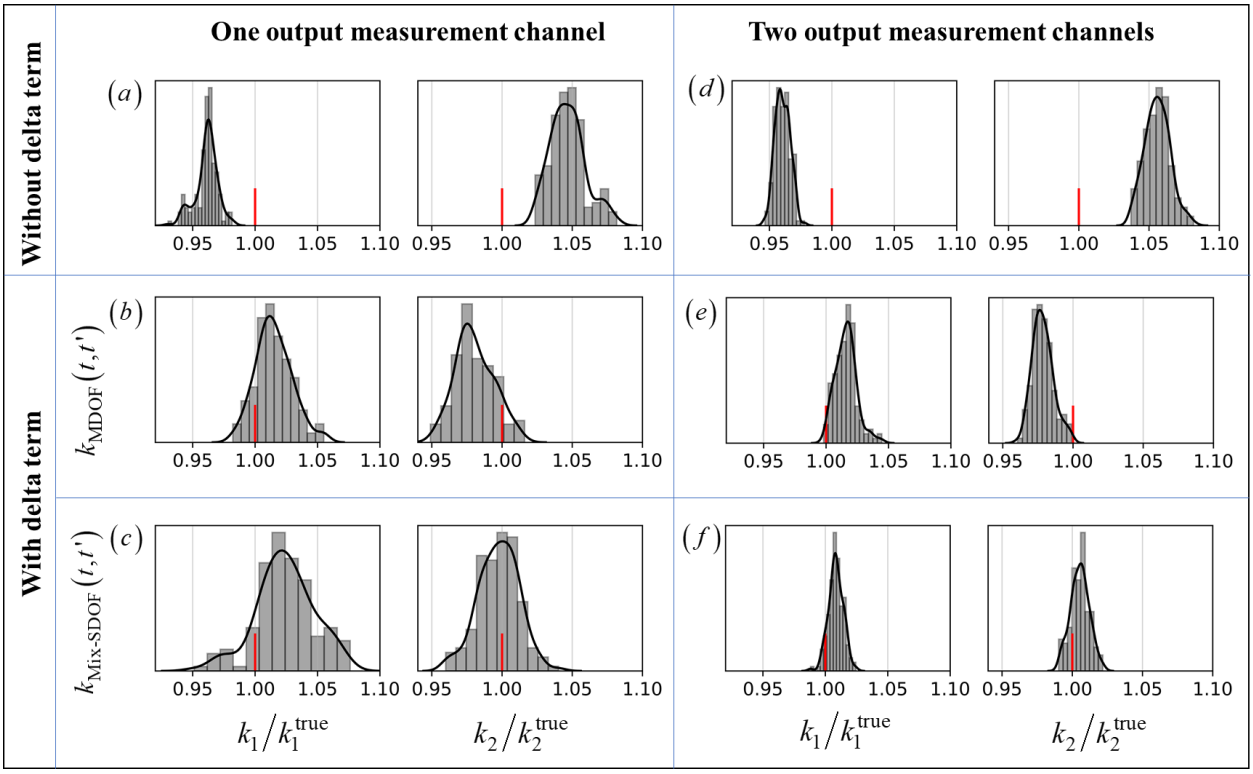

Figure 3.14: Comparison of posterior marginal distributions of physical parameters with the corresponding true parameter values (indicated by red lines) for the cases of model calibration without and with delta term.

3.7 Overview of the Proposed Approach

For the generic case of MDOF systems with multiple output measurement channels, the measurement equation for model calibration purposes is given by

$$\text{At time step } k: \quad \mathbf{y}_k = \underbrace{\mathbf{h}(t_k, \mathbf{u}_{1:k}; \boldsymbol{\theta})}_{\text{mathematical model}} + \underbrace{\boldsymbol{\delta}(t_k)}_{\text{delta}} + \underbrace{\mathbf{w}(t_k)}_{\text{error/ noise}} ; \quad k \in [1, 2, ..., N] \tag{3.26}$$

The random process $\mathbf{w}(t)$ is modeled as a zero-mean white noise process (see Eq. (3.19)). The random process $\boldsymbol{\delta}(t)$ is modeled as a zero-mean Gaussian process with covariance kernel $\mathbf{k}(t, t'; \boldsymbol{\beta})$, where $\boldsymbol{\beta}$ are the parameters of the kernel, as

$$\boldsymbol{\delta}(t) \sim \mathcal{GP}\left(\mathbf{0}, \mathbf{k}(t,t';\boldsymbol{\beta})\right); \qquad \mathbf{k}(t,t';\boldsymbol{\beta}) = \begin{pmatrix} \ddots & & 0 \\ & k^{(j,j)}(t,t') & \\ 0 & & \ddots \end{pmatrix} \in \mathbb{R}^{n_{\mathbf{y}} \times n_{\mathbf{y}}} \tag{3.27}$$

MDOF Covariance Function Approach: $k^{(j,j)}(t,t';\boldsymbol{\beta}) = k^{(j,j)}_{\text{MDOF}}(t,t';\boldsymbol{\beta})$, where $k^{(j,j)}_{\text{MDOF}}(t,t';\boldsymbol{\beta})$ denotes the diagonal element, at the DOF corresponding to the $j-th$ measurement channel, of the auto/cross-correlation matrix shown in Appendix A. The hyperparameters are $\boldsymbol{\beta} = \left[\phi_0^{GP}, \left(\boldsymbol{\theta}^{GP}\right)^T\right]^T \in \mathbb{R}^{n_{\boldsymbol{\theta}}+1}$.

Mixture of SDOF Covariance Functions Approach: $k^{(j,j)}(t,t';\boldsymbol{\beta}) = k^{(j,j)}_{\text{Mix-SDOF}}(t,t';\boldsymbol{\beta})$ where $k^{(j,j)}_{\text{Mix-SDOF}}\left(t,t';\boldsymbol{\beta}^{(j)}\right) = \sum_{i=1}^{m} k_{\text{SDOF}}\left(t,t';\boldsymbol{\beta}_i^{(j)}\right)$, and $\boldsymbol{\beta}_i^{(j)} == \left[\nu_i^{GP^{(j)}}, \omega_{0,i}^{GP}, \xi_i^{GP}\right]^T \in \mathbb{R}^3$. This approach is also directly applicable to multi-variate input excitation.

The proposed approaches and power spectral density – covariance function pair are appropriate to account for model form uncertainty in the model calibration of linear dynamic systems if model discrepancy time histories are known/believed/assumed to be stationary processes. Although stationarity of the model discrepancy time history is required in this paper, which implies stationarity of the linear elastic system response and therefore of the excitation, limited relaxation of this requirement still yields successful results. This was shown in the first illustration example where the wind excitation is stationary, but the system response is not strictly stationary due to the at rest initial conditions, and in the second illustration example where the input earthquake excitation and therefore the system response are not strictly stationary. The proposed approach in this paper does not apply directly to linear dynamic systems subjected to strongly nonstationary (in both amplitude and frequency content) excitation

and to nonlinear (elastic and hysteretic) dynamic systems subjected to broadband stationary or nonstationary excitations. In both these cases, the proposed approach could be extended by using a nonstationary covariance kernel and/or by including the input loading $\mathbf{u}$ in the input of the delta process in addition to the time t.

3.8 Conclusions

This paper proposes a generic methodology to account for the model form uncertainty in Bayesian calibration of linear dynamic systems. The proposed methodology is based on the Kennedy and O'Hagan (KOH) approach – add a delta term to the measurement equation to explicitly account for the model form uncertainty. This paper extends the KOH approach to account for model form uncertainty in linear systems subjected to dynamic loading (i.e., linear dynamic systems). A novel power spectral density – covariance kernel pair based on the theory of random vibrations is proposed to capture common model discrepancy time histories arising in linear dynamic systems. Model calibration without and with the delta term is illustrated using a benchmark linear SDOF system subjected to wind loading and the corresponding estimates of unknown physical parameters are compared. The key findings are:

(1) The calibration performed without the delta term resulted in a posterior probability distribution of the unknown physical parameters the support of which does not contain the true parameter values. The bias persists and the estimates become more confident about incorrect parameter values with an increase in the sampling rate of the measurement data. This bias does not improve (i.e., reduce) with an increase in the duration of the input-output measurement data.

(2) The calibration performed with the delta term (with the proposed covariance kernel) resulted in a posterior distribution of the physical parameters with a support enclosing the true parameter values. The parameter estimates become more confident about the true parameter values when increasing the duration of the measurement data as this increases the amount of information about the parameters in the data. The posterior distribution of the physical parameters does not change when increasing the sampling rate of the measurements as this does not add any new information about the parameters.

Similar findings have been observed with the KOH framework in other application areas. Our findings are novel in the context of linear dynamic systems.

"Two novel approaches to constructing a covariance kernel, namely the "MDOF Covariance Function Approach" and the "Mixture of SDOF Covariance Functions Approach", are also proposed in this paper to accurately account for model form uncertainty arising in linear MDOF systems with single and multiple output measurement channels. The effectiveness of these kernels is illustrated by calibrating a 2-DOF structural system subjected to earthquake base excitation. The proposed methodology to account for model form uncertainty enables physical model parameters to be estimated/calibrated as such (and not as tuning parameters with non-physical values). The proposed approaches and power spectral density – covariance function pair are appropriate to account for model form uncertainty in the model calibration of linear dynamic systems if model discrepancy time histories are known/believed/assumed to be stationary processes. Although the examples provided in the paper are 2D low-dimensional problems with single excitation, the proposed approaches to represent the model form uncertainty in linear dynamic systems can be applied/adapted to 3D structures with multi-variate input loading and

multiple-output measurement channels. We believe that the "mixture of SDOF covariance functions approach" is a generic method to construct the kernel of the delta process and thus should be a default choice. This generic method also allows to represent the model discrepancy flexibly but informatively in the context of linear dynamic systems. This is a crucial aspect since incorrect modeling of the model discrepancy can lead to biased parameter estimates."

In future work, other forms of modeling errors (e.g., approximations about geometries, FE mesh size, boundary and loading conditions, energy dissipation mechanisms, non-structural components, material properties, and material constitutive models) need to be investigated to further validate the robustness of the proposed covariance kernels. Additional investigation is needed to account for model form uncertainty using the proposed methodology considering measurement data from heterogenous sensor arrays. While our examples focus on displacement measurements, other types of observations, such as absolute acceleration, can also be used in our framework. The power spectral density shown for displacements in Section 3.4 could be used directly or a similar procedure could be used to derive the power spectral density of alternative observable quantities. The KOH approach suffers from the issue of identifiability – compensation/confounding between the delta term $\delta(.)$ and the physical parameters $\boldsymbol{\theta}$ (Brynjarsdóttir and O'Hagan 2014). To minimize this confounding, it is important to use the best and most realistic modeling choices for the delta term along with the best prior information about the physical parameters (Brynjarsdóttir and O'Hagan 2014). The proposed covariance kernels model the delta term informatively to help reduce the confounding effect. This confounding issue needs to be further investigated in future work. The extension of the proposed methodology to account for model form uncertainty in linear dynamic systems subjected to strongly nonstationary (in both amplitude and frequency content) excitation and to nonlinear (elastic and

hysteretic) dynamic systems subjected to broadband stationary or nonstationary excitations is currently being investigated by the authors.

3.9 Appendix A: Power spectral density matrix and auto/cross-correlation matrix of response of MDOF systems subjected to white noise base excitation

The power spectral density matrix and auto/cross-correlation matrix of the displacement response (at all degrees of freedom) of a linear MDOF system subjected to white noise base excitation are briefly summarized below. The equation of motion of an n-degree-of-freedom linear system with classical damping subjected to a single loading (forcing) function can be expressed as

$$\mathbf{M}\ddot{\mathbf{q}}(t)+\mathbf{C}\dot{\mathbf{q}}(t)+\mathbf{K}\mathbf{q}(t)=\mathbf{p}F(t) \tag{3.28}$$

where $\mathbf{M}$, $\mathbf{C}$, and $\mathbf{K}$ denote the $n\times n$ mass, damping, and stiffness matrices, respectively, $\mathbf{q}$ is the $n\times 1$ vector of nodal displacements, $F(t)$ is the loading (forcing) function considered here as a stationary random process, and $\mathbf{p}$ is the $n\times 1$ load influence vector that distributes $F(t)$ to the DOF's of the structure. Using modal decomposition, the nodal displacement vector can be written as

$$\mathbf{q}(t)=\sum_{i=1}^{n}\boldsymbol{\varphi}_i\,\Gamma_i\,s_i(t) \tag{3.29}$$

where $\boldsymbol{\varphi}_i$ denotes the $i-th$ mode shape/eigenvector, $\Gamma_i = \left(\boldsymbol{\varphi}_i^T \mathbf{p}\right) \Big/ \left(\boldsymbol{\varphi}_i^T \mathbf{M} \boldsymbol{\varphi}_i\right)$ is the participation factor for the $i-th$ mode, and $s_i(t)$ is the standardized modal displacement response for the $i-th$ mode. The standardized modal equations of motions are given by

$$\ddot{s}_i(t) + 2\xi_i \omega_i \dot{s}_i(t) + \omega_i^2 s_i(t) = F(t), \quad i = 1, ..., n \tag{3.30}$$

where ω_i and ξ_i denote the $i-th$ mode natural frequency and damping ratio, respectively. Eq. (3.29) can be re-written as $\mathbf{q}(t) = \boldsymbol{\Phi}\boldsymbol{\Gamma}\mathbf{s}(t)$ where

$$\boldsymbol{\Phi} = \begin{bmatrix} \cdots & \boldsymbol{\varphi}_i & \cdots \end{bmatrix}_{n\times n}, \quad \boldsymbol{\Gamma} = \begin{bmatrix} \ddots & & \mathbf{0} \\ & \Gamma_i & \\ \mathbf{0} & & \ddots \end{bmatrix}_{n\times n}, \quad \mathbf{s}(t) = \begin{bmatrix} \vdots \\ s_i(t) \\ \vdots \end{bmatrix}_{n\times 1} \tag{3.31}$$

Let $\boldsymbol{\Phi}_{\mathbf{qq}}(\omega)$ and $\boldsymbol{\Phi}_{\mathbf{ss}}(\omega)$ denote the power spectral density matrices of the stationary response vectors $\mathbf{q}(t)$ and $\mathbf{s}(t)$, respectively. Then (Lutes and Sarkani 2004),

$$\boldsymbol{\Phi}_{\mathbf{qq}}(\omega) = (\boldsymbol{\Phi}\boldsymbol{\Gamma})\boldsymbol{\Phi}_{\mathbf{ss}}(\omega)(\boldsymbol{\Phi}\boldsymbol{\Gamma})^T \tag{3.32}$$

The auto/cross cross-correlation matrix $\mathbf{R}_{\mathbf{qq}}(\tau)$ of the displacement response vector $\mathbf{q}(t)$ can be expressed as

$$\begin{aligned} \mathbf{R}_{\mathbf{qq}}(\tau) &= (\boldsymbol{\Phi}\boldsymbol{\Gamma})\mathbf{R}_{\mathbf{ss}}(\tau)(\boldsymbol{\Phi}\boldsymbol{\Gamma})^T \\ &= \sum_{i=1}^{n}\sum_{j=1}^{n} (\boldsymbol{\Phi}\boldsymbol{\Gamma})_i \mathbf{R}_{s_i s_j}(\tau)(\boldsymbol{\Phi}\boldsymbol{\Gamma})_j \end{aligned} \tag{3.33}$$

where τ denotes the time lag, $\mathbf{R}_{\mathbf{ss}}(\tau) = \left[\mathbf{R}_{s_i s_j}(\tau)\right]_{n\times n}$ is the auto/cross-correlation matrix of the normalized modal displacement response vector $\mathbf{s}(t)$. If the single loading function $F(t)$

is a zero-mean white noise process of mean square ϕ_0, then from the theory of random vibrations, the auto/cross-correlation matrix $\mathbf{R}_{s_i s_j}(\tau)$ is given by

$$\mathbf{R}_{s_i s_j}(\tau) = \pi \phi_0 \left[\alpha_{ij}\, g_{1j}(|\tau|) + \beta_{ij}\, g_{2j}(|\tau|) \right]$$

where
$$g_{1j}(|\tau|) = e^{-\xi_j \omega_j |\tau|} \left[\cos\left(\omega_{D_j} |\tau|\right) + \frac{\xi_j}{\sqrt{1-(\xi_j)^2}} \sin\left(\omega_{D_j} |\tau|\right) \right]$$

$$g_{2j}(|\tau|) = \frac{1}{\omega_{D_j}} e^{-\xi_j \omega_j |\tau|} \left[\sin\left(\omega_{D_j} |\tau|\right) \right] \tag{3.34}$$

$$\omega_{D_j} = \omega_j \sqrt{1-(\xi_j)^2}; \quad \alpha_{ij} = 4\frac{\omega_i \xi_i + \omega_j \xi_j}{l_{ij}}; \quad \beta_{ij} = 2\frac{\left(\omega_i^2 - \omega_j^2\right)}{l_{ij}}$$

$$l_{ij} = \left(\omega_i^2 - \omega_j^2\right)^2 + 4\omega_i \omega_j \left(\omega_i \xi_i + \omega_j \xi_j\right)\left(\omega_i \xi_j + \omega_j \xi_i\right)$$

Consider the 2-DOF system with parameters $m_1 = m_2 = 46\ kN \cdot s^2/m$, $k_1^{\text{true}} = 17 \times 10^3\ kN/m$, $k_2^{\text{true}} = 42 \times 10^3\ kN/m$, $k = 8.5 \times 10^3\ kN/m$, and $\xi_1 = \xi_2 = 0.05$ defined in Section 3.6. The terms of the power spectral density matrix $\mathbf{\Phi_{qq}}(\omega)$ and auto/cross-correlation matrix $\mathbf{R_{qq}}(\tau)$ of the displacement response vector $\mathbf{q}(t) = \left[q_1(t), q_2(t)\right]^T$ ($q_1(t)$ and $q_1(t)$ are depicted in Figure 3.13a) are plotted in Figure A.1.

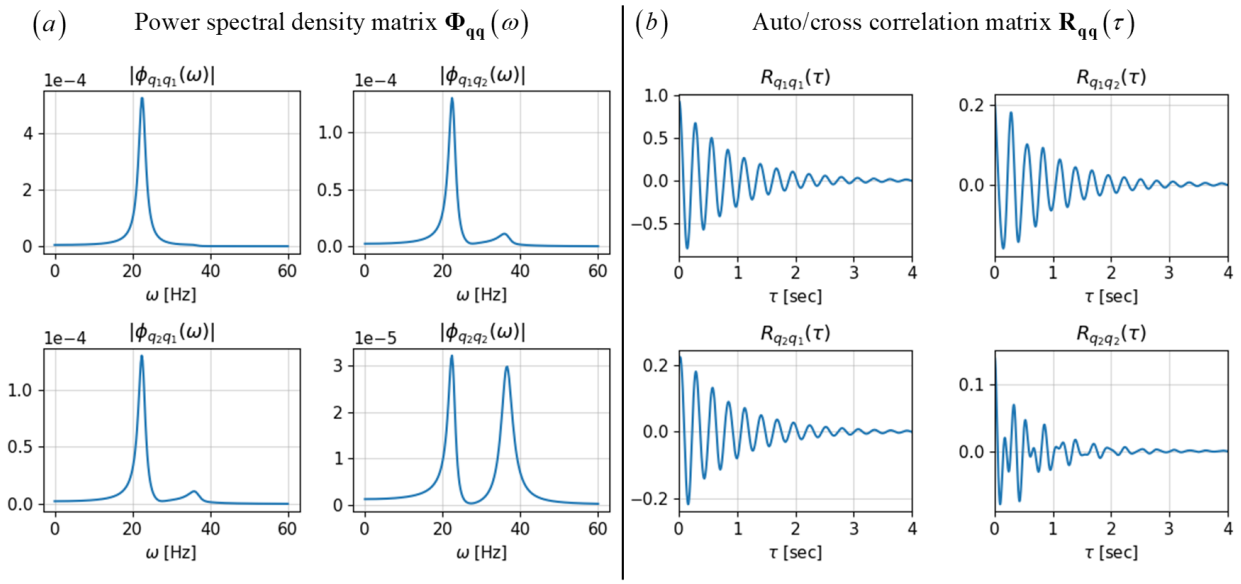

Figure A.1: (a) Power spectral density matrix (magnitude) and (b) auto/cross-correlation matrix of displacement response vector for 2-DOF illustration/application example

3.10 Appendix B: Alternatives to Fully Bayesian Approach

3.10.1 Integrated Likelihood Approach

The integrated likelihood approach (Wolpert et al. 1999) focuses on directly obtaining the posterior $p(\boldsymbol{\theta} \mid \mathbf{u}_{1:N}, \mathbf{y}_{1:N})$ by integrating out the hyperparameters $\{\boldsymbol{\beta}, \sigma\}$ as

$$p(\boldsymbol{\theta} \mid \mathbf{u}_{1:N}, \mathbf{y}_{1:N}) \propto \underbrace{\left(\int_{\sigma} \int_{\boldsymbol{\beta}} p(\mathbf{y}_{1:N} \mid \mathbf{u}_{1:N}, \boldsymbol{\theta}, \boldsymbol{\beta}, \sigma)\, p(\boldsymbol{\beta})\, p(\sigma)\, d\boldsymbol{\beta}\, d\sigma \right)}_{\text{integrated likelihood}} \times p(\boldsymbol{\theta}) \tag{3.35}$$

The multi-dimensional integral over the hyperparameters shown in Eq. (3.35) is analytically intractable in most cases. It can be approximated using numerical quadrature. Unlike the fully Bayesian approach, the integrated likelihood approach does not attempt to learn the hyperparameters $\{\boldsymbol{\beta}, \sigma\}$. The hyperparameters are treated as nuisance parameters and integrated out straight from the start. Nuisance parameters are parameters which are not of immediate/direct

interest, $\{\boldsymbol{\beta}, \sigma\}$ in our case, but must be accounted for to learn the parameters which are of interest, physical parameters $\boldsymbol{\theta}$ in our case. In this approach, the distribution of the hyperparameters is never updated. Only the distribution of the physical parameters $\boldsymbol{\theta}$ is updated accounting for the uncertainty of the hyperparameters $\{\boldsymbol{\beta}, \sigma\}$ encoded in their prior distribution $p(\boldsymbol{\beta})\, p(\sigma)$. The posterior predictive distribution is then obtained as

$$p\left(y_j^* \mid \mathbf{u}_{1:j}^*, \mathcal{D}\right) = \int_{\boldsymbol{\theta}} \left(\int_{\sigma} \int_{\boldsymbol{\beta}} p\left(y_j^* \mid \mathbf{u}_{1:j}^*, \boldsymbol{\theta}, \boldsymbol{\beta}, \sigma, \mathcal{D}\right) p(\boldsymbol{\beta})\, p(\sigma)\, d\boldsymbol{\beta}\, d\sigma \right) \times p(\boldsymbol{\theta} \mid \mathcal{D})\, d\boldsymbol{\theta} \tag{3.36}$$

3.10.2 Modular Bayesian Approach

The modular Bayesian approach for model calibration was introduced by KOH in (Kennedy and O'Hagan 2001) as a practical alternative to the fully Bayesian approach. This modular approach first focuses on deriving plausible estimates of the hyperparameters $\{\boldsymbol{\beta}, \sigma\}$ and then on inferring physical parameters $\boldsymbol{\theta}$ conditioned on the estimated hyperparameter values. The hyperparameters can be estimated using

$$p(\boldsymbol{\beta}, \sigma \mid \mathbf{u}_{1:N}, \mathbf{y}_{1:N}) \propto \left(\int_{\boldsymbol{\theta}} p(\mathbf{y}_{1:N} \mid \mathbf{u}_{1:N}, \boldsymbol{\theta}, \boldsymbol{\beta}, \sigma)\, p(\boldsymbol{\theta}) \right) \times p(\boldsymbol{\beta})\, p(\sigma) \tag{3.37}$$

The maximum likelihood estimate or maximum a posteriori estimate can be used as a plausible estimate of the hyperparameters, denoted by $\left\{\hat{\boldsymbol{\beta}}, \hat{\sigma}\right\}$. Instead of the posterior $p(\boldsymbol{\theta} \mid \mathbf{u}_{1:N}, \mathbf{y}_{1:N})$, a posterior of the physical parameters $\boldsymbol{\theta}$ conditioned on the estimated values of the hyperparameters $\left\{\hat{\boldsymbol{\beta}}, \hat{\sigma}\right\}$ is considered in this approach. This conditioned posterior is given by

$$p\left(\boldsymbol{\theta} \mid \mathbf{u}_{1:N}, \mathbf{y}_{1:N}, \hat{\boldsymbol{\beta}}, \hat{\sigma}\right) \propto p\left(\mathbf{y}_{1:N} \mid \mathbf{u}_{1:N}, \boldsymbol{\theta}, \hat{\boldsymbol{\beta}}, \hat{\sigma}\right) \times p(\boldsymbol{\theta}) \tag{3.38}$$

Hence, the modular Bayesian approach does not account for the estimation uncertainty of the hyperparameters in the model calibration. In this approach, a posterior predictive distribution conditioned on the estimated hyperparameters $\left\{\hat{\boldsymbol{\beta}}, \hat{\sigma}\right\}$ is used for response prediction. It is obtained as

$$p\left(y_j^* \mid \mathbf{u}_{1:j}^*, \mathcal{D}, \hat{\boldsymbol{\beta}}, \hat{\sigma}\right) = \int_{\boldsymbol{\theta}} p\left(y_j^* \mid \mathbf{u}_{1:j}^*, \boldsymbol{\theta}, \hat{\boldsymbol{\beta}}, \hat{\sigma}, \mathcal{D}\right) \times p\left(\boldsymbol{\theta} \mid \mathcal{D}, \hat{\boldsymbol{\beta}}, \hat{\sigma}\right) d\boldsymbol{\theta} \tag{3.39}$$

To further reduce the computational complexity of model calibration, the mathematical model $\left\{\boldsymbol{\theta} \to h\left(t_k, \mathbf{u}_{1:k}; \boldsymbol{\theta}\right)\right\}$ is modeled using Gaussian process regression in (Kennedy and O'Hagan 2001).

3.11 Acknowledgements

Funding for this work by the U.S. Army Corps of Engineers through the U.S. Army Engineer Research and Development Center Research Cooperative Agreement W912HZ-17-2-0024 is gratefully acknowledged. Chapter 3, in full, had been submitted for publication of the material as it may appear in the following paper (the dissertation author is the first author of this paper):

Ramancha, M. K., Conte, J. P., and Parno, M. D. (2022). "Accounting for model form uncertainty in Bayesian calibration of linear dynamic systems." Mechanical Systems and Signal Processing, 171, 108871. https://doi.org/10.1016/j.ymssp.2022.108871

3.12 Preview to Chapter 4

Bayesian model updating of large-scale civil infrastructure system using high-fidelity FE model is computationally extremely expensive as it requires repeated evaluations of the high-fidelity FE model. Surrogate modeling can be used as the fast emulators of the FE model to

decrease the model updating run time. Chapter 4 considers Bayesian model updating using direct FE model evaluation versus surrogate model evaluations in the context of updating a high-fidelity FE model of the miter gate structural system.

4 Bayesian Model Updating with Finite Element vs. Surrogate Models: Application to a Miter Gate Structural System

4.1 Abstract

Bayesian finite element (FE) model updating using direct model evaluations of large-scale high-fidelity FE models is extremely computationally expensive. Surrogate models can be used as fast emulators of FE models to accelerate the model calibration process. The physics/mechanics-based FE models are still the underpinning behind the surrogate models. This paper evaluates the loss in accuracy and the gain in computational time while performing Bayesian model updating by using surrogate model evaluations compared to using direct FE model evaluations. This evaluation is crucial before entirely relying on surrogate models in model updating for structural health monitoring (SHM) and damage prognosis (DP) purposes. This paper also demonstrates Bayesian updating and surrogate model construction of large-scale high-fidelity FE models of infrastructure systems. In this regard, the miter gate structural system is considered as the testbed structure. Three predominant damage modes (loss of contact between gate and wall, loss of thickness due to corrosion, and loss of tension in the diagonal rods) are considered for model updating purposes. The high-fidelity FE model of the gate is constructed in the Abaqus FEA software and has 97201 nodes, 94955 elements, and 550488 free degrees of freedom. Bayesian model updating is performed using direct FE evaluations by leveraging parallel computing. Two types of surrogates, namely polynomial chaos expansion (PCE) and Gaussian process regression (GPR), are developed for the miter gate. Model updating is

performed again using the trained surrogate models, and the updating results are compared with their counterparts obtained using the direct FE evaluation results. FE model updating is with respect to the FE model parameters which are also the input parameters of the surrogate models. The posterior distribution of the FE model parameters obtained using the trained surrogates are sufficiently accurate with respect to the posterior obtained utilizing the direct FE evaluations. In addition, a decrease in the computational time of ~4 times was observed when using surrogate model evaluations instead of direct FE evaluations for model updating.

Keywords: Bayesian model updating, surrogate modeling, large-scale systems, high-fidelity FE models, miter gate, polynomial chaos expansion, Gaussian process regression

4.2 Introduction

Degrading infrastructure conditions have a cascading impact on a nation's economy. The American Society of Civil Engineers (ASCE) 2021 report card rated America's infrastructure as C- (mediocre) (American Society of Civil Engineers 2021). Given this, there is an operational need for structural health monitoring (SHM) and damage prognosis (DP) for large-scale infrastructure systems. Well-calibrated physics/mechanics-based finite element (FE) models can be leveraged for comprehensive and accurate damage identification (existence, localization, classification, extent) and damage prognosis in such systems. The process of calibrating a FE model of the system with sensor measurement data collected from the system using the Bayesian inference framework is known as Bayesian FE model updating (Yuen 2010). Such a process can form the core of a "digital twin" emulator of the system behavior over its life cycle.

The last few decades have witnessed tremendous progress in modeling and analysis methods for civil engineering structural, geo-structural, and soil-foundation-structural systems

subjected to static, quasi-static, and dynamic loading, mainly from natural hazards such as earthquakes. Mechanics-based nonlinear FE models (of various complexities) of civil engineering systems (e.g., buildings, bridges, dams, miter gates) are now able to capture the damage and failure mechanisms developing in such systems in a critical loading environment or progressively over time (i.e., wear and tear). Numerical models have increased in fidelity, becoming more complex and potentially more accurate. But the computational time to run an analysis using such numerical models is still prodigious even with the latest computing resources. In addition, updating the FE model requires executing the model multiple times, making it an extremely computationally expensive undertaking for large-scale high-fidelity FE models.

Surrogate models can be used as fast emulators of FE models to accelerate the model updating process (Forrester et al. 2008). The key idea is to replace an expensive-to-evaluate FE model fully or partially with a cheaper-to-evaluate surrogate model for updating purposes. Note that the mechanics-based FE model is still the underpinning behind the surrogate model. The surrogate model of a physical system is just used to accelerate model calibration computations but not as a complete replacement of the FE model. After performing model updating, the mechanics-based FE model should be used for SHM/DP purposes as the surrogate model by itself has no physical basis or meaning. There also exist some limitations in surrogate modeling of physical systems. As mentioned, a surrogate model is just a mapping between the designated FE inputs and outputs. After training, the output response of the expensive to evaluate FE model at designated output can be obtained cheaply by just evaluating the trained surrogate model. However, if we want to know the output response of the system at an undesignated output (i.e., type of output different than the designated output used to train the surrogate model), then we

must rely on the expensive to evaluate FE model. In addition, if the FE model is modified or the designated inputs-outputs are changed/updated, the entire surrogate model needs to be retrained to correspond to the modified FE model with updated FE input and output designations.

Previous work in model updating of civil engineering systems focused on using simplified empirical or semi-empirical models. Unlike full-scale high-fidelity physics-based models, these empirical models cannot be used for damage classification, extent, and prognosis. Some recent studies (Astroza et al. 2015; Ebrahimian et al. 2017; Moaveni et al. 2010; Ramancha et al. 2020a, 2022) focus on using physics-based models for model updating. However, these studies do not use surrogate modeling. Surrogate modeling is a relatively new area of research, and its applicability to Bayesian updating of FE models of large-scale civil infrastructure systems is seldom studied in the literature and is the focus of this paper. Few studies (Jin and Jung 2016; Vega and Todd 2020) focus on surrogate modeling for the purposes of FE model updating. However, these studies do not present any comparative model updating results when relying on FE models vs. surrogate models. Before entirely relying on surrogate models in model updating for SHM/DP purposes, it is crucial to evaluate the loss in accuracy and the gain in computational time when using trained surrogate models instead of physics-based FE models in Bayesian model updating, so that appropriate judgment may be applied in surrogate model design, use, and application. This is the done in this paper in the context of updating a full-scale high-fidelity FE model.

This paper considers Bayesian model updating of a miter gate structural system using a full-scale high-fidelity FE model considering three predominant damage modes occurring in such systems. Model updating is first performed using direct FE model evaluations. Then, two global surrogate models of the FE model are constructed using polynomial chaos expansion

(PCE) and Gaussian process regression (GPR) techniques to accelerate the model updating process. Model updating is repeated using surrogate model evaluations in the updating process. Finally, the loss of accuracy in the model updating results and gain in computational time (which includes the training time of the surrogate models) are investigated and compared when model evaluations are performed using trained surrogate models instead of FE models in model updating. The main objective of this paper is not to develop new surrogate modeling techniques; rather, it is to perform a comparative study to analyze the advantages and disadvantages of using surrogate models for model updating purposes and to fill the gap in the literature in the context of full-scale high-fidelity FE models of civil infrastructure systems. In addition, this paper also demonstrates the procedures for surrogate model construction and FE model updating of miter gate structural systems. These procedures can be adapted for any structural system.

This paper is outlined as follows. Section 4.3 presents an overview of the Bayesian FE model updating framework and describes the challenges in updating large-scale systems. Section 4.4 presents the surrogate modeling workflow and the overview of PCE and GPR surrogate modeling techniques. Section 4.5 focuses on the miter gate application example, describes the considered damage/failure mechanisms, shows surrogate modeling of miter gate system, and model updating using direct FE vs surrogate model evaluations.

4.3 Bayesian Finite Element Model Updating

FE model updating aims to estimate the unknown parameters of the FE model using measurement data. Let h be the FE model of the system of interest developed using as-built drawings and with explicitly formulated assumptions and hypotheses. FE models contain parameters known with little/no uncertainty (e.g., dimensions of the system) and known with

significant uncertainty (e.g., the strength of concrete). The latter are referred to as unknown parameters in this paper. Let $\boldsymbol{\theta} \in \Omega_{\boldsymbol{\theta}} \subset \mathbb{R}^{n_{\boldsymbol{\theta}}}$ represent the time-invariant unknown parameter vector of the FE model h, where $n_{\boldsymbol{\theta}}$ denotes the number of unknown parameters. These unknown parameters need to be estimated using input-output measurement data from the system. Sensors are deployed on and around the system to collect input excitation (from various sources) and output response (at several locations) measurement data. Collecting the data from large-scale structural systems is generally challenged by susceptibility to environmental/operational changes and installation and maintenance concerns, resulting in being the economically expensive part of model updating. The raw data acquired using the sensors also need to be pre-processed (accessed, moved, organized, transformed, and cleansed) for FE model updating.

Let $\mathbf{u} \in \mathbb{R}^{n_{\mathbf{u}}}$ be the measured input (i.e., loading) and $\mathbf{y} \in \mathbb{R}^{n_{\mathbf{y}}}$ be the measured output response of the system, where $n_{\mathbf{u}}$ and $n_{\mathbf{y}}$ denote the number of input and output measurement channels. Let $\mathbf{h}(\mathbf{u};\boldsymbol{\theta}) \in \mathbb{R}^{n_{\mathbf{y}}}$ be the response predicted by the FE model, at the locations of the sensors measuring the output response, to the input $\mathbf{u}$, parameterized by the unknown parameter vector $\boldsymbol{\theta}$. FE model updating aims to find the range of values of the unknown parameter vector $\boldsymbol{\theta}$ that are consistent with the measurement data $(\mathbf{u},\mathbf{y})$. Numerous real-world sources of uncertainty need to be accounted for in the FE model updating process. These include measurement noise in input and output measurement data due to various sources of noise in the measurement process (e.g., sensor, cable and data acquisition noise), model form uncertainty arising from modeling assumptions or unmodeled physics, uncertainty in model parameters (given a model form) due to lack of knowledge, and environmental variability.

The two approaches for FE model updating are the classical (deterministic) and Bayesian. In classical model updating, the unknown parameter vector $\boldsymbol{\theta}$ is estimated to minimize the error (e.g., L2 norm) between the output measurements $\mathbf{y}$ and the FE response $\mathbf{h}(\mathbf{u};\boldsymbol{\theta})$. Computational optimization techniques are used to perform this minimization. Classical model updating does not accurately account for all uncertainties resulting in overfitting and incorrect parameter estimates and does not attempt to quantify the estimation uncertainty of the unknown parameter vector $\boldsymbol{\theta}$. Classical approaches are also not good at handling multiple solutions that usually exist in inverse problems. On the other hand, the probabilistic Bayesian methodology is a rigorous probabilistic framework that can accurately account for the various sources of uncertainty in the model updating process. The unknown parameters in the vector $\boldsymbol{\theta}$ are modeled as random variables, and the prior knowledge is incorporated using a probability distribution $p(\boldsymbol{\theta})$. In Bayesian model updating, this prior distribution $p(\boldsymbol{\theta})$ is updated to a posterior distribution $p(\boldsymbol{\theta}|\mathbf{u},\mathbf{y})$ accounting for the measurement data $(\mathbf{u},\mathbf{y})$ using Eq. (4.1). The posterior distribution $p(\boldsymbol{\theta}|\mathbf{u},\mathbf{y})$ encodes the remaining estimation uncertainty after model updating.

The prior distribution is formulated using domain knowledge and expert opinion. For example, if an unknown parameter is the yield strength of steel, then the nominal value provided by the manufacturer can be used to construct its prior. In civil structural systems, some prior knowledge is available for most physical parameters (at least a nominal value and/or bounds of the parameters are typically known). If no prior knowledge exists about a parameter, a non-informative prior can be used. Converting expert knowledge or prior information into the prior probability distribution $p(\boldsymbol{\theta})$ is not a focus of this paper (refer to (Jaynes 1968) for this issue).

$$p(\boldsymbol{\theta}|\mathbf{u},\mathbf{y}) = \frac{p(\mathbf{y}|\mathbf{u},\boldsymbol{\theta}) \times p(\boldsymbol{\theta})}{p(\mathbf{y}|\mathbf{u})} \tag{4.1}$$

In Eq. (4.1), $p(\mathbf{y}\,|\,\mathbf{u},\boldsymbol{\theta}) \equiv L(\boldsymbol{\theta})$ is the likelihood function (also referred to as goodness of fit function) viewed as a function of $\boldsymbol{\theta}$. $L(\boldsymbol{\theta})$ can be viewed as a distribution over $\boldsymbol{\theta}$ according to the likelihood of observing the observed measurement data. $L(\boldsymbol{\theta}_1) > L(\boldsymbol{\theta}_2)$ indicates that the observed measurement data is more likely for $\boldsymbol{\theta} = \boldsymbol{\theta}_1$ than for $\boldsymbol{\theta} = \boldsymbol{\theta}_2$. In Bayesian model updating, the denominator $p(\mathbf{y}\,|\,\mathbf{u})$ is just a normalizing constant that ensures the posterior $p(\boldsymbol{\theta}\,|\,\mathbf{u},\mathbf{y})$ integrates to one. Thus,

$$p(\boldsymbol{\theta}\,|\,\mathbf{u},\mathbf{y}) \propto p(\mathbf{y}\,|\,\mathbf{u},\boldsymbol{\theta}) \times p(\boldsymbol{\theta}) \tag{4.2}$$

The posterior, likelihood, and prior in Eq. (4.2) are all viewed as functions of $\boldsymbol{\theta}$ in FE model updating. The likelihood function is formulated using a measurement equation – a model of the measurement process. A measurement equation is a joint statistical-physical model that relates the unknown parameter vector $\boldsymbol{\theta}$ to the output measurements $\mathbf{y}$. Most FE model updating methods use the following measurement equation:

$$\underset{\text{output measurements}}{\mathbf{y}} = \underbrace{\mathbf{h}(\mathbf{u};\boldsymbol{\theta})}_{\text{FE response}} + \underset{\text{error / noise}}{\mathbf{w}} \tag{4.3}$$

In Eq. (4.3), the error/noise term $\mathbf{w} \in \mathbb{R}^{n_\mathbf{y}}$ captures the difference between the measured output $\mathbf{y}$ and FE predicted response $\mathbf{h}(\mathbf{u};\boldsymbol{\theta})$, and all the sources of real-world uncertainty are lumped and accounted for in the noise term $\mathbf{w}$. Hence, $\mathbf{w}$ is modeled as a vector of random variables (or random vector). In this paper, the probability distribution of the random vector $\mathbf{w}$ is assumed as a zero-mean Gaussian distribution as

$$\mathbf{w} \sim \mathcal{N}\left(\mathbf{0}, \boldsymbol{\Sigma}_\mathbf{w}\right) \tag{4.4}$$

where $\mathcal{N}(\mathbf{0}, \boldsymbol{\Sigma}_{\mathbf{w}})$ denotes the multi-variate Gaussian distribution with mean vector $\mathbf{0}$ and covariance matrix $\boldsymbol{\Sigma}_{\mathbf{w}}$. Using Eq. (4.3) and Eq. (4.4), the likelihood function $p(\mathbf{y}|\mathbf{u},\boldsymbol{\theta})$ is given by

$$p(\mathbf{y}|\mathbf{u},\boldsymbol{\theta}) = \mathcal{N}(\mathbf{h}(\mathbf{u};\boldsymbol{\theta}), \boldsymbol{\Sigma}_{\mathbf{w}}) \tag{4.5}$$

The likelihood shown in Eq. (4.5) when viewed as a function of $\boldsymbol{\theta}$ is Gaussian if and only if $\mathbf{h}(\mathbf{u};\boldsymbol{\theta})$ is a linear function of $\boldsymbol{\theta}$. In most cases, $\mathbf{h}(\mathbf{u};\boldsymbol{\theta})$ is nonlinear in $\boldsymbol{\theta}$ (and often not explicitly available), thus the likelihood viewed as a function of $\boldsymbol{\theta}$ is some undefined/complicated function.

4.3.1 Challenges in FE Model Updating of Large-scale Structural Systems

Deriving the posterior $p(\boldsymbol{\theta}|\mathbf{u},\mathbf{y})$ analytically is not possible for most cases of FE model updating. Methods such as Laplace approximation or variational Bayes approximate the joint posterior distribution analytically (Bishop 2006). These approximations offer fast computability and scalability. However, the accuracy of such approximations is an open question and cannot be improved with more intensive computations. Alternatively, simulation-based methods can be used to draw samples from the posterior distribution $p(\boldsymbol{\theta}|\mathbf{u},\mathbf{y})$ (Bishop 2006). These samples can then be used to approximate the posterior distribution. The accuracy of this approximation increases with the number of samples generated, and thus is only limited by the available computational resources. Popular simulation-based methods include rejection sampling, importance sampling, particle filtering (PF), Markov chain Monte Carlo (MCMC) sampling, and Transitional MCMC (TMCMC) sampling. All these methods require repeated evaluations of the likelihood function which in turn requires repeated evaluations of the FE model. High-fidelity FE

models of large-scale structural systems are computationally intensive to evaluate (especially in the case of nonlinear material and/or geometric models), and often contain numerous unknown model parameters. Thus, sampling the high-dimensional joint posterior $p(\boldsymbol{\theta}|\mathbf{u},\mathbf{y})$ involving large-scale FE models is an extremely computationally costly endeavor. A few approaches can be used to mitigate the computational burden of FE model updating of large-scale structural systems. They include: (1) using efficient sampling algorithms, (2) leveraging parallel computing, (3) using surrogate modeling, and (4) reducing the dimensionality of the unknown parameter vector $\boldsymbol{\theta}$. These aspects are described below.

MCMC to obtain samples from the posterior distribution is the workhorse method in model calibration. However, the repeated evaluations of the FE model are sequential which is a considerable limitation in model updating of large-scale systems. Performing each individual FE analysis on parallel machines is a viable choice to reduce the computational time. In this regard, FE analysis software frameworks/architectures such as Abaqus FEA and OpenSees use domain-level parallelization to split the FE model into topological domains and assign each domain to a processor. They also support a message passing interface (MPI) and thread-based parallelization. Alternatively, methods such as TMCMC and PF progress sequentially in stages, and the repeated FE model evaluations within each stage can be performed in parallel. Hence these methods are more appropriate to perform model updating of large-scale FE models using high-performance computing (HPC) resources. In this paper, TMCMC (Ching and Chen 2007; Minson et al. 2013) is used for drawing samples from the posterior distribution (see Section 4.3.2 for more details). Other methods such as adaptive and multi-stage MCMC methods have been developed recently for efficient sampling of the posterior distribution.

Another approach to reducing the computational burden of model updating is to decrease the cost of the likelihood function evaluations. This can be achieved by approximating the FE model or the likelihood function using surrogate models. This paper considers the approximation of the FE model using a global surrogate model. The idea is to replace an expensive-to-evaluate FE model fully with a cheap-to-evaluate surrogate model (Forrester et al. 2008). The surrogate model is constructed by regression of the data simulated using the input-output relation/mapping of the FE model. Techniques such as reduced-order models and hierarchical multi-fidelity models (FE models spanning different fidelity levels) can be used to alleviate the computational runtime of FE model updating (Frangos et al. 2010); these aspects are outside the scope of this paper.

Large-scale structural systems have several damage and failure modes, and each damage/failure mode is typically characterized by a finite subset of unknown parameters contributing to the overall dimensionality of the unknown parameter vector. Such large-scale systems also exhibit spatial variability of some properties (e.g., material properties), which requires modeling these properties using random fields, leading to high dimensionality of the unknown parameter vector. Using techniques such as the truncated Karhunen–Loève expansion instead of a stochastic (or random field) mesh allows representing a random field with a relatively small number of random variables. The input-output measurement data may not provide (sufficient) information about all the unknown parameters. A parameter screening and selection process should be performed to select the most influent parameters to be used in the updating process (Saltelli et al. 2007). Sensitivity and identifiability analyses can be performed to identify the influential parameters (Ramancha et al. 2022).

4.3.2 Sampling Posterior Distribution using TMCMC

The idea behind TMCMC is to avoid sampling directly the target distribution (i.e., posterior $p(\boldsymbol{\theta}|\mathbf{u},\mathbf{y})$) but rather sample an easier-to-sample distribution and then weigh, resample, and perturb the samples in a series of stages to approximate the target distribution. To achieve this, TMCMC constructs a series of intermediate distributions $p(\boldsymbol{\theta}|\mathbf{u},\mathbf{y})_j$, $j=0,1,...,m$, referred to as tempered posteriors, that start from the prior distribution $p(\boldsymbol{\theta})$ (easy to sample) and converge to the posterior distribution $p(\boldsymbol{\theta}|\mathbf{u},\mathbf{y})$ (hard to sample) as

$$p(\boldsymbol{\theta}|\mathbf{u},\mathbf{y})_j \propto p(\mathbf{y}|\mathbf{u},\boldsymbol{\theta})^{\beta_j} \times p(\boldsymbol{\theta}), \quad j=0,1,...,m, \quad 0=\beta_0<\beta_1<...<\beta_m=1 \tag{4.6}$$

where β_j is the tempering parameter at stage j. At the initial stage ($j=0$), the tempered posterior $p(\boldsymbol{\theta}|\mathbf{u},\mathbf{y})_0$ is just the prior $p(\boldsymbol{\theta})$ since $\beta_0=0$, and at the final stage ($j=m$), the tempered posterior $p(\boldsymbol{\theta}|\mathbf{u},\mathbf{y})_m$ is the target posterior $p(\boldsymbol{\theta}|\mathbf{u},\mathbf{y})$ since $\beta_m=1$. The tempered posterior distribution $p(\boldsymbol{\theta}|\mathbf{u},\mathbf{y})_j$ at each stage j is approximated by a set of weighted samples (also known as particles). The j^{th} stage tempered posterior $p(\boldsymbol{\theta}|\mathbf{u},\mathbf{y})_j$ particles are obtained by weighing, resampling, and perturbing (using Markov chain Monte Carlo) the particles approximating the $(j-1)^{th}$ stage tempered posterior $p(\boldsymbol{\theta}|\mathbf{u},\mathbf{y})_{j-1}$. In plain English, the samples representing the prior distribution (stage $j=0$) are weighed, resampled, and perturbed multiple times, once at every stage, until they approximate the posterior distribution (stage $j=m$). In this paper, resampling is performed using random sampling, and the perturbation of particles is performed using a few MCMC steps with the Metropolis-Hastings algorithm. At each stage, each particle's perturbation (through a few MCMC steps) is independent of the others and hence these particle perturbations can be parallelized. However, note that the TMCMC stages still proceed

sequentially and thus cannot be parallelized. Refer to (Ching and Chen 2007; Minson et al. 2013) for the theory behind the TMCMC algorithm and refer to Table 2 of (Ramancha et al. 2022) for the TMCMC algorithm used in this paper.

4.4 Surrogate Modeling

Surrogate modeling can be used to reduce the computational time of expensive physics/mechanics-based numerical simulations by replacing them with approximate functions that are much faster to evaluate. As the name suggests, the surrogate model is used as a substitute for the FE model. Note that the physics-based model is still the underpinning behind the surrogate model construction. Surrogate modeling can be used for model calibration, identifiability and sensitivity analysis, uncertainty quantification, engineering design, optimization, and for any purpose that requires repeated model evaluations. In the literature, surrogate models are also known as response surface models, metamodels, or model emulators. The goal is to construct a cheap-to-evaluate "surrogate" model g that emulates the response of an expensive-to-evaluate mathematical model h (Forrester et al. 2008; Gramacy 2020).

Let $z \in \Omega_z \subset \mathbb{R}$ be a scalar output FE response of interest of FE model $h(.)$ parameterized by $\mathbf{x} \in \Omega_{\mathbf{x}} \subset \mathbb{R}^{n_{\mathbf{x}}}$, i.e., $z = h(\mathbf{x})$. Vector $\mathbf{x}$ contains quantities such as unknown parameters and input loading parameters of the FE model. The FE output/response of interest z is assumed scalar in this section to illustrate the surrogate modeling. In general, a surrogate model is constructed for each FE output of interest. The surrogate model is a mapping $g : \Omega_{\mathbf{x}} \to \Omega_z$, where $g(\mathbf{x})$ denotes the surrogate predicted response at $\mathbf{x}$. For building a surrogate model, the FE model $h(.)$ is assumed continuous in $\mathbf{x}$ and is known at n discrete

observations or samples $\{\mathbf{x}^{(i)} \rightarrow z^{(i)} = h(\mathbf{x}^{(i)}) \mid i = 1,...,n\}$. Such model regularity assumption is needed for surrogate modeling. Under this setting, the objective is to construct an approximation g for cheaper prediction of the FE response of interest at any $\mathbf{x}$.

Local and global are the two primary variants of surrogate modeling. In local surrogate modeling, the goal is to approximate the FE model only in a certain local region of interest of the parameter space $\Omega_{\mathbf{x}}$, e.g., where the posterior distribution is mainly concentrated (Li and Marzouk 2014; Takhtaganov and Müller 2018). Global surrogate modeling aims at approximating the FE model over the entire parameter space $\Omega_{\mathbf{x}}$. This paper considers global surrogate modeling.

4.4.1 Surrogate Modeling Workflow

There exist numerous approaches for surrogate modeling in the literature. However, they all follow a similar workflow (Forrester et al. 2008) (Figure 4.1): (1) Generating initial samples of parameter vector $\mathbf{x}$ by a sampling strategy or design of computer experiments, (2) evaluating the FE model at these samples to generate a training data set, (3) fitting or training the surrogate model, (4) assessing the fitted surrogate model, and (5) enhancing or updating the training data.

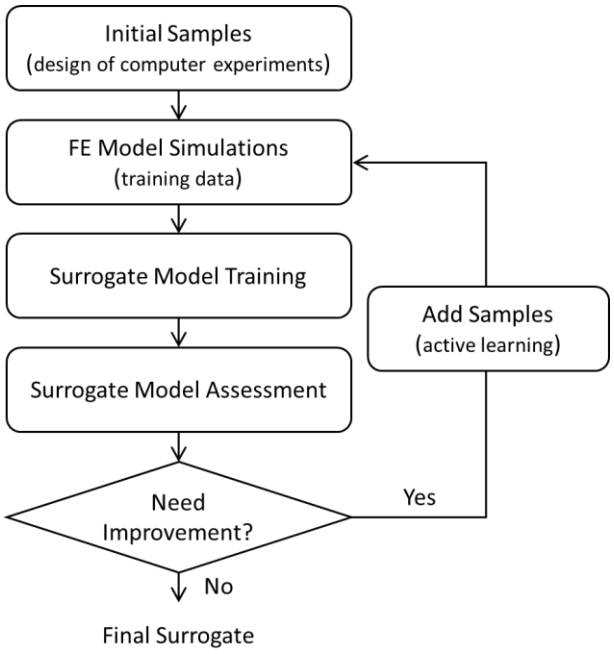

Figure 4.1: Surrogate modeling workflow.

4.4.1.1 Sampling Strategy/ Design of Computer Experiments

The goal is to construct a surrogate model for the entire parameter space $\Omega_{\mathbf{x}}$ (global surrogate). In such a case, space-filling or exploratory designs are primarily used as a sampling strategy (Santner et al. 2003). In such designs, the sample points are spread throughout the parameter space $\Omega_{\mathbf{x}}$ as uniformly as possible. Such uniform spreading is ideal if one has no reason to sample a particular region of parameter space more densely than other regions. Full-factorial design, designs based on measures of distance (e.g., maximin distance design), designs based on pseudo-random sampling (e.g., uniformly distributed random numbers/sequences, Latin hypercube sampling), designs based on quasi-random sampling (e.g., Sobol sequence, Halton sequence, Hammersley set) are methods available for space-filling (Santner et al. 2003). In this paper, Sobol sequence is used for space-filling. The sequence property allows adding new training points to the training set without discarding the previous training samples. Thus, the new

training set (previous samples + new samples) maintains the space-filling nature. Therefore, if the surrogate model needs improvement at the surrogate model assessment stage, new training points can be added to the original training set, while maintaining the space-filling nature. Let $\{\mathbf{x}^{(i)} \mid i = 1,...,n\}$ be the initial training samples, where n denotes the number of initial samples.

4.4.1.2 FE Model Evaluations

Once the initial training samples $\{\mathbf{x}^{(i)} \mid i = 1,...,n\}$ are determined, the FE model $h(\mathbf{x})$ needs to be evaluated at these training samples to obtain the response of interest z. Parallel computing can be leveraged since here the FE analyses are independent of each other. After assembling the initial training samples and their corresponding FE outputs, the initial training dataset is defined by $\{\mathbf{x}^{(i)} \rightarrow z^{(i)} = h(\mathbf{x}^{(i)}) \mid i = 1,...,n\}$.

4.4.1.3 Surrogate Model Construction

The goal is to construct a global surrogate model over the entire parameter space $\Omega_{\mathbf{x}}$. As defined earlier, the surrogate model is a mapping $g : \Omega_{\mathbf{x}} \rightarrow \Omega_z$ and $g(\mathbf{x})$ denotes the surrogate predicted response at $\mathbf{x}$. The loss function is the cost $L[g(\mathbf{x}), z]$ of predicting $g(\mathbf{x})$ when the truth is z (FE response). The loss function is usually zero if there is no error and positive otherwise, for example, the squared error loss $L[g(\mathbf{x}), z] = (z - g(\mathbf{x}))^2$. The goal is to find the optimum surrogate model g that minimizes the loss $L[g(\boldsymbol{\theta}), z]$. Constructing the optimal surrogate or training the surrogate model depends on the type of surrogate model. There exist many types of surrogate models in the literature; popular ones include PCE, GPR, support vector machines, and artificial neural networks. This paper considers the PCE and GPR surrogate

modeling methods, the training of which are briefly described in Sections 4.4.2 and 4.4.3, respectively.

4.4.1.4 Surrogate Model Assessment

Let $\hat{g}(\mathbf{x})$ be the fitted/trained surrogate model with training data $t = \{(\mathbf{x}^{(i)}, z^{(i)}) \mid i = 1,...,n\}$. A fitted model usually does well on the training data but may not generalize well. Techniques such as split sampling, cross validation, or bootstrapping can be used to assess the generalization ability of the fitted surrogate model. This paper uses split sampling, which requires a test set different from the training set to assess the surrogate model. The error of the fitted surrogate model $\hat{g}(\mathbf{x})$ on the test set $t' = \{(\mathbf{x}'^{(i)}, z'^{(i)}) \mid i = 1,...,n'\}$ can be computed as

$$err = \frac{1}{n'} \sum_{i=1}^{n'} L\left[\hat{g}(\mathbf{x}'^{(i)}), z'^{(i)} \right] \tag{4.7}$$

where err provides an estimate of the average generalization error of the fitted surrogate model $\hat{g}(\mathbf{x})$.

4.4.1.5 Enhancing the Training Data

If the test set error err is larger than the acceptable threshold, the existing training set can be enhanced by adding new training samples. Since the Sobol sequence is used in this paper as the space-filling strategy, the most straightforward approach is to add the subsequent samples of the Sobol sequence as new training points to the existing training set. Thus, the new training set (existing training set + new samples) maintains the space-filling property. However, one could also add new training samples at strategic locations (a process known as active learning)

(Liu et al. 2017). For example, when using a GPR surrogate, new training samples can be added at places where the variance of the fitted surrogate is high.

4.4.2 Polynomial Chaos Expansion Overview

PCE is the most celebrated method for uncertainty propagation and computing Sobol indices in variance-based global sensitivity analysis (Smith 2013; Sudret 2007, 2014). PCE is used in this paper as a surrogate modeling tool. The FE model h is viewed as a mapping between the parameter vector $\mathbf{x} \in \Omega_{\mathbf{x}} \subset \mathbb{R}^{n_{\mathbf{x}}}$ and scalar output $z \in \Omega_z \subset \mathbb{R}$. The probability distribution of $\mathbf{x}$ is denoted by $p(\mathbf{x})$. Let us define the following function space:

$$\mathcal{F} = \{ f : \mathbb{R}^{n_{\mathbf{x}}} \to \mathbb{R} \text{ such that } E_{\mathbf{x}}\left[f^2(\mathbf{x}) \right] < \infty \} \tag{4.8}$$

where $E_{\mathbf{x}}\left[f^2(\mathbf{x}) \right] = \int_{\mathbf{x}} f^2(\mathbf{x})\, p(\mathbf{x})\, d\mathbf{x}$. The functional space $\mathcal{F}$ is a collection of functions ($\mathbb{R}^{n_{\mathbf{x}}} \to \mathbb{R}$) that have finite variance or finite second moment under $p(\mathbf{x})$. It can be shown that $\mathcal{F}$ is a vector space ($\forall f_1, f_2 \in \mathcal{F}$ and $\forall a, b \in \mathbb{R}, a\, f_1 + b\, f_2 \in \mathcal{F}$). Let us also define a function $\langle .,. \rangle : \mathcal{F} \times \mathcal{F} \to \mathbb{R}$ as

$$\langle f_1(\mathbf{x}), f_2(\mathbf{x}) \rangle = E_{\mathbf{x}}\left[f_1(\mathbf{x})\, f_2(\mathbf{x}) \right] = \int_{\mathbf{x}} f_1(\mathbf{x})\, f_2(\mathbf{x})\, p(\mathbf{x})\, d\mathbf{x}, \quad f_1, f_2 \in \mathcal{F} \tag{4.9}$$

The function $\langle .,. \rangle$ is an inner product, as it satisfies all properties of an inner product. The functional space $\mathcal{F}$ defined in Eq. (4.8) with the inner product defined in Eq. (4.9) is a Hilbert space. Note that a Hilbert space is a generalization of the standard Euclidean space and all the theorems of vector algebra (or linear algebra) for Euclidean spaces (e.g., orthonormality, normalization, orthonormal basis, Gram-Schmidt orthogonalization procedure) are also valid for our Hilbert space $\mathcal{F}$. For example, any vector in the standard Euclidean vector space $\mathcal{V}$ can be

expressed as a linear combination of the orthonormal basis vectors of $\mathcal{V}$. This is also valid for our Hilbert space $\mathcal{F}$.

Let sequence of functions $\phi_1(\mathbf{x}), \phi_2(\mathbf{x}), ... \in \mathcal{F}$ form an orthonormal basis of the functional space $\mathcal{F}$. So, the sequence of functions must satisfy $\langle \phi_i(\mathbf{x}), \phi_j(\mathbf{x}) \rangle = 0 \; \forall i \neq j$ and $\langle \phi_i(\mathbf{x}), \phi_i(\mathbf{x}) \rangle = 1 \; \forall i$. Assuming the FE model $h(\mathbf{x})$ belongs to the functional space $\mathcal{F}$, i.e., $h(\mathbf{x}) \in \mathcal{F}$ (equivalent to assuming that $h : \mathbb{R}^{n_\mathbf{x}} \to \mathbb{R}$ is a function with finite variance), $h(\mathbf{x})$ of space $\mathcal{F}$ can be expressed as

$$h(\mathbf{x}) = \sum_{i=1}^{\infty} c_i \, \phi_i(\mathbf{x}) \quad with \quad c_i = \langle h(\mathbf{x}), \phi_i(\mathbf{x}) \rangle \tag{4.10}$$

where $\{c_i\}_{i=1}^{\infty}$ are the coefficients. Eq. (4.10) is an infinite orthogonal series expansion of function $h(\mathbf{x})$. In addition, as the basis $\phi_1(\mathbf{x}), \phi_2(\mathbf{x}), ... \in \mathcal{F}$ is made of orthonormal polynomials, Eq. (4.10) is termed an orthonormal polynomial expansion or polynomial chaos expansion of $h(\mathbf{x})$.

There are many approaches to find a set of orthonormal polynomials that form an orthonormal basis of the functional space $\mathcal{F}$. One such approach is by using Gram-Schmidt orthogonalization procedure. For the case of a scalar unknown parameter x (or parameter vector $\mathbf{x}$ contains only one element x), one can start with the monomial sequence $1, x, x^2, x^3, ...$ and perform the Gram-Schmidt orthogonalization procedure to build the orthonormal basis $\phi_1(x), \phi_2(x), ... \in \mathcal{F}$. Classical families of orthogonal polynomials have been discovered previously to solve various problems of physics, engineering, etc. (Sudret 2014). Note that the orthogonal polynomials sequence will depend on the probability distribution function $p(x)$. For

the vector case of unknown parameters $\mathbf{x}=\left[x_1,...,x_{n_\mathbf{x}}\right]^T$, the orthonormal basis of the functional space $\mathcal{F}$ ($\{\phi_i(\mathbf{x})\}_{i=1}^{\infty}$) can be built using Gram-Schmidt orthogonalization procedure as well. For the special case when $\mathbf{x}=\left[x_1,...,x_{n_\mathbf{x}}\right]^T$ contains statistically independent components (i.e., $p(\mathbf{x})=\prod_{j=1}^{n_\mathbf{x}} p(x_j)$), the orthonormal polynomial sequence $\{\phi_i(\mathbf{x})\}_{i=1}^{\infty}$ can be built by taking the tensor product of the orthonormal polynomial sequences $\{\phi_{ij}(\mathbf{x})\}_{i=1}^{\infty}$ of component x_j $(j=1,\ldots,n_\mathbf{x})$.

The PCE of model h given by Eq. (4.10) is an infinite series expansion, which cannot be handled in practice. A truncation should be performed to enable practical computations. The orthonormal polynomial $\phi_i(\mathbf{x})\in\mathcal{F}$ of polynomial degree ρ is of the form

$$\phi_i(\mathbf{x})=\sum_{i_1+...+i_{n_\mathbf{x}}\le\rho} a_{i_1...i_{n_\mathbf{x}}} x_1^{i_1}...x_{n_\mathbf{x}}^{i_{n_\mathbf{x}}};\quad i_1,...,i_{n_\mathbf{x}}\in W \tag{4.11}$$

where W represents the set of whole numbers. Note that the degree of a polynomial is the highest degree of all its monomials (individual terms) and the degree of a monomial is the sum of all exponents of all variables ($x_1,...,x_{n_\mathbf{x}}$).

The standard way of truncation is to consider all orthonormal polynomials from the sequence $\{\phi_i(\mathbf{x})\}_{i=1}^{\infty}$ that have a polynomial degree less than ρ (defined by the modeler). The exponents $i_1,\ldots,i_{n_\mathbf{x}}$ satisfy $i_1+\ldots+i_{n_\mathbf{x}}\le\rho$. The hyperbolic cross truncation scheme is another scheme to further reduce the number of terms from the standard truncation (Sudret 2014). The idea behind it is to only include the terms for which the exponents $i_1,\ldots,i_{n_\mathbf{x}}$ satisfy

$\left((i_1)^{1/\alpha}+\ldots+(i_{n_{\mathbf{x}}})^{1/\alpha}\right)^{\alpha}\leq\rho$ where α is the cross-truncation factor. If $\alpha=1$, the hyperbolic truncation scheme reduces to the standard truncation scheme.

The truncated PCE considering only orthonormal basis functions $\phi_i(\mathbf{x})'s$ according to some selected truncation scheme is given by

$$h(\mathbf{x})\approx\underbrace{\sum_{i=1}^{P}c_i\,\phi_i(\mathbf{x})}_{=g(\mathbf{x})}\quad with\quad c_i=\left\langle h(\mathbf{x}),\phi_i(\mathbf{x})\right\rangle \tag{4.12}$$

where P is the total number of $\phi_i(\mathbf{x})'s$ in accordance with the selected truncation scheme. This truncated PCE approximation of the FE model h can be used as the surrogate model g.

Training the surrogate model involves computing the coefficients $\{c_i\}_{i=1}^{P}$. The integral structure of the coefficients $c_i=\left\langle h(\mathbf{x}),\phi_i(\mathbf{x})\right\rangle=\int_{\mathbf{x}}\left[h(\mathbf{x})\,\phi_i(\mathbf{x})\right]p(\mathbf{x})d\mathbf{x}$ can be exploited to compute them. Integration methods using quadrature rules (Gaussian quadrature or Clenshaw-Curtis quadrature) and sparse grids (e.g., Smolyak's sparse grid), Monte Carlo integration, or Bayesian quadrature can be used to numerically evaluate the integral (Smith 2013). In this paper, we use the least-squares method to compute the coefficients. This approach is simpler and does not exploit the integral structure of the coefficients.

In this approach, the FE response ($h(\mathbf{x})$ or z) is considered as the sum of a truncated series ($g(\mathbf{x})$, shown in Eq. (4.12)) and a residual term (ε) as

$$z=g(\mathbf{x})+\varepsilon\;;\quad g(\mathbf{x})=\sum_{j=1}^{P}c_j\,\phi_j(\mathbf{x}) \tag{4.13}$$

We consider the squared error loss, i.e., $L\left[g(\mathbf{x}), z\right] = \left(z - g(\mathbf{x})\right)^2$, as loss function and assume a zero-mean residual term ε. This is a typical linear regression problem using basis functions $\{\phi_j(\mathbf{x}),\ j = 1, ..., n\}$ subject to a least-squares minimization. Hence, the decision rule is given by

$$\text{Decision rule}: \quad \hat{\mathbf{c}} = \arg\min_{\mathbf{c}} \ \frac{1}{n} \sum_{i=1}^{n} \left[z^{(i)} - \sum_{j=1}^{P} c_j \, \phi_j(\mathbf{x}^{(i)}) \right]^2 \tag{4.14}$$

For the training samples $t = \{(\mathbf{x}^{(i)}, z^{(i)}) \,|\, i = 1, ..., n\}$, Eq. (4.13) can be written as

$$\underbrace{\begin{pmatrix} z^{(1)} \\ \vdots \\ z^{(n)} \end{pmatrix}_{n\times 1}}_{\mathbf{z}} = \underbrace{\begin{pmatrix} \phi_1(\mathbf{x}^{(1)}) & \cdots & \phi_P(\mathbf{x}^{(1)}) \\ \vdots & \ddots & \vdots \\ \phi_1(\mathbf{x}^{(n)}) & \cdots & \phi_p(\mathbf{x}^{(n)}) \end{pmatrix}_{n\times P}}_{\mathbf{\Phi}} \underbrace{\begin{pmatrix} c_1 \\ \vdots \\ c_P \end{pmatrix}_{P\times 1}}_{\mathbf{c}} + \underbrace{\begin{pmatrix} \varepsilon_1 \\ \vdots \\ \varepsilon_n \end{pmatrix}_{n\times 1}}_{\boldsymbol{\varepsilon}} \tag{4.15}$$

where $\mathbf{z} \in \mathbb{R}^n$ denotes the vector of FE responses, $\mathbf{\Phi} \in \mathbb{R}^{n\times P}$ denotes the design matrix, $\mathbf{c} \in \mathbb{R}^P$ is the vector of unknown coefficients of the PCE surrogate model, and $\boldsymbol{\varepsilon} \in \mathbb{R}^n$ is the residual vector. The decision rule in Eq. (4.14) leads to the following normal equations:

$$(\mathbf{\Phi}^T \mathbf{\Phi})\, \hat{\mathbf{c}} = \mathbf{\Phi}^T \, \mathbf{z} \tag{4.16}$$

If $n > P$ and $rank(\mathbf{\Phi}) = P$, then the estimate of $\mathbf{c}$ according to the decision rule in Eq. (4.14) is

$$\hat{\mathbf{c}} = (\mathbf{\Phi}^T \mathbf{\Phi})^{-1} \mathbf{\Phi}^T \, \mathbf{z} \tag{4.17}$$

If $rank(\mathbf{\Phi}) < P$ and/or $n < P$, the normal equations in Eq. (4.16) have infinite solutions for $\hat{\mathbf{c}}$. In this case, out of all the possible solutions, the sparse solutions ($\hat{\mathbf{c}}$ that contains a small number of non-zero coefficients) can be obtained by solving the regularized least squares

problem (regularized with the L1 norm of $\mathbf{c}$). This is referred to as the Lasso regression method of which the decision rule of which is given by

$$\text{Decision rule}: \quad \hat{\mathbf{c}} = \arg\min_{\mathbf{c}} \ \frac{1}{n}\sum_{i=1}^{n}\left[z^{(i)} - \sum_{j=1}^{P} c_j \, \phi_j(\mathbf{x}^{(i)}) \right]^2 + \lambda \sum_{j=1}^{P} \left| c_j \right| \tag{4.18}$$

The least angle regression (LARS) algorithm can be used to efficiently solve the Lasso regression problem (Blatman and Sudret 2011; Hastie et al. 2009). As the value of λ increases, the sparsity of the solution $\hat{\mathbf{c}}$ increases. The optimum value of λ, controlling the level of sparsity in the coefficients $\hat{\mathbf{c}}$, is selected using a cross-validation technique in this paper.

Selecting the truncation polynomial degree ρ can be difficult in practice. In this paper, we select a large enough ρ, resulting in a very large value of P. This most likely lands the regression problem in the $n < P$ scenario – high dimensional regression. We perform Lasso regression using the LARS algorithm. Since Lasso encourages sparsity in coefficients, the corresponding coefficients of polynomial terms that are not required will automatically shrink to zero (Hastie et al. 2009). (Chrisnata et al. 2019; Lovett et al. 2018; Rao and Prabhakaran 2014).

4.4.3 Gaussian Process Regression Overview

Gaussian processes for nonlinear curve fitting have been used increasingly in surrogate modeling. Recall that the surrogate model is a mapping $g : \Omega_{\mathbf{x}} \to \Omega_z$. This mapping $g(.)$ is unknown and modeled as a random process (or field). The Gaussian process model is a flexible and convenient class of models to represent the random process $g(.)$ (Rasmussen and Williams 2005). For surrogate modeling, $g(\mathbf{x})$ is modeled as a zero-mean Gaussian process with covariance function $k(\mathbf{x}, \mathbf{x}')$ denoted as

$$g(\mathbf{x}) \sim \mathcal{GP}\left(0, k(\mathbf{x}, \mathbf{x}')\right) \tag{4.19}$$

The choice of covariance function determines almost all the generalization properties of $g(\mathbf{x})$. The training data consists of $t = \{\mathbf{X}, \mathbf{z}\}$ where $\mathbf{X} = \left\{\mathbf{x}^{(1)}, ..., \mathbf{x}^{(n)}\right\}$ and $\mathbf{z} = \left[z^{(1)}, ..., z^{(n)}\right]^T$. We assume that this training data is obtained from the following measurement model:

$$z = g(\mathbf{x}) + \varepsilon \; ; \quad g(\mathbf{x}) \sim \mathcal{GP}\left(0, k(\mathbf{x}, \mathbf{x}')\right) \quad \text{and} \quad \varepsilon \sim \mathcal{N}(0, \sigma_\varepsilon^2) \tag{4.20}$$

where $g(\mathbf{x})$ and ε are statistically independent. From Eqs. (4.19) and (4.20), the Gaussian process $g(\mathbf{x})$ conditioned on the training data t is also a Gaussian process with mean function $\tilde{m}(\mathbf{x})$ and covariance function $\tilde{k}(\mathbf{x}, \mathbf{x}')$ as (Rasmussen and Williams 2005)

$$g(\mathbf{x}) \,|\, t \;\sim\; \mathcal{GP}\left(\tilde{m}(\mathbf{x}), \tilde{k}(\mathbf{x}, \mathbf{x}')\right) \tag{4.21}$$

where

$$\begin{aligned} \tilde{m}(\mathbf{x}) &= \mathbf{K}(\mathbf{x}, \mathbf{X}) \times \left(\mathbf{K}(\mathbf{X}, \mathbf{X}) + \sigma_\varepsilon^2 \mathbf{I}_n\right)^{-1} \times (\mathbf{z}) \\ \tilde{k}(\mathbf{x}, \mathbf{x}') &= k(\mathbf{x}, \mathbf{x}') - \mathbf{K}(\mathbf{x}, \mathbf{X}) \times \left(\mathbf{K}(\mathbf{X}, \mathbf{X}) + \sigma_\varepsilon^2 \mathbf{I}_n\right)^{-1} \times \mathbf{K}(\mathbf{X}, \mathbf{x}') \end{aligned} \tag{4.22}$$

in which

$$\begin{aligned} \mathbf{K}(\mathbf{X}, \mathbf{X}) &= \begin{pmatrix} k(\mathbf{x}^{(1)}, \mathbf{x}^{(1)}) & \cdots & k(\mathbf{x}^{(1)}, \mathbf{x}^{(n)}) \\ \vdots & \ddots & \vdots \\ k(\mathbf{x}^{(n)}, \mathbf{x}^{(1)}) & \cdots & k(\mathbf{x}^{(n)}, \mathbf{x}^{(n)}) \end{pmatrix} \in \mathbb{R}^{n \times n} \\ \mathbf{K}(\mathbf{x}, \mathbf{X}) &= \begin{pmatrix} k(\mathbf{x}, \mathbf{x}^{(1)}) & \cdots & k(\mathbf{x}, \mathbf{x}^{(n)}) \end{pmatrix} \in \mathbb{R}^{1 \times n} \\ \mathbf{K}(\mathbf{X}, \mathbf{x}) &= \mathbf{K}(\mathbf{x}, \mathbf{X})^T \in \mathbb{R}^{n \times 1} \end{aligned} \tag{4.23}$$

From Eqs. (4.20) and (4.21), the predictive distribution $p(z \,|\, \mathbf{x}, t)$ (for predicting the response at $\mathbf{x}$ conditioned on the training data t) is given by

$$p\left(z \mid \mathbf{x}, t\right) = \mathcal{N}\left(\tilde{m}(\mathbf{x}), \tilde{k}(\mathbf{x}, \mathbf{x}) + \sigma_{\varepsilon}^2\right) \tag{4.24}$$

The mean function $\tilde{m}(\mathbf{x})$ is, by definition, the fitted surrogate model $\hat{g}(\mathbf{x})$, i.e.,

$$\hat{g}(\mathbf{x}) = \tilde{m}(\mathbf{x}) \tag{4.25}$$

Let $\boldsymbol{\gamma}$ be the parameters of the covariance function $k(\mathbf{x}, \mathbf{x}')$. For example, the length scale l and variance σ^2 are the parameters $\boldsymbol{\gamma}$ of the standard radial basis covariance function defined as

$$k(\mathbf{x}, \mathbf{x}') = \sigma^2 \exp\left(-\frac{1}{2l^2}\sum_{i=1}^{n_{\mathbf{x}}}\left(x_i - x_i'\right)^2\right), \quad \mathbf{x} \in \mathbb{R}^{n_{\mathbf{x}}} \tag{4.26}$$

The hyperparameters $\{\boldsymbol{\gamma}, \sigma_{\varepsilon}\}$ can be obtained utilizing the training data $t = \{\mathbf{X}, \mathbf{z}\}$ with the following application of Bayes theorem:

$$p\left(\boldsymbol{\gamma}, \sigma_{\varepsilon} \mid \mathbf{X}, \mathbf{z}\right) \propto p\left(\mathbf{z} \mid \mathbf{X}, \boldsymbol{\gamma}, \sigma_{\varepsilon}\right) \times p\left(\boldsymbol{\gamma}, \sigma_{\varepsilon}\right) \tag{4.27}$$

Using Eq. (4.20), the likelihood function $p\left(\mathbf{z} \mid \mathbf{X}, \boldsymbol{\gamma}, \sigma_{\varepsilon}\right)$ is given by

$$p\left(\mathbf{z} \mid \mathbf{X}, \boldsymbol{\gamma}, \sigma_{\varepsilon}\right) = \mathcal{N}\left(\mathbf{0}, \mathbf{K}\left(\mathbf{X}, \mathbf{X}; \boldsymbol{\gamma}\right) + \sigma_{\varepsilon}^2 \mathbf{I}_n\right) \tag{4.28}$$

Note that the dependence of $\mathbf{K}(\mathbf{X}, \mathbf{X})$ on the hyperparameter vector $\boldsymbol{\gamma}$ is shown explicitly in Eq. (4.28). Instead of obtaining the full posterior distribution $p\left(\boldsymbol{\gamma}, \sigma_{\varepsilon} \mid \mathbf{X}, \mathbf{z}\right)$, the maximum likelihood estimate, denoted by $\{\hat{\boldsymbol{\gamma}}, \hat{\sigma}_{\varepsilon}\}$, is used in this paper as a plausible estimate of the parameters $\{\boldsymbol{\gamma}, \sigma_{\varepsilon}\}$ (Rasmussen and Williams 2005). Thus,

$$\begin{aligned}\hat{\boldsymbol{\gamma}}, \hat{\sigma}_{\varepsilon} &= \arg\max_{\boldsymbol{\gamma}, \sigma_{\varepsilon}} \left\{\log p\left(\mathbf{z} \mid \mathbf{X}, \boldsymbol{\gamma}, \sigma_{\varepsilon}\right)\right\} \\ &= \arg\max_{\boldsymbol{\gamma}, \sigma_{\varepsilon}} \left\{-\frac{1}{2}\mathbf{z}^T\left(\mathbf{K}\left(\mathbf{X}, \mathbf{X}; \boldsymbol{\gamma}\right) + \sigma_{\varepsilon}^2 \mathbf{I}_n\right)^{-1}\mathbf{z} - \frac{1}{2}\log\left|\mathbf{K}\left(\mathbf{X}, \mathbf{X}; \boldsymbol{\gamma}\right) + \sigma_{\varepsilon}^2 \mathbf{I}_n\right| - \frac{n}{2}\log 2\pi\right\}\end{aligned} \tag{4.29}$$

The Broyden–Fletcher–Goldfarb–Shanno (BFGS) algorithm is used to solve the unconstrained nonlinear optimization problem defined in Eq. (4.29) (Kane and Rao 2018; Lovett et al. 2020; Rao and Vardy 2016).

4.5 Application Example

The inland waterways of the United States consist of more than 25,000 miles of navigable waters. During most seasons, navigation through many of the inland waterways is not possible without the use of hydraulic infrastructure. Wicket dams are installed to maintain an operational water elevation suitable for navigation, leading to discontinuities in water elevation along the inland waterways. Therefore, navigation/lock chambers have been constructed for cargo ships to transition between different water elevations (Figure 4.2).

Miter gates (sets of two leaves) are steel structures that allow passage of cargo ships through the navigation chamber so that the water level can be raised or lowered. Each navigation chamber has two miter gates, the upper and lower gates. Figure 4.2 shows a vessel approaching the upper gate from the upstream end and the flow of water from upstream to the navigation chamber through the upper culver valves.

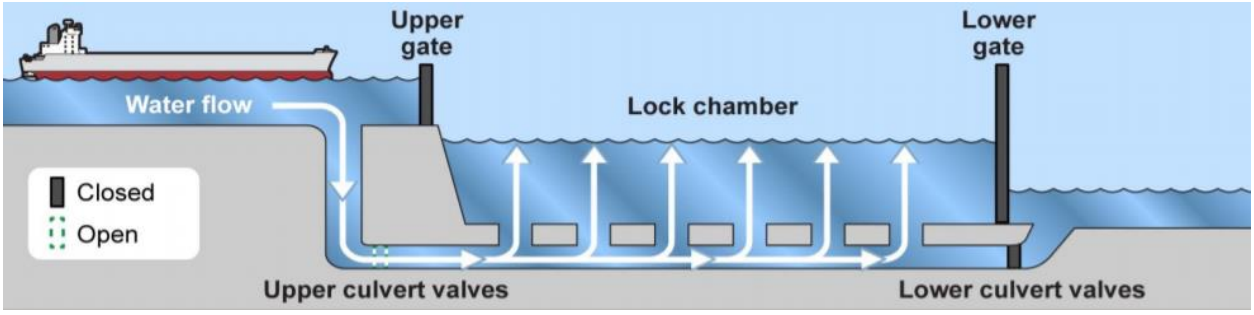

Figure 4.2: Navigation Chamber (Government Accountability Office 2018).

Figure 4.3a shows the actual miter gate (in its closed configuration) while Figure 4.3b, Figure 4.3c, and Figure 4.3d show a schematic representation of the plan view, elevation view

with various gate components labeled, and side view with the upstream and downstream water elevations of the closed gate. The U.S. Army Corps of Engineers (USACE) maintains and operates 236 gates at 191 sites in the United States (Eick et al. 2018b). In a recent survey, it was found that more than half of these structural assets have surpassed their 50-year economic design life (Foltz 2017).

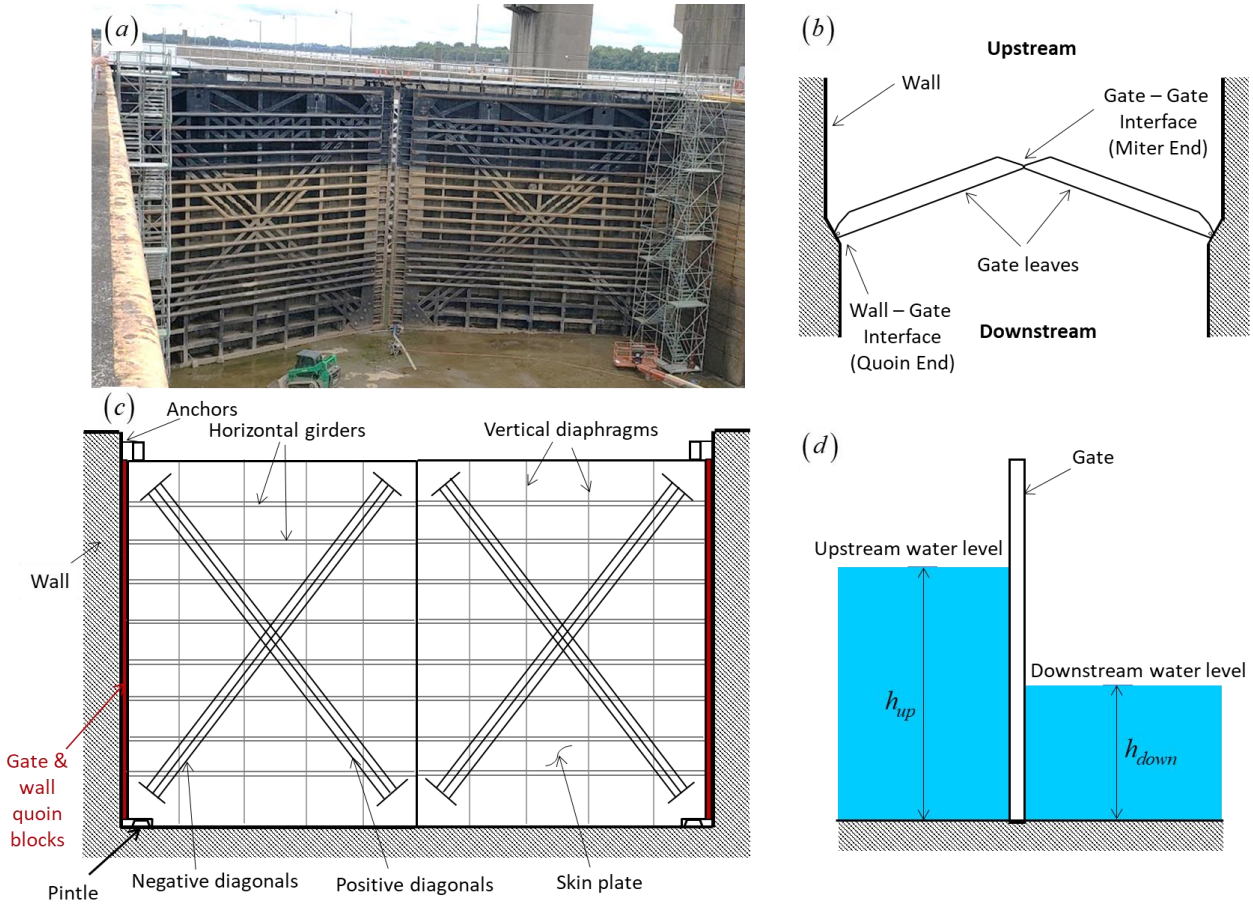

Figure 4.3: (a) Real miter gate (John T. Meyers locks, Kentucky, USA along the Ohio River), (b) top view, (c) elevation view, and (d) side view schematic of the gate.

4.5.1 Finite Element Model

The Greenup miter gate located in Kentucky, USA, along the Ohio River is considered as the testbed structure in this paper. A full-scale, mechanics-based, high-fidelity FE model of the

gate was developed using the Abaqus FEA software. Figure 4.4a and Figure 4.4b show the assembly view and mesh of the FE model, respectively. The geometric model of the gate is discretized (meshed) into 3D linear shell elements (using Abaqus element types S4R and S3R) except for the diagonal rods and anchors that are discretized into beam elements (using Abaqus element type B31). 3D shell elements are used instead of 3D solid elements to reduce the computational cost of the FE analysis. The full-scale FE model of the gate includes 97201 nodes and 94955 elements resulting in 550488 free degrees of freedom (translations and rotations).

The Greenup gate is equipped with strain gauges at various locations on the gate for damage detection purposes. The 46 uniaxial strain sensors used in this study, displayed according to their exact locations on the actual Greenup gate, are shown in the assembly view of the gate (Figure 4.4a). Greenup is a relatively new gate and the FE model considered herein was previously validated, assuming undamaged condition, using the strain data recorded from the uniaxial strain gauges installed on the gate (Eick et al. 2018a).

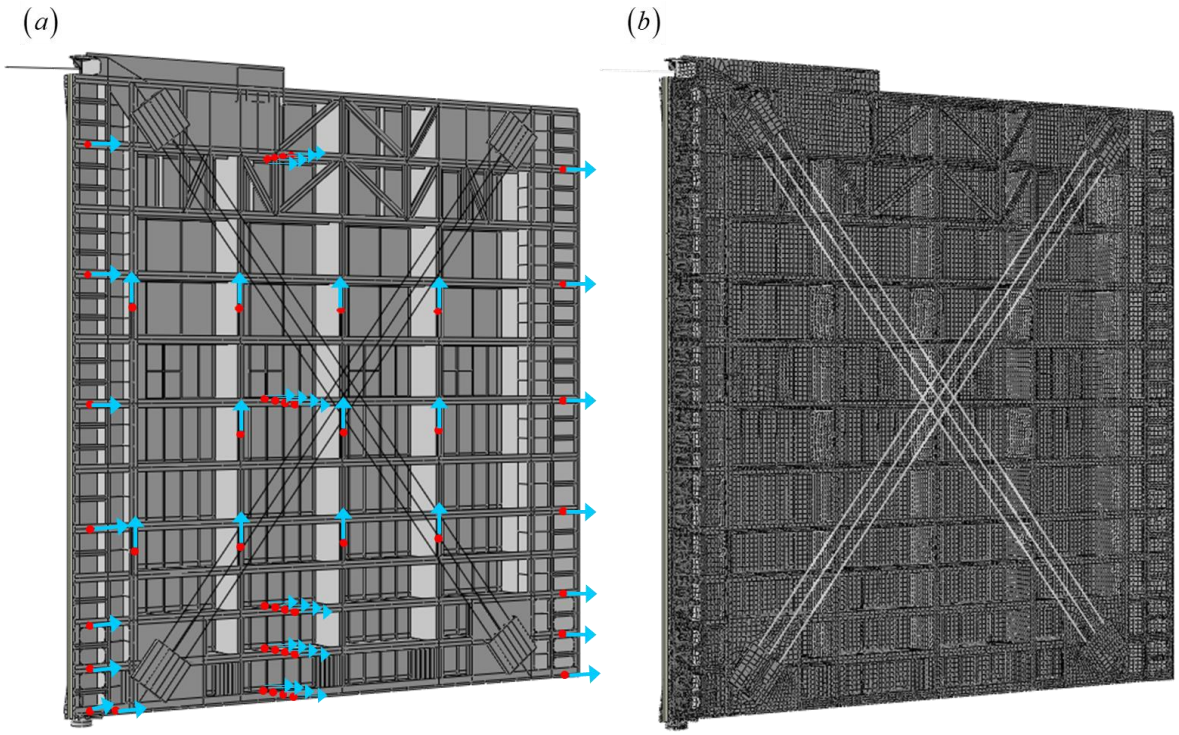

Figure 4.4: (a) Assembly view (red dots indicate locations of uniaxial strain gauges and blue arrows indicate their orientations), and (b) mesh of the FE model.

4.5.2 Damage Modes

As revealed by inspection results, some of the aspects of concern from an SHM perspective are (Eick et al. 2018b): (1) loss of contact or formation of a gap at the gate-wall and/or gate-gate interface; (2) loss of thickness in the gate components due to corrosion; (3) loss of tension in the diagonals resulting in gate misalignment; (4) cracking due to fatigue in various gate members such as welded connections of horizontal girders, skin plates, and pintles; (5) damage due to barge impact; and (6) general wear and tear of gate components. The first three aspects of concern are considered in this paper, and the unknown parameters associated with these damage modes are estimated using the FE model updating framework described in Section 4.3.

4.5.2.1 Loss of Contact between Gate and Wall

A miter gate experiences everyday time-varying hydraulic loads during operations. When the gate is closed, the hydrostatic loads are transferred from skin plate to vertical diaphragms and from there to horizontal girders. The gate components are labeled in Figure 4.3b and Figure 4.3c. The loads from the horizontal girders are transferred to the quoin and miter ends. The horizontal loads collected at the quoin end are transferred to the wall from gate top to bottom through quoin blocks (shown in red color in Figure 4.3c). The loads collected at the miter end are transferred to the other gate leaf.

Figure 4.5 show the gate quoin block and wall quoin block which are attached to the gate and wall, respectively. The quoin blocks (gate and wall) are also illustrated in Figure 4.3c. The hydraulic load is transferred from the gate to the wall, from top to bottom, through these quoin blocks.

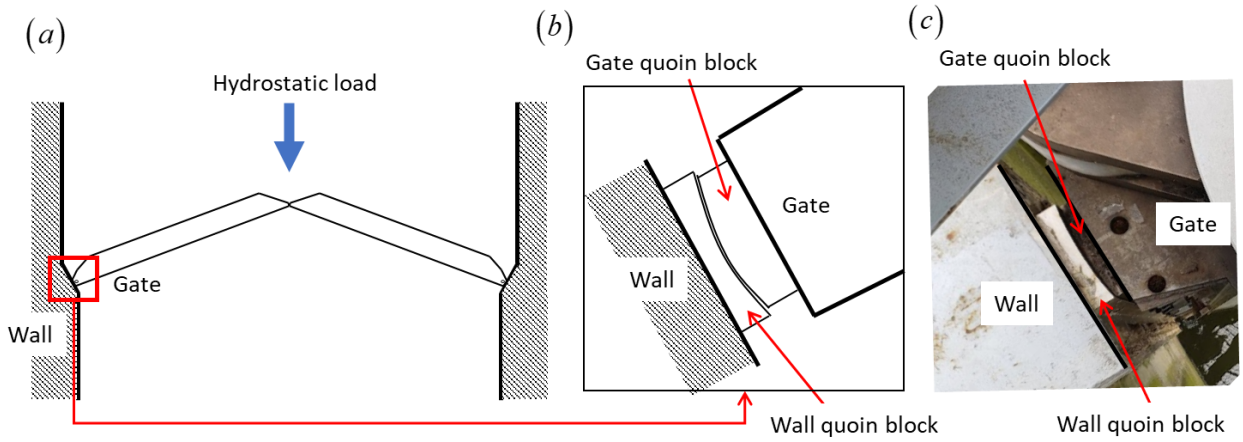

Figure 4.5: (a) Plan view with hydrostatic loading, (b) quoin blocks schematic, and (c) picture of quoin blocks from a real miter gate.

The loss of contact between the quoin blocks (through the formation of gap) is a common problem; it changes the load path causing the gate internal forces to redistribute leading to high stresses in undesirable parts of the gate. The internal force redistribution causes the gap to grow,

eventually leading to failure of the miter gate. For instance, the horizontal loads should not be supported by the pintle region as per design. However, the development of such a gap at the bottom of the gate leads to force aggregation in the pintle region. This is hugely problematic as this force redistribution in a region prone to fatigue cracking reduces the remaining useful life of the miter gate system.

In this study, only the loss of contact between the wall and the gate at the bottom near the pintle area is considered and is referred to as the "gap" from now on. The gap is visually inaccessible during operations, as the bottom part of the gate is always submerged under water during operations. For continuous operations, the idea is to estimate the amount of loss of contact (referred to as gap length) using the FE model updating framework and the strain measurement data.

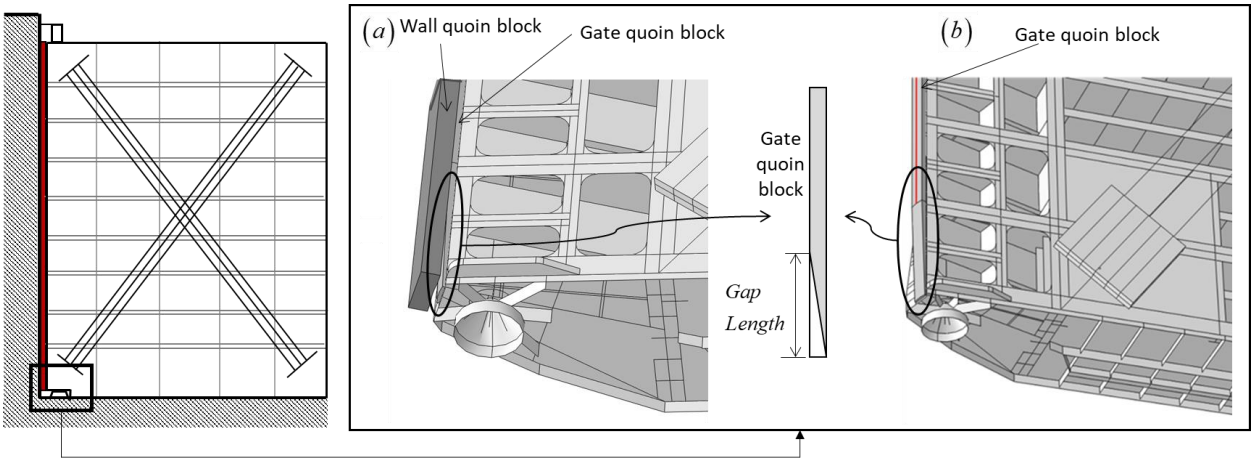

Figure 4.6: (a) Ideal approach (contact-type constraint between gate quoin block and wall quoin block), and (b) simplified approach (pinned boundary condition along the gate quoin block above the gap).

The ideal (most accurate) approach to modeling the gap between the wall and gate quoin blocks at the bottom of the gate (in the FE model) is by introducing a contact-type constraint between them (Figure 4.6a). However, in this paper, we employ a simplified approach where a pinned boundary condition is directly imposed along the gate quoin block above the gap instead

of modeling the wall quoin block and inserting a contact-type constraint between the two quoin blocks to support the gate laterally. To model the effect of a gap formation of length *GapLength* , the gate quoin block is left unrestrained (i.e., unpinned) over the length of the gap as shown in Figure 4.6b. The Ideal approach (contact-type constraint) captures the effect of partial gap closure after the gate is subjected to the hydrostatic loads. This approach requires a nonlinear FE analysis using an incremental-iterative solution strategy and is computationally very expensive. However, since the portion of the gap which closes is small under most hydrostatic loading scenarios, the simplified approach is a reasonable choice and is computationally highly advantageous.

4.5.2.2 Loss of Thickness due to Uniform Corrosion

A miter gate can be subdivided into three environmental zones defined by the upstream/downstream water elevations ((Estes et al. 2004; Evans et al. 2019)): (1) the atmospheric zone, (2) the splash zone, and (3) the submerged zone as shown in Figure 4.7a (side view of the gate). Figure 4.7b shows a real miter gate (from the John T. Myers locks along the Ohio River in Kentucky, USA) depicting the three zones. The atmospheric zone is the region of the gate that is generally not in contact with water even when the water elevation changes. This zone incurs the least damage due to corrosion and is visually accessible for monitoring (Spencer et al. 2019). The splash zone is the region of the gate that is in contact with air and water mainly from the changes in water elevation that allow the passage of marine transportation. This zone incurs the greatest damage due to corrosion, which is attributed to the water elevation changes in the chamber (Melchers 2004). Finally, the submerged zone is the region of the gate that is always underwater during operations. Monitoring for corrosion in the splash and submerged areas is not trivial as these regions are typically visually inaccessible while a miter gate is in operations.

Dewatering a lock chamber for inspections or sending a diver is a costly endeavor as it halts the navigation through the chamber.

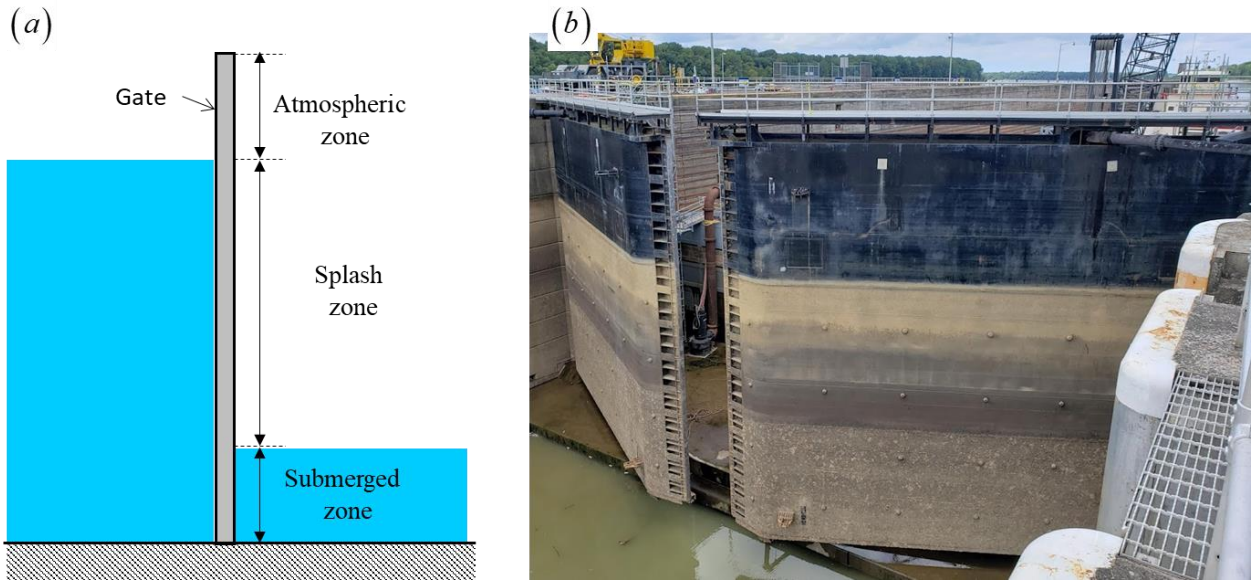

Figure 4.7: (a) Side view schematic of the gate showing the three environmental zones, and (b) picture of a real miter gate depicting the three zones.

In this study, only uniform corrosion in the splash and submerged zones is considered. In the FE model, corrosion is modelled as a uniform thickness loss in the steel plates (e.g., girder webs, girder flanges, and skin plates) in each zone. (Estes et al. 2004). The losses of thickness in the splash and submerged zones are denoted by parameters $Tl_{spl.}$ and $Tl_{sub.}$, respectively. Based on the design drawings of the Greenup gate provided by USACE, the following initial thicknesses (at pristine condition) are used: (1) $12.7mm$ for the skin plates, horizontal girder webs, and vertical girders; (2) $15.9mm$ for the end vertical girder web (at each side of a gate leaf).

4.5.2.3 Loss of Tension in the Diagonal Rods

The diagonal rods across the gate are pretensioned to resist torsional loads during opening and closing of the gate (Eick et al. 2018b). It also resists sagging of the gate due to its self-weight and keeps the gate plumb for achieving good miter contact. The diagonals gradually lose tension over time causing stress redistribution inside the gate. For FE modeling and parameter estimation, it is assumed that the three positive diagonal rods have the same remaining tension, $P_{pos.}$, and the three negative diagonal rods have the same remaining tension, $P_{neg.}$. Based on the design drawings of the Greenup gate provided by USACE, the initial tension is $965MPa$ for each of the positive diagonal rods and $620MPa$ for each of the negative diagonal rods.

4.5.3 Surrogate Modeling

A global surrogate of the miter gate FE model is developed in this section. The unknown parameter vector is $\boldsymbol{\theta} = [GapLen., P_{pos.}, P_{neg.}, Tl_{spl.}, Tl_{sub.}]^T$ and the input loading vector is $\mathbf{u} = [h_{down}, h_{up}]^T$ where h_{up} and h_{down} denote the upstream and downstream water elevation levels, respectively (as depicted in Figure 4.3d). The idea is to construct a surrogate model that maps parameters $\mathbf{x} = \left[\boldsymbol{\theta}^T, \mathbf{u}^T\right]^T \in \mathbb{R}^7$ to the FE output response of interest (strain at each of the 46 uniaxial strain gauge locations) $\mathbf{z} \in \mathbb{R}^{46}$.

In this paper, we used an Intel Xeon W-2155 @ 3.30 GHz CPU with 10 cores / 20 threads and 128 GB RAM workstation for FE analysis, surrogate model construction, and FE model updating. This computer is simply referred to as the workstation henceforth.

Table 4.1: Upper and lower bounds of parameters for space filling.

	Unknown parameters					Input loading	
bounds	*GapLen.* [m]	$P_{pos.}$ [MPa]	$P_{neg.}$ [MPa]	$Tl_{spl.}$ [mm]	$Tl_{sub.}$ [mm]	h_{down} [m]	h_{up} [m]
lower	0.0	0.0	0.0	0.0	0.0	2.5	12.7
upper	4.6	965	620	10.0	10.0	5.8	15.2

The lower and upper bounds (for space filling) of five unknown and two input loading parameters are shown in Table 4.1. These values are chosen based on the literature ((Eick et al. 2018b; Estes et al. 2004)) and discussions with USACE engineers. The Sobol quasi-random sequence is used as the space filling method and the first 200 samples of the sequence, $\{\mathbf{x}^{(i)} | \ i = 1, ..., 200\}$, are drawn and utilized. The FE model is evaluated at these sample points and the strain at each of the 46 strain gauge locations is recorded $\{\mathbf{z}^{(i)} = \mathbf{h}(\mathbf{x}^{(i)}) \in \mathbb{R}^{46} \mid \ i = 1, ..., 200\}$. Parallel computing is leveraged since the FE analyses are independent of one another. Ten FE analyses are performed in parallel, one on each core of the workstation. The runtime of each FE analysis is in the range 2 min ± 10 sec on a single core (two threads) of the workstation. The domain decomposition capability of Abaqus FEA is used to distribute each FE analysis on two threads. The first 100 samples are used as test samples for surrogate model assessment and the next 100 samples are used as initial training samples for surrogate model construction. Therefore, the test set and initial training set are given by $t' = \{(\mathbf{x}^{(i)}, \mathbf{z}^{(i)}) | \ i = 1, ..., 100\}$ and $t = \{(\mathbf{x}^{(i)}, \mathbf{z}^{(i)}) | \ i = 101, ..., 200\}$, respectively.

A surrogate model is typically constructed considering each output measurement channel separately, thus requiring constructing 46 different surrogate models for the miter gate application example in this paper. However, principal component analysis (PCA) can be used to

reduce the dimensionality of the output space since the strains at closely spaced strain gauge locations are correlated.

A PCA is performed on the training data matrix $\mathbf{Z} = \left[\mathbf{z}^{(101)}, ..., \mathbf{z}^{(200)} \right] \in \mathbb{R}^{46\times 100}$. A centered data matrix $\mathbf{Z}_c \in \mathbb{R}^{46\times 100}$ is created as

$$\mathbf{Z}_c = \mathbf{Z} - \frac{1}{n}\mathbf{Z}\,\mathbf{1}\,\mathbf{1}^T \quad \text{where } \mathbf{1} = [1, ..., 1]^T \in \mathbb{R}^{100\times 1} \tag{4.30}$$

The sample covariance matrix $\mathbf{\Sigma} \in \mathbb{R}^{46\times 46}$ of the training data is given by

$$\mathbf{\Sigma} = \frac{1}{100-1}\mathbf{Z}_c\,\mathbf{Z}_c^T \tag{4.31}$$

The singular value decomposition of $\mathbf{Z}_c^T$ is given by

$$\underset{100\times 46}{\mathbf{Z}_c^T} = \underset{100\times 46}{\mathbf{U}}\ \underset{46\times 46}{\mathbf{\Pi}}\ \underset{46\times 46}{\mathbf{V}^T} \text{ with } \mathbf{U}^T\mathbf{U} = \mathbf{I} \text{ and } \mathbf{V}^T\mathbf{V} = \mathbf{I} \tag{4.32}$$

where the columns of $\mathbf{U}$ and $\mathbf{V}$ are the left singular and right singular vectors, respectively, and $\mathbf{\Pi}$ is a diagonal matrix of singular values. Using Eq. (4.32), the sample covariance matrix $\mathbf{\Sigma}$ given in Eq. (4.31) becomes

$$\mathbf{\Sigma} = \mathbf{V}\left(\frac{1}{100-1}\mathbf{\Pi}^2\right)\mathbf{V}^T \tag{4.33}$$

Noting that $\mathbf{V} \in \mathbb{R}^{46\times 46}$ is an orthonormal matrix and $\mathbf{\Pi}^2 \in \mathbb{R}^{46\times 46}$ is a diagonal matrix, Eq. (4.33) is the eigenvalue decomposition of $\mathbf{\Sigma} \in \mathbb{R}^{46\times 46}$. The eigenvectors of $\mathbf{\Sigma}$ are the columns of $\mathbf{V}$ (also known as principal components) and the eigenvalues of $\mathbf{\Sigma}$ are ${\sigma_k}^2 = \pi_k^2/(100-1)$, $k = 1, ..., 46$. ${\sigma_k}^2$ is also the variance of the training data along the principal component $\mathbf{v}_k \in \mathbb{R}^{46\times 1}$.

Let n^{PCA} be the number of principal components required to capture more than 95% of the variance of the training data. It was found that $n^{PCA}=6$ for the training data matrix $\mathbf{Z}\in\mathbb{R}^{46\times100}$. Using the computed principal components, any vector $\mathbf{z}\in\mathbb{R}^{46\times1}$ can be transformed to $\mathbf{z}^{PCA}=\left[\cdots,z_k^{PCA},\cdots\right]^T\in\mathbb{R}^{n^{PCA}\times1}$ and vice versa as

$$\underset{n^{PCA}\times1}{\mathbf{z}^{PCA}}=\underbrace{\left[\mathbf{v}_1,\ldots,\mathbf{v}_{n^{PCA}}\right]^T}_{n^{PCA}\times46}\underset{46\times1}{\mathbf{z}}\;;\quad\underset{46\times1}{\mathbf{z}}\approx\underbrace{\left[\mathbf{v}_1,\ldots,\mathbf{v}_{n^{PCA}}\right]}_{\mathbf{V}_{PCA}=46\times n^{PCA}}\underset{n^{PCA}\times1}{\mathbf{z}^{PCA}}\tag{4.34}$$

where $\mathbf{v}_k\in\mathbb{R}^{46\times1}$ is the $k-th$ eigenvector, and the eigenvectors are ordered in the decreasing magnitude of their corresponding eigenvalues $\sigma_i{}^2$. Only n^{PCA} surrogate models now need to be constructed, one for each principal component $z_k^{PCA},\ k\in\{1,2,...,n^{PCA}\}$.

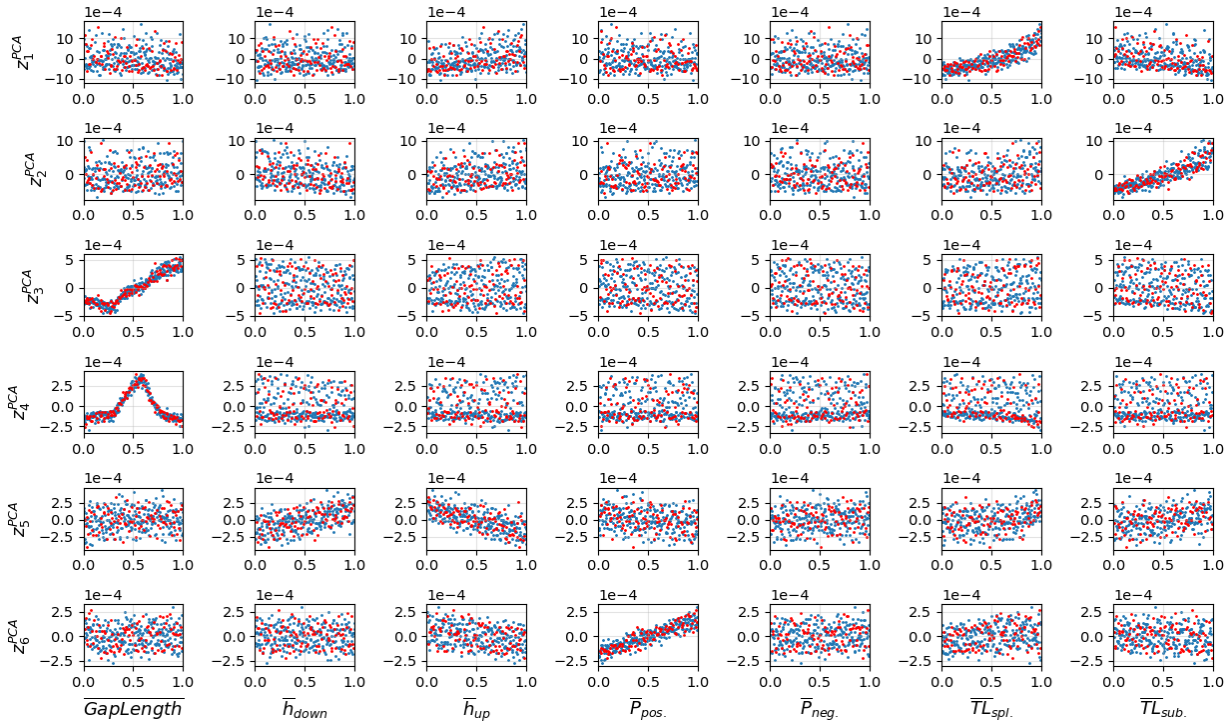

Figure 4.8: Scatter plot of sample points from final training set (blue) and test set (red).

Let g_k denote the surrogate model that maps $\mathbf{x}$ to the output z_k^{PCA} and let the trained/fitted surrogate model be denoted by $\hat{g}_k$. The training of PCE and GPR surrogate models for the miter gate FE model are described in Sections 4.4.2 and 4.4.3, respectively. After surrogate model construction, the fitted surrogate model $\hat{g}_k$ is assessed by computing the root mean square error (RMSE) over the test set $t' = \{(\mathbf{x}^{(i)}, \mathbf{z}^{(i)}) \mid i = 1, ..., 100\}$ as

$$err_k = \sqrt{\frac{1}{100}\sum_{i=1}^{100}\left(z_k^{(i)PCA} - \hat{g}_k(\mathbf{x}^{(i)})\right)^2}, \quad k \in \{1, 2, ..., n^{PCA}\} \tag{4.35}$$

where $z_k^{(i)PCA} = \left[\mathbf{V}^T \mathbf{z}^{(i)}\right]_k$. If err_k is less than some specified threshold for all $k \in \{1, 2, ..., n^{PCA}\}$, then the fitted surrogate models $\hat{g}_k,\ k \in \{1, 2, ..., n^{PCA}\}$ are final. Otherwise, the training set is enhanced by adding new sample points and the surrogate model is trained again. At every iteration, the training set is enhanced by adding ten subsequent sample points to the Sobol sequence. Thus, after the first iteration, the ten subsequent sample points are $\{\mathbf{x}^{(i)} \mid i = 201, ..., 210\}$ and the enhanced training set is $t = \{(\mathbf{x}^{(i)}, \mathbf{z}^{(i)}) \mid i = 101, ..., 210\}$. The surrogate model is now retrained using the enhanced training set.

Table 4.2 shows the pseudo-code of the surrogate model construction procedure used in this paper. After 15 iterations, it was observed that 6 principal components are sufficient to capture more than 95% of the variability of the training data (thus $n^{PCA} = 6$) with the test errors $err_k\ \forall k \in \{1, 2, ..., 6\}$ within the acceptable threshold for PCE and GPR surrogates (see Sections 4.4.2 and 4.4.3 for more details). Hence, the final training set is $t = \{(\mathbf{x}^{(i)}, \mathbf{z}^{(i)}) \mid i = 101, ..., 350\}$ for both the PCE and GPR surrogates. The scatter plot of the test set t' and final training set t is

shown in Figure 4.8. The vertical axes correspond to the PCA transformed FE output $\mathbf{z}^{PCA}$ and the horizontal axes correspond to $\mathbf{x}$ with each component of $\mathbf{x}$ normalized as

$$\bar{x}_j = \left(\frac{x_j - lower_j}{upper_j - lower_j} \right) \tag{4.36}$$

where $\bar{x}_j$ denotes the normalized version of x_j. The bounds of each component x_j of $\mathbf{x}$, $lower_j$ and $upper_j$, are provided in Table 4.1. The subplot at grid location (k, j) of Figure 4.8 shows the sample points $\{(\bar{x}_j^{(i)}, z_k^{(i)PCA}) \mid i = 1, ..., 350\}$ in the scatter plot. The red dots correspond to the test set $(i = 1{:}100)$ while the blue dots correspond to the final training set $(i = 101{:}350)$. From the scatter subplots, it can be seen that z_1^{PCA} is sensitive to $Tl_{spl.}$, z_2^{PCA} to $Tl_{sub.}$, z_3^{PCA} and z_4^{PCA} to *GapLen.*, z_5^{PCA} to h_{up} and h_{down}, z_6^{PCA} to $P_{pos.}$.

Table 4.2: Surrogate model construction procedure (pseudo code).

Initialize: Draw sequence of sample points from Sobol sequence, $\{\mathbf{x}^{(i)} | \ i = 1, ..., 200\}$

Run FE analyses $\{\mathbf{z}^{(i)} = \mathbf{h}(\mathbf{x}^{(i)}) \in \mathbb{R}^{46} \mid \ i = 1, ..., 200\}$

Initial training set: $t = \{(\mathbf{x}^{(i)}, \mathbf{z}^{(i)}) | \ i = 101, ..., 200\}$, test set: $t' = \{(\mathbf{x}^{(i)}, \mathbf{z}^{(i)}) | \ i = 1, ..., 100\}$

Initialize iteration number: $iterNum = 1$

while true **do**

Perform PCA of the training data matrix $\mathbf{Z}$ and obtain n^{PCA} and $\mathbf{V}$ (Eq. (4.34))

Construct the surrogate models $g_k, \ k = 1, ..., n^{PCA}$ using training set t (Note: g_k denotes the surrogate model that maps $\mathbf{x}$ to the output z_k^{PCA})

Compute the test error err_k for each fitted surrogate $\hat{g}_k$

if $\min(err_k) < threshold$

break

else

Update the training set $t = \{(\mathbf{x}^{(i)}, \mathbf{z}^{(i)}) | \ i = 101, ..., 200 + 10 \times iterNum\}$

Update the training data matrix $\mathbf{Z} = \left[\mathbf{z}^{(101)}, ..., \mathbf{z}^{(200 + 10 \times iterNum)} \right]$

$iterNum = iterNum + 1$

end

end

4.5.3.1 PCE Surrogate Model Training

To construct the PCE surrogate models, the probability distribution $p(\mathbf{x})$ is taken as

$$p(\mathbf{x}) = \prod_{j=1}^{7} p(x_j); \quad p(x_j) \sim \mathcal{U}\left(lower_j, upper_j\right) \tag{4.37}$$

where $\mathcal{U}\left(lower_j, upper_j\right)$ denotes a uniform distribution with lower bound $lower_j$ and upper bound $upper_j$. The bounds of each component x_j of $\mathbf{x}$, $lower_j$ and $upper_j$, are shown in

Table 4.1. The uniform distribution is chosen in order to fill the parameter space uniformly for PCE construction. However, note that the prior probability distribution of the unknown parameters in FE model updating (Section 4.5.5) is taken as normal. The constructed PCE surrogate can be used to replace the FE model in model updating for any prior probability distribution.

For the vector case $\mathbf{x} = [x_1, \ldots, x_7]^T$ with independent components, the orthonormal polynomial sequence $\{\phi_i(\mathbf{x})\}_{i=1}^{\infty}$ can be constructed by building an orthonormal polynomial sequence $\{\phi_i(x_j)\}_{i=1}^{\infty}$ for each component x_j and then taking their tensor product. Since $p(x_j) \sim \mathcal{U}(lower_j, upper_j)$, the orthonormal Legendre polynomials form the orthonormal polynomial sequence $\{\phi_i(x_j)\}_{i=1}^{\infty}$ for component x_j, i.e.,

$$\begin{aligned} &\phi_1(x_j) = 1, \quad \phi_2(x_j) = \sqrt{3}\,\tilde{x}_j, \quad \phi_2(x_j) = \frac{\sqrt{5}}{2}(3\,\tilde{x}_j^2 - 1), \quad \ldots \\ &\text{where} \quad \tilde{x}_j = 2\left(\frac{x_j - lower_j}{upper_j - lower_j}\right) - 1 \end{aligned} \tag{4.38}$$

Truncation is performed by considering only the orthonormal polynomials from the sequence $\{\phi_i(\mathbf{x})\}_{i=1}^{\infty}$ that have a polynomial degree less than $\rho = 13$. Hyperbolic cross truncation with cross-truncation factor $\alpha = 0.5$ is also employed to further reduce the number of orthonormal polynomials. This leads to a total number of polynomials considered in the truncated PCE expansion of $P = 589$. Lasso regression with the LARS algorithm is used to compute the coefficients $\{c_i\}_{i=1}^{589}$. The optimum value of λ (amount of penalization) in Eq. (4.18) is obtained using a 5-fold cross-validation technique. Note that this PCE surrogate training is

performed for each surrogate g_k, $k \in \{1, 2, ..., n^{PCA}\}$ at each iteration shown in Table 4.2. After 15 iterations, $n^{PCA} = 6$ and the final fitted PCE surrogates are $\hat{g}_k$, $k \in \{1, 2, ..., 6\}$. The number of zero coefficients out of 589 coefficients, and the test error err_k (root mean square error) of the final fitted surrogates $\hat{g}_k$, $k \in \{1, 2, ..., 6\}$ are reported in Table 4.3. The table also shows the relative root mean square error over test set of the final fitted surrogates $\hat{g}_k$, $k \in \{1, 2, ..., 6\}$, which is defined as

$$RRMSE_k = \frac{\sqrt{\frac{1}{100}\sum_{i=1}^{100}\left(z_k^{(i)PCA} - \hat{g}_k(\mathbf{x}^{(i)})\right)^2}}{\sqrt{\frac{1}{100}\sum_{i=1}^{100}\left(z_k^{(i)PCA}\right)^2}}, \quad k \in \{1, 2, ..., n^{PCA}\} \tag{4.39}$$

The relative root mean square error over test set is below 10% for all the fitted PCE surrogates $\hat{g}_k$, $k \in \{1, 2, ..., 6\}$.

Table 4.3: Final fitted PCE surrogate details.

	Fitted surrogate models					
	$\hat{g}_1$	$\hat{g}_2$	$\hat{g}_3$	$\hat{g}_4$	$\hat{g}_5$	$\hat{g}_6$
# zero coeff. /589	468	465	412	445	415	443
Test error err_k	0.08×10^{-4}	0.05×10^{-4}	0.11×10^{-4}	0.19×10^{-4}	0.04×10^{-4}	0.03×10^{-4}
$RRMSE_k$ (test set)	1.5 %	1.6 %	4.3 %	9.2 %	2.6 %	2.9 %

Figure 4.9a shows the fitted PCE surrogate $\hat{g}_3$ as a function of $\bar{x}_1$ (*GapLen.* normalized using Eq. (4.36)), while the remaining parameters are fixed at the mid value of their corresponding range, i.e., $\bar{x}_j = 0.5$ $(j = 2, ..., 7)$. The blue dots indicate the final training set, and the red dots indicate the test set. This is a slice plot of the fitted PCE surrogate, and it shows that the fitted PCE surrogate captures very well the highly nonlinear mapping from the FE parameter

GapLength to the PCA transformed FE response z_3^{PCA}. Similarly, Figure 4.9b and Figure 4.9c show the fitted PCE surrogate $\hat{g}_4$ and $\hat{g}_1$ as a function of $\overline{x}_1$ (normalized *GapLen.*) and $\overline{x}_4$ (normalized $Tl_{spl.}$), respectively, while the remaining parameters are fixed at their mid value; again the PCE surrogates capture very well the nonlinear mappings between FE model parameters and transformed FE responses.

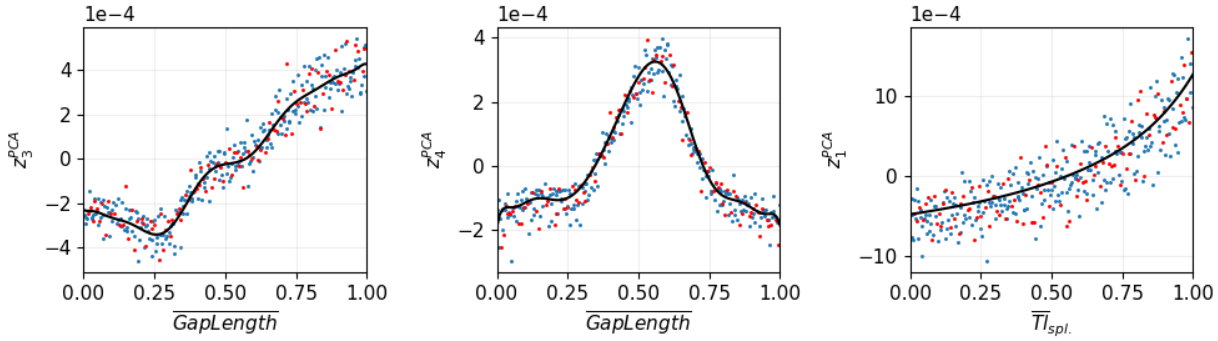

Figure 4.9: Final fitted PCE surrogates as a function of a parameter (black line) along with final training set (blue dots) and test set (red dots).

Figure 4.10a compares all PCE surrogates predicted responses $\hat{g}_k(\mathbf{x}^{(i)})$ $(\forall k = 1,...,6$ and $\forall i = 1,...,350)$ with the PCA transformed FE responses $z_k^{(i)PCA}$ $(\forall k = 1,...,6$ and $\forall i = 1,...,350)$. Figure 4.10b plots the residuals $r_k^{(i)}$ $(\forall k = 1,...,6$ and $\forall i = 1,...,350)$ versus all PCE surrogate predicted responses $\hat{g}_k(\mathbf{x}^{(i)})$ $(\forall k = 1,...,6$ and $\forall i = 1,...,350)$ where the residual $r_k^{(i)}$ is defined as $r_k^{(i)} = z_k^{(i)PCA} - \hat{g}_k(\mathbf{x}^{(i)})$. The blue dots indicate the final training set $i = 101,...,350$ and the red dots indicate the test set $i = 1,...,100$. Figure 4.10a shows a very high correlation between the fitted PCE surrogate responses and corresponding PCA transformed FE responses. Figure 4.10b shows that the residuals are clustered around zero and the relative root mean square error of the

fitted PCE surrogate on the training and test sets are 1.4% and 3.5%, respectively. Both these figures indicate that the fitted PCE surrogate models predict very well the PCA transformed FE responses.

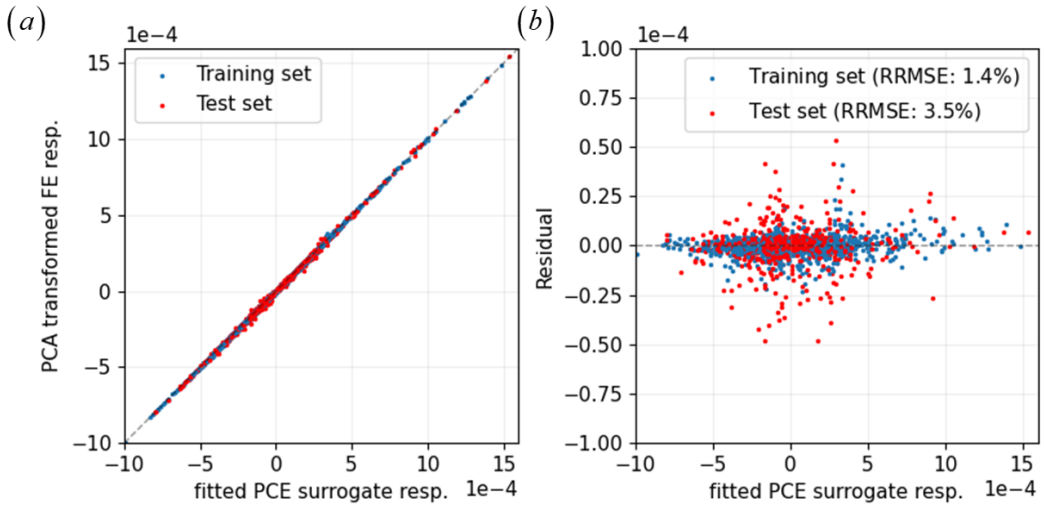

Figure 4.10: (a) PCA transformed FE response versus PCE surrogate predictions, and (b) residuals versus PCE surrogate predictions.

The total runtime to obtain the final fitted PCE surrogate model (i.e., running the algorithm outlined in Table 4.2 for 15 iterations) is 15.2hrs on the workstation. Parallel computing is leveraged to perform the FE analyses needed to construct the initial training set, the test set, and while enhancing the training set at each iteration defined in Table 4.2.

4.5.3.2 GPR Surrogate Model Training

The covariance function $k(\mathbf{x},\mathbf{x}')$ in Eq. (4.19) is taken as $k(\mathbf{x},\mathbf{x}')=\prod_{j=1}^{7}k(x_j,x_j')$, where each $k(x_j,x_j')$ is modeled using the radial basis kernel (or covariance) function with length scale l_j and variance s_j^2 as

$$k(x_j, x'_j) = s_j^2 \exp\left(-\frac{1}{2\, l_j^2} \left(x_j - x'_j \right)^2 \right) \tag{4.40}$$

The hyperparameters $\boldsymbol{\gamma} = \left\{ s_j, l_j \right\}_{j=1:7}$ and σ_ε are estimated by solving an MLE problem (Eq. (4.29)) using the BFGS algorithm. Note that other kernels such as the Matérn class of covariance functions can also be used instead of the standard (most popular) radial basis kernel. After 15 iterations, $n^{PCA} = 6$ and the final fitted GPR surrogates are $\hat{g}_k$, $k \in \{1, 2, ..., 6\}$; the test errors err_k, $k \in \{1, 2, ..., 6\}$, are reported in Table 4.4. The table also shows the relative root mean square error over test set (defined in Eq. (4.39)) of the final fitted surrogates $\hat{g}_k$, $k \in \{1, 2, ..., 6\}$. The relative root mean square error over test set is below 10% for all the fitted GPR surrogates $\hat{g}_k$, $k \in \{1, 2, ..., 6\}$.

Table 4.4: Final fitted GPR surrogate test errors.

	$\hat{g}_1$	$\hat{g}_2$	$\hat{g}_3$	$\hat{g}_4$	$\hat{g}_5$	$\hat{g}_6$
Test error err_k	0.14×10^{-4}	0.11×10^{-4}	0.09×10^{-4}	0.07×10^{-4}	0.14×10^{-4}	0.06×10^{-4}
$RRMSE_k$ (test set)	2.7 %	3.1 %	3.4 %	4.0 %	9.1 %	5.3 %

Similar to Figure 4.9, the final fitted GPR surrogates $\hat{g}_3$, $\hat{g}_4$, and, $\hat{g}_1$ as a function of $\bar{x}_1$ (normalized *GapLen.*), $\bar{x}_1$, and, $\bar{x}_4$ (normalized $Tl_{spl.}$), respectively, are shown (black lines) in Figure 4.11. In each subplot, the remaining parameters are fixed at the mid value of their corresponding range. These slice plots indicate that the fitted GPR surrogates capture very well the highly nonlinear mappings from the FE model parameters to the PCA transformed FE responses.

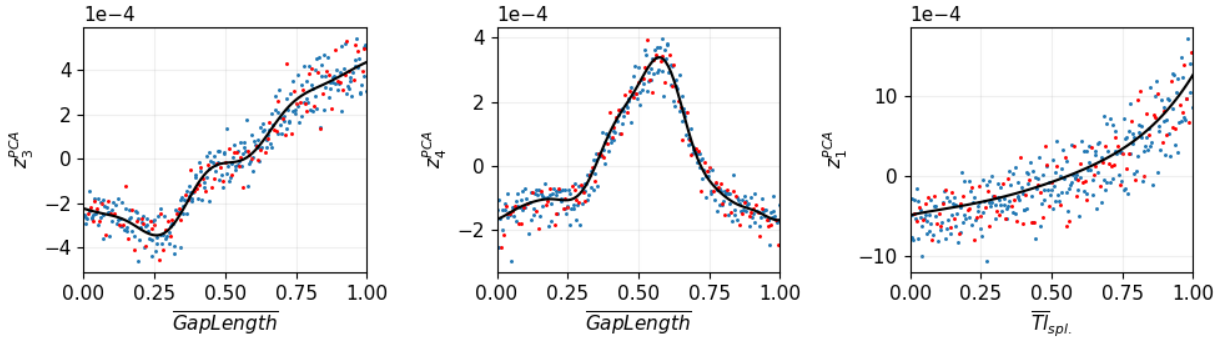

Figure 4.11: Final fitted GPR surrogates as a function of a parameter (black line) along with final training set (blue dots) and test set (red dots).

Like in Figure 4.10, the PCA transformed FE responses $z_k^{(i)PCA}$ $(\forall k = 1, ..., 6$ and $\forall i = 1, ..., 350)$ and residuals $r_k^{(i)}$ $(\forall k = 1, ..., 6$ and $\forall i = 1, ..., 350)$ are plotted versus the corresponding GPR surrogate predicted responses $\hat{g}_k(\mathbf{x}^{(i)})$ $(\forall k = 1, ..., 6$ and $\forall i = 1, ..., 350)$ in Figure 4.12. Figure 4.12a shows a very high correlation between the fitted GPR surrogate responses and corresponding PCA transformed FE responses. Figure 4.12b shows that the residuals are symmetrically clustered around zero and the relative root mean square error of the fitted GPR surrogates on the training and test sets are 2.7% and 3.6%, respectively. Both these figures indicate that the fitted GPR surrogate models predict very well the PCA transformed FE responses.

The total runtime to obtain the final fitted GPR surrogate model (i.e., running the algorithm outlined in Table 4.2 for 15 iterations) is 15.3hrs on the workstation. Parallel computing is leveraged to conduct the FE analyses required to construct the initial training set, the test set, and while enhancing the training set at each iteration defined in Table 4.2.

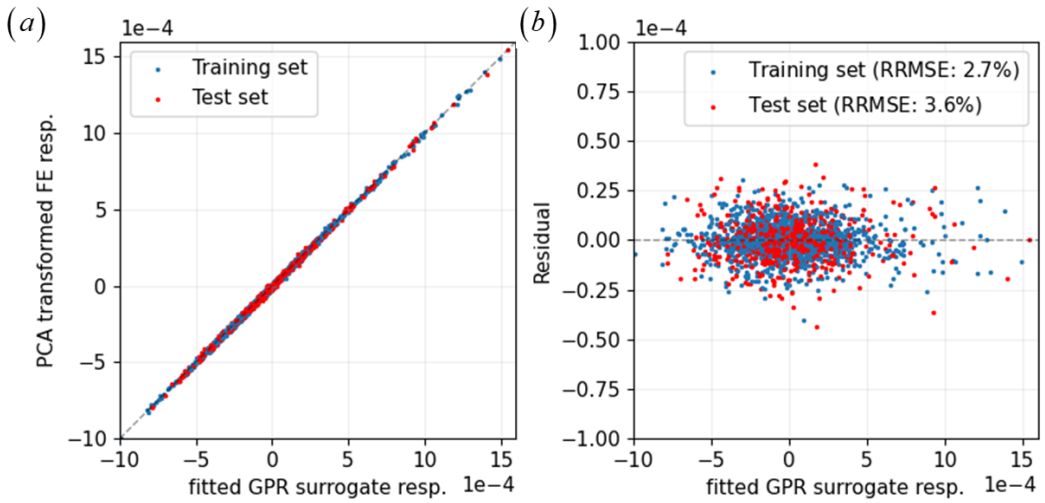

Figure 4.12: (a) PCA transformed FE response versus GPR surrogate predictions, and (b) residuals versus GPR surrogate predictions.

4.5.4 Measurement Data Simulation

Two sets of strain measurement data $\mathcal{D}_i \ (i=1,2)$ are generated, and the model updating is performed considering each measurement data set separately. To generate each data set $\mathcal{D}_i \ (i=1,2)$, the FE model parameters are set to the parameter values shown in Table 4.5. The corresponding input loading parameters $\mathbf{u}=\left[h_{down}, h_{up}\right]^T$ defined in Table 4.5 are used and the uniaxial strains are recorded at the 46 strain gauge locations (Figure 4.4a) on the FE model. To simulate sensor measurement noise, a random Gaussian noise of standard deviation 0.2×10^{-4} (Eick et al. 2018a) is added to each of the 46 recorded (computed) strain measurements, assuming statistical independence of the measurement noise across different strain measurements. The polluted strain response is taken as the simulated strain measurement data $\mathbf{y}\in\mathbb{R}^{46\times1}$.

Table 4.5: Parameter values to simulate the strain measurement data.

	Unknown parameters					Input loading	
Data set	*GapLen.* [m]	$P_{pos.}$ [MPa]	$P_{neg.}$ [MPa]	$Tl_{spl.}$ [mm]	$Tl_{sub.}$ [mm]	h_{down} [m]	h_{up} [m]
$\mathcal{D}_1$	1.16	531	482	2.53	1.38	3.9	13.7
$\mathcal{D}_2$	4.06	241	289	5.80	3.10	4.9	14.4

4.5.5 FE Model Updating

The FE model updating procedure described in Section 4.3 is employed to obtain the posterior distribution of the unknown parameter vector $\boldsymbol{\theta}$ considering each strain measurement data set separately. Let us first consider the simulated data set $\mathcal{D}_1$ for model updating. The covariance matrix $\boldsymbol{\Sigma}_{\mathbf{w}}$ of error/noise term $\mathbf{w}$ (Eq. (4.4)) in the measurement equation is modeled as $\boldsymbol{\Sigma}_{\mathbf{w}} = \sigma_{\mathbf{w}}^2 \mathbf{I}_{46}$ where $\mathbf{I}_{46}$ denotes the identity matrix of size 46. The parameter $\sigma_{\mathbf{w}}$ is also unknown and is inferred jointly with the unknown parameter vector $\boldsymbol{\theta}$. The samples of the joint posterior distribution $p(\boldsymbol{\theta}, \sigma_{\mathbf{w}} \mid \mathbf{u}, \mathbf{y})$ are obtained using the TMCMC sampling method described in Section 4.3.2.

To construct the joint prior distribution $p(\boldsymbol{\theta}, \sigma_{\mathbf{w}})$, $\boldsymbol{\theta}$ and $\sigma_{\mathbf{w}}$ are assumed statistically independent, i.e., $p(\boldsymbol{\theta}, \sigma_{\mathbf{w}}) = p(\boldsymbol{\theta})\, p(\sigma_{\mathbf{w}})$. In addition, the components of $\boldsymbol{\theta}$ are assumed mutually statistically independent to construct the prior $p(\boldsymbol{\theta})$. The prior distribution of each component of $\boldsymbol{\theta}$ is taken as $p(GapLen.) = \mathcal{U}(0, 4.6m)$, $p(P_{pos.}) = \mathcal{N}\left(620MPa, (345MPa)^2\right)$, $p(P_{neg.}) = \mathcal{N}\left(345MPa, (345MPa)^2\right)$, $p(Tl_{spl.}) = \mathcal{N}\left(3mm, (1.5mm)^2\right)$,

$p(Tl_{sub.}) = \mathcal{N}\left(1.5mm, (1.5mm)^2\right)$. All distributions are truncated with their corresponding upper and lower bounds given in Table 4.1. The prior of $\sigma_{\mathbf{w}}$ is taken as $p(\sigma_{\mathbf{w}}) = \mathcal{N}(0, 0.7\times10^{-4})$ (true value of $\sigma_{\mathbf{w}}$ is 0.2×10^{-4}) and is truncated at zero (half normal distribution).

In the TMCMC method to obtain samples of the joint posterior distribution $p(\boldsymbol{\theta}, \sigma_{\mathbf{w}} \mid \mathbf{u}, \mathbf{y})$, 250 particles are used to approximate the intermediate distribution at every stage. The number of MCMC steps in the perturbation phase of each TMCMC stage is set to 15. Direct FE model evaluations are utilized to evaluate the likelihood function in the TMCMC algorithm to obtain the joint posterior samples.

The kernel density estimates (KDEs) of the marginal distribution of each component of $\boldsymbol{\theta}$ constructed using 250 samples at the first TMCMC stage (prior samples) and last TMCMC stage (posterior samples) are shown in Figure 4.13 for the strain measurement data set $\mathcal{D}_1$. In each plot, the red dashed line represents the prior KDE, the green dashed line represents the posterior KDE obtained utilizing direct FE model evaluations, and the black vertical line indicates the true parameter value. In this figure, each component of $\boldsymbol{\theta}$ is normalized according to Eq. (4.36). The total runtime to obtain the 250 posterior samples using TMCMC and relying on direct FE model evaluations is 60.2hrs on the workstation. Parallel computing (10 FE analyses performed in parallel, one on each core) is leveraged in the perturbation phase at each stage of the TMCMC algorithm.

FE model updating is repeated to obtain the samples of the joint posterior now utilizing the developed surrogate models for evaluating the likelihood function in the TMCMC algorithm. The KDEs of the marginal distribution of each component of $\boldsymbol{\theta}$ obtained using 250 samples at the last TMCMC stage (posterior samples) while employing the constructed PCE and GPR

surrogates for model evaluations are shown in Figure 4.13 in orange solid and blue solid lines, respectively. It is observed that the marginal posterior KDEs obtained using direct FE model evaluations, and evaluations of the constructed PCE and GPR surrogate models to compute the likelihood function are qualitatively similar.

The total runtime to obtain the 250 posterior samples using TMCMC and the constructed PCE or GPR surrogate models is ~1min on the workstation. Parallel computing (10 surrogate model evaluations performed in parallel, one on each core) is leveraged in the perturbation phase at each stage of the TMCMC algorithm. Note that when using surrogate model evaluations in the Bayesian model updating, it is feasible to draw, at very low computational cost, many more than 250 samples from the posterior distribution of $\boldsymbol{\theta}$. However, for a fair comparison (in terms of accuracy and computational time) of the model updating results obtained when utilizing direct FE vs surrogate model evaluations, we chose to approximate the posterior with 250 samples in each case.

Table 4.6 compares the total runtimes to perform the Bayesian model updating when using direct FE model versus surrogate model evaluations to compute the likelihood function. For the considered miter gate study on the workstation, a ~4-fold reduction in computational time is observed when using the surrogate models instead of the FE model for the likelihood function evaluations in Bayesian model updating.

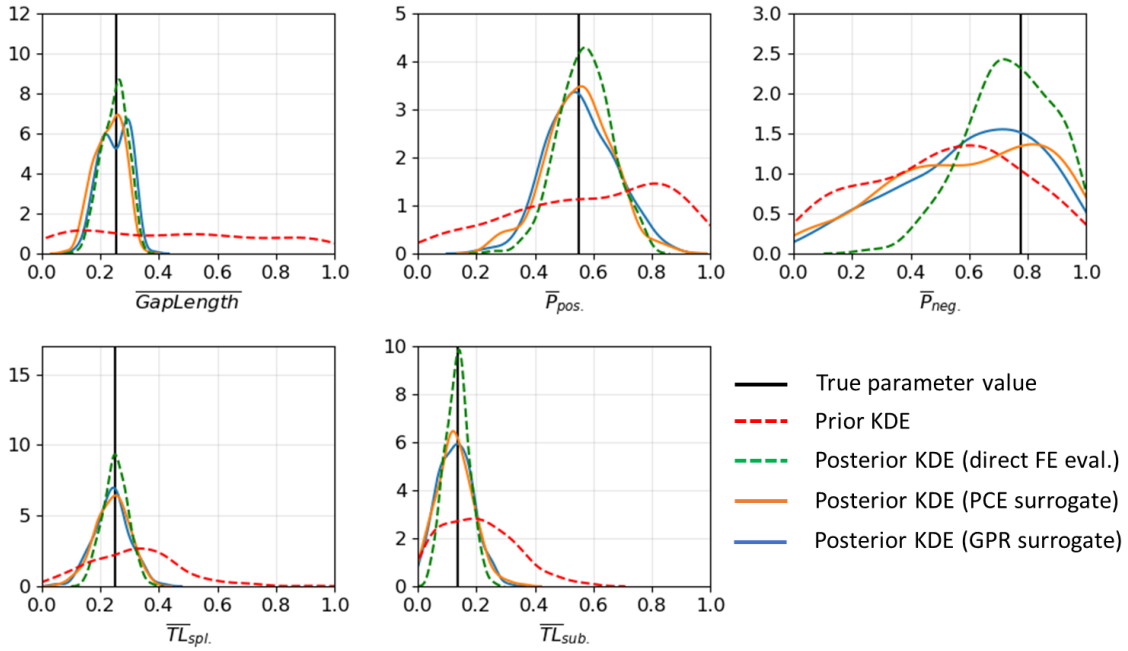

Figure 4.13: Marginal kernel density estimates (KDEs) of each component of $\boldsymbol{\theta}$ for the strain measurement data set $\mathcal{D}_1$.

The FE model updating procedure is now repeated considering the strain measurement data set $\mathcal{D}_2$ using the same prior distribution. Similar to Figure 4.13, Figure 4.14 compares the marginal posterior KDEs obtained utilizing direct FE model evaluations, and evaluations of the constructed PCE and GPR surrogate models. Again, it is observed that the marginal posterior KDEs obtained utilizing direct FE model versus PCE and GPR surrogate model evaluations for the likelihood function evaluations are qualitatively similar.

Table 4.6: Total runtimes to perform Bayesian model updating for measurement data set $\mathcal{D}_1$ or $\mathcal{D}_2$

	Runtime on the workstation (Intel Xeon W-2155 @ 3.30 GHz CPU with 10 cores / 20 threads and 128 GB RAM workstation)		
	Surrogate model construction	TMCMC (250 samples)	Total
Direct FE model	-	~60hrs	~60hrs
PCE surrogate	~15hrs	~1min	~15hrs
GPR surrogate	~15hrs	~1min	~15hrs

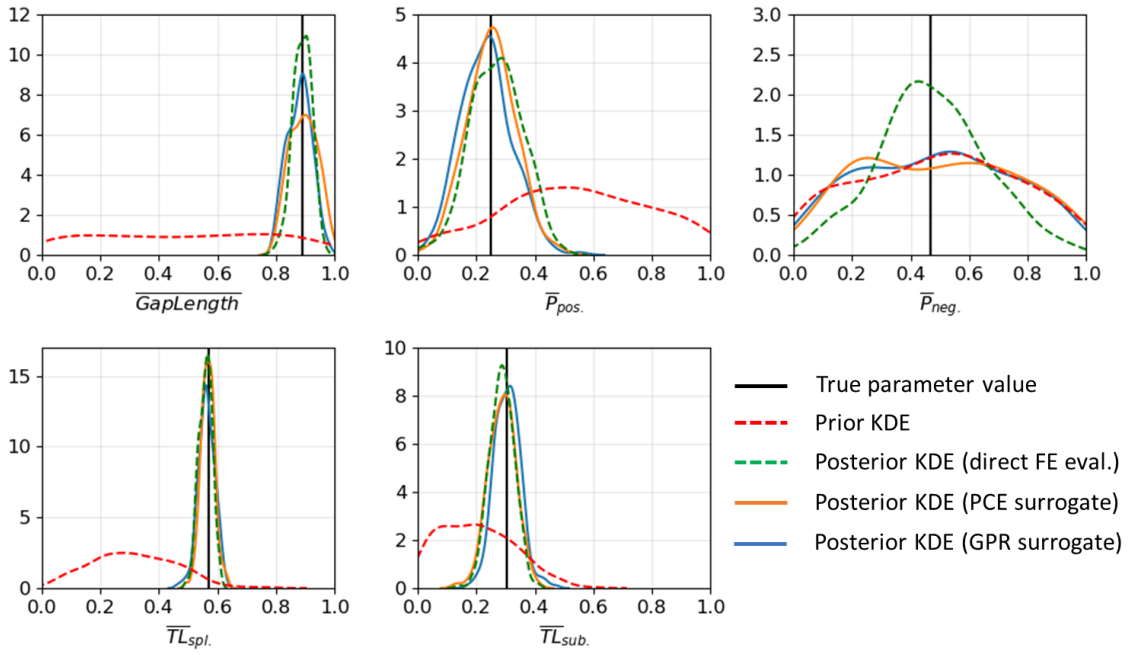

Figure 4.14: Marginal kernel density estimates (KDEs) of each component of $\boldsymbol{\theta}$ for the strain measurement data set $\mathcal{D}_2$.

4.6 Conclusions

This paper compares the Bayesian model updating results in the context of high-fidelity FE models of a large-scale civil structure when the updating is performed utilizing direct FE

evaluations versus surrogate model evaluations. In this regard, a miter gate structural system is used as the testbed structure, and the polynomial chaos expansion and Gaussian process regression methods are used as surrogate modeling techniques. Three common (dominant) damage modes of miter gate systems are considered for Bayesian model updating purposes using simulated strain measurement data. Five system parameters associated with these three damage modes are estimated in the model updating process. It took ~60hrs to perform model updating using the TMCMC algorithm when using direct FE evaluations on an Intel Xeon W-2155 @ 3.30 GHz CPU with 10 cores / 20 threads and 128 GB RAM workstation. Parallel computing was leveraged at each stage of the TMCMC algorithm. In contrast, it took ~15hrs to construct the PCE or GPR surrogate model and ~1min to perform Bayesian model updating using the surrogate model evaluations. Compared to the kernel density estimates of the posterior marginal distributions of the unknown parameters obtained using direct FE evaluations, those obtained using surrogate model evaluations were found sufficiently accurate (qualitatively). Thus, for the considered miter gate testbed application, Bayesian FE model updating relying on surrogate model evaluations is ~4 times faster than when using direct FE model evaluations and provides relatively accurate posterior results (compared to those obtained using direct FE evaluations). Investigations of the efficiency and accuracy of Bayesian FE model updating (for large-scale civil infrastructure systems) based on surrogates of the FE model, such as the study presented in this paper, are necessary before completely relying on surrogate models in Bayesian model updating, which in turn can be used for SHM/DP purposes.

4.7 Acknowledgements

Funding for this work by the U.S. Army Corps of Engineers through the U.S. Army Engineer Research and Development Center Research Cooperative Agreement W912HZ-17-2-0024 is gratefully acknowledged. The authors would also like to thank Prof. Matthew Parno, Research Assistant Professor at Dartmouth College, for some ideas used in the paper. This document has been approved by Los Alamos National Laboratory for unlimited public release (LA-UR-21-28985). Chapter 4, in full, had been submitted for publication of the material as it may appear in the following paper (the dissertation author is the first author of this paper):

Ramancha, M. K., Vega, M. A., Conte, J. P., Todd, M. D., and Hu, Z. (2022). "Bayesian model updating with finite element vs. surrogate models: application to a miter gate structural system." Submitted to *Engineering Structures*.

4.8 Preview to Chapter 5

Chapters 2, 3, and 4 develops the Bayesian FE model updating considering simulated measurment data. The goal of the next chapter is on validating the developed Bayesian FE model updating using real experimental data. In this regard, the model updating framework is applied to a full-scale bridge column which was tested on the large high-performance outdoor shake table (LHPOST) here at UC San Diego in 2010 .This column was subjected to a series of ten earthquake ground motion records and was densely instrumented with an array of 278 heterogeneous sensors. The data measured by these sensors is used for FE model updating of the bridge column. Validating the Bayesian FE model updating framework using real data for different levels of nonlinearity (in the structural response behavior) is necessary for real world SHM/DP of any civil infrastructure system.

5 Bayesian Nonlinear Finite Element Model Updating of a Full-Scale Bridge-Column using Sequential Monte Carlo

5.1 Abstract

Digital twin-based approaches for structural health monitoring (SHM) and damage prognosis (DP) are emerging as a powerful framework for intelligent maintenance of civil structures and infrastructure systems. Model updating of nonlinear mechanics-based Finite Element (FE) models using input and output measurement data with advanced Bayesian inference methods is an effective way of constructing a digital twin. In this regard, the nonlinear FE model updating of a full-scale reinforced-concrete bridge column subjected to seismic excitations applied by a large shake table is considered in this paper. This bridge column, designed according to US seismic design provisions, was tested on the NEES@UCSD Large High-Performance Outdoor Shake Table (LHPOST). The column was subjected to a sequence of ten recorded earthquake ground motions and was densely instrumented with an array of 278 sensors consisting of strain gauges, linear and string potentiometers, accelerometers and Global Positioning System (GPS) based displacement sensors to measure local and global responses during testing. This heterogeneous dataset is used to estimate/update the material and damping parameters of the developed mechanics-based distributed plasticity FE model of the bridge column. The sequential Monte Carlo (SMC) method (set of advanced simulation-based Bayesian inference methods) is used herein for the model updating process. The inherent architecture of SMC methods allows for parallel model evaluations, which is ideal for updating computationally expensive models.

Keywords: Bayesian Inference, Digital Twin, Finite Element, Model Updating, Sequential Monte Carlo, Structural Health Monitoring, Full-Scale Structural Systems, Earthquake.

5.2 Introduction

Structural health monitoring (SHM) is the general process of making an assessment, utilizing measurement data, about the current ability of the system to perform its intended design functions. Damage prognosis or prognostics (DP) extends this process by combining it with a probabilistic description of future loading to estimate metrics such as remaining useful life (RUL) of the system (Kadry 2012). With the tremendous increase in computational capabilities and with the advent of new algorithms to solve complex machine learning tasks, the statistical pattern recognition paradigm for SHM/DP of civil structures is gaining popularity among researchers. This paradigm is especially attractive because it offers the possibility of automating the SHM process, i.e., removing the need for interventions of human experts as far as possible. One main objective of the SHM system is to detect, localize, classify and quantify the damage on the structure of interest (Farrar and Worden 2007). To achieve this, in a pattern recognition perspective, the data corresponding to all the conceivable damage states/mechanisms of the structure of interest are required (Farrar and Worden 2012). One of the potential ways of obtaining this data for civil infrastructure systems is using digital twins/cyber models (hybrid data-physics models). A potential way of constructing digital twins for full-scale structural systems is by using the finite element (FE) model updating framework.

The last few decades have witnessed tremendous progress in nonlinear modeling and analysis methods for civil engineering structural, geo-structural, and soil-foundation-structural

systems subjected to static, quasi-static, and dynamic loading, particularly from natural hazards such as earthquakes. Mechanics-based nonlinear FE models (of various complexities) of civil engineering systems (e.g., buildings, bridges, dams, miter gates) are now able to capture the damage and failure mechanisms developing in such systems in critical loading environment. The current state-of-the-art nonlinear FE modeling techniques allow reasonably accurate predictions of the actual response of civil structural systems if realistic and "well-calibrated" values are used for the unknown parameters of the FE model. These parameters for civil systems generally include inertial, damping, hysteretic material law, loading, boundary conditions, and geometric parameters. When input-output measurement data are available, the FE model updating framework allows to estimate/update the unknown parameters of the FE model (Astroza et al. 2015, 2019a; Ebrahimian et al. 2017; Ramancha et al. 2020b). The Bayesian approach to model updating is attractive because it accounts for various sources of uncertainties observed in the real world (i.e., noisy output measurements, unknown/partially known/noisy input measurements, uncertainty in FE model parameters, FE model form uncertainty) during estimating/updating the unknown parameters and characterizes the remaining estimation uncertainty. This confidence level associated with the parameter estimates is extremely useful for SHM/DP as it supports rigorous decision-making. In Bayesian model updating, the modeler needs to specify the probabilistic description of unknown parameters (referred to as prior knowledge). The prior knowledge is then updated (referred to as posterior) accounting for the measurement data using Bayesian inference. The FE model characterized by the posterior probabilistic description of the unknown parameters is referred to as the updated FE model. This updated model, which is essentially a fusion of heterogeneous measurement data and a physics-based FE model, is the digital twin/cyber model and can be utilized for SHM/DP purposes.

Bayesian Nonlinear FE Model updating of a full-scale reinforced-concrete bridge column tested on the large high-performance outdoor shake table (LHPOST) at UC San Diego (UCSD) (Schoettler, Restrepo, Guerrini 2015) is considered in this paper. The bridge column was subjected to a sequence of ten recorded earthquake ground motions (uniaxial excitation) and was densely instrumented with an array of 278 sensors consisting of strain gauges, linear and string potentiometers, accelerometers and Global Positioning System (GPS) based displacement sensors to measure local and global responses during testing. First, a frame-type FE model with distributed plasticity of the bridge column is developed. Then, the measurement data from the first earthquake excitation (EQ1) are used to update five key structural parameters (Young's modulus of concrete E_c and steel E_s; Rayleigh damping model parameters a_1 and a_2; and tensile strength of concrete f_{ct} and tension stiffening parameter β) of the nonlinear FE model using the sequential Monte Carlo (SMC) method (Ching and Chen 2007; Minson et al. 2013) – a class of Bayesian inference methods. The novelty of this study lies in the use of real-world input-output measurement data of a full-scale structural system to update a detailed mechanics-based nonlinear finite element model using a "fully" Bayesian inference technique (SMC).

5.3 Finite Element Model Updating using Bayesian Inference

Let $\mathbf{u}_k \in \mathbb{R}^{n_\mathbf{u}}$ and $\mathbf{y}_k \in \mathbb{R}^{n_\mathbf{y}}$ denote the vector of measured input and output responses, respectively, of the structure of interest at the time t_k (or time step k). These measurements are obtained from the heterogeneous sensor array mounted on the real structure. Assuming the measurement responses are obtained for N time steps, the measured/observed input-output

dataset is $\mathcal{D}=(\mathbf{u},\mathbf{y})$, where $\mathbf{u}=\left[\mathbf{u}_1^T,\mathbf{u}_2^T,...,\mathbf{u}_N^T\right]^T\in\mathbb{R}^{(n_{\mathbf{u}}\times N)\times 1}$ and $\mathbf{y}=\left[\mathbf{y}_1^T,\mathbf{y}_2^T,...,\mathbf{y}_N^T\right]^T\in\mathbb{R}^{(n_{\mathbf{y}}\times N)\times 1}$.

At time step k, let $\mathbf{y}_k^{FE}=\mathbf{h}_k\left(\mathbf{u}_{1:k};\boldsymbol{\theta}\right)\in\mathbb{R}^{n_{\mathbf{y}}}$ denote the response predicted by the FE model $\mathbf{h}$ parameterized by the unknown parameter vector $\boldsymbol{\theta}\in\mathbb{R}^{n_{\boldsymbol{\theta}}}$ when subjected to the measured input time-history $\mathbf{u}_{1:k}=\left[\mathbf{u}_1^T,\mathbf{u}_2^T,...,\mathbf{u}_k^T\right]^T\in\mathbb{R}^{(n_{\mathbf{u}}\times k)\times 1}$. For the methodology described in this paper, the parameter vector $\boldsymbol{\theta}$ can include any unknown time-invariant parameters such as inertial, damping, hysteretic material law, loading, boundary conditions and geometric parameters of the FE model. In practice, the measured response $\mathbf{y}$ and the FE predicted response $\mathbf{y}^{FE}$ do not match due to numerous sources of uncertainty (Chatfield 1995). These include

(1) Uncertainty in the measured output due to sensor noise

(2) Unmeasured/partially measured input and sensor noise associated with measured inputs

(3) Uncertainty about the structure/form of the model, i.e., the selected model class cannot represent the real system. This model form error, if not accounted for, can introduce bias in estimation and handicap the predictive utility of the model.

(4) Uncertainty about the parameters of the model, assuming the structure/form of the model is known.

Put in simple terms, the goal of Bayesian model updating is to estimate/update the unknown parameter vector $\boldsymbol{\theta}$ accounting for all the pertinent sources of uncertainties and characterize the remaining estimation uncertainty. To achieve this, first, the likelihood function should be constructed using a measurement equation, i.e., a model of the measurement process.

This is also referred to as a joint statistical-physical model that relates model parameters to measurements/observations. The following measurement equation is used in this paper

$$\text{Measument equation at time step } k \rightarrow \quad \underset{\text{measured output}}{\mathbf{y}_k} = \underbrace{\mathbf{h}_k\left(\mathbf{u}_{1:k};\boldsymbol{\theta}\right)}_{\text{FE predicted response}} + \underset{\text{error/noise}}{\mathbf{w}_k} \tag{5.1}$$

where $\mathbf{w}_k = \left[w_{1,k}, w_{2,k}, ..., w_{n_\mathbf{y},k} \right]^T$ is the measurement error/noise at time step k and $w_{i,k}$ denotes the discrepancy between measured and FE predicted responses corresponding to the i^{th} output measurement channel at time step k. In the measurement equation, the noise term, lumping all the sources of uncertainties, is assumed additive to the FE predicted response. Therefore, the accurate statistical description model of the noise process $\mathbf{w} = \left[\mathbf{w}_1^T, \mathbf{w}_2^T, ..., \mathbf{w}_N^T \right]^T$ is crucial in Bayesian inference. In this paper, the noise process $\mathbf{w}$ is assumed temporally white ($\mathbf{w}_1, \mathbf{w}_2, ...$ are statistically independent) and random vector $\mathbf{w}_k$ is assumed to follow a zero-mean Gaussian probability density function (PDF) with independent components (i.e., noise/error terms across all measurement channels are assumed statistically independent).

$$\mathbf{w}_k \sim \mathcal{N}\left(\underset{n_\mathbf{y}\times 1}{\mathbf{0}}, \boldsymbol{\Sigma} = \begin{pmatrix} \sigma_1^2 & 0 & \cdots & 0 \\ 0 & \sigma_2^2 & \cdots & 0 \\ \vdots & \vdots & \ddots & \vdots \\ 0 & 0 & \cdots & \sigma_{n_\mathbf{y}}^2 \end{pmatrix}_{n_\mathbf{y}\times n_\mathbf{y}} \right); \mathbf{w} \sim \mathcal{N}\left(\underset{\left(n_\mathbf{y}\times N\right)\times 1}{\mathbf{0}}, \begin{pmatrix} \boldsymbol{\Sigma} & \mathbf{0} & \cdots & \mathbf{0} \\ \mathbf{0} & \boldsymbol{\Sigma} & \cdots & \mathbf{0} \\ \vdots & \vdots & \ddots & \vdots \\ \mathbf{0} & \mathbf{0} & \cdots & \boldsymbol{\Sigma} \end{pmatrix}_{\left(n_\mathbf{y}\times N\right)\times\left(n_\mathbf{y}\times N\right)} \right) \tag{5.2}$$

where σ_i^2 denote the variance of the discrepancy between measured and predicted responses of the i^{th} output measurement channel. These noise variances are also typically unknown in the real world. Therefore, in this paper, the unknown vector $\boldsymbol{\sigma} = \left[\sigma_1, \sigma_2, ..., \sigma_{n_\mathbf{y}} \right]^T$ is estimated/updated jointly with the unknown FE model parameter vector $\boldsymbol{\theta}$. With the

measurement model described by Equations (5.1) and (5.2), the likelihood function for the unknown parameters $\boldsymbol{\theta}$ and $\boldsymbol{\sigma}$ is given by

$$\begin{aligned} p(\mathbf{y}\,|\,\mathbf{u},\boldsymbol{\theta},\boldsymbol{\sigma}) &= \prod_{k=1}^{N} p(\mathbf{y}_k\,|\,\mathbf{u}_{1:k},\boldsymbol{\theta},\boldsymbol{\sigma}) \\ &= \prod_{k=1}^{N} \frac{1}{(2\pi)^{n_{\mathbf{y}}/2}} |\boldsymbol{\Sigma}|^{-1/2} \exp\left\{ -\frac{1}{2}\left[\mathbf{y}_k - \mathbf{h}_k(\mathbf{u}_{1:k};\boldsymbol{\theta})\right] \boldsymbol{\Sigma}^{-1} \left[\mathbf{y}_k - \mathbf{h}_k(\mathbf{u}_{1:k};\boldsymbol{\theta})\right]^T \right\} \end{aligned} \tag{5.3}$$

The modeler also needs to specify the prior PDF of the unknown parameter vector , $p(\boldsymbol{\theta},\boldsymbol{\sigma})$. The prior PDF is then updated to obtain the posterior PDF, which accounts for the prior knowledge and the observed data, using Bayes rule as

$$p(\boldsymbol{\theta},\boldsymbol{\sigma}\,|\,\mathcal{D}) \equiv \underbrace{p(\boldsymbol{\theta},\boldsymbol{\sigma}\,|\,\mathbf{u},\mathbf{y})}_{posterior} = \frac{\overbrace{p(\mathbf{y}\,|\,\mathbf{u},\boldsymbol{\theta},\boldsymbol{\sigma})}^{likelihood} \times \overbrace{p(\boldsymbol{\theta},\boldsymbol{\sigma})}^{prior}}{\underbrace{p(\mathbf{u},\mathbf{y})}_{evidence}} \tag{5.4}$$

However, determining analytically the complete joint posterior is an intractable problem. Many numerical approximations methods such as Bayesian Kalman filters, particle filters, Markov chain Monte Carlo methods (MCMC), sequential Monte Carlo (SMC) methods (SMC), etc., have been developed to perform this computation and most of these methods rely on sampling the joint posterior. In this paper, SMC is used to sample the joint posterior PDF defined in Equation (4).

5.3.1 Sequential Monte Carlo

SMC methods are a class of Bayesian inference techniques that sample the joint posterior PDF of the unknown parameters. In the literature, there are several closely related algorithms that are referred to as transitional Markov chain Monte Carlo, particle filters, bootstrap filters, condensation algorithm, survival of the fittest and population Monte Carlo (Kemp 2003). SMC

methods do not require the Gaussian assumption about the prior and posterior PDFs of the unknown parameters, an inherent assumption in Bayesian Kalman filters (e.g., unscented Kalman filter, extended Kalman filter). Unlike standard MCMC methods, SMC methods are parallelizable, they can be used to perform model updating of high-fidelity large-scale nonlinear FE models using high-performance computing (HPC) resources.

The idea of SMC is to sample from a series of simpler intermediate PDFs that converge to the target posterior PDF, thus circumventing the need to directly sample the target posterior. To achieve this, SMC samplers proceed through a series of stages, starting from the prior distribution until the posterior distribution. All these distributions (called tempered posterior distributions) are controlled by the tempering parameter β as

$$p\left(\boldsymbol{\theta},\boldsymbol{\sigma}\,|\,\mathbf{u},\mathbf{y}\right)_{\beta} \propto p\left(\mathbf{y}\,|\,\mathbf{u},\boldsymbol{\theta},\boldsymbol{\sigma}\right)^{\beta} \times p\left(\boldsymbol{\theta},\boldsymbol{\sigma}\right) \tag{5.5}$$

When $\beta = 0$, the tempered posterior is just the prior PDF and when $\beta = 1$ the tempered posterior is the true posterior PDF. The SMC sampler starts with $\beta = 0$ and progresses by monotonically increasing the value of β, at each stage, until it reaches the value of 1. The tempered posterior distribution at every stage in SMC is represented by a set of weighted samples (also called particles). Also, at each stage, SMC uses independent Markov chains (which start at the samples of the current tempered posterior distribution) to reach the next tempered posterior distribution. Therefore, the SMC sampling algorithm can also be thought of as a parallel MCMC algorithm that can effectively sample high-dimensional parameter spaces (Minson et al. 2013). Due to its inherent parallel nature, SMC can be used to efficiently perform model updating of high-fidelity large-scale nonlinear FE models using high-performance computing resources. In contrast to MCMC, SMC can effectively sample from posterior distributions with flat peaks and multiple peaks which arise in non-identifiable and locally-

identifiable problems, respectively. SMC also computes the model evidence (denominator of Equation (4)) as a by-product, which can then be used for Bayesian model class selection and model averaging (Ching and Chen 2007). The SMC algorithm used in this paper to sample the joint posterior in Equation (4) is presented in Table 5.1.

Table 5.1: Sequential Monte Carlo Algorithm

Notation: N_p : number of particles , ESS : effective sample size , β : tempering parameter , j : stage number $\boldsymbol{\alpha} = \left[\boldsymbol{\theta}^T, \boldsymbol{\sigma}^T \right]^T$: unknown parameter vector to be updated , $\boldsymbol{\alpha}_j^i$: i^{th} particle of $\boldsymbol{\alpha}$ at stage j
Initialize: N_p , $j = 0$, $ESS_0 = N_p$, $\beta_0 = 0$, Generate N_p samples $\left\{ \boldsymbol{\alpha}_{j=0}^i ;\ i = 1,...,N_p \right\}$ from the prior PDF $p(\boldsymbol{\alpha})$
while $\beta_j < 1$: stage number $j = j + 1$ choose $\tilde{\beta}_j$ such that $ESS_j = 0.95 \times ESS_{j-1}$, $\beta_j = \min\left(\tilde{\beta}_j, 1\right)$ weighting: $w_j^i = p\left(\mathbf{y} \mid \mathbf{u}, \boldsymbol{\alpha}_{j-1}^i\right)^{\beta_j - \beta_{j-1}}$ for $i = 1,...,N_p$ resampling: $\tilde{\boldsymbol{\alpha}}_j^i = \boldsymbol{\alpha}_{j-1}^l$ with probability w_j^l for $i = 1,...,N_p$ perturbation: start an MCMC chain at $\tilde{\boldsymbol{\alpha}}_j^i$ and take N_{MCMC} steps with target distribution $p(\boldsymbol{\alpha} \mid \mathbf{u}, \mathbf{y})_{\beta_j}$ for each $i = 1,...,N_p$. Gather last sample of each MCMC chain to obtain $\left\{ \boldsymbol{\alpha}_j^i ; i = 1,...,N_p \right\}$ **end**
save last stage $m = j$ $\left\{ \boldsymbol{\alpha}_m^i ; i = 1,...,N_p \right\}$ are the samples of the target posterior $p(\boldsymbol{\alpha} \mid \mathbf{u}, \mathbf{y})$

5.4 Full-scale reinforced-concrete bridge Column

A full-scale reinforced-concrete bridge column was tested on the large high-performance outdoor shake table (LHPOST) at the University of California, San Diego (UCSD) from July through September 2010 (Schoettler, Restrepo, Guerrini 2015) (see Figure 5.1). The 7.3m (24ft) high and 1.2m (4ft) diameter column was designed and detailed according to the California Department of Transportation (Caltrans) seismic design guidelines. The objective of the test was to validate the current seismic design guidelines in terms of the structural seismic response of bridge columns. For this purpose, the column was tested under dynamic loading conditions by subjecting it to a series of ten earthquake ground motion records (uniaxial excitation along the table's longitudinal axis or east-west direction). A concrete superstructure block weighing 2.32MN (522 kips) was cast on top of the column for mobilizing the inertial forces during the dynamic tests. This block was designed such that its center-of-mass coincided with the top of the column. This test specimen was densely instrumented with an array of 278 sensors consisting of strain gauges, linear and string potentiometers, accelerometers and Global Positioning System (GPS) based displacement sensors to measure local and global responses during testing (Schoettler, Restrepo, Guerrini 2015).

Figure 5.1: Full-scale reinforced-concrete bridge column tested on the LHPOST@UCSD

5.4.1 Finite Element Model of the column

With a height-to-diameter ratio of 6, the test specimen was intended to respond in the nonlinear range with predominant flexural behavior. FE models using beam-column elements with distributed plasticity have been proven to capture the observed nonlinear behavior of such flexural dominated systems extremely well. Due to their accuracy in matching experimental results, formulation simplicity, and computation feasibility and efficiency, such FE model types are widely used in research and engineering practice (Taucer 2019). In this paper, the 7.3m (24ft) tall bridge column is modeled using two nonlinear fiber-section Euler-Bernoulli force-based beam-column elements. The top and bottom element have five and two Gauss-Lobatto integration points (monitored cross-sections), respectively, along the length of each element (see Figure 5.2). Each element cross-section is discretized into longitudinal fibers as shown in Figure 5.2. The section nonlinear response behavior is simulated from the uniaxial material constitutive laws used for the fibers. Uniaxial Popovics material model (Popovics 1973) is used for modeling confined and unconfined concrete behavior at the fiber level and the Dodd Restrepo Carreno uniaxial steel material model (Dodd and Restrepo-Posada 1995) is used for modeling

longitudinal steel fibers as shown in Figure 5.2. The effects of nonlinear geometry are accounted for using the corotational formulation. The inherent damping properties representing sources of energy dissipation beyond the hysteretic energy dissipated through inelastic material behavior are modeled using Rayleigh damping (proportional to the mass matrix $\mathbf{M}$ and initial tangent stiffness matrix $\mathbf{K}_T$). The footing is approximated as a fixed restraint and the inertial effect of the superstructure is lumped on the top node of the column.

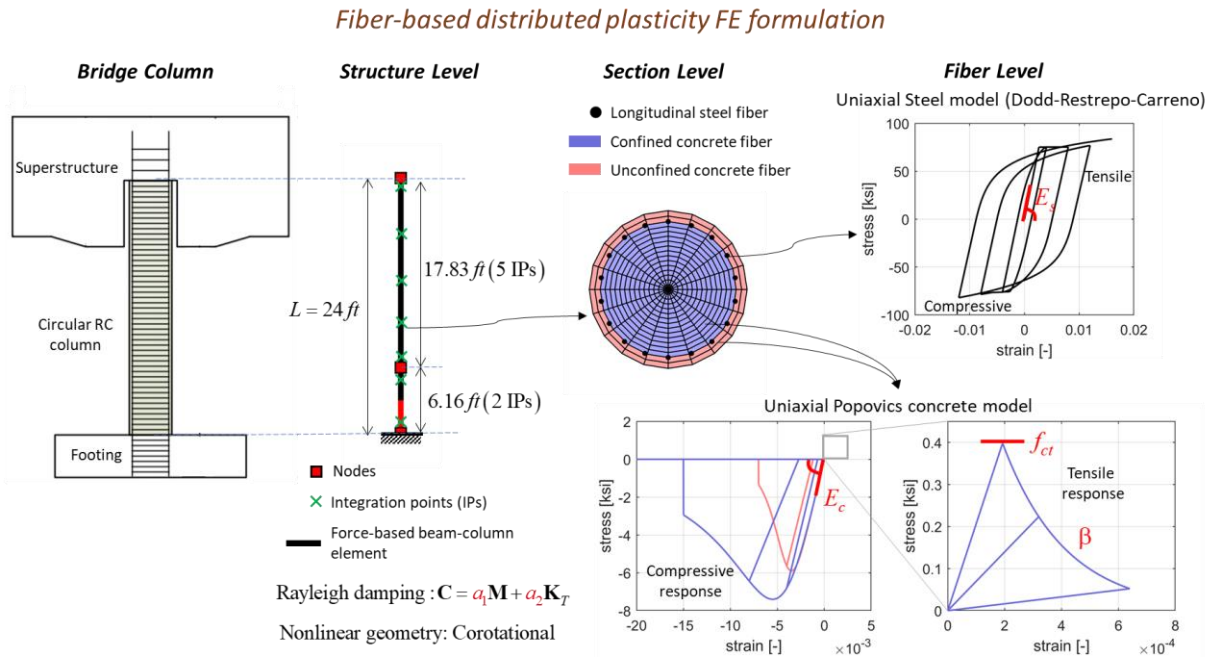

Figure 5.2: Finite Element Model Hierarchy of Bridge Column

5.4.2 FE Model Updating Setup

The measured input-output data corresponding to the first earthquake excitation (EQ1) are utilized to update the developed FE model of the column. During EQ1 excitation, it was observed that the column response was essentially linear elastic with no observable damage. Only hairline cracks (less than 0.1mm wide) were observed at the base of the column (above the footing) (Schoettler, Restrepo, Guerrini 2015). Therefore, only the parameters that govern the

linear elastic behavior of the column (Young's modulus of concrete E_c and steel E_s; Rayleigh damping parameters corresponding to EQ1 a_1^{EQ1} and a_2^{EQ1}) along with the tensile strength of concrete, parameter f_{ct}, and tension stiffening parameter of concrete model, parameter β, are assumed unknown and estimated using the measured input-output data; thus, $\boldsymbol{\theta} = \left[E_c, E_s, f_{ct}, \beta, a_1^{EQ1}, a_2^{EQ1} \right]^T \in \mathbb{R}^{6\times 1}$ (see Figure 5.2).

The parameters of concrete (E_c, f_{ct}, and β), steel (E_s), and Rayleigh damping model (a_1^{EQ1} and a_2^{EQ1}) were determined experimentally by testing 6 *in* x 12 *in* concrete cylinders, reinforcing steel bars, and subjecting the column to white noise excitation, respectively. These experimentally determined parameter values (reported in (Schoettler, Restrepo, Guerrini 2015)) are shown in Table 5.2 and will be referred to as parameter values reported in the PEER report or PEER parameters in brief. These reported values are utilized to construct the prior PDF. To construct the prior PDF, lower and upper bounds to each parameter are set according to literature and expert opinion. These bounds are essential and allow the parameter values to lie within the range set by bounds after calibration. Without bounds, the physical parameters might act as tuning parameter in the model calibration and lose their physical meaning. That is, the parameter values of physical parameters after calibration can be completely non-physical values as the parameters are merely tuned to fit the FE model to the measurement data.

The accelerometers mounted at the footing of the column are used as the measured EQ1 input excitation to the column (see Figure 5.3). This measured column base acceleration is then used as input data $\mathbf{u}$ in model updating. The accelerometers and displacement string potentiometers mounted on the superstructure mass are used to reconstruct the absolute horizontal and rotational acceleration response and relative (to the base of the column) horizontal

displacement response at the top of the column. This reconstructed absolute acceleration and relative displacement responses are used as output data $\mathbf{y}$ in model updating. Thus,

$$\mathbf{y}_k = \begin{bmatrix} \text{Absolute Horizontal Acceleration of the top of the column at time step } k \\ \text{Absolute Rotational Acceleration of the top of the column at time step } k \\ \text{Relative Horizontal Displacement at the top of the column at time step } k \end{bmatrix} \in \mathbb{R}^{3\times 1} \quad (5.6)$$

The measurement equation described in Equation (5.1) is utilized for model updating. The noise/error term $\mathbf{w}_k$ is assumed to have Gaussian independent components white in time, i.e., $\mathbf{w}$ is modeled as a vector Gaussian white noise, i.e.,

$$\mathbf{w}_k \sim \mathcal{N}\left(\mathbf{0}, \begin{pmatrix} \sigma^2_{hor-accel} & 0 & 0 \\ 0 & \sigma^2_{rot-accel} & 0 \\ 0 & 0 & \sigma^2_{hor-disp} \end{pmatrix}\right) \quad \text{and} \quad \mathbf{w} \sim \mathcal{N}\left(\mathbf{0}, \begin{pmatrix} \boldsymbol{\Sigma} & \mathbf{0} & \cdots & \mathbf{0} \\ \mathbf{0} & \boldsymbol{\Sigma} & \cdots & \mathbf{0} \\ \vdots & \vdots & \ddots & \vdots \\ \mathbf{0} & \mathbf{0} & \cdots & \boldsymbol{\Sigma} \end{pmatrix}\right) \quad (5.7)$$

where $\sigma^2_{hor-accel}$, $\sigma^2_{rot-accel}$, and $\sigma^2_{hor-disp}$ denote the variance of the discrepancy between measured and FE predicted responses for the horizontal acceleration, rotational acceleration, and horizontal displacement response quantities, respectively.

The six parameters of the FE model ($\boldsymbol{\theta} = \left[E_c, E_s, f_{ct}, \beta, a_1^{EQ1}, a_2^{EQ1}\right]^T \in \mathbb{R}^{6\times 1}$) together with the noise standard deviations $\sigma_{hor-accel}$, $\sigma_{rot-accel}$, and $\sigma_{hor-disp}$ are estimated using the SMC algorithm described in Table 5.1. The prior PDF is constructed by assuming that the nine parameters are mutually statistically independent. Truncated normal distributions with mean values taken as the parameter values reported in the PEER report are used to construct the prior PDF of the FE model parameters $E_c, E_s, f_{ct},$ and β. Truncated is performed using the lower and upper bounds shown in Table 5.2. The standard deviations of the priors are selected to obtain coefficients of variation of 0.30, 0.20, 0.60, and 0.60 for $E_c, E_s, f_{ct},$ and β, respectively.

Uniform prior with bounds shown in Table 5.2 is used as priors for damping parameters a_1^{EQ1}, a_2^{EQ1}. Half normal distributions are used as priors for noise parameters $\sigma_{hor-accel}$, $\sigma_{rot-accel}$, and $\sigma_{hor-disp}$, respectively. At each stage of SMC, the tempered posterior is represented using $N_p = 1000$ particles and during the perturbation phase, the number of MCMC steps is set as $N_{MCMC} = 5$. Parallel computing (message passing interface MPI) across 20 compute nodes (1000 cores) on Frontera supercomputer is used for evaluating the likelihood function at every step of the perturbation phase of each SMC stage. It took ~6 min to obtain 1000 samples of the posterior using SMC algorithm considering only EQ1 data.

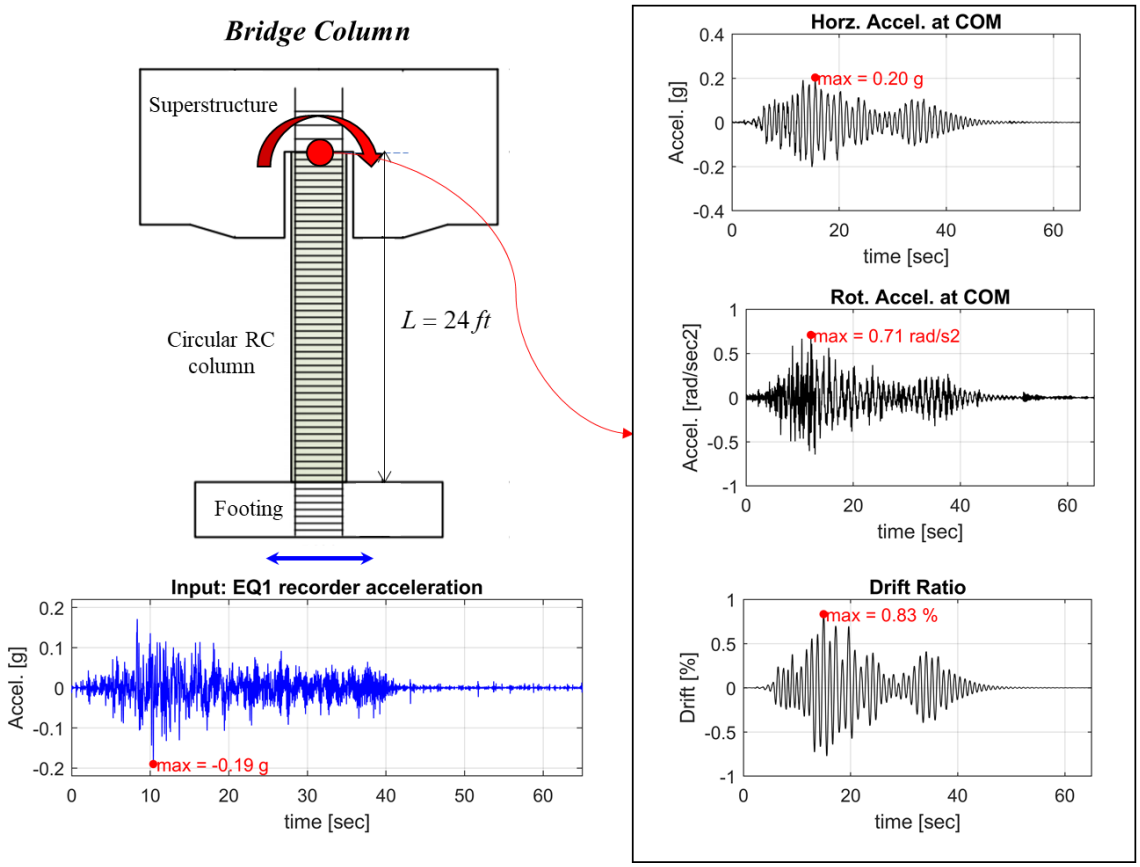

Figure 5.3: Input (acceleration at top of footing) and output (absolute horizontal and rotational acceleration and drift ratio at the top of the column) measurement data for model updating.

5.4.3 Results

5.4.3.1 Posterior after calibrating using EQ1 data

The pair plot of six unknown FE parameters constructed using the posterior samples obtained from SMC is shown in Figure 5.4. In the figure, the posterior samples are normalized with PEER values shown in Table 5.2. The plots along the diagonal show the histogram and kernel density estimates of the marginal posterior PDF of each parameter (normalized with PEER values). The marginal posterior PDFs are very sharp (conveyed by very small coefficients of variation, CV), implying that the remaining estimation uncertainty after model updating is very low. The plots above the diagonal show the posterior samples in the space of every parameter pair and the plots below the diagonal show the contour plots of the corresponding kernel density estimates where r is the Pearson correlation coefficient. The sample mean values of the posterior SMC samples are compared in Table 5.2 with the corresponding parameter values reported in the PEER report. The marginal posterior PDFs are very sharp (conveyed by very small coefficients of variation in Table 5.2), implying that the remaining estimation uncertainty after model updating is very low.

Table 5.2: Parameter values reported in PEER report vs the mean values of the posterior SMC samples

Parameter	**Values from PEER report**	**Bounds**	**Sample mean of SMC posterior samples**	**Coefficient of variation of marginal posterior**
E_c	$22.9\ GPa$	$\pm 20\%$	$0.80 * 22.9\ GPa$	$2.5\ * 10^{-4}$
E_s	$196\ GPa$	$\pm 8\%$	$0.94 * 196\ GPa$	$5.3\ * 10^{-4}$
f_{ct}	$2.1\ MPa$	$9\% - 21\%$ of f_c'	$1.7 * 2.1\ MPa$	$5.2\ * 10^{-4}$
β	0.1	$0.05 - 0.7$	$3.7 * 0.1$	$4.5\ * 10^{-2}$
a_1^{EQ1} a_2^{EQ1}	$\xi_1^{EQ1} = 4.3\ \%$ $\xi_2^{EQ1} = 1.3\ \%$	$0.5 - 3\%$ for ξ_1^{EQ1} and ξ_2^{EQ1}	$\xi_1^{EQ1} = 1.0\ \%$ $\xi_2^{EQ1} = 3\ \%$	$1.0\ * 10^{-2}$ $1.4\ * 10^{-3}$

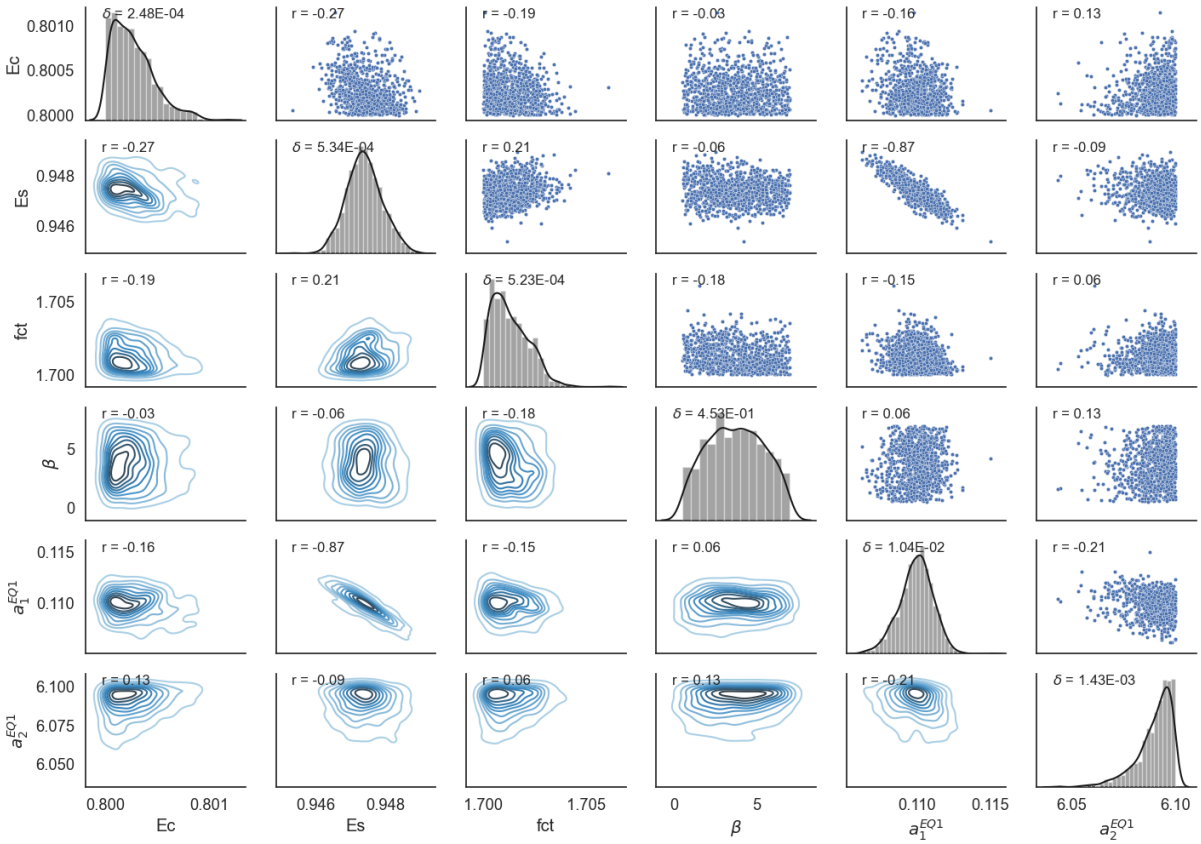

Figure 5.4: Pair plot using normalized posterior samples of six unknown FE parameters obtained using sequential Monte Carlo

5.4.3.2 Response comparison before and after calibration using EQ1 data

The FE predicted acceleration and relative displacement responses of the bridge column obtained using the parameter values reported in the PEER report (i.e., before FE model updating) and using the sample mean values of the posterior SMC samples (i.e., after FE model updating) are compared with the experimentally measured responses in Figure 5.5. The relative-root-mean-square error (RRMSE) is used as a metric to measure the discrepancy between two time series. The FE responses predicted using the PEER parameters (i.e., before FE model updating) match poorly the corresponding experimental responses (high RRMSE), while the responses predicted using the sample mean of the posterior samples (i.e., after FE model updating) match the experimental responses very well (low RRMSE). This demonstrates that by fusing detailed

mechanics-based FE modeling with input-output measurement data through Bayesian inference, one can capture the observed response of a full-scale structural system extremely well.

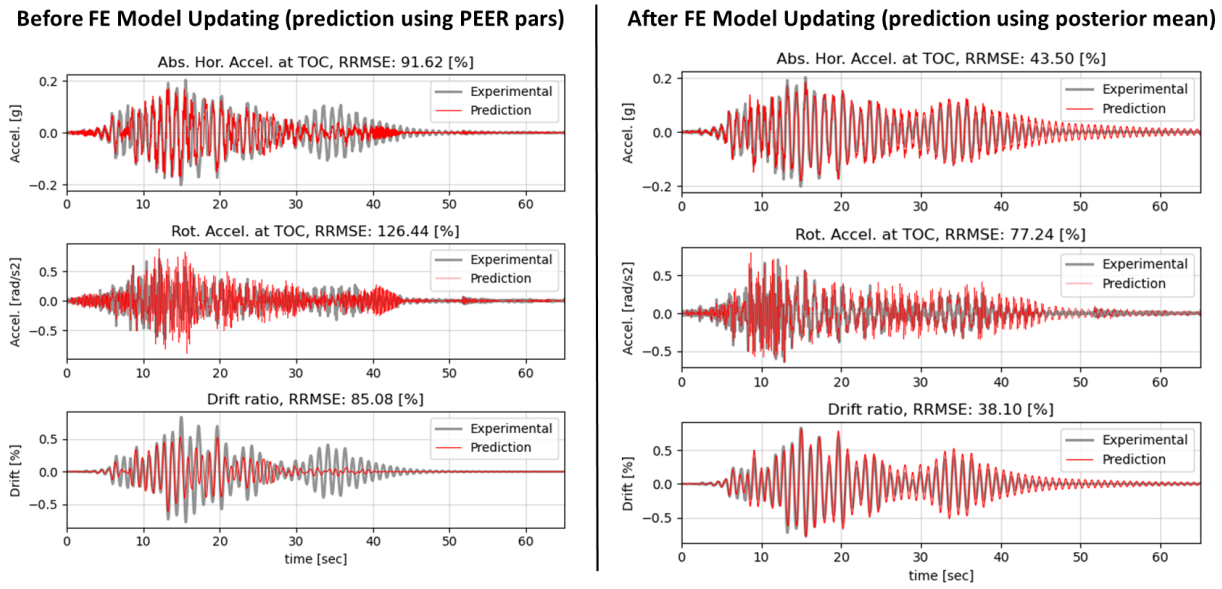

Figure 5.5: Response prediction of the FE model vs experimentally measured response, before and after model updating

5.4.3.3 Response prediction before and after calibration using EQ1 data

Figure 5.6 compares the experimentally measured drift response of the column for EQ1 to EQ4 with the FE predicted drift response. In Figure 5.6a, the FE prediction is performed using the PEER parameters, i.e., before FE model updating. The FE predicted response before model updating does not match well with that of the experimental response as conveyed by the high RRMSE (show in Figure 5.6a). In Figure 5.6b, the FE prediction is performed using the posterior sample mean given in (), i.e., after model updating using EQ1 data. Now the FE predicted response matches very well with the experimental response for EQ1 since the Bayesian calibration finds parameter values such that there is a good match between FE predicted and measured response. No improvement in FE response predicted is observed for EQ2 after model updating using EQ1 data as conveyed by no change in RRMSE (EQ2) which is 93%. A slight

improvement in response prediction is observed for EQ3 and EQ4 after model updating compared to before model updating using EQ1 data as conveyed by decrease in RRMSE (EQ3) from 51% to 46% and RRMSE (EQ4) from 52% to 49%.

Note that the bridge column was in a different nonlinear regime during each earthquake excitation during the experiment. For example, during EQ1 excitation, the column was pretty much linear elastic with tensile cracking observed at the base and after EQ3 excitation, a fully developed plastic hinge was formed at the base of the column. Therefore, one cannot expect a great improvement in results for EQ3 prediction (fully nonlinear regime) by calibrating the FE model using EQ1 data (linear elastic regime + tensile cracking only). This throws some light at the practical limitations of a living digital twin for response prediction.

5.4.3.4 FE model updating and response prediction after updating using EQ2 data

The FE model updating of the bridge column is repeated but now only considering the data corresponding to EQ2 excitation. Yielding of the steel rebars was observed during EQ2 excitation in the experiment. Therefore, the yield strength of steel parameter f_y is estimated in addition to $E_c, E_s, f_{ct}, \beta, a_1^{EQ2}$, and a_2^{EQ2}. In Figure 5.6c, the FE prediction is performed using the posterior sample mean after model updating using EQ2 data. As expected, the FE predicted response matches very well with the experimental response for EQ2 as conveyed by low RRMSE (EQ2) of 33% since the Bayesian calibration finds parameter values to yield a good match between FE predicted and measured responses. A slight improvement in response prediction is again observed for EQ3 and EQ4 after model updating using EQ2 data compared after model updating using EQ1 data as conveyed by decrease in RRMSE (EQ3) from 46% to 40% and RRMSE (EQ4) from 49% to 44%. However, the FE response does not match well with

the experimental response in EQ1 regime and in fact, a decrease in quality of the fit is observed as conveyed by increase in RRMSE (EQ1) from 38% to 67%. This can be attributed to the selected FE model being not perfect (as in the case of most models in the real world), i.e., having model discrepancy. The developed fiber-based distributed plasticity FE model of the column does not capture flexure-shear interaction and the bar pullout is not modeled. For these reasons, due to model discrepancy, the physical parameters merely act as tuning parameters during model calibration. However, the parameter values after calibration at least stay in the physical range as the prior distribution is bounded. In a hypothetical scenario with a perfect model with no missing physics, we could expect the FE response prediction quality in Figure 5.6c to remain similar to Figure 5.6b in the EQ1 regime. However, these aspects need to be further studied and are beyond the scope of this thesis. This throws some additional light at the limitations of a living digital twin with imperfect models (as all models are wrong).

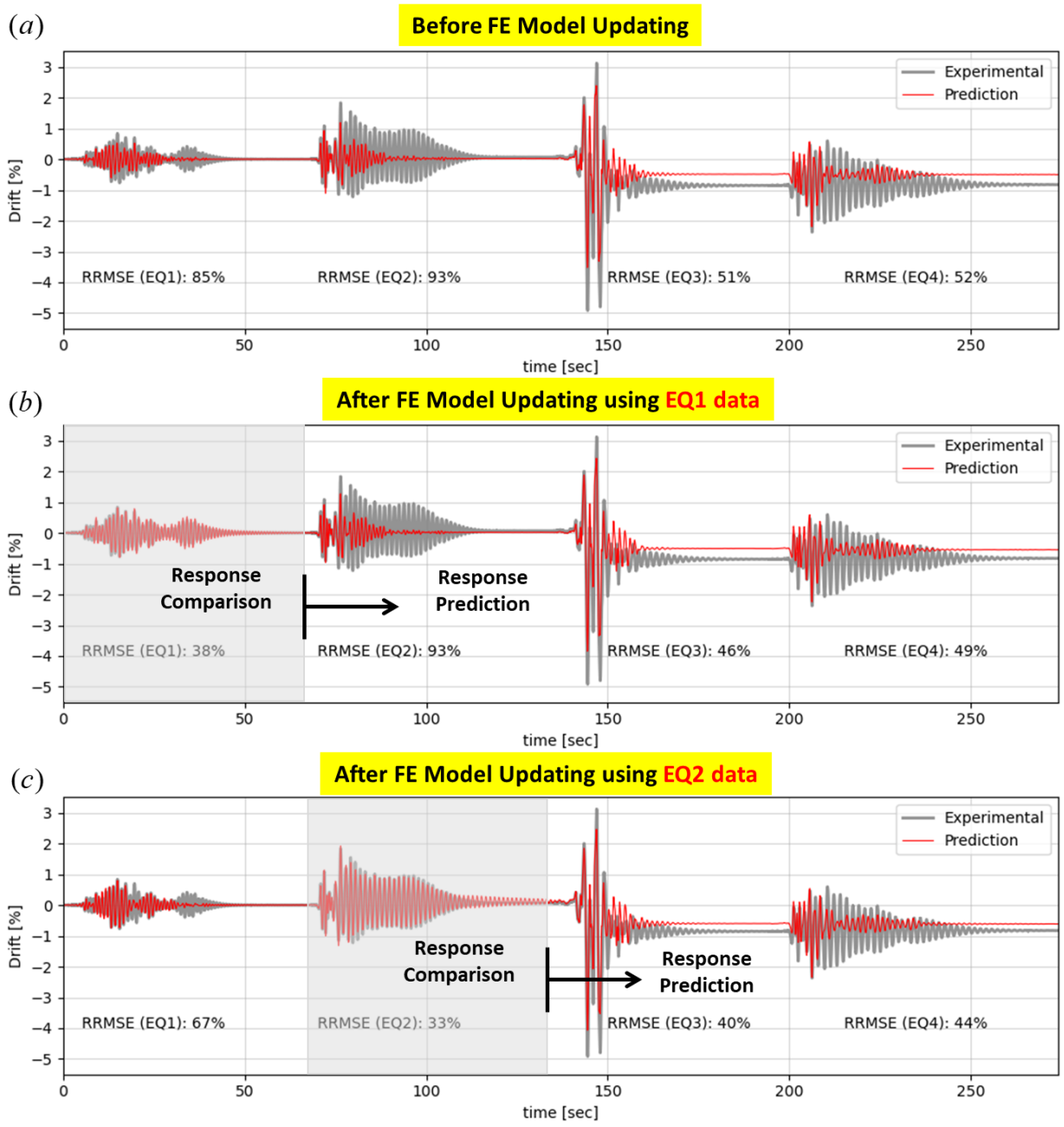

Figure 5.6: Drift response comparison of the FE model (a) before model updating, (b) after model updating using EQ1 data, and (c) after model updating using EQ2 data with the experimentally measured drift response.

5.5 Conclusions

This paper focuses on model updating of civil structures using Bayesian inference. A full-scale reinforced-concrete bridge column tested on the LHPOST@UCSD is selected as the testbed structure. The parameters of the FE model are updated using the sequential Monte Carlo method, a fully Bayesian inference method, using measured input-output data corresponding to the earthquake excitation applied by the shake table. The framework shown here can be used to tune the unknown parameters of the FE model to match the measured response (model calibration). The updated nonlinear FE model acts as a digital twin of the structure of interest and can subsequently be interrogated for the presence, location, type, and extent of damage (i.e., losses in stiffness, strength, ductility capacity, …) in the structure. The updated FE model can also be used to better predict the future performance/functionality of the structure by using it in conjunction with probabilistic descriptions of future loading (damage prognosis). The chapter also illustrates the concept of a living digital twin of structural systems and highlights its potential limitations.

5.6 Acknowledgements

Funding for this work was provided by the U.S. Army Corps of Engineers through the U.S. Army Engineer Research and Development Center Research Cooperative Agreement W912HZ-17-2-0024. Chapter 5 is partially a reprint of the material as it appears in the following paper (the dissertation author is the first author of this paper):

Ramancha, M. K., Astroza, R., Conte, J. P., Restrepo, J. I., and Todd, M. D. (2020). "Bayesian nonlinear finite element model updating of a full-scale bridge-column using sequential monte carlo." *Model Validation and Uncertainty Quantification*, 389–397. https://doi.org/10.1007/978-3-030-47638-0_43

6 Conclusions

6.1 Summary of Research Work

This dissertation presents a framework for model updating in the time domain using Bayesian inference and shows its application to civil infrastructure systems using mechanics-based finite element (FE) models. The advantage of model updating in the time domain is that it can be applied to update a linear or a nonlinear FE model. The updated FE model of the system can then be used for structural health monitoring (SHM) and damage prognosis (DP) purposes for optimal risk-based operations and infrastructure asset management. Model updating of civil infrastructure systems is challenging due to the sheer complexity of modeling them and the presence of wide-ranging real-world uncertainties that need to be accounted for in the model updating process. In addition, the computational cost of FE model evaluations is still prodigious, making the updating process a computationally highly expensive endeavor, and the non-identifiability of parameters poses significant challenges in the model updating process. Some of these challenges are addressed in this dissertation.

Chapter 2 presents a framework for model updating and identifiability assessment of mechanics-based FE models. The discrepancy between the measured output and FE predicted response is modeled as a zero-mean Gaussian white noise independent across measurement channels in the updating framework. A FE model of a large-scale civil structural system will likely contain non-identifiable parameters. Methods based on the Fisher information matrix and global sensitivity analysis are formulated in Chapter 2 to detect the practically locally identifiable and influent parameters, respectively. The model updating and identifiability methodologies are applied to an idealized 2D nonlinear FE model of Pine flat concrete gravity

dam. Simulated data is used for model updating, and only uncertainty in input and output measurement data due to sensor measurement noise is considered in the data simulation stage. It is also shown that the non-identifiable model parameters can result in undesirable non-uniqueness in the parameter estimates when the inference is performed using methods that rely on point estimates (e.g., Kalman filter and its variants), motivating the need for model identifiability analysis before model updating in practice.

In Chapter 3, the model updating framework presented in Chapter 2 is extended to account for model form uncertainty focusing only on linear dynamic systems. Modeling the discrepancy between the measured output and FE predicted response as a zero-mean Gaussian white noise independent across measurement channels is not accurate in the presence of model form error. Accounting for model form uncertainty is highly challenging, especially in structural systems due to abundant possible modeling errors. The extended framework is based on the Kennedy and O'Hagan (KOH) approach – add a delta term to the measurement equation to explicitly account for the model form uncertainty. A novel power spectral density – covariance kernel pair based on random vibrations theory is proposed to capture common model discrepancy time histories arising in linear dynamic systems. The presented extended framework is validated on 1-DOF and 2-DOF simple structural benchmark problems using simulated data. Uncertainties due to measurement noise and modeling error are considered in data simulation. The model updating performed without the delta term (i.e., using the framework shown in Chapter 2) resulted in a posterior probability distribution of the unknown physical parameters the support of which does not contain the true parameter values. However, the calibration performed with the delta term (i.e., using the extended framework shown in Chapter 3) resulted in a posterior distribution of the unknown physical parameters whose support contains the true

parameter values. Thus, the extended framework enables the physical parameters to remain as such and not act as mere tuning parameters.

Chapter 4 describes computational hurdles in updating mechanics-based FE models of civil infrastructure systems and focuses on surrogate modeling to minimize the computational cost. Two types of surrogate modeling techniques, Gaussian process regression and polynomial chaos expansion, are considered in the chapter. The goal is to investigate the loss of accuracy and gain in computational time when performing model updating using direct FE evaluations versus surrogate evaluations. In this regard, the Greenup miter gate is used as the testbed structure, and three predominant damage modes are considered for the model updating. In addition, simulated measurement data is used for model updating, and only uncertainty due to measurement noise is considered for data simulation. For the considered miter gate testbed application, Bayesian FE model updating relying on surrogate model evaluations is ~4 times faster than when using direct FE model evaluations and provides relatively accurate posterior results (compared to those obtained using direct FE evaluations). Studies of the type presented in this chapter are necessary before entirely relying on surrogate models in Bayesian model updating to be used for SHM/DP purposes.

Most research in updating mechanics-based FE models focuses on simulated data. Chapter 5 attempts to validate the Bayesian FE model updating framework using experimental data. In this regard, a full-scale bridge column tested on the UC San Diego large high-performance outdoor shake table is selected as the testbed structure. The specimen was densely instrumented with a heterogenous sensor array to measure global and local responses of the system and was subjected to a series of ten earthquakes. Through this loading protocol, the specimen experienced various levels of nonlinearity from pristine condition to collapse. Thus,

the measurement dataset contains data of the structure at different nonlinear regimes throughout its life cycle and is ideal for validating the framework. Chapter 5 also illustrates the concept of a living digital twin.

6.2 Recommendations for Future Research

This dissertation scratches the surface of an emerging topic, cybermodeling based SHM/DP for optimal asset management of structural systems. Digital twins form the core of the cybermodel and Bayesian model updating framework used in this dissertation to develop digital twins of structural systems. Physics/mechanics-based models underpin the digital twin and are needed to bring the predictive capabilities to the cybermodels. There are four key phases in cybermodeling for SHM/DP: (1) Sensor placement and data collection, (2) Physics/mechanics-based modeling of the system/asset of interest, (3) Model updating using Bayesian inference, and (4) Decision making using the updated model (aka digital twin). Numerous challenges exist in each phase of cybermodeling that need to be studied further to enable robust SHM/DP of structural systems. The scope of research and/or challenges corresponding to each phase are described in the following subsections.

6.2.1 Sensor placement and data collection

Sensors are deployed on and around the system to collect input excitation (from various sources) and output response (at several locations) measurement data. Collecting the data from large-scale structural systems is generally challenged by susceptibility to environmental/operational changes and installation and maintenance concerns for the sensors and data acquisition system, resulting in the economically expensive part of model updating. The raw

data acquired from the sensors also need to be pre-processed (accessed, moved, organized, transformed, and cleansed) for FE model updating. Therefore, limited financial resources need to be allocated optimally. Significant research already exists in the literature for optimal sensor selection and sensor placement. This research needs to be extended to be applicable to large-scale civil structures. Ideally, the data collected from the optimally designed sensor array should enable detection of all the potential damage modes of the system and should possibly enable unique estimation of all the unknown parameters in the FE model updating phase.

6.2.2 Physics/mechanics-based modeling of the system

Identifying potential failure modes and the sequence of damage stages leading to the identified failure modes are essential aspects for the SHM/DP of any civil infrastructure system. Civil structures are complex and have several sequences of damage states that lead to failure. The potential failure modes need to be carefully studied for a system of interest and the FE model should be able to capture these potential damage and failure modes, preferably using mechanics-based modeling. Tremendous progress in FE modeling techniques and analysis methods over the last few decades enables us to appropriately capture the complex behavior of large-scale civil structural systems subjected to static, quasi-static, and dynamic loading, particularly in the case of natural hazards, such as earthquakes. Physics/mechanics-based nonlinear FE models of civil structural systems (e.g., buildings, bridges, dams, miter gates) can reasonably capture the damage and failure mechanisms developing in such systems under critical loading environments or due to progressive deterioration over time. Even though mechanics-based FE models are extensively used for design and analysis of civil infrastructure systems, they are seldom used for structural health monitoring and damage prognosis purposes. Future

research needs to focus on this aspect. Each civil structure is different; hence it needs a different FE model, and the model should be developed by an individual with domain knowledge (expert), i.e., the FE model should be vetted before being subjected to Bayesian updating and then used for SHM/DP purposes. Boundary conditions and initial conditions of the system should be carefully identified and should be appropriately imposed on the FE model for accurate SHM/DP. Thus, developing digital twins is currently an expert-driven task.

6.2.3 Model updating using Bayesian inference

FE model updating is a research area that has taken significant strides in the past decade. However, many hurdles for updating mechanics-based FE model of civil structures still remain and must be carefully studied. The major challenge is listing all the sources of uncertainty and appropriately accounting for them by suitably formulating the measurement equation in the Bayesian FE model updating framework. Some of the real-world uncertainties in civil structures are due to noisy output measurements, unknown/partially known/noisy input measurements, uncertainty in FE model parameters, FE model form uncertainty, environmental variability, and operational variability. Most research work in FE model updating of structural systems focused on accounting for measurement noise in input and output measurements using simulated data. Chapter 3 of this dissertation focused on accounting for model form uncertainty using the KOH approach but only applicable to linear dynamic FE models. More research is needed to develop a framework to account for model form error in nonlinear FE models – an extremely challenging task. Uncertainty due to environmental variability is another area less focused on in the literature. More work is needed to account and compensate for it appropriately in the model updating framework. This dissertation mainly considers a single measurement dataset (containing multiple

input and/or output measurement channels) for model updating using Bayesian inference. However, in some cases, multiple measurement datasets can be used simultaneously for model updating using the hierarchical Bayesian inference framework. This framework might allow to account comprehensively for all sources of uncertainty. This aspect needs to be carefully studied further. After a framework is developed to account properly for all sources of uncertainty, research is necessary to validate the framework using real measurement data in various nonlinear regimes of the structure to update a mechanics-based nonlinear FE model (that can capture the potential failure modes of the structure).

Bayesian FE model updating using simulation-based approaches is exceptionally computationally demanding as it requires repeated evaluation of an expensive-to-evaluate high-fidelity FE model. A few approaches can be used to mitigate the computational burden of FE model updating for large-scale structural systems. They include: (1) using efficient sampling algorithms, (2) leveraging parallel computing, (3) using reduced-order models or surrogate models, and (4) reducing the dimensionality of the unknown parameter vector $\boldsymbol{\theta}$. The repeated model evaluations in MCMC sampling (workhorse method for Bayesian inference) are sequential – not ideal for updating expensive-to-evaluate FE models. Sampling methods such as Transitional MCMC and particle filters progress sequentially in stages, and the repeated FE model evaluations within each stage can be performed in parallel. Other methods such as adaptive and multi-stage MCMC methods have been developed recently for efficient sampling of the posterior distribution. More research is needed to develop new efficient sampling algorithms tailored to update expensive-to-evaluate FE models. Software architectures/packages need to be developed that enable seamless integration of FE models (or numerical discretization of partial differential equations) with computational Bayesian methods for model updating. If the

algorithms support parallelization, one can leverage high-performance computing resources such as supercomputers to speed up the model updating process. Message passing interface (MPI) can be used to send parallel jobs (such as parallel FE model evaluations) on supercomputers.

Surrogate models as fast emulators of expensive-to-evaluate mathematical models is an area of research that has seen tremendous interest in recent years. Most research focused on surrogate modeling of linear and nonlinear FE models subject to static loading using machine learning models (e.g., neural networks, Gaussian processes, polynomial regression, and support vector machine). However, for comprehensive and robust SHM/DP purposes, surrogate modeling of linear and nonlinear FE models subject to dynamic loading should be addressed – an area still mainly untapped in the existing literature. Nonlinear FE models of civil structures are path-dependent. Thus, techniques such as GP-NARX (Gaussian processes – nonlinear autoregressive models with exogenous inputs), PCE-NARX (polynomial chaos expansion-NARX), and LSTM (long short-term memory) models can be leveraged to approximate the dynamic input-output behavior of nonlinear path-dependent FE models.

6.2.4 Decision making using the updated model

Decision-making is the most influential part of cybermodeling for SHM/DP and most important for the stakeholders. The Bayesian decision theory framework can be combined with the updated FE model (aka the digital twin) to enable robust risk-informed decision making for intelligent asset management – the goal of the cybermodel. More research is needed in this area.

6.3 Final Thoughts

A lot of research, industry-academia partnerships, and investments are needed to enable the development of robust digital twins at scale. We can envision a future where all the assets in a portfolio have their corresponding digital twins that dynamically update enabling robust and intelligent decision making at the portfolio level. This vision can be extrapolated for intelligent infrastructure management at the city or the country level. We still have a long way to go to achieve this objective.

References

Aldrich, J. (2002). “How Likelihood and Identification went Bayesian.” *International Statistical Review*, 70(1), 79–98.

American Society of Civil Engineers. (2021). *A Comprehensive Assessment of America’s Infrastructure*. *ASCE*.

Astroza, R., Alessandri, A., and Conte, J. P. (2019a). “A dual adaptive filtering approach for nonlinear finite element model updating accounting for modeling uncertainty.” *Mechanical Systems and Signal Processing*, Elsevier Ltd, 115, 782–800.

Astroza, R., Ebrahimian, H., and Conte, J. P. (2015). “Material parameter identification in distributed plasticity FE models of frame-type structures using nonlinear stochastic filtering.” *Journal of Engineering Mechanics, ASCE*, 141(5).

Astroza, R., Ebrahimian, H., and Conte, J. P. (2019b). “Performance comparison of Kalman−based filters for nonlinear structural finite element model updating.” *Journal of Sound and Vibration*, 438, 520–542.

Astroza, R., Ebrahimian, H., Conte, J. P., Restrepo, J. I., and Hutchinson, T. C. (2016). “System identification of a full-scale five-story reinforced concrete building tested on the NEES-UCSD shake table.” *Structural Control and Health Monitoring*, 23(3), 535–559.

Behmanesh, I., Moaveni, B., Lombaert, G., and Papadimitriou, C. (2015). “Hierarchical Bayesian model updating for structural identification.” *Mechanical Systems and Signal Processing*, Elsevier, 64–65, 360–376.

Bhrushundi, A., Hosseini, K., Lovett, S., and Rao, S. (2019). “Torus polynomials: An algebraic approach to ACC lower bounds.” *Leibniz International Proceedings in Informatics, LIPIcs*.

Bishop, C. M. (2006). *Pattern Recognition and Machine Learning*. Springer.

Blatman, G., and Sudret, B. (2011). “Adaptive sparse polynomial chaos expansion based on least angle regression.” *Journal of Computational Physics*, 230(6), 2345–2367.

Brand, B., Dollar, D. A., Hasan, H., Hernadez, L., Nuss, L. K., Rowell, R., and Willliam A, W. (2014). “Selecting Analytic Tools for Concrete Dams Adressing Key Events Along Potential Failure Mode Paths.” *FEMA P-1016*.

Brouwer, A. F., and Eisenberg, M. C. (2018). “The underlying connections between identifiability, active subspaces, and parameter space dimension reduction.” *arXiv:1802.05641*, 1–42.

Brynjarsdóttir, J., and O’Hagan, A. (2014). “Learning about physical parameters: the importance of model discrepancy.” *Inverse Problems*, 30(11), 114007.

Chatfield, C. (1995). “Model Uncertainty, Data Mining and Statistical Inference.” *Journal of the Royal Statistical Society. Series A (Statistics in Society)*, 158(3), 419–466.

Chatzi, E. N., and Smyth, A. W. (2009). “The unscented Kalman filter and particle filter methods for nonlinear structural system identification with non-collocated heterogeneous sensing.” *Structural Control and Health Monitoring*, 16(1), 99–123.

Chatzis, M. N., Chatzi, E. N., and Smyth, A. W. (2015). “On the observability and identifiability of nonlinear structural and mechanical systems.” *Structural Control and Health Monitoring*, 22(3), 574–593.

Ching, J., and Chen, Y. C. (2007). “Transitional Markov chain Monte Carlo method for Bayesian model updating, model class selection, and model averaging.” *Journal of Engineering Mechanics, ASCE*, 133(7), 816–832.

Chis, O.-T., Villaverde, A. F., Banga, J. R., and Balsa-Canto, E. (2016). “On the relationship between sloppiness and identifiability.” *Mathematical Biosciences*, 282, 147–161.

Chrisnata, J., Kiah, H. M., Rao, S., Vardy, A., Yaakobi, E., and Yao, H. (2019). “On the Number of Distinct k-Decks: Enumeration and Bounds.” *Proceedings - 2019 19th International Symposium on Communications and Information Technologies, ISCIT 2019*.

Constantine, P. G. (2015). *Active Subspaces*. *Active Subspaces*, Society for Industrial and Applied Mathematics, Philadelphia, PA.

Conte, J. P., Vijalapura, P. K., and Meghella, M. (2003). “Consistent Finite-Element Response Sensitivity Analysis.” *Journal of Engineering Mechanics, ASCE*, 129(12), 1380–1393.

Diakonikolas, I., Gouleakis, T., Kane, D. M., and Rao, S. (2019). “Communication and Memory Efficient Testing of Discrete Distributions.”

Dobre, S., Bastogne, T., and Richard, A. (2010). “Global sensitivity and identifiability implications in systems biology.” *IFAC Proceedings Volumes*, 43(6), 54–59.

Dodd, L. L., and Restrepo-Posada, J. I. (1995). “Model for Predicting Cyclic Behavior of Reinforcing Steel.” *Journal of Structural Engineering*, 121(3), 433–445.

Doebling, S. W., Farrar, C. R., and Prime, M. B. (1998). “A Summary Review of Vibration-Based Damage Identification Methods.” *The Shock and Vibration Digest*, 30(2), 91–105.

Ebrahimian, H., Astroza, R., and Conte, J. P. (2015). “Extended Kalman filter for material parameter estimation in nonlinear structural finite element models using direct differentiation method.” *Earthquake Engineering & Structural Dynamics*, 44(10), 1495–1522.

Ebrahimian, H., Astroza, R., Conte, J. P., and Bitmead, R. R. (2019). “Information-Theoretic Approach for Identifiability Assessment of Nonlinear Structural Finite-Element Models.” *Journal of Engineering Mechanics, ASCE*, 145(7), 04019039.

Ebrahimian, H., Astroza, R., Conte, J. P., and de Callafon, R. A. (2017). “Nonlinear finite element model updating for damage identification of civil structures using batch Bayesian estimation.” *Mechanical Systems and Signal Processing*, Elsevier, 84, 194–222.

Ebrahimian, H., Astroza, R., Conte, J. P., and Papadimitriou, C. (2018). “Bayesian optimal estimation for output-only nonlinear system and damage identification of civil structures.” *Structural Control and Health Monitoring*, 25(4).

Eick, B. A., Treece, Z. R., Spencer, B. F., Smith, M. D., Sweeney, S. C., Alexander, Q. G., and Foltz, S. D. (2018a). “Automated damage detection in miter gates of navigation locks.” *Structural Control and Health Monitoring*, 25(1), 1–18.

Eick, B. A., Treece, Z. R., Spencer, B. J. F., Smith, M. D., Sweeney, S. C., Alexander, Q. G., and

Foltz, S. D. (2018b). *Miter Gate Gap Detection Using Principal Component Analysis*. ERDC CHAMPAIGN United States.

Eisenberg, M. C., and Hayashi, M. A. L. (2014). "Determining identifiable parameter combinations using subset profiling." *Mathematical Biosciences*, 256, 116–126.

Estes, A. C., Frangopol, D. M., and Foltz, S. D. (2004). "Updating reliability of steel miter gates on locks and dams using visual inspection results." *Engineering Structures*, 26(3), 319–333.

Evans, J., Tallent, J., Brown, R., Netchaev, A., and Thurmer, C. (2019). *Determining miter gate plate corrosion and thickness of anti-corrosion coatings; and development of a mobile sensor inspection platform*. ERDC Vicksburg United States, MS.

Farrar, C. R., Doebling, S. W., and Nix, D. A. (2001). "Vibration–based structural damage identification." *Philosophical Transactions of the Royal Society of London. Series A: Mathematical, Physical and Engineering Sciences*, (N. A. J. Lieven and D. J. Ewins, eds.), 359(1778), 131–149.

Farrar, C. R., and Lieven, N. A. J. (2007). "Damage prognosis: the future of structural health monitoring." *Philosophical Transactions of the Royal Society A: Mathematical, Physical and Engineering Sciences*, 365(1851), 623–632.

Farrar, C. R., and Worden, K. (2007). "An introduction to structural health monitoring." *Philosophical Transactions of the Royal Society A: Mathematical, Physical and Engineering Sciences*, 365(1851), 303–315.

Farrar, C. R., and Worden, K. (2012). *Structural Health Monitoring*. *Structural Health Monitoring: A Machine Learning Perspective*, John Wiley & Sons, Ltd, Chichester, UK.

Foltz, S. D. (2017). *Investigation of Mechanical Breakdowns Leading to Lock Closures*. ERDC-CERL CHAMPAIGN United States.

Forrester, A. I. J., Sóbester, A., and Keane, A. J. (2008). *Engineering Design via Surrogate Modelling*. *Engineering Design via Surrogate Modelling*, Wiley.

Frangos, M., Marzouk, Y., Willcox, K., and van Bloemen Waanders, B. (2010). "Surrogate and reduced-order modeling: a comparison of approaches for large-scale statistical inverse problems." *Large-Scale Inverse Problems and Quantification of Uncertainty*, John Wiley & Sons, Ltd, Chichester, UK, 123–149.

Ghahramani, Z. (2013). "Bayesian non-parametrics and the probabilistic approach to modelling." *Philosophical Transactions of the Royal Society A: Mathematical, Physical and Engineering Sciences*, 371(1984), 20110553.

Goulet, J. A., and Smith, I. F. C. (2013). "Structural identification with systematic errors and unknown uncertainty dependencies." *Computers & Structures*, Elsevier Ltd, 128, 251–258.

Goulet, J. A., Texier, M., Michel, C., Smith, I. F. C., and Chouinard, L. (2014). "Quantifying the Effects of Modeling Simplifications for Structural Identification of Bridges." *Journal of Bridge Engineering*, 19(1), 59–71.

Government Accountability Office. (2018). *Assessing Risks and Measuring Performance Could Improve Maritime Transportation.* GAO-18-610.

Gramacy, R. B. (2020). *Surrogates: Gaussian Process Modeling, Design, and Optimization for*

the Applied Sciences. Chapman and Hall/CRC.

Hall, J. F., and Chopra, A. K. (1980). "Dynamic response of embankment concrete-gravity and arch dams including hydrodynamic interaction." *Report No. UCB/EERC-80/39, Earthquake Engineering Research Center, University of California, Berkeley, CA*.

Hastie, T., Tibshirani, R., and Friedman, J. (2009). *The Elements of Statistical Learning - Dama Mining, Inference, and Prediction*. Springer series in statistics New York.

Hemez, F. M., and Farrar, C. R. (2014). "A Brief History of 30 Years of Model Updating in Structural Dynamics." *Conference Proceedings of the Society for Experimental Mechanics Series*, 53–71.

Heredia-Zavoni, E., and Esteva, L. (1998). "Optimal instrumentation of uncertain structural systems subject to earthquake ground motions." *Earthquake Engineering & Structural Dynamics*, 27(4), 343–362.

Hines, K. E., Middendorf, T. R., and Aldrich, R. W. (2014). "Determination of parameter identifiability in nonlinear biophysical models: A Bayesian approach." *The Journal of General Physiology*, 143(3), 401–416.

Hofstetter, G., Simo, J. C., and Taylor, R. L. (1993). "A modified cap model: Closest point solution algorithms." *Computers and Structures*, 46(2), 203–214.

Hu, Z., and Mahadevan, S. (2019). "Probability models for data-Driven global sensitivity analysis." *Reliability Engineering & System Safety*, 187, 40–57.

Jaynes, E. T. (1968). "Prior probabilities." *IEEE Transactions on Systems Science and Cybernetics*, IEEE, 4(3), 227–241.

Jin, S.-S., and Jung, H.-J. (2016). "Sequential surrogate modeling for efficient finite element model updating." *Computers & Structures*, Elsevier Ltd, 168, 30–45.

Jung, D., Ramanan, N., Amjadi, M., Karingula, S. R., Taylor, J., and Coelho Jr, C. N. (2021). "Time Series Anomaly Detection with label-free Model Selection."

Kadry, S. (2012). "Diagnostics and prognostics of engineering systems: Methods and techniques." *Diagnostics and Prognostics of Engineering Systems: Methods and Techniques*, (November), 1–433.

Kane, D., Lovett, S., and Rao, S. (2019). "The Independence Number of the Birkhoff Polytope Graph, and Applications to Maximally Recoverable Codes." *SIAM Journal on Computing*.

Kane, D., and Rao, S. (2018). "A PRG for boolean PTF of degree 2 with seed length subpolynomial in E and logarithmic in N." *Leibniz International Proceedings in Informatics, LIPIcs*.

Karingula, S. R., and Lovett, S. (2020). "Singularity of random integer matrices with large entries."

Karingula, S. R., Ramanan, N., Tahmasbi, R., Amjadi, M., Jung, D., Si, R., Thimmisetty, C., Cabrera, L. P., Sayer, M., and Coelho Jr, C. N. (2021). "Boosted Embeddings for Time Series Forecasting."

Kay, S. M. (1993). *Fundamentals of Statistical Signal Processing: Estimation Theory*. *Prentice-Hall, Inc.*

Kemp, F. (2003). “An Introduction to Sequential Monte Carlo Methods.” *Journal of the Royal Statistical Society: Series D (The Statistician)*, 52(4), 694–695.

Kennedy, M. C., and O’Hagan, A. (2001). “Bayesian calibration of computer models.” *Journal of the Royal Statistical Society: Series B (Statistical Methodology)*, 63(3), 425–464.

Kirkegaard, P. H., and Brincker, R. (1994). “On the optimal location of sensors for parametric identification of linear structural systems.” *Mechanical Systems and Signal Processing*, 8(6), 639–647.

Kucherenko, S., and Iooss, B. (2017). “Derivative-Based Global Sensitivity Measures.” *Handbook of Uncertainty Quantification*, Springer International Publishing, Cham, 1241–1263.

Kucherenko, S., Rodriguez-Fernandez, M., Pantelides, C., and Shah, N. (2009). “Monte Carlo evaluation of derivative-based global sensitivity measures.” *Reliability Engineering & System Safety*, 94(7), 1135–1148.

Lei, C. L., Ghosh, S., Whittaker, D. G., Aboelkassem, Y., Beattie, K. A., Cantwell, C. D., Delhaas, T., Houston, C., Novaes, G. M., Panfilov, A. V., Pathmanathan, P., Riabiz, M., dos Santos, R. W., Walmsley, J., Worden, K., Mirams, G. R., and Wilkinson, R. D. (2020). “Considering discrepancy when calibrating a mechanistic electrophysiology model.” *Philosophical Transactions of the Royal Society A: Mathematical, Physical and Engineering Sciences*, 378(2173), 20190349.

Li, J., and Marzouk, Y. M. (2014). “Adaptive construction of surrogates for the Bayesian solution of inverse problems.” *SIAM Journal on Scientific Computing*, SIAM, 36(3), A1163–A1186.

Liu, H., Cai, J., and Ong, Y.-S. (2017). “An adaptive sampling approach for Kriging metamodeling by maximizing expected prediction error.” *Computers & Chemical Engineering*, Elsevier Ltd, 106, 171–182.

Lovett, S., Rao, S., and Vardy, A. (2018). “Probabilistic existence of large sets of designs.” *Proceedings of the Annual ACM-SIAM Symposium on Discrete Algorithms*.

Lovett, S., Rao, S., and Vardy, A. (2020). “Probabilistic existence of large sets of designs.” *Journal of Combinatorial Theory. Series A*.

Lutes, L. D., and Sarkani, S. (2004). *Random Vibrations: Analysis of Structural and Mechanical Systems*. Elsevier.

McKenna, F., Fenves, G. L., and Scott, M. H. (2000). “Open System for Earthquake Engineering Simulation.”

Melchers, R. E. (2004). “Mathematical modeling of the effect of water velocity on the marine immersion corrosion of mild steel coupons.” *Corrosion*, 60(5), 471–478.

van der Merwe, R., and Wan, E. (2004). “Sigma-Point Kalman Filters for Probabilistic Inference in Dynamic State-Space Models.” *Ph.D. Dissertation, OGI School of Science & Engineering, Oregon Health & Science University*.

Minson, S. E., Simons, M., and Beck, J. L. (2013). “Bayesian inversion for finite fault earthquake source models I—theory and algorithm.” *Geophysical Journal International*,

194(3), 1701–1726.

Moaveni, B., He, X., Conte, J. P., and Restrepo, J. I. (2010). "Damage identification study of a seven-story full-scale building slice tested on the UCSD-NEES shake table." *Structural Safety*, Elsevier Ltd, 32(5), 347–356.

Moaveni, B., He, X., Conte, J. P., Restrepo, J. I., and Panagiotou, M. (2011). "System Identification Study of a 7-Story Full-Scale Building Slice Tested on the UCSD-NEES Shake Table." *Journal of Structural Engineering, ASCE*, 137(6), 705–717.

Papadimitriou, C., Beck, J. L., and Au, S.-K. (2000). "Entropy-Based Optimal Sensor Location for Structural Model Updating." *Journal of Vibration and Control*, 6(5), 781–800.

Plumlee, M. (2017). "Bayesian Calibration of Inexact Computer Models." *Journal of the American Statistical Association*, Taylor & Francis, 112(519), 1274–1285.

Popovics, S. (1973). "A numerical approach to the complete stress-strain curve of concrete." *Cement and Concrete Research*, Pergamon, 3(5), 583–599.

Ramancha, M. K., Astroza, R., Conte, J. P., Restrepo, J. I., and Todd, M. D. (2020a). "Bayesian nonlinear finite element model updating of a full-scale bridge-column using sequential monte carlo." *Model Validation and Uncertainty Quantification*, 389–397.

Ramancha, M. K., Astroza, R., Madarshahian, R., and Conte, J. P. (2022). "Bayesian updating and identifiability assessment of nonlinear finite element models." *Mechanical Systems and Signal Processing*, 167, 108517.

Ramancha, M. K., Madarshahian, R., Astroza, R., and Conte, J. P. (2020b). "Non-unique Estimates in Material Parameter Identification of Nonlinear FE Models Governed by Multiaxial Material Models Using Unscented Kalman Filtering." *Conference Proceedings of the Society for Experimental Mechanics Series*, 257–265.

Rao, K. S., and Prabhakaran, V. M. (2014). "A New Upperbound for the Oblivious Transfer Capacity of Discrete Memoryless Channels." *IEEE Information Theory Workshop*.

Rao, S., and Vardy, A. (2016). "Lower Bound on the Redundancy of PIR Codes."

Rasmussen, C. E., and Williams, C. K. I. (2005). *Gaussian Processes for Machine Learning*. The MIT Press.

Raue, A., Kreutz, C., Maiwald, T., Bachmann, J., Schilling, M., Klingmüller, U., and Timmer, J. (2009). "Structural and practical identifiability analysis of partially observed dynamical models by exploiting the profile likelihood." *Bioinformatics*, 25(15), 1923–1929.

Raue, A., Kreutz, C., Theis, F. J., and Timmer, J. (2013). "Joining forces of Bayesian and frequentist methodology: a study for inference in the presence of non-identifiability." *Philosophical Transactions of the Royal Society A: Mathematical, Physical and Engineering Sciences*, 371(1984), 20110544.

Rea, D., Liaw, C. Y., and Chopra, A. K. (1974). "Mathematical models for the dynamic analysis of concrete gravity dams." *Earthquake Engineering & Structural Dynamics*, 3(3), 249–258.

Rothenberg, T. J. (1971). "Identification in Parametric Models." *Econometrica*, 39(3), 577.

Saltelli, A. (2002). "Making best use of model evaluations to compute sensitivity indices." *Computer Physics Communications*, 145(2), 280–297.

Saltelli, A., Annoni, P., Azzini, I., Campolongo, F., Ratto, M., and Tarantola, S. (2010). "Variance based sensitivity analysis of model output. Design and estimator for the total sensitivity index." *Computer Physics Communications*, 181(2), 259–270.

Saltelli, A., Ratto, M., Andres, T., Campolongo, F., Cariboni, J., Gatelli, D., Saisana, M., and Tarantola, S. (2007). *Global Sensitivity Analysis. The Primer*. *Global Sensitivity Analysis. The Primer*, John Wiley & Sons, Ltd, Chichester, UK.

San Martın, E., and González, J. (2010). "Bayesian identifiability: Contributions to an inconclusive debate." *Chilian Journal of Statistics*, 1(2), 69–91.

Sandler, I. S., Dimaggio, F. L., and Baladi, G. Y. (1976). "Generalized Cap Model for Geological Materials." *Journal of the Geotechnical Engineering Division, ASCE*, 102(7), 683–699.

Santner, T. J., Williams, B. J., Notz, W. I., and Williams, B. J. (2003). *The design and analysis of computer experiments*. Springer.

Sargsyan, K., Huan, X., and Najm, H. N. (2019). "Embedded Model Error Representation for Bayesian Model Calibration." *International Journal for Uncertainty Quantification*, 9(4), 365–394.

Sargsyan, K., Najm, H. N., and Ghanem, R. (2015). "On the Statistical Calibration of Physical Models." *International Journal of Chemical Kinetics*, 47(4), 246–276.

Sarkka, S. (2013). *Bayesian Filtering and Smoothing*. *Bayesian Filtering and Smoothing*, Cambridge University Press, Cambridge.

Schoettler, Restrepo, Guerrini, D. C. (2015). "A Full-Scale, Single-Column Bridge Bent Tested by Shake-Table Excitation." *PEER Report*, 11(3), 555–565.

Scott, M. H., and Haukaas, T. (2008). "Software Framework for Parameter Updating and Finite-Element Response Sensitivity Analysis." *Journal of Computing in Civil Engineering, ASCE*, 22(5), 281–291.

Shen, Z. (2019). "Spectral kernels for Gaussian processes." Aalto University.

Simo, J. C., Ju, J., Pister, K. S., and Taylor, R. L. (1988). "Assessment of cap model: consistent return algorithms and rate-dependent extension." *Journal of Engineering Mechanics, ASCE*, 114(2), 191–218.

Simoen, E., Papadimitriou, C., and Lombaert, G. (2013). "On prediction error correlation in Bayesian model updating." *Journal of Sound and Vibration*, Elsevier, 332(18), 4136–4152.

Simon, D. (2006). *Optimal State Estimation*. *Optimal State Estimation: Kalman, H∞, and Nonlinear Approaches*, John Wiley & Sons, Inc., Hoboken, NJ, USA.

Smith, R. C. (2013). *Uncertainty Quantification: Theory, Implementation, and Applications*. Siam.

Sobol', I. M. (2001). "Global sensitivity indices for nonlinear mathematical models and their Monte Carlo estimates." *Mathematics and Computers in Simulation*, 55(1–3), 271–280.

Sobol', I. M., and Kucherenko, S. (2009). "Derivative based global sensitivity measures and their link with global sensitivity indices." *Mathematics and Computers in Simulation*, 79(10), 3009–3017.

Spencer, B. F., Hoskere, V., and Narazaki, Y. (2019). “Advances in computer vision-based civil infrastructure inspection and monitoring.” *Engineering*, Chinese Academy of Engineering, 5(2), 199–222.

Stuart, A. M. (2010). “Inverse problems: A Bayesian perspective.” *Acta Numerica*, 19(May 2010), 451–559.

Sudret, B. (2007). “Uncertainty propagation and sensitivity analysis in mechanical models–Contributions to structural reliability and stochastic spectral methods.” *Habilitation à Diriger des Recherches, Université Blaise Pascal, Clermont-Ferrand, France*.

Sudret, B. (2014). “Polynomial chaos expansions and stochastic finite element methods.” *Risk and reliability in geotechnical engineering*, CRC Press Boca Raton, FL, 265–300.

Takhtaganov, T., and Müller, J. (2018). “Adaptive Gaussian process surrogates for Bayesian inference.” *arXiv:1809.10784v1*.

Tarantola, A. (2005). *Inverse Problem Theory and Methods for Model Parameter Estimation*. Society for Industrial and Applied Mathematics.

Taucer, F. F. (2019). “A Fiber Beam-Column Element for Seismic Response Analysis of Reinforced Concrete Structures A FIBER BEAM-COLUMN ELEMENT FOR SEISMIC RESPONSE ANALYSIS by Research Assistant Enrico Spacone and Filip C . Filippou Associate Professor Department of Civil Engin.” (December 2014).

Udwadia, F. E. (1994). “Methodology for Optimum Sensor Locations for Parameter Identification in Dynamic Systems.” *Journal of Engineering Mechanics, ASCE*, 120(2), 368–390.

Vega, M. A., Ramancha, M. K., Conte, J. P., and Todd, M. D. (2020). “Efficient Bayesian Inference of Miter Gates Using High-Fidelity Models.” *Model Validation and Uncertainty Quantification*, 375–382.

Vega, M. A., and Todd, M. D. (2020). “A variational Bayesian neural network for structural health monitoring and cost-informed decision-making in miter gates.” *Structural Health Monitoring*, SAGE Publications Sage UK: London, England, (Special Issue: A Value of Information Perspective), 1–15.

Wechsler, S., Izbicki, R., and Esteves, L. G. (2013). “A Bayesian Look at Nonidentifiability: A Simple Example.” *The American Statistician*, 67(2), 90–93.

Wilson, A., and Adams, R. (2013). “Gaussian process kernels for pattern discovery and extrapolation.” *International conference on machine learning*, PMLR, 1067–1075.

Wolpert, R. L., Liseo, B., and Berger, J. O. (1999). “Integrated likelihood methods for eliminating nuisance parameters.” *Statistical Science*, Institute of Mathematical Statistics, 14(1), 1–28.

Woodbury, D., and Junkins, J. (2010). “On the Consider Kalman Filter.” *AIAA Guidance, Navigation, and Control Conference*, American Institute of Aeronautics and Astronautics, Reston, Virigina.

Yang, J. N., Xia, Y., and Loh, C.-H. (2014). “Damage Detection of Hysteretic Structures with a Pinching Effect.” *Journal of Engineering Mechanics, ASCE*, 140(3), 462–472.

Yucesan, Y. A., Von Zuben, A., Viana, F., and Mahfoud, J. (2020). “Estimating Parameters and Discrepancy of Computer Models with Graphs and Neural Networks.” *AIAA AVIATION 2020 FORUM*, American Institute of Aeronautics and Astronautics, Reston, Virginia, 1–14.

Yuen, K.-V., and Kuok, S.-C. (2015). “Efficient Bayesian sensor placement algorithm for structural identification: a general approach for multi-type sensory systems.” *Earthquake Engineering & Structural Dynamics*, 44(5), 757–774.

Yuen, K. V. (2010). *Bayesian Methods for Structural Dynamics and Civil Engineering*. John Wiley & Sons, Ltd, Chichester, UK.

Zhou, C., Liu, F., Tang, C., and Wang, W. (2017). “Global Sensitivity Analysis of Uncertain Input Variables in Structural Models.” *Journal of Engineering Mechanics, ASCE*, 143(12), 04017138.